Advanced Perspectives in the Vapor-Phase Deposition of Multifunctional Metal Oxide Nanomaterials

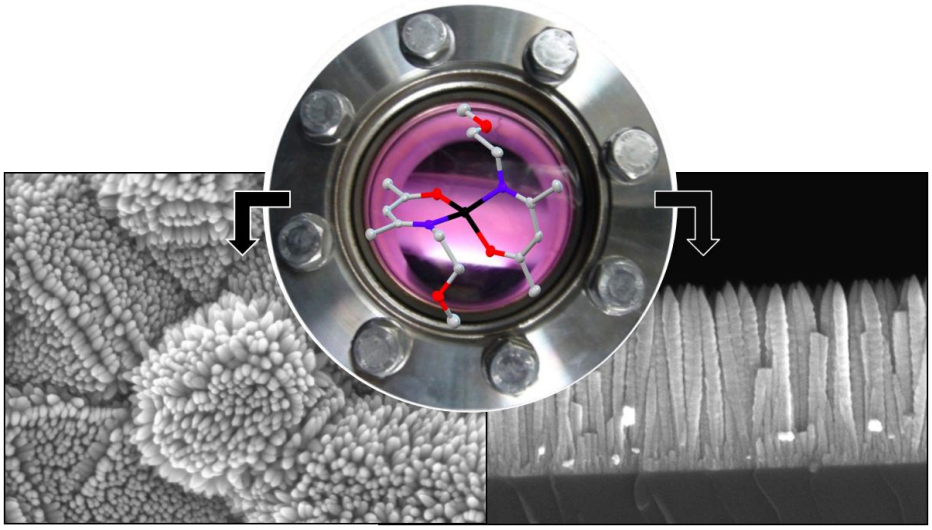

Dissertation

Daniela Bekermann

Advanced Perspectives in the Vapor-Phase Deposition of Multifunctional Metal Oxide Nanomaterials

Dissertation

zur Erlangung der Doktorwürde

der Fakultät für Chemie der Ruhr-Universität Bochum

vorgelegt von

M.Sc. Daniela Bekermann

Bochum, April 2012

This dissertation is based on the experimental work carried out during the period from August 2008 to July 2011 under the supervision of Prof. Dr. R. A Fischer at the Chair of Inorganic Chemistry II, *Organometallics & Materials*, Ruhr-University Bochum, Germany.

Referees

Prof. Dr. Roland A. Fischer
Dr. Davide Barreca

Herewith I declare that I have written this thesis myself and without any other help or sources which are not specifically and explicitly marked or named in this dissertation. Furthermore, I declare that I have not applied to any other review procedure or submitted this thesis in the same, similar or different form to another faculty or university as a dissertation.

Daniela Bekermann.

Meinen Eltern - Dirk und Monika Bekermann

Wissenschaft:

„*Die systematische Klassifizierung der Erfahrung*.“ - Sinclair Lewis

„*Die Voraussicht von Wiederholungen.*“ - Antoine de Saint-Exupéry

„*Ein erstklassiges Möbelstück für das Oberstübchen eines Mannes, der gesunden Menschenverstand im Erdgeschoß hat.*“ - Oliver Wendell Holmes sen.

Mein besonderer Dank gilt *Prof. Dr. Roland Augustinus Fischer*, für das entgegengebrachte Vertrauen in meine Arbeit, die gewährten Freiheiten, und vor allem für die Motivation und Perspektiven, die er mir in meiner Promotionszeit gegeben hat.

Acknowledgements

Prior to all, I want to thank my supervisors *Prof. R. A. Fischer* and *Dr. D. Barreca*, who, by their complementary teaching and leading personalities, view of life and great kindness, made it not only possible for me, to learn a great deal of chemistry and materials science but also for life.

I also greatly acknowledge *Prof. A. Devi* and *Dr. A. Gasparotto* who always found the time for scientific discussions, practical help and their great support in general.

Researchers who shared work, beers and spritz with me are overall *Dr. M. Walawalkar*, *Dott. M. Gavagnin* and *Dr. Q. Simon*.

A big "thank you" is dedicated to *S. Pankau* for her support in administrative issues and her positive spirit.

I want to thank all co-workers and collaboration partners who contributed to this work:

- *Prof. E. Comini* and *Prof. G. Sberveglieri* for the cooperation in gas sensing measurements
- *Dr. V. Gombac* and *Prof. P. Fornasiero* for the photocatalytic H_2 production testings
- *Prof. U. Lavrenčič-Štangar* for PSH and PCO characterizations
- *Prof. C. Sada* for SIMS measurements
- *Dr. O. I. Lebedev, Dr. S. Turner* and *Prof. G. Van Tendeloo* for TEM analyses
- *Dr. C. Maccato* for the excellent FE-SEM measurements and Italian food
- *Dr. A. Ludwig* who performed PL measurements with me
- *Dr. D. Rogalla* and *Dr. H.-W. Becker* for performing and teaching RBS
- *K. Xu* and *M. Banerjee* for zinc precursor supply

I want to thank all the members of the ACII group and the Padova group for the good working atmosphere. Special thanks are dedicated to the former *office 2/26*, for an unforgettable time at and outside the RUB, and their friendship.

For their continuous support and motivation during the last years, I want to thank *my family* and *Marco*.

These research activities have received funding from

- the European Community's 7^{th} Framework Program (FP7/2007-2013, grant agreement n° ENHANCE-238409).
- Collaborative Research Centre (SFB) 558: Metal-substrate interactions in heterogeneous catalysis.

I greatly acknowledge everybody who supported me, applying for the grants, namely *Prof. Dr. Roland A. Fischer, Dr. Davide Barreca, Prof. Anjana Devi, Dr. Mrinal Walawalkar* and *Dr. Erik Bründermann*.

Table of Contents

List of Abbreviations

1	$[Zn\{[(CH_3OCH_2CH_2)N]C(CH_3)=C(H)C(CH_3)=O\}_2]$
2	$[Zn\{[(CH_3OCH_2CH_2CH_2)N]C(CH_3)=C(H)C(CH_3)=O\}_2]$
3	$[Co(dpm)_2]$
4	$[Co(hfa)_2 \cdot TMEDA]$
1D, 2D, 3D	one dimensional, two dimensional, three dimensional

A

α	Auger parameter, absorption coefficient
A	area, absorbance
acac	acetylacetonate
AFM	Atomic Force Microscopy
at.	atomic
ALD	Atomic Layer Deposition

B

β	heating rate
B_0	magnetic field
BE	binding energy
Bu	butyl
^{n}Bu	*n*-butyl
^{t}Bu	*tert*-butyl

C

CVD	Chemical Vapor Deposition
Cp	cyclopentadienyl

D

d	distance between crystal planes, diameter, crystallite size
DEA	*N*,*N*'-diethylethylenediamine
DEZ	diethylzinc
DMAEH	2-dimethylaminoethanol
DMAPH	dimethylamino-2-propanol
DMZ	dimethylzinc
dpm	2,2,6,6-tetramethyl-3,5-heptanedionate
DTA	Differential Thermal Analysis

E

e^-	electron

E	energy
E_C	conduction band
E_F	Fermi level
E_g	band gap
E_V	valence band
EA	Elemental Analysis
EDXS	Energy Dispersive X-ray Spectroscopy
EELS	Electron Energy Loss Spectroscopy
EI-MS	Electron Impact Mass Spectrometry
Et	ethyl

F

FE-SEM	Field Emission SEM
FT-IR	Fourier Transform Infrared Spectroscopy
FWHM	full width at half-maximum

G

γ	magnetogyric constant
G	conductance
GB	grain boundary
GC	Gas Chromatography
GIXRD	Glancing Incidence XRD
GR	growth rate

H

h	Planck constant
h^+	hole
HAADF	high angle annular dark field
HEC	hydroxyethyl-cellulose
hfa	1,1,1,5,5,5-hexafluoro-2,4-pentanedionate
HR-TEM	high resolution-TEM
HOTPA	hydroxyterephthalic acid
HPLC-FLD	High Performance Liquid Chromatography with Fluorescence Detection

I

I	Intensity
JCPDS	Joint Committee on Powder Diffraction Standards
IR	infrared

K

k	rate constant
KE	kinetic energy

L

λ	wavelength
L	ligand
L_d	Debye length

M

m	mass
μ	magnetic moment
Me	methyl
MBE	Molecular Beam Epitaxy
MFC	mass flow controller
m.p.	melting point

N

n	integer number
v	frequency
NP	nanoparticle
NaTPA	sodium terephthalate
NMR	Nuclear Magnetic Resonance Spectroscopy
NR	nanorod

O

O_i	interstitial oxygen

P

p	pressure
P	power
PC	photocatalysis
PCO	photocatalytic oxidation
PE	primary electron
PECVD	Plasma Enhanced CVD
Ph	phenyl
PL	Photoluminescence (Spectroscopy)
PLD	Pulsed Laser Deposition
Pr	propyl
^{i}Pr	*iso*-propyl
PSH	photo-induced superhydrophilicity
θ	generic angle

Q

Φ	work function

Q	Selectivity

R

R	resistance
RBS	Rutherford Backscattering Spectroscopy
RF	radio frequency
RMS	root mean square
RT	room temperature

S

S	atomic sensitivity factor, sensor response
σ	electron shielding, chemical shift
SC	semiconductor
SE	secondary electron
SEM	Scanning Electron Microscopy
SF	stacking fault
SIMS	Secondary Ion Mass Spectrometry
S/N	signal-to-noise (ratio)
SPR	Surface Plasmon Resonance
STEM	Scanning Transmission Electron Microscopy

T

t	time, thickness
T	temperature, transmittance
T_{vap}	evaporation temperature
THF	tetrahydrofuran
THP	tetrahydropyran
TEM	Transmission Electron Microscopy
tetraglyme	$Me(OCH_2CH_2)_4OMe$
TG	Thermogravimetry
TMEDA	*N*,*N*,*N'*,*N'*-tetramethylethylenediamine
tmp	2,2,6,6-tetramethylpiperidino
TMP	turbo molecular pump
TMS	trimethylsilyl group
TPA	terephthalic acid
tta	2-theonyltrifluoroacetonate

U

UV	ultraviolet

V

V_O	oxygen vacancy

V_{Zn}	zinc vacancy
Vis	visible

W

ω	Larmor frequency, resonance frequency
WCA	water contact angle
WT	working temperature

X

$\boldsymbol{x}$	molar fraction
XE-AES	X-ray Excited Auger Electron Spectroscopy
XPS	X-ray Photoelectron Spectroscopy
XRD	X-ray Diffraction

Z

z	ion charge
Zn_i	interstitial zinc

1. Introduction

❖ 1.1 Introduction

The assignment "nano" is usually given to materials whose structural features exhibit at least one dimension in the sub-100-nanometer range, consisting of a few hundred of thousands of atoms or molecules. [*Cademartiri-2009, Elias-2010, Herron-1998, Rao-2004*] Size (i.e. the scale threshold) however, is not everything, since even nanomaterials physico-chemical properties vary significantly from those of the bulk counterparts, [*Rao-2004*, *Herron-1998*] resulting in unique functional characteristics for a variety of applications. [*Barreca-2011-A, Barreca-2011-B, Bekermann-2010-A, Choy-2003, Curri-2010, Gasparotto-2011, Rao-2004, Tricoli-2009, Trindade-2001, Wang-2011-A, Xia-2003*] Nanosystem design and fabrication, especially for metal oxide based materials, are generally performed to attain the following main attributes:

(i) A high surface area, usually related to an enhanced reactivity. This feature is of outermost importance in surface sensitive processes, such as catalysis, photocatalysis and gas sensing. [*Barreca-2011-B, Lee-2009-A, Özgür-2005, Shifu-2009, Si-2006, Trindade-2001*]

(ii) Quantum confinement effects, mainly exploited for photo-activated processes and sensing, since variations in nanoparticle sizes result in significant alterations of the charge carrier behaviour. [*Barreca-2011-B, Curri-2010, Gong-2000, Lee-2009-A, Özgür-2005, Rao-2004, Trindade-2001, Zhuge-2010*]

(iii) Control of surface active sites and defects incorporation, a useful mean to tailor the system chemical, physical and functional properties. [*Dong-2008, Du-2008, Fu-2007-A, Rao-2004*]

As a matter of fact, nano-physics and nano-chemistry are governed by many factors, like material composition, structure and morphological organization, [*Cademartiri-2009, Elias-2010, Rao-2004*] and their control promises new perspectives both in science and in technology. [*Chithrani-2009, Elias-2010, Hu*-2008, *Özgür-2005, Rao-2004*] As a consequence, various types of nanostructures, supported or unsupported, ranging from 0D to 2D materials (see **figure 1.1**), have been synthesized and thoroughly investigated.

0D nanocrystals have reduced sizes (below 100 nm) in all three dimensions and their size and shape determine their functionality. For example, peculiar optical properties like Surface Plasmon Resonance are directly determined by the nanoparticle (NP) shape,

dimensions and mutual interactions. [*Seyed-Razavi-2010*] In addition, NP size and exposed facets are known to affect the system catalytic activity and selectivity. [*Seyed-Razavi-2010*] Furthermore, gas sensing performances of metal oxide nanomaterials can be greatly enhanced when one of the characteristics becomes comparable or smaller than the Debye length[1]. [*Lee-2009-B*, *Barreca-2010-A*]

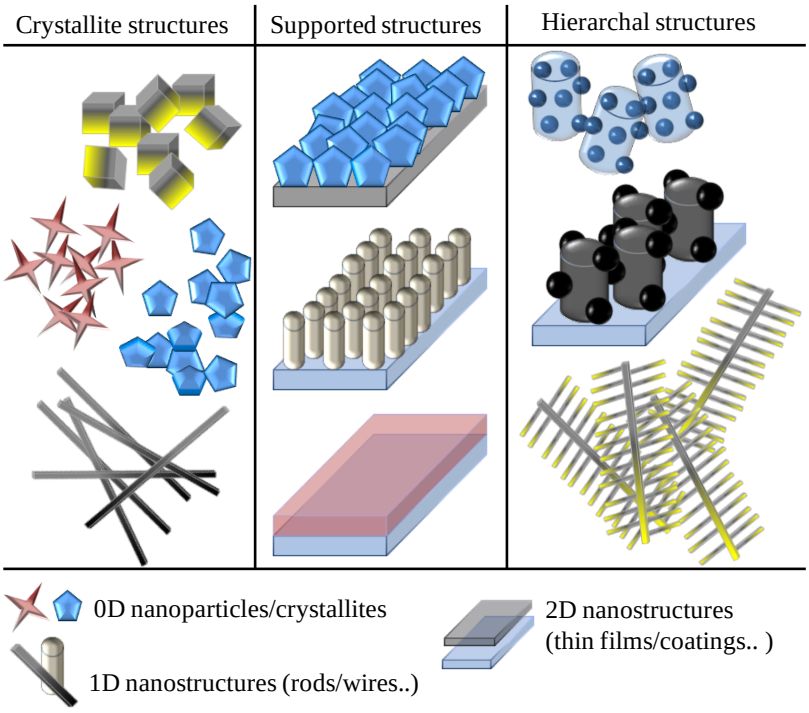

Figure 1.1: Sketch of various types of nanosystems.

In the past years, increasing interest was dedicated to the development and investigation of 1D nanostructures due to their various outstanding properties. [*Comini-2009-A*, *Özgür-2005*, *Prades-2009*] For instance, ZnO nanowires showed superior photo-detection performances compared to 2D ZnO thin films. [*Prades-2008*] This result was attributed to various factors, including a prolonged lifetime of the photo-generated carriers and an improved trapping of the incident photons in comparison to ZnO thin films. [*Prades-2008*] ZnO NR arrays have also received considerable attention for their advanced photo-activated functions, regarding, in particular, photo-induced superhydrophilicity (PSH), for

[1] The Debye length is the scale over which significant charge separation is probable. In the case of semiconductors, the electrical conductivity processes are dependent on this parameter, being $L_D = [(k\ T\ \varepsilon) / (q^2\ n)]^{1/2}$, where k is the Boltzmann constant, T the temperature, ε the dielectric constant, q the electron charge and n the carrier concentration. [*Comini-2009-A*, *Mizsei-1995*, *Ogawa-1982*]

self-cleaning applications, and photocatalysis (PC), for pollutant degradation. [*Badre-2009*, *Liu-2009-A*, *Sun-2005*, *Wan-2005*]

2D nanodeposits, such as supported nanostructure and thin films, are also widely used as functional coatings, from corrosion protection up to microelectronics and photovoltaic applications. [*Choy-2003*, *Hsieh-2008*]

Apart from 0D particles, 1D materials and 2D films, more complex systems, like hierarchal structures (**figure 1.1**), have gained growing attention for the direct dependence of their properties on spatial organization. [*Lee-2009-A*, *Morkoç-2009*] For instance, it was demonstrated that the use of these assemblies can be beneficial for gas sensing applications, by providing a high surface area and nanosize effects along with effective gas diffusion toward the entire sensing surfaces *via* the porous structures. [*Lee-2009-A*]

Increasing efforts have also been focused on the preparation of nanoheterostructures. [*Bekermann-2012*, *Higashiwaki-2009*, *Lee-2009-A*, *Meyyappan-2009*, *Na-2011*, *Simon-2011*] In fact, the combination of the advantages of nanoscale materials combined with the synergistic coupling of the component features, paves the way to the development of systems endowed with unprecedented properties. [*Fu-2007-A*, *Kim-2005-A*, *Gao-2005*] In this context, among the various systems, ZnO-Co_3O_4 systems have received attention for their magnetic, [*Martín-González-2008*] catalytic, [*Llorca-2008*, *Rubio-Marcos-2010*] photocatalytic [*Kanjwal-2011*] and gas sensing properties. [*Na-2011*] In addition, two main aspects to be considered in heterostructures are the formations of Schottky and *p*/*n* junctions, occuring at metal/semiconductor (SC) and *p*/*n*-type SC interfaces, respectively. These phenomena typically result in rectifiying effects and enhanced electron/hole (e^-/h^+) separation, with a favourable impact especially on photocatalytic and sensing performances. [*Bekermann-2012*, *Kim-2005-A*, *Na-2011*, *Shifu-2009*, *Simon-2011*] Particularly in the nanoregime, interactions resulting from the contact of two components are of great importance, since a high spatial density of interfaces is generated when the components are brought in intimate contact. [*Fu-2007-A*]

Basing on the above considerations, the design of multifunctional oxide nanomaterials requires the development of proper synthetic procedures, enabling a fine control of their chemico-physical features, and characterized by a low environmental impact.

❖ 1.2 Thesis Outline

❖ 1.2.1 Application Fields and Open Challenges

In this thesis, the development of multifunctional nanomaterials (based on ZnO, Co_3O_4, Ag/ZnO and Co_3O_4/ZnO) for applications in the following main fields has been addressed:

(1) solid state gas sensing;

(2) PSH and photocatalytic oxidation (PCO) properties for pollutant degradation;

(3) photocatalytic H_2 production, starting from aqueous solutions of suitable oxygenates, under both UV-Vis and Vis light irradiation.

The interest in (1) is motivated by the increasing concern regarding the effects of pollution on health and safety, stimulating remarkable efforts toward real-time environmental monitoring. [*Barreca-2011-C, Comini-2009-A, Comini-2010, Li-2009-A, Prades-2009*] Since the performances of solid state gas sensors are directly dependent on the surface and morphology of the active material, [*Basu-2008, Lupan-2010*] an interesting challenge concerns the controlled fabrication of oxide-based low-dimensional nanomaterials with a high surface-to-volume ratio, possessing electrical properties very sensitive to surface-adsorbed species. [*Barreca-2011-C, Comini-2010, Li-2009-A*] In particular, efforts have been aimed at achieving improved sensing performances by a careful control of the material structure, composition and spatial organization.

Regarding (2), the photo-activity of the synthesized oxide nanostructures has been studied using water contact angle (WCA) measurements and photocatalytic oxidation of terephthalic acid (TPA). PSH properties, meaning photo-activated hydrophobic-to-superhydrophilic conversion, can be investigated by monitoring the evolution of the WCA of a water droplet on the nanomaterial surface as a function of the UV irradiation time, as done in this work. [*Bekermann-2010-A*] The term "superhydrophilicity" is used if the WCA << 90°. The self-cleaning activity of the synthesized materials upon photo-activation was investigated *via* a highly sensitive PCO method based on the monitoring of a TPA oxidation product, namely hydroxyterephthalic acid (HOTPA). [*Černigoj-2010*] For both PSH and PCO the requirement is the generation and separation of electrons and holes upon light absorption by the SC material. In the case of PSH, the activation promotes the dissociative chemisorption of H_2O and thus hydrophilic behaviour. [*Fujishima-2000*] The mechanism generally accepted for PCO involves the photo-generation of highly reactive radicals, which can subsequently decompose organic

compounds. [*Bekermann-2010-A*, *Fujishima-2000*] Overall, PSH and PCO properties of SC nanostructures open up attractive perspectives for the eventual development of stimuli-responsive systems. [*Badre-2009, Bekermann-2010-A, Liu-2009-A, Sun-2005, Wan-2005*]

As concerns (3), the widespread interest in sustainable H_2 generation is due to its high demand not only in industrial processes, [*Armaroli-2011, Reisner-2011*] but more importantly as an energy vector, due to the depletion of fossil sources. [*Ni-2007-A, Cargnello-2011*] Up to date, one of the most sustainable routes, the generation of H_2 from photocatalytic water-splitting, has been widely investigated but remains extremely challenging, especially in terms of the process efficiency. [*Cargnello-2011*] In a different way, H_2 production by photoreforming of biomasses, such as alcohols, is much less investigated and offers an attractive alternative. [*Navarro-2009, Fu-2008*] Photo-reforming is based on the oxidation of the feedstock to CO_2 under the generation of H_2 (reaction 1.1), catalyzed by a suitable photo-activated semiconductor material.

$$C_nH_mO_k + (2n - k)\ H_2O \rightarrow n\ CO_2 + (2n + m/2 - k)\ H_2 \qquad \text{(reaction 1.1)}$$

In this work, water/alcohol (methanol or ethanol) mixtures have been used for preliminary tests. [*Montini-2011*] In order to fully exploit the potential of this process, it is of paramount importance to develop catalytic systems that are not affected by leaching or poisoning phenomena and possess a high efficiency, in particular upon Vis activation. Accordingly, herein novel nanosystems for photocatalytic H_2 production have been developed and tested, namely pure and F-doped Co_3O_4 and Ag/ZnO nanocomposites.

❖ 1.2.2. Methods and Materials

❖ *Deposition methods*

In the present thesis, the main attention is devoted to exploiting vapor-phase processes, namely Chemical Vapor Deposition (CVD), both thermal and Plasma Enhanced (PECVD), and sputtering, and their synergistic combination, to obtain specific kinds of functional nanomaterials. CVD relies on the activation of gaseous reactants near or on a substrate surface, leading to the synthesis of the target material by chemical reaction. [*Choy-2003*, *Pierson-1999*] The activation can occur thermally, by heating the substrate, or, in the case of PECVD, by cold reactive plasma (see **chapter 2**). The main advantages

of the CVD technique are flexibility, the possibility of large-scale production, moderate process temperatures, conformal step coverage and the ability to grow various nanostructures by suitable choice of the experimental parameters. [*Choy-2003*, *Pierson-1999*, *Tricoli-2009*] Due to the unique plasma activation, PECVD additionally offers more degrees of freedom in the processing conditions and the use of lower substrate temperatures compared to other vapor-phase methods. [*Choy-2003*, *Gasparotto-2011*, *Zheng-2010-A*] The precursors used in CVD processes play a key role, since their decomposition leads directly to the formation of the desired material. [*Choy-2003*, *McElwee-White-2006*, *Pierson-1999*] To this regard, in this work, efforts were further devoted to the synthesis and characterization of suitable Zn and Co precursors.

As regards sputtering, the source materials (here Ag) is placed in vacuum and exposed to a plasma, resulting in the ejection of target atoms and subsequent deposition of the reactive particles on the substrate (**chapter 2**). Due to the high infiltration power and low temperatures required (down to the room one), sputtering is a valuable technique for the synthesis of nanocomposites. [*Barreca-2008-A*, *Simon-2011*]

The potential of these techniques has been successfully used for the development of ZnO and Co_3O_4 nanomaterials, for their controlled modifications, and for the ultimate preparation of ZnO and Co_3O_4 heterostructures.

- *ZnO*

ZnO, a biosafe *n*-type semiconductor with a wide direct band gap (E_g = 3.4 eV) and a large exciton binding energy (60 meV), [*Bekermann-2010-B*, *Morkoç-2009*] can be grown in an extremely wide range of morphologies [*Calestani-2010*, *Fu-2007-B*, *Kuang-2005*, *Morkoç-2009*, *Wang-2008-A*, *Zhou-2006*] and enabled the development of several ZnO-based systems for a variety of advanced applications. [*Kuang-2005*, *Wang-2005-A*] ZnO NR arrays have received considerable attention for their advanced photo-activated functions, in particular PSH and PC properties, [*Badre-2009*, *Bekermann-2010-A*, *Liu-2009-A*, *Sun-2005*, *Wan-2005*] and for gas sensing of various analytes. [*Barreca-2010-A*, *Kang-2006*, *Özgür-2005*, *Öztürk-2011*] In spite of the numerous works on ZnO, the rational design of 1D ZnO nanosystems still deserves further investigations, in order to understand fundamental phenomena in low-dimensional structures and to implement innovative multifunctional materials. [*Bekermann-2010-B*, *Scalisi-2008*, *Wang-2008-A*]

❖ *Co_3O_4*

Subsequently, the attention has been devoted to Co_3O_4, a mixed valence *p*-type semiconductor with a spinel structure, particularly interesting due to its high catalytic activity, making it an attractive candidate for H_2 production and gas sensing. [*Barreca-2010-B*, *Barreca-2011-C*, *Choi-2010*, *Ikeda-1998*, *Ikeda-1999*] Beyond the control of the system nano-organization, efforts were dedicated to fluorine-doping of the obtained Co_3O_4 nanosystems. Fluorine-doping has been reported to improve functional performances of *n*-type semiconductors and never been investigated before for Co_3O_4 nanomaterials. [*Barreca-2011-C*, *Chen-2010-A*, *Liu-2010*, *Pawar-2008*, *Zhao-2010*] Indeed, the controlled introduction of fluorine has been revealed to be a key tool in order to achieve superior functional performances.

❖ *Ag/ZnO*

Beyond the study of columnar ZnO arrays, the attention has also been focused on Ag/ZnO composites, characterized by controlled distribution of metal nanoparticels. Photocatalytic and gas sensing properties can be improved by the synergistic combination of nanostructured ZnO with metal NPs, which, beside their inherent catalytic activity, promote an enhancement of charge carrier separation due to Schottky barriers at the metal/oxide interface. [*Fu-2007-A*, *Zeng-2008*, *Barreca-2011-A*]. Among the different metals, silver has a great potential to enhance ZnO photo-activity [*Height-2006*, *Lu-2008*, *Tan-2008*, *Lin-2009*] and gas sensing performances, [*Comini-2009-A*, *Basu-2009*] but only a few reports have been focused on Ag/ZnO systems for these applications up to date. [*Xiang-2010*]

❖ *Co_3O_4/ZnO*

Finally, on the basis of previous results, the last part of the activities has been concentrated on Co_3O_4/ZnO nanosystems, in order to develop gas sensors and photo-active materials with improved functional performances. [*Na-2011*, *Shifu-2009*] To this regard, apart from the synergistic combination of the inherent properties of the single-phase materials and nanoscale effects, the formation of *p*/*n* junction at interfaces enables

an enhanced separation of photo-generated carriers and more extended depletion layers in sensing process. [*Zhuge-2010*, *Hsieh-2008*, *Shifu-2009*, *Kim-2005-A*, *Na-2011*] However, only very limited literature on the formation and functionality of Co_3O_4/ZnO nanoheterostructures is available so far.

❖ *Characterization Techniques*

The composition and molecular structure of the developed precursors has been determined by Elemental Analysis (EA), Nuclear Magnetic Resonance Spectroscopy (NMR) and Single Crystal X-ray Diffraction (XRD). In addition, Electron Impact Mass Spectrometry (EI-MS) and Thermogravimetry/Differential Thermal Analysis (TG/DTA) were performed in order to study the fragmentation and thermal properties of the zinc and cobalt precursor molecules.

Subsequently, a detailed compositional, morphological and microstructural and optical characterization of the obtained nanosystems has been carried out by means of a multi-technique approach. Complementary bulk and surface investigation techniques allowed obtaining a thorough and detailed picture of the system properties and their interrelations with the synthesis conditions. This activity, representing a considerable part of the thesis, has been performed by means of the following techniques:

(I) Field Emission Scanning Electron Microscopy (FE-SEM) and Atomic Force Microscopy (AFM), for the study of the nanosystems morphology and its interrelations with the synthesis conditions.

(II) Energy Dispersive X-ray Spectroscopy (EDXS) and Rutherford Backscattering Spectroscopy (RBS) to obtain compositional information on the investigated nanomaterials. To collect further quantitative data on the system surface and in-depth chemical composition, X-ray Photoelectron Spectroscopy (XPS), X-ray Excited Auger Electron Spectroscopy (XE-AES) and Secondary Ion Mass Spectrometry (SIMS) were utilized.

(III) X-ray Diffraction (XRD) and Transmission Electron Microscopy (TEM) to achieve a thorough insight into the systems microstructural features.

(IV) Fourier Transform Infrared Spectroscopy (FT-IR), Ultraviolet/Visible Light Spectroscopy (UV-Vis) and Photoluminescence Spectroscopy (PL) to obtain further information on the material composition and optical properties.

❖ 1.2.3 Outline

In this thesis, the development of multifunctional ZnO, Co_3O_4, Ag/ZnO and Co_3O_4/ZnO nanomaterials is pursued by bottom-up techniques, namely CVD, PECVD, sputtering and their combinations (**figure 1.2**). Indeed, the results and discussions part will illustrate that the adopted strategies open up attractive perspectives for the design of nanostructured materials with specific applicative aims.

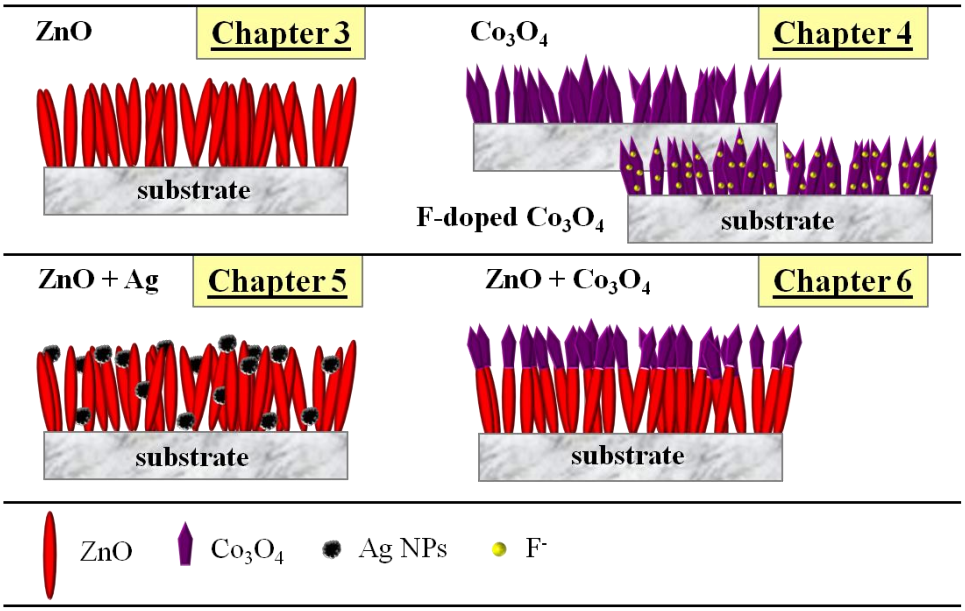

Figure 1.2: Schematic representation of the functional nanomaterials presented in this work.

In particular, **chapter 2** provides the basic principles and advantages for the CVD and sputtering processes, highlighting their role for the growth of nanostructures and composites. Furthermore, the choice of the zinc and cobalt CVD precursors used in this thesis is discussed in the context of the state of the art state in Zn and Co precursor chemistry.

Chapter 3 deals with the CVD and PECVD of ZnO nanodeposits. The application of suitable metal organic Zn precursors, $[Zn\{[(CH_2)_xOCH_3]NC(CH_3)=C(H)C(CH_3)=O\}_2]$ (**1**: x = 2; **2**: x = 3), led to the obtainment of pure ZnO nanomaterials, whose morphology, structure and composition have been studied as a function of the adopted process parameters. The 1D nanorod (NR) arrays, derived from PECVD, were investigated regarding their activity in PSH and PCO and sensing properties of various analytes (CH_3CH_2OH, CH_3COCH_3, CO, H_2, CH_4, O_3 and NO_2).

In **chapter 4**, the PECVD of Co_3O_4 nanosystems from the metal organic sources, [$Co(dpm)_2$] (**3**) (dpm = 2,2,6,6-tetramethyl-3,5-heptanedionate) and [$Co(hfa)_2$·TMEDA] (**4**) (hfa = 1,1,1,5,5,5-hexafluoro-2,4-pentanedionate; TMEDA = *N,N,N',N'*-tetramethylethylenediamine), is described. In PECVD, the use of **3** yielded pure Co_3O_4 nanodeposits, whereas precursor **4** enabled in-situ fluorine-doping of the spinel by generation of fluorine radicals in the reactive plasmas. The material features were characterized by a combined analyses technique and the resulting impact on the functional performances in the photocatalytic H_2 production and detection of ethanol and acetone were studied.

Ag/ZnO nanoheterostructures (**chapter 5**) have been obtained by a hybrid approach, using PECVD of ZnO and sputtering of Ag nanoparticles. The influence of the silver amount and distribution, controlled by the processing parameters, on the functionality in H_2 photocatalytic generation and sensing has been investigated in detail.

In **chapter 6**, the development of Co_3O_4/ZnO nanocomposites of varying Co_3O_4 amount via a two-step PECVD is shown. A multi-characterization technique has been adopted to investigate the morphological, structural and compositional features of the composite materials. Preliminary tests, studying their PSH and PCO properties were performed, and their application in the gas-phase detection of acetone, ethanol and nitrogen dioxide is also discussed.

Summary and perspectives of the present work are presented in **chapter 7**.

In the experimental section (**chapter 8**), the synthesis and characterization of the applied precursor compounds (**1**, **2**, **3**, and **4**) is briefly discussed. The used reactor set-ups are also described, and an overview of the applied deposition parameters for the nanomaterials presented in **chapters 3 – 6** is provided. Finally, the analytic methods, carried out for the precursor and nanodeposit characterization, and for the functional characterization, are described.

2. Vapor-phase Deposition Approaches: CVD, Sputtering and Hybrid Routes

❖ 2.1 Abstract

In the present chapter, first, the general motivation for the development of nanomaterials by vapor-phase deposition approaches is presented (**2.2**). In the following paragraphs, the basic principles and advantages of the adopted techniques, CVD (**2.3**), PECVD (**2.4**), sputtering (**2.5**) and hybrid approaches (**2.6**), are briefly described, highlighting their importance for the growth of the oxide nanomaterials developed in the present thesis. **Paragraphs 2.7** and **2.8** give a brief overview of the state of the art in zinc and cobalt precursor chemistry, respectively, pointing out the benefits of the precursors used in this thesis.

❖ 2.2 Introduction

Basing on the main applicative challenges in nanomaterial synthesis discussed in **chapter 1**, versatile low-temperature processes are required to control the system composition, nanostructure and morphological organization. The tailoring of such features is essential in order to exploit the nanosystem properties that underpin advanced applications. [*Gasparotto-2011*, *Morkoç-2009*] Various nanomaterials preparation methods and properties are extensively reviewed in numerous articles, reports and books, ranging from nanopowders by precipitation, to supported 1D materials by template routes, up to various kinds of hierarchical nanostructures. [*Curri-2010*, *Gasparotto-2011*, *Rao-2004*, *Wang-2008-B*, *Wang-2011-A*, *Xia-2003*, *Zhai-2010*]

At variance with top-down approaches, like etching, lithography or ion beam milling, that often require harsh conditions and do not enable a high control on the system nano-organization, bottom-up approaches, based on the controlled assembly of atomic/molecular units, can be considered a more amenable choice. [*Comini-2009-A*, *Elias-2010*] As a matter of facts, CVD and sputtering processes belong to this category.

The general benefits of CVD among other synthesis techniques are its conformal deposition also on 3D complex architectures and ability to produce a large variety of pure nanostructures with controlled crystallinity. [*Becker-2009*, *Choy-2003*, *Pierson-1999*, *Tricoli-2009*] Compared to wet chemical approaches, CVD methods are favorable to

attain higher system purity and to avoid drying steps. Furthermore, in contrast to physical vapor deposition processes, they have not the drawback of line-of-sight deposition. The deposition rates achieved by CVD are relatively high and no ultrahigh vacuum is necessary. CVD technology is very versatile in the choice of various physical and chemical experimental parameters, allowing a fine-tuning of the eventual system properties. [*Choy-2003, Dong-2008, Liang-2011, Pierson-1999, Seshan-2002*]

The main drawback of relatively high substrate temperatures, often ascribed to the classical thermal CVD, can be easily overcome by a proper choice of the process activation mode. [*Barreca-2011-D, Gangil-2007, Higashiwaki-2009, Pierson-1999, Zheng-2010-A*] In this way, depositions of various materials also on heat-sensitive substrates are possible.

Among physical techniques, sputtering, Molecular Beam Epitaxy (MBE), Pulsed Laser Deposition (PLD) and thermal evaporation have been widely used to produce epitaxial materials with well controlled stoichiometry and doping level. [*Fu-2007-A*] Yet, thermal evaporation often requires extremely high vaporization temperatures, [*Katti-2003*, *Xu-2007*] and MBE/PLD involve high energy dissipation, being thus not amenable for practical applications. [*Pierson-1999*, *Si-2006*] In contrast, sputtering can be carried out at low temperatures, even down to the room one, [*Barreca-2011-A*, *Hsieh-2011*, *Simon-2011*] and requires a less complex instrumental apparatus. [*Pierson-1999*]

❖ 2.3 Thermal CVD

In the "classical" and up to date mainly applied thermal CVD, the reagents (metal organic precursors, compounds, reactive gases) are vaporized, transported into the reaction chamber and thermally activated/decomposed on a hot substrate surface to form the target material by chemical reaction. [*Choy-2003*, *Pierson-1999*] CVD is an especially favorable technique for the controlled bottom-up growth of nanomaterials without any need of catalyst introduction. Yet, a main critical issue in this context is the choice of proper molecular precursors, whose features have a significant influence on the resulting material properties. [*Bandoli-2009*, *Choy-2003*, *Pierson-1999*] To this regard, **paragraphs 2.7** and **2.8** give overviews over of the state of the art in zinc and cobalt precursor chemistry, respectively.

Although not being the "softest" of the CVD related methods, thermal CVD enables to obtain a variety of nanosystems, either single-phase or composites. In 2007, for the first time, functional TiO_2-ZnO nanodeposits were prepared by CVD. [*Barreca-2007-A*] The choice of suitable metal organic precursors and reactant gas enabled the growth of oriented ZnO nanocrystallites and subsequent single phase TiO_2 on top at 350 - 400°C. In addition, this method proved the ability of CVD as a versatile tool to achieve an easy control of the system morphology, structure, and chemical composition. Atmospheric pressure CVD has been reported by Saitoh et al. for the growth of MgO-ZnO whiskers, deposited from Ti and Zn isopropoxides at 500 – 650°C. [*Saitoh-2002*] Becker et al. reported on an improved $Cu/ZnO/Al_2O_3$ nanocatalyst for methanol synthesis, [*Becker-2010*] underlining the importance of novel CVD processes for the development of functional nanoheterostructures. The controlled dispersion and shape uniformity of the resulting nanostructures is hardly achievable by other bottom-up methods, and represents an inherent advantage of CVD processes in general. [*Liang-2011*]

❖ 2.4 PECVD

As anticipated by its name, Plasma Assisted CVD takes advantage of the activation of gaseous precursors in the CVD chamber by non-equilibrium plasma. [*Gasparotto-2011*] In comparison to conventional CVD processes, PECVD offers more degrees of freedom in processing parameters as well as reasonable deposition rates and high crystalline quality. A key advantage of PECVD is the growth of supported materials at lower substrate temperatures and in a more energy-efficient way compared to other deposition techniques. [*Choy-2003*, *Gasparotto-2011*, *Higashiwaki-2009*, *Seshan-2002*] The reason is the generation of a weakly ionized non-equilibrium plasma, characterized by a much higher temperature for electrons ($\approx 10^4$ K) than for ions. [*Choy-2003*, *Gasparotto-2011*] The different mobility of such species induces the build-up of an electric field (the sheath field) perpendicular to the solid surface at the plasma-solid interface. This phenomenon accelerates cations towards the forming system, with its consequent bombardment and the development of peculiar growth directions and structural orientations. In the case of porous/rough substrates, ion bombardment and the associated local energy transfer result in a typical infiltration power, enabling deposition to occur not only at the surface, but even in the inner system regions. Such effects, in synergy with the excitation, ionization

and dissociation of gas molecules promoted by "hot" electrons, activate a unique gas-phase and surface chemistry, diversifying material features from those obtained by conventional gas-based synthetic routes. A distinctive property of cold plasmas is their high chemical reactivity even in the absence of external thermal supplies, a key feature for the processing of heat-sensitive materials at temperatures close to the room one. In addition, the temperature-dependent competition between growth and ablation phenomena may result in a unique nano-organization. [*Gasparotto-2011*]

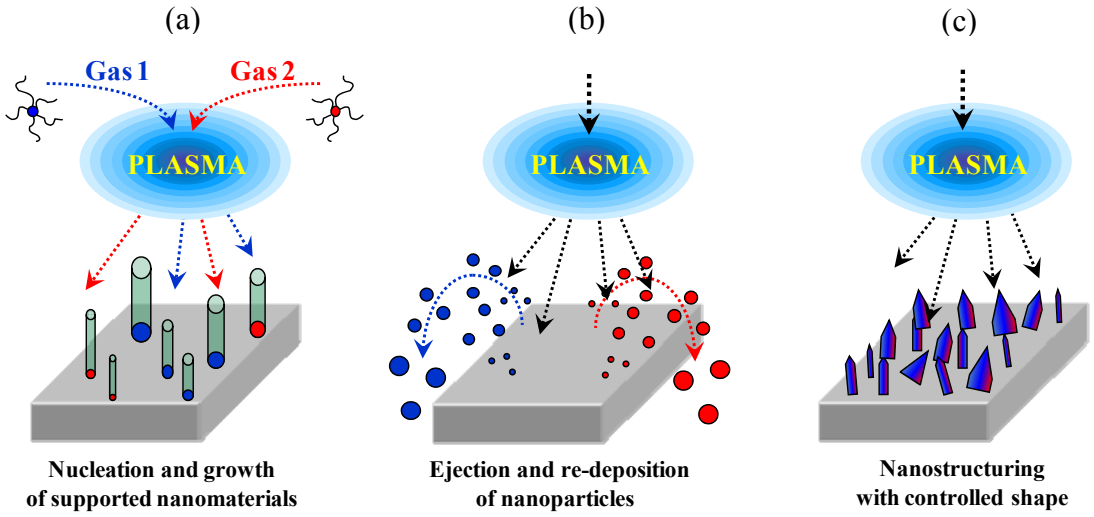

Figure 2.1: Sketch of three different plasma-assisted routes to nanomaterials: (a) PECVD; (b) sputtering; (c) surface modification.

Among plasma assisted methods, three main approaches are especially promising for the mild processing of nanomaterials (**figure 2.1**): [*Zheng-2010-A*]

(a) PECVD, where gaseous molecular precursors are introduced into the plasma, whose role is either to activate the sole precursor, or to avoid/enhance peculiar growth effects on the substrate surface.

(b) Sputtering, involving the plasma bombardment of an externally biased target and the consequent ejection of neutral and charged species, enabling a high versatility in the preparation of supported nanoparticles or nanocomposites (see **2.5**). [*Armelao-2009*, *Barreca-2008-A*]

(c) Plasma treatment of solid materials, based on the exploitation of bombardment and etching effects to modify the system surface, producing the target nanostructures. [*Ostrikov-2010*]

In general, deposition, ablation and surface modification processes are always concurrent and the predominance of one over the others can be attained by a judicious choice of the experimental parameters, including pressure, power density, flow rates and plasma composition. [*Ostrikov-2006*, *Xu-2006-A*, *Zheng-2010-A*]

Various PECVD syntheses of ZnO nanorods on various substrates have been reported (for instance [*Liu-2004-A*]). Romero-Gómez et al. investigated the morphology dependence of the ZnO nanodeposits on the plasma composition and growth temperature, [*Romero-Gómez*] starting from diethylzinc (DEZ) as the zinc precursor in various environments (O_2, O_2/H_2, O_2/Ar or O_2/N_2). Two positive effects of Plasma Enhanced CVD were illustrated by this work. Very low substrate temperatures were used, down to the room one, and the functional properties of the nanostructured ZnO could be tuned as a function of the processing conditions. As regards PECVD of cobalt oxide, very limited literature is available to date. Nonetheless, these reports demonstrated the possibility of high dispersion of the material, difficult to achieve by other methods. [*Koyano-1996*, *Tyczkowski-2007*]

In addition, PECVD can be effectively used for the growth of in-situ doped materials. [*Gangil-2007*, *Gong-2000, Higashiwaki-2009*] For instance, Gangil et al. obtained ZnO:N/ZnO (*p*/*n*) junctions by PECVD from DEZ and O_2 and N_2 as reactive gases. [*Gangil-2007*] As a matter of fact, *p*-doping of ZnO is usually challenging and often toxic or corrosive nitrogen sources are used. Thanks to the high reactivity of the plasma process, the introduction of N radicals into the ZnO structure could be achieved starting from N_2 in the reaction atmosphere. In the framework of this thesis, the ability of PECVD to achieve an effective anion in-situ doping of metal oxides has been proved in the obtainment of Co_3O_4 nanosystems (see **chapter 4**). [*Barreca-2011-C*]

❖ 2.5 Sputtering

Beside PECVD, sputtering (**figure 2.1 (b)**) is another favorable synthesis technique exploiting the benefits of cold plasmas for the bottom-up preparation of supported nanomaterials. Unlike most other physical processes, sputtering can be carried out at low temperatures, down to the room one, allowing facile combination with other deposition methods to form nanocomposites (see **2.6**). [*Barreca-2011-A, Simon-2011*] Other

advantages are the good sample/substrate adhesion, ease of compositional control and possibility to perform etching processes. [*Pierson-1999*, *Seshan-2002*]

In a typical sputtering process, the source material is placed in vacuum and exposed to a glow discharge or plasma, whose bombardment causes the ejection of atoms or low nuclearity fragments, that subsequently undergo nucleation and growth phenomena on the substrate surface. The main drawbacks are line-of-sight deposition and restriction in terms of nanoarchitecture design, being limited to the formation of films and particles. [*Pierson-1999*]

Apart from the low processing temperatures required, a major advantage of sputtering for composite formation is due to its inherent infiltration power in porous matrices, [*Simon-2011*] as further pointed out in the next paragraph (**2.6**).

In particular, sputtering is an important technique for the growth of metal thin films and fine dispersed metal particles. For instance, Tan et al. used the sputtering technique for the Ag loading of a highly porous ZnO system, and proposed that metal particle aggregation can potentially be reduced in comparison to the often applied wet-phase synthesis. [*Tan-2008*] Another recent example was given by Hsieh et al., who synthesized Ag-SiO_2 nanocomposites by sputtering for optical studies. [*Hsieh-2011*] The choice of the technique was motivated by the need of avoiding solid state reactions, and achieving a fine control of the overall composition.

❖ 2.6 "Hybrid" Approach: CVD + Sputtering

Research efforts towards the achievement of advanced functional nanoheterostructures have prompted the combination of the versatile "CVD" tool with the advantages of other deposition techniques. In this way, several composite materials with appealing and novel chemico-physical features have been prepared, with promising applications in gas sensors, [*Barreca-2011-A*, *Su-2011*], field emission devices, [*Tsukazaki-2008*] diodes, [*Bayram-2009, Jeong-2009*], photocatalytic H_2 generation, [*Simon-2011*] photovoltaics and fuel cells. [*Kronawitter-2011*, *Wang-2011-B*] In this context, the above mentioned flexibility and low deposition temperatures required for CVD and sputtering renders their combination a promising strategy for the development of nanocomposites, as further shown in the following examples.

For instance, ZnO *p*/*n* junction materials have been fabricated by the sputtering of *n*-ZnO and CVD of *p*-ZnO, and showed promising performances in hydrogen detection. [*Hazra-2006*]. Jeong et al. proposed CVD-grown Cu_2O onto a sputtered ZnO film as a rectifying system to be integrated into solar cells or diodes. [*Jeong-2009*] In our group, CuO-TiO_2 nanocomposites were successfully prepared by a two-step thermal CVD process and functionalized with Au nanoparticles by radio frequency (RF) sputtering. [*Barreca-2011-A*] Under mild conditions tailored composites could be obtained avoiding the occurrence of solid state reactions. Similarly, Au sputtering has been performed on CVD-grown nanostructured Co_3O_4 and enabled to avoid alterations of the Co_3O_4 matrix, attaining a controlled dispersion of the Au particles. [*Barreca-2010-B*] Both Au-loaded CuO-TiO_2 and Au-Co_3O_4 have been successfully used as solid state gas sensors. These examples of controlled nanocomposite design further underpin the importance of hybrid CVD/sputtering for multifunctional nanosystems. In this thesis, a hybrid approach using PECVD and RF sputtering enabled the design of Ag/ZnO nanostructures for the H_2 photo-production and sensing (**chapter 5**).

❖ 2.7 Zinc Precursor Chemistry

To date, the most widely used precursors for the depositon of ZnO (dimethylzinc (DMZ) and DEZ) are problematic in terms of handling and can lead to pre-reactions due to their high air and moisture sensitivity. [*Jeong-2007*, *Jeong-2008*, *Kumar-2011, Liu-2004-A*, *Morkoç-2009*, *Yamaoka-2008*] The development of alkyl zinc adducts and alkyl zinc alkoxides prevented pre-mature reactions, but still these compounds are highly air sensitive, and some of them tend to polymerization. In order to overcome these problems and to gain a better control of the growth process, attempts towards more stable metal organic sources have been made, mainly concentrating on β–diketonates. [*Barreca-2007-B*, *Malandrino-2008*] These compounds however often suffer from low volatility, sintering or possess a narrow temperature window between vaporization and decomposition. [*Ali-2009*, *Black-2008*, *Scalisi-2008*] In this context, a key aim of this thesis was the synthesis of suitable precursors to be used for the CVD of ZnO-based nanomaterials. In **paragraph 8.1**, the preparation and thermal analysis of $[Zn\{[(CH_2)_xOCH_3]NC(CH_3)=C(H)C(CH_3)=O\}_2]$ (**1**: $x = 2$; **2**: $x = 3$) is described, and their successful application for the preparation of pure and <001> oriented ZnO is

demonstrated in **chapter 3**. The advantages of monomeric complexes **1** and **2** are that they can be handled on air and evaporate from their melt, avoiding thus changes in the evaporation rate due to altering of the crystallite size upon heating. [*Gulino-2003-A*, *Hitchman-1995*, *Malandrino-2005*] In addition, their constant vaporization rate and clean decomposition patterns can improve ZnO growth processes by preventing difficulties related to high-temperature vaporization and carbon incorporation. For comparison, **table 2.1** summarizes the most important classes of zinc compounds in view of ZnO vapor deposition (CVD and Atomic Layer Deposition (ALD)). (According to the high number of reports on zinc metal organic sources, only selected examples are listed.)

T**able 2.1**: Overview over the most common types of zinc precursors reported in literature. The evaporation temperatures (T_{vap}) provided refer either to the sublimation (indicated by ^{s}) or CVD/ALD conditions reported. Boiling points are marked by a *. (Abbreviations: m.p. = melting point, RT = room temperature, Me = methyl, Et = ethyl, Pr = propyl, Bu = butyl, Ph = phenyl.)

Precursor	**m.p. /°C**	**T_{vap} /°C (p/mbar)**	**Comments**	**References**
Dialkyl zinc	< 0	~ RT	extremely air and moisture sensitive; pyrophoric; pre-reaction possible	[*Auld-1994*, *Jones-1995*, *Kumar-2011, Malandrino-2005, Morkoç-2009*]
[Me_2Zn] (DMZ)	-42	<RT		[*Hu-1991*, *Smith-1995*, *Wright-1984*]
[Et_2Zn] (DEZ)	-28	RT (0.013)		[*Hu-1992*, *Kim-2009-A*, *Yang-2009*]
DMZ cyclic ether adducts (tetrahydrofuran (C_4H_8O, THF), tetrahydropyran ($C_5H_{10}O$, THP) and furan (C_4H_4O))		20 (1 atm); 50 (5)	air sensitive; slow deposition rates	[*Jones-1995*, *Kaufmann-1989*, *Black-2010*]
DMZ/DEZ ether adducts			highly air sensitive	
[Me_2Zn·(1,4-dioxane)]	66		polymeric	
[Me_2Zn·(1,2-dimethoxyethane)]	5.5		----	
[Me_2Zn·(1,4-thioxane)]	-----		polymeric	[*Ashraf-2011*]
1,4-dioxane ($C_4H_8O_2$); 1,2-dimethoxyethane ($C_4H_{10}O_2$); 1,4-thioxane (C_4H_8OS)				
DMZ amine adducts			air sensitive; tend to oligomerization	
[Me_2Zn·NEt_3]	< RT	17.5 (1 atm)		[*Wright-1989*]
[MeZn·TMEDA]$_2$	110-	^{s}75 (0.013)		[*Coates-1965*]

[Me_2Zn·TMEDA]	111 57-58	^{s}35 (0.013)		[*Coates-1965*]

Alkyl zinc alkoxides		^{s}>80 (0.13)	air sensitive; generally tetrameric	[*Auld-1994*, *Coates-1965*, *Jones-1995*]
[$MeZn(OMe_2)_2$]	190-191	^{s}60 (10^{-4})	decomposes upon melting	[*Coates-1965*]
[$MeZn(O^{i}Pr)$]		70 (20)	single source precursor	[*Auld-1994*]
[$EtZn(O^{i}Pr)$]	258-260		decomposes upon melting	[*Coates-1965*]
[$MeZn(O^{t}Bu)$]		80 or 150 (0.013); ^{s}95 (10^{-4})	single source precursor; decomposition at 150°C	[*Auld-1994*, *Coates-1965*]
[$EtZn(O^{t}Bu)$]		^{S}105 (10^{-4})		[*Coates-1965*]
[$MeZn(OPh)$]	219-221		decomposes upon melting; decomposition at 120°C	[*Coates-1965*]

(Alkyl) zinc amides			air sensitive	
[$EtZn(NEt_2)$]	< RT	*70-72 (0.25)	air sensitive and thermally unstable above ~40°C	[*Suh-1999*]
[$EtZn(NPh_2)_2]_2$	99-100			[*Coates-1965*]
[$(Me_2N)_2Zn]_x$	270-290		decomposes upon melting	[*Coates-1965*]
[$Zn\{N(SiMe_3)_2\}_2$] (TMS = trimethylsilyl)	12.5	50 (10) *82 (0.67)	CVD of Zn_2SiO_4 or Zn_3N_2; incorporates carbon at low temperatures	[*Maile-2005*, *Suh-2001-A*]
[$ZnN(^{i}Pr\{TMS\})_2$] [$ZnN(^{s}Bu\{TMS\})_2$] [$ZnN(^{t}Bu\{TMS\})_2$] [$ZnN(^{i}Bu\{TMS\})_2$]	---- ---- 47 76-77	*54 (0.08) *53 (0.03) *65 (0.07) *75 (0.01)	extremely air and moisture sensitive; TG: weight loss and 0% residue	[*Gaul-2000*]
[$Zn\{N(^{t}Bu)(TMS)\}_2$]	35-40	*70-80 (0.25)	can form silicon oxide	[*Rees-1992*, *Suh-2001-A*]
[$Zn(tmp)_2$] (tmp = 2,2,6,6-tetramethylpiperidino)		^{s}75-80 (0.013); 70 (1atm)	low growth rate	[*Suh-2001*]

$Zn(MeCOO)_2$ ($MeCO_2$ = acetate)	252	240	air stable; single source precursor; incorporates carbon	[*Jain-1998*, *Wu-2002*]

β-Diketonates			air stable	
$[Zn(dpm)_2]$	132-134		suffers from sintering	[*Ni-2005*]
$[Zn(hfa)_2 \cdot TMEDA]$	106-108	60 (10)	not suitable for all CVD/ALD techniques due to F-content	[*Barreca-2007-B*, *Ni-2005*]
$[Zn(hfa)_2 \cdot DEA]$ (DEA = *N*,*N*'-diethylethylenediamine)	64-66	68 (4)	not suitable for all CVD/ALD techniques due to F-content	[*Ni-2005*]
$[Zn(hfa)_2 \cdot 2H_2O \{Me(OCH_2CH_2)_xOMe\}]$ (x = 2-4)			water of hydration must be removed before effective use	[*Ni-2005*]
$[Zn(acac)_2 \cdot xH_2O]$ (acac = acetylacetonate, OC(Me)CHC(Me)O)	132-138	75 (3)	single source precursor; degree of hydration changes thermal properties; difficult to predict melting, vaporization and sublimation regions;	[*Baxter-2009*, *Minami-1994*, *Ni-2005*]
$[Zn(acac)_2]$	129		partial decomposition occurs along with other processes (melting, vaporization, sublimation)	[*Arii-2006*]
$[Zn(tta)_2 \cdot (TMEDA)]$ (tta = 2-theonyltrifluoroacetonate)	128-130	170 (4)	high evaporation temperature	[*Malandrino-2005*]

Ketoiminates			compromise between volatility and air stability	
$[Zn\{(^{n}Bu)NC(Me)=CHC(Me)=O\}_2]$	72	205 (1atm)	incorporates carbon (~26.2%)	[*Matthews-2006*]
$[Zn\{(^{i}Pr)NC(Me)=CHC(OEt)=O\}_2]$	109	225 (1atm)	incorporates carbon (~8.7%)	[*Matthews-2006*]
$[Zn\{[(CH_2)_2OCH_3]NC(CH_3)=C(H)C(CH_3)=O\}_2]$ (**1**)	57	120-140 (1)	see **paragraph 8.1** and **chapter 3**	[*Bekermann-2010-B, Bekermann-2010-C*]
$[Zn\{[(CH_2)_3OCH_3]NC(CH_3)=C(H)C(CH_3)=O\}_2]$ (**2**)	60	130-150 (1-10)	see **paragraph 8.1** and **chapter 3**	[*Bekermann-2010-B, Bekermann-2010-C, Bekermann-2011*]

❖ 2.8 Cobalt Precursor Chemistry

Deposition of cobalt or cobalt oxides has been performed by various type of precursors. Among them, salts, such as cobalt(II) acetate or cobalt(III) nitride, do not enable a controllable mass supply, whereas volatile metal organic compounds, typically with carbonyl and cyclopentadienyl ligands, suffer from low thermal stability, side reactions in the gas phase, toxicity and elevated activation temperatures. [*Bandoli-2009*, *Lee-2006-B*, *Li-2008-D*, *Premkumar-2007*, *Tyczkowski-2007*] Efforts toward Co precursor development were also devoted to the synthesis of liquid amidinates and hydrides, which showed to be volatile, however air sensitive. [*Li-2008-D*, *Choi-2003*] In contrast, cobalt *β*–diketonate precursors are mostly air stable, but some tend to oligomerize and show no clean decomposition behaviour (e.g. $[Co(acac)_2]$, $[Co(acac)_2{\cdot}(DMAPH)]_2$ (DMAPH = dimethylamino-2-propanol), $[Co\{OC(R)CHC(R)O\}_3]$ (R = alkyl group), $[Co(hfa)_2(H_2O)_2]$). [*Bandoli-2009*, *Gulino-2003*, *Lee-2010*, *Pasko-2004-A*] As a consequence, various strategies have been employed to tailor the thermal properties of Co β–diketonates, involving the use of fluorine containing ligands, bulky groups to increase steric hindrance, and the synthesis of Co(II) chelates (see **table 2.2**). In the present thesis, $[Co(dpm)_2]$ (**3**) $[Co(hfa)_2{\cdot}(TMEDA)]$ (**4**) have been chosen as precursors in Co_3O_4 deposition, due to their air stablity and appreciable volatility (see **paragraph 8.2** and **chapter 4**). In addition, **4** has been utilized for controlled F-doping of the cobalt oxide materials.

T**able 2.2**: Overview over the most common types of Co precursors reported in literature. The evaporation temperatures (T_{vap}) provided refer either to the sublimation (indicated by "^{S}") or CVD/ALD conditions reported. (Abbreviations: m.p. = melting point, RT = room temperature, Me = methyl, Et = ethyl, Pr = propyl, Bu = butyl, Cp = cyclopentadienyl, Ph = phenyl)

Precursor	**m.p. /°C**	**T_{vap} /°C (p/mbar)**	**Comment**	**Reference**
Salts			no controlled and reproducible mass supply	[*Bandoli-2009*]
$Co(NO_3)_3$		^{S}35 (0.07); RT (1.6-3.1)	extremely air- and water-sensitive	[*Bandoli-2009*, *Colombo-1998*]
$Co(OCOCH_3)_2$	298			[*Koyano-1996*, *Maruyama-1991*]

Organo metallic compounds			undesired gas phase reactions; low thermal stability; high deposition temperature	[*Bandoli-2009*]
$[Co_2(CO)_8]$	n.a.	n.a. (flash point -23)	extreme toxicity; highly air sensitive; thermal degradation in the gas phase; incorporates carbon	[*Bandoli-2009*, *Lee-2006-B*, *Premkumar-2007*]
$[Co(Cp)_2]$	170-180	RT (3.5)	air sensitive;	[*Bandoli-2009*, *Diskus-2011*, *Lee-2006*]
Other carbonyl and Cp cobalt compounds				
$[Co(Cp)(CO)_2]$	< RT	RT (0.45-0.47)	incorporates carbon	[*Li-2008-D*, *Tyczkowski-2007*]
$[Co(CO)_3NO]$	< RT		only Co was obtained	[*Li-2008-D*]

β–Diketonates				
$[Co(acac)_2]$	165-170	^{s}100-120 ($2.7\cdot10^{-4}$); 170 (100)	formation of oligomeric structures can occur; carbon incorporation possible	[*Backman-2009*, *Cotton-1964*, *Fujii-1995*, *Maruyama-1996*, *Pasko-2004*, *Pasko-2004-A*, *Premkumar-2007*]
$[Co(acac)_3]$	210	180 (100)	residual mass TG: 22.61%	[*Backman-2009*, *Lee-2010*]
$[Co(acac)_2\cdot TMEDA]$		^{s}70 ($2.7\cdot10^{-4}$)	TG: no one-step weight loss	[*Pasko-2004*, *Pasko-2004-A*]
$[Co(acac)_2\cdot DMAPH]_2$		^{s}80 ($1\cdot10^{-4}$)	dimeric; sublimation under partial decomposition	[*Pasko-2004-A*]
$[Co(acac)_2\cdot DMAEH]_2$ (DMAEH = 2-dimethylaminoethanol)		^{s}90 ($1\cdot10^{-4}$)	sublimation under partial decomposition	[*Pasko-2004-A*]
$[Co(dpm)_2]$ (**3**)	140-144	90 (1-10); 120 (0.01)	see **paragraph 8.2** and **chapter 4**	[*Barreca-2001*, *Cotton-1964*, *Klepper-2007-A*]
$[Co(dpm)_3]$	247		residual mass TG: 0%	[*Lee-2010*]
$[Co\{OC(^{i}Pr)CHC(^{i}Pr)O\}_3]$	157		residual mass TG: 1.45%	[*Lee-2010*]
$[Co\{OC(Me)CHC(Me)O\}_3]$	53.5		residual mass TG: 10.80%	[*Lee-2010*]
$[Co(dpm)_2\cdot TMEDA]$		^{s}125 ($3\cdot10^{-4}$)	less volatile than $Co(dpm)_2$; TG: no one-step weight loss	[*Pasko-2004*, *Pasko-2004-A*]
$[Co(hfa)_2\cdot 2H_2O\cdot$tetraglyme] (tetraglyme = $Me(OCH_2CH_2)_4OMe$)	57	110 (2.7-6.7)	water molecules can induce uncontrolled decomposition or pre-reactions; TG: no one-step weight loss	[*Gulino-2003-A*]

$[Co(hfa)_2(H_2O)_2]$	172	105-110 (2.7-8)	water molecules can induce uncontrolled decomposition or pre-reactions; TG: no one-step weight loss	[*Bandoli-2009*, *Gulino-2003*]
$[Co(hfa)_2 \cdot (TMEDA)]$ (**4**)	92-94	60 (1-10)	see **paragraph 8.2** and **chapter 4**; not suitable for all CVD/ALD techniques due to F-content	[*Bandoli-2009*, *Barreca-2010-D*, *Gasparotto-2011-A*]

Amidinates				
$[Co(^{i}Pr(NC(Me)N)^{i}Pr)_2]$	84	65 (0.4)	ALD of Co and CoO; low growth rates	[*Li-2008-D*, *Lim-2003-A*, *Lim-2003-B*]
$[Co(^{t}Bu(NC(Me)N)^{t}Bu)_2]$	90			[*Li-2008-D*, *Lim-2003-B*]
$[Co(^{t}Bu(NC(^{n}Bu)N)Et)]$	-21			[*Li-2008-D*]
$[Co(^{t}Bu(NC(Et)N)Et)]$	-17			[*Li-2008-D*]
$[Co(^{t}Bu(NC(Me)N)Et)]$	37			[*Li-2008-D*]

Hydrides		55-115 (0.013-6.67)	air sensitive; to date only CVD of Co	[*Choi-2003*]
$[HCo\{EtOP(OMe)_2\}_4]$	>RT	^{s}77 (0.07)		
$[HCo\{MeOP(OEt)_2\}_4]$	>RT	^{s}80 (0.07)		
$[HCo\{^{i}PrOP(OMe)_2\}_4]$	>RT	^{s}90 (0.07)		
$[HCo\{^{n}PrOP(OMe)_2\}_4]$	<RT	volatile		
$[HCo\{^{i}BuOP(OMe)_2\}_4]$	<RT	volatile		[*Choi-2003*]
$[HCo\{^{n}BuOP(OMe)_2\}_4]$	<RT	volatile		
$[HCo\{PhOP(OMe)_2\}_4]$	<RT	volatile		
$[HCo\{^{i}BuOP(OEt)_2\}_4]$	<RT	volatile		
$[HCo\{PhCH_2OP(OEt)_2\}_4]$	<RT	volatile		

3. Zinc Oxide Nanostructures

❖ 3.1 Abstract

In this chapter, the development of functional ZnO nanostructures, the core of this work, is described. After a short introduction (**3.2**), in **paragraph 3.3**, the CVD of supported ZnO materials testing zinc precursors $[Zn\{[(CH_2)_xOCH_3]NC(CH_3)=C(H)C(CH_3)=O\}_2]$ (**1**: $x = 2$; **2**: $x = 3$) (see **2.7** and **8.1**) is reported.[1] ZnO films were grown on silicon and borosilicate glass substrates at temperatures between 400 and 700°C using oxygen as reactive gas (**paragraph 3.3.1**). XRD, FE-SEM, AFM (**3.3.2**), RBS, XPS/XE-AES (**3.3.3**), UV-Vis spectroscopy and PL analyses (**3.3.4**) revealed the obtained of pure and <001> oriented ZnO films at optimal growth temperatures of 500 and 600°C.

Subsequently, the growth of ZnO nanorods by PECVD from **1** and **2** on different substrates for different kinds of applications is extensively discussed (**paragraph 3.4**).[2] 1D ZnO nano-assemblies were grown on Si(100) and on Al_2O_3 substrates using temperatures between 100 and 400°C and RF-power values of 10 - 40 W (**paragraph 3.4.1**). The morphology and structure of the synthesized ZnO nanosystems were thoroughly analyzed by FE-SEM, Glancing Incidence (GI)XRD and high resolution (HR)-TEM (**paragraph 3.4.2**). [*Bekermann-2010-B*] The composition was studied by EDXS, SIMS and XPS/XE-AES, evidencing the formation of highly pure ZnO (**paragraph 3.4.3**). In addition, PL measurements were carried out to gain information on the optical properties (**paragraph 3.4.4**). PECVD from **1** and **2** yielded the selective formation of highly pure and *c*-axis oriented NRs on Si(100) substrates, at temperatures as low as 200 - 300°C, in the absence of any catalyst.[2(a-b)] A phenomenological growth

[1] *(a)* [*Bekermann-2010-C*] D. Bekermann, D. Rogalla, H.-W. Becker, M. Winter, R.A. Fischer, A. Devi, Eur. J. Inorg. Chem. (2010) 1366; *(b)* [*Bekermann-2011*] D. Bekermann, A. Ludwig, T. Toader, C. Maccato, D. Barreca, A. Gasparotto, C. Bock, A.D. Wieck, U. Kunze, E. Tondello, R.A. Fischer, A. Devi, Chem. Vap. Deposition 17 (2011) 155.

[2] *(a)* [*Bekermann-2010-B*] D. Bekermann, A. Gasparotto, D. Barreca, L. Bovo, A. Devi, R.A. Fischer, O.I. Lebedev, C. Maccato, E. Tondello, G. Van Tendeloo, Cryst. Growth Des. 10 (2010) 2011; *(b)* [*Barreca-2010-G*] D. Barreca, D. Bekermann, A. Devi, R.A. Fischer, A. Gasparotto, C. Maccato, E. Tondello, M. Rossi, S. Orlanducci, M.L. Terranova, Chem. Phys. Lett. 500 (2010) 287; *(c)* [*Barreca-2010-A*] D. Barreca, D. Bekermann, E. Comini, A. Devi, R.A. Fischer, A. Gasparotto, C. Maccato, C. Sada, G. Sberveglieri, E. Tondello, CrystEngComm 12 (2010) 3419; *(d)* [*Barreca-2010-C*] D. Barreca, D. Bekermann, E. Comini, A. Devi, R.A. Fischer, A. Gasparotto, C. Maccato, G. Sberveglieri, E. Tondello, Sens. Actuators, B 149 (2010) 1; *(e)* [*Bekermann-2010-A*] D. Bekermann, A. Gasparotto, D. Barreca, A. Devi, R.A. Fischer, M. Kete, U. Lavrenčič Štangar, O.I. Lebedev, C. Maccato, E. Tondello, G. Van Tendeloo, ChemPhysChem 11 (2010) 2337.

mode based on the ZnO crystal structure, as well as on electric field effects in the used PECVD configuration, was proposed to explain the selective formation of anisotropic 1D nanosystem [*Jeong-2007*, *Jeong-2008*, *Liu-2004-A*, *Yamaoka-2008*] The growth of the thus obtained (200 - 300°C, 20W) ZnO NR arrays on alumina resulted in urchin-like nanosystems. [3] The obtained results pave the way to the possible growth of ZnO nanorods with tailored features on various substrates, an important goal for the development of advanced nanomaterials and nanodevices for diverse functional properties.

In this regard, in **paragraphs 3.4.5** and **3.4.6**, the application of the silicon and alumina based ZnO NR arrays in PSH, PCO,[4] and the sensing of selected pollutants,[3,5] respectively, is presented. The PSH and PCO performances of the silicon supported ZnO NR arrays were superior to those of the benchmark material (Pilkington® glass) and ZnO materials tested under similar conditions. In the gas sensing of various reducing and oxidizing gases (CH_3CH_2OH, CH_3COCH_3, H_2, CH_4, NO_2, O_3, CO) ZnO urchin-like structures on Al_2O_3 demonstrated outstanding properties, showing higher responses and sensitivity, improved kinetics and reversibility compared to ZnO systems reported in literature.

❖ 3.2 Introduction

Zinc oxide is an important, wide band gap ($E_g \approx 3.4$ eV) semiconductor material possessing interesting electrical, optical, piezoelectric, and photoconducting properties. [*Morkoç-2009*, *Wang-2008-E*, *Wei-2011*] In addition, ZnO is chemically and thermally stable, as well as biosafe and environment friendly. [*Bekermann-2010-B*, *Morkoç-2009*, *Wei-2011*] As a result, it has received widespread and significant attention for various technological applications, ranging from optics and optoelectronics to gas sensing and photocatalysis. [*Badre-2009*, *Barreca-2010-A*, *Bekermann-2010-A*, *Cho-2009*, *Kang-2006*, *Kuang-2005*, *Liu-2009-A*, *Özgür-2005*, *Öztürk-2011*, *Sun-2005*, *Wan-2005*, *Wang-*

[3] [*Barreca-2010-A*] D. Barreca, D. Bekermann, E. Comini, A. Devi, R.A. Fischer, A. Gasparotto, C. Maccato, C. Sada, G. Sberveglieri, E. Tondello, CrystEngComm 12 (2010) 3419.

[4] [*Bekermann-2010-A*] D. Bekermann, A. Gasparotto, D. Barreca, A. Devi, R.A. Fischer, M. Kete, U. Lavrenčič Štangar, O.I. Lebedev, C. Maccato, E. Tondello, G. Van Tendeloo, ChemPhysChem 11 (2010) 2337.

[5] [*Barreca-2010-C*] D. Barreca, D. Bekermann, E. Comini, A. Devi, R.A. Fischer, A. Gasparotto, C. Maccato, G. Sberveglieri, E. Tondello, Sens. Actuators, B 149 (2010) 1.

2005-A, *Wang-2008-E*, *Wei-2011*] Despite the high number of publications and patents on ZnO, the rational design of 1D ZnO nanosystems still deserves further attention, not only for the understanding of fundamental phenomena in low-dimensional structures, but also for the implementation of innovative multifunctional materials. [*Wang-2008-A*, *Bekermann-2010-B*, *Scalisi-2008*]

There have been various reports on the fabrication of ZnO thin films or nanostructures, including thermal evaporation, sputtering, PLD, MBE, sol-gel, ALD, and CVD. [*Barreca-2007-B*, *Morkoc-2009*, *Park-2008*, *Periasamy-2009*, *Scalisi-2008*] Among them, the latter (see also **chapter 2**) is by far the most promising technique for large scale production, and more importantly, by varying the CVD process parameters and nature of the precursors, it is possible to regulate the morphology and structure of the films. The commonly used zinc precursors for ZnO CVD are based on dialkylzinc in combination with an oxygen source. Nevertheless, these compounds are pyrophoric and extremely reactive (see **2.7**). More stable compounds on the other hand suffer from sintering or low volatility (**2.7**). As a consequence, CVD of ZnO from newly designed precursors still deserves further investigation. To this regard, a key point of the present work was the use of the bis(ketoiminato) zinc(II) compounds **1** and **2**, adopted for the first time in the CVD of ZnO materials. In particular, our interest has been devoted to the use of PECVD with the aim to grow 1D nanostructures and to softening deposition conditions compared to previous vapor phase approaches. So far, PECVD of ZnO nanorods has been hardly performed, [*Han-2010*, *Jeong-2007*, *Pedersen-2011*] and usually the materials growth involved the use of elevated temperatures (often 400°C or higher), annealing, high input powers and pyrophoric precursors (mainly DEZ) [*Han-2010*, *Jeong-2007*, *Jeong-2008*, *Liu-2004-A*, *Pedersen-2011*, *Yamaoka-2008*]. However, it is highly desirable to develop low-temperature processes to grow ZnO NR arrays with small diameter and high crystallinity, for device fabrication requiring a reduced amount of energy. [*Cho-2009*]

Recently, ZnO NR arrays have received considerable attention for their advanced photo-activated functions, regarding in particular PSH and photocatalysis that pave the way to the development of stimuli-responsive systems, including intelligent microfluidic and laboratory-on-chip devices, self-cleaning surfaces and degradation of environmental pollutants. [*Badre-2009, Bekermann-2010-A, Liu-2009-A, Papadopoulou-2009*, *Sun-2005*, *Wan-2005*, *Wang-2008-E*] So far, most reports have focused on ZnO powder materials, that suffer from undesired particle aggregation and can hardly be separated from the reacting aqueous suspensions, a major problem for use in photocatalytic

processes. [*Wang-2008-E*, *Wang-2011-C*] Supported ZnO NRs allow to overcome these problems and represent highly favorable architectures for light trapping. [*Prades-2008*, *Wang-2008-C*, *Wan-2005*, *Wang-2011-C*, *Zhang-2009-A*, *Zhou-2008*] Furthermore, for PSH and PCO applications, a high surface-to-volume ratio enables a faster arrival of photo-generated electrons and holes to the NRs surface, reducing detrimental recombination phenomena. [*Wan-2005*, *Wang-2011-C*, *Zhang-2009-A*] The remaining big challenge to tailor wettability and optimize photocatalytic behaviour by control over surface geometry and chemistry is to develop simple, low-cost and reliable synthetic methods for ZnO nanoarchitectures with high stability and convenient reuse. [*Papadopoulou-2009*, *Wang-2008-E*, *Wang-2011-C*]

Among the various applications, 1D zinc oxide assemblies have also attracted great interest for gas sensing of various analytes. In this work, the monitoring of CH_3CH_2OH and CH_3COCH_3, relevant for applications in breath analyzers and food control, [*Barreca-2007-A*, *Kwak-2008*] and the detection of flammable/toxic gases (O_3, NO_2, CO, H_2 and CH_4), extremely important for human health, safety and environmental reasons, [*Bhattacharyy-2006*, *Chang-2008*, *Chatterjee-1999*, *Dayan-1997*, *Hazra-2006*, *Kang-2006*, *Lupan-2010*, *Wu-2008-A*] have been addressed. An open challenge in the field of gas sensing by ZnO is the use of moderate working temperatures to increase operational safety and reduce power dissipation, yet maintaining a long range stability and high responses to low concentrations of testing gases. [*Barreca-2010-A*, *Barreca-2010-C*, *Bhattacharyy-2007*, *Bhattacharyy-2008-A*, *Bie-2007*, *Das-2010*, *Li-2007-B*, *Qurashi-2009*] To this regard, use of 1D zinc oxide assemblies enables higher detection efficiencies at low operating temperatures, along with fast responses and easy recovery capability, [*Hsueh-2007-B*, *Li-2007-B*, *Li-2009-B*, *Qi-2008*, *Zeng-2009-B*] thanks to their high surface-to-volume ratio and lateral dimensions comparable to the extension of the surface space-charge region. [*Tricoli-2010*] Since the performances of solid state gas sensors are directly dependent on the surface and morphology of the active material, [*Basu-2008*, *Lupan-2010*] a relevant area of focus in nanoscience involves the integration of 1D nanoscale building blocks into higher-order architectures, from vertically and horizontally aligned ZnO 1D arrays to assemblies combining the properties of 1D and 3D materials, like urchin-like systems. [*Elias-2010*] The fabrication of urchin-like ZnO NR arrays can hardly be found in the literature [*Elias-2010*] and their utilization in gas sensing devices has never been described before. [*Barreca-2010-A*]

❖ 3.3 Thermal CVD of ZnO Nanostructures on Si(100) and Borosilicate Glass

❖ 3.3.1 Deposition Procedure

CVD experiments from precursors [Zn{[$(CH_2)_x$$OCH_3$]$NC(CH_3)$=C(H)$C(CH_3)$=O}$_2$] (**1**: x = 2; **2**: x = 3) were performed in a custom-built (see **8.3.1**), horizontal, cold-wall reactor using N_2 (6.0) and O_2 (4.5) as carrier and reactive gases, respectively. Prior to each deposition, Si(100) and borosilicate glass substrates were ultrasonically cleaned in ethanol (10 min), distilled water (10 min), and dried in air. Film growth using both the precursors was conducted in the temperature range 400 – 700°C. For all depositions the total pressure and deposition time were 10.0 mbar and 90 min, respectively, while N_2 and O_2 flow rates were kept constant at 50 sccm. The vaporization temperature was maintained at 130°C for both precursors.

	T (°C)	Structural features	GR (Å/min)
Pre-cursor **1**	450	amorphous	4
	500	(001) oriented	9
	600		21
	650		22
	700		5
Pre-cursor **2**	400	amorphous	6
	500	(001) oriented	16
	600		22
	700		19

Table 3.1: Deposition temperature, GR and structural features for representative ZnO films grown from precursors **1** and **2** (p = 10 mbar, time = 90 min, T_{vap} = 130°C).

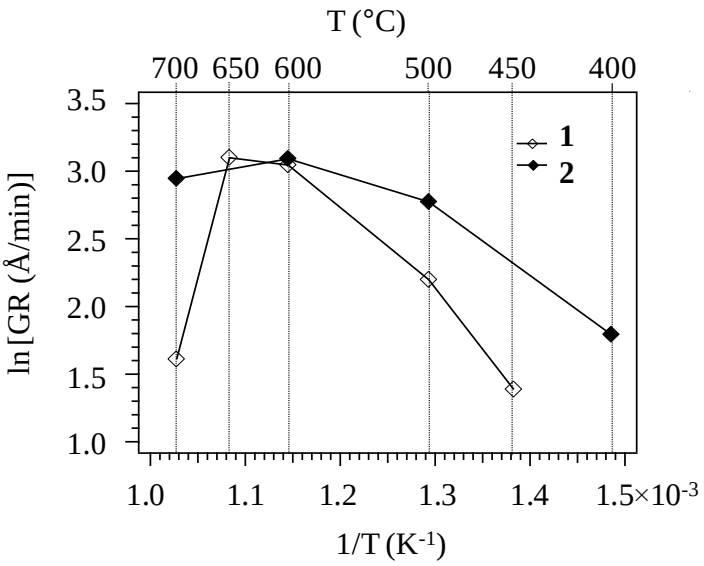

Figure 3.1: Arrhenius plot of the GR of ZnO as a function of substrate temperature (1/*T*).

ZnO thin films could be reproducibly grown on both Si(100) and borosilicate glass substrates. They were very uniform, adherent to the substrate (scotch-tape test), and shiny in appearance. **Table 3.1** gives an overview of the relevant CVD ZnO samples analyzed in the present work. The growth rate (GR) of ZnO from both compounds increased up to

600°C (maximum GR ~ 20 Å/min), corresponding to the region of kinetic control dominated by the precursor thermal decomposition on the substrate surface (**figure 3.1**). The growth rates obtained from compound **2** were slightly higher than in the case of **1** at lower temperatures (400 – 500°C). The slightly lower GRs in the case of precursor **1** could be due to a lower decomposition rate of this precursor. From the Arrhenius plot (**figure 3.1**), a slightly lower activation energy for **2** compared to **1** is observed. At the optimized temperature for deposition (600°C), the growth rates were almost the same. Beyond 600°C, the GRs decrease which can be typically related to depletion.

❖ 3.3.2 Morphology and Structure

The film crystallinity as a function of the substrate temperature was investigated by XRD measurements and relevant structural features are summarized in **table 3.1**. Similar results were obtained on both Si(100) and glass substrates. The temperature onset for the crystallization of the ZnO wurtzite hexagonal phase [*JCPDS-A*] was found to be 500°C. **Figure 3.2** displays the XRD patterns recorded on samples obtained from precursor **2** that were all characterized by the presence of a single reflection at $2\theta = 34.5°$, corresponding to the (002) ZnO planes. In line with previous observations regarding various ZnO systems, [*Morkoc-2009*, *Park-2008*, *Liu-2004-A, Jeong-2004, Park-2002, Wu-2002*, *Park-2005, Kitamura-2008*] this feature indicated a strong preferred orientation with the <001> direction normal to the substrate surface, and could be explained basing on the ZnO wurtzite structure, consisting of alternate O and Zn crystallographic planes stacked along the *c*-axis. The spontaneous polarization along this direction triggers the <001> orientation, due to the tendency to satisfy the decrease in the overall free energy. [*Morkoc-2009*, *Barreca-2007-B*, *Park-2008*] Irrespective of the precursor used, the highest raw intensity of the (002) diffraction peak was observed at 600°C, the temperature corresponding to the highest film thickness (see above).

An insight into the surface morphology was gained by a combined FE-SEM and AFM investigation. For both precursors, growth at $T < 500$°C resulted in the formation of smooth and almost featureless coatings, in agreement with the absence of reflections in the corresponding XRD patterns. An increase in the growth temperatures, however, produced different morphological features. Representative SEM images of ZnO deposits on Si(100) and borosilicate substrates are shown in **figure 3.3**. In the case of precursor **1**

(**figure 3.3 (a)**), film growth at 500°C produced a densely packed, columnar-like ZnO thin film with spherically topped columns. Correspondingly, AFM investigation (**figure 3.4 (a)**) displayed a relatively smooth surface, with a root mean square (RMS) roughness close to 3 nm. An increase in the deposition temperature to 600°C resulted in the formation of interwoven 2D-like porous structures (**figure 3.3 (a)**). Under these conditions, cross-sectional SEM images showed the growth of a very rough film, in agreement with AFM images (**figure 3.4 (a)**) and the corresponding RMS roughness was as high as 42 nm. In the case of precursor **1**, a further increase in the substrate temperature to 700°C led to the formation of a film composed of interconnected aggregates (average size ~ 100 nm), resulting in a more compact cross sectional assembly and an appreciably lower overall thickness.

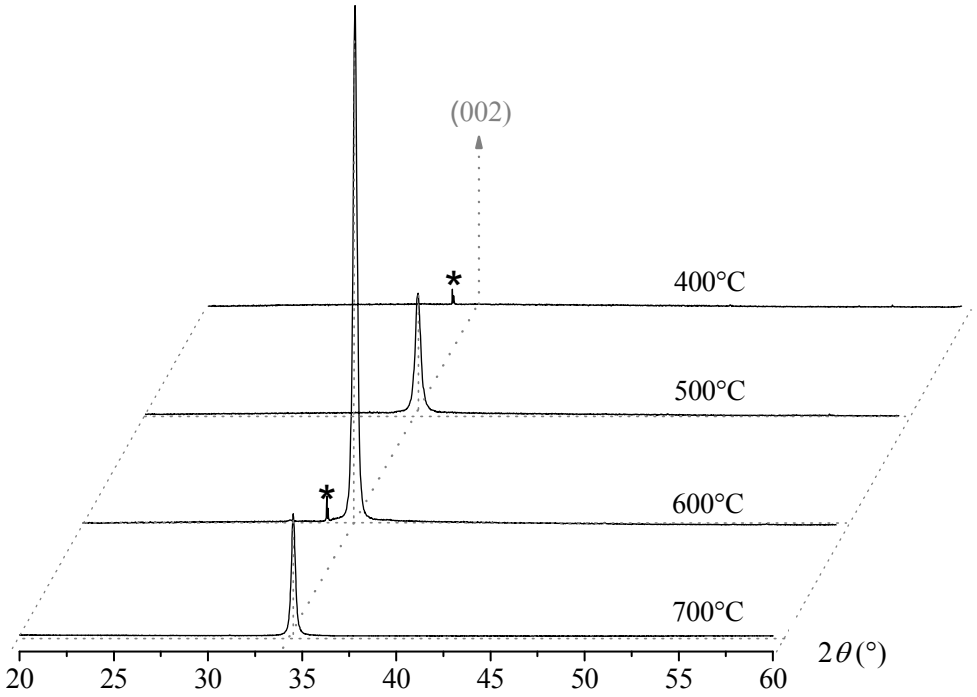

Figure 3.2: XRD patterns of ZnO films grown from precursor **2** as a function of growth temperature. Reflections from the Si substrate are marked with an asterisk.

For precursor **2** (**figure 3.3 (b)**), growth at 500°C resulted in uniform and smooth coatings, and the corresponding RMS roughness was 5 nm (see also AFM images in **figure 3.4 (b)**). FE-SEM and AFM results correlate to a good extent, confirming the presence of well interconnected aggregates with typical sizes of ~ 50 nm (**figure 3.3 (b)**, plane-view). At 500°C, cross-sectional images revealed the occurrence of a columnar-like growth, which appeared even more distinct upon raising the temperature to 600°C. These

findings were in line with XRD results (see above) that suggested a high structural ordering for films obtained at this deposition temperature. In addition, at 600°C the sample surface was characterized by the presence of agglomerates (average size ~ 470 nm) evenly distributed throughout the film and directly protruding from the underlying columnar structures, as clearly shown by the cross-sectional image. Correspondingly, the RMS roughness evaluated by AFM analysis was 25 nm (**figure 3.4**). The growth on borosilicate substrates at 600°C (**figure 3.3 (b)**, bottom) resulted in a surface topography dominated by densely packed aggregates (d ~ 150 nm) uniformly interconnected among themselves. Cross-sectional analyses showed the presence of a rather compact film, with a mean thickness of 230 nm, corresponding to a growth rate of 25 Å/min.

(a)

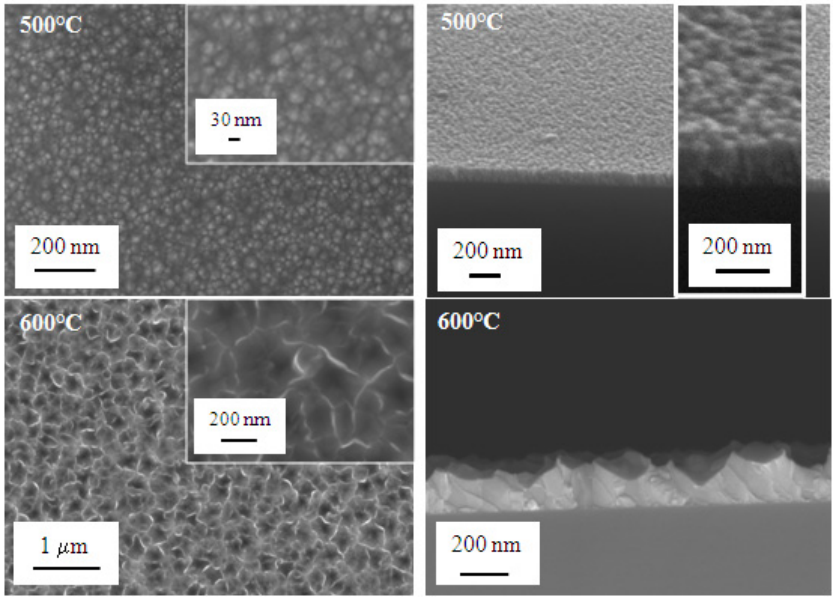

(b)

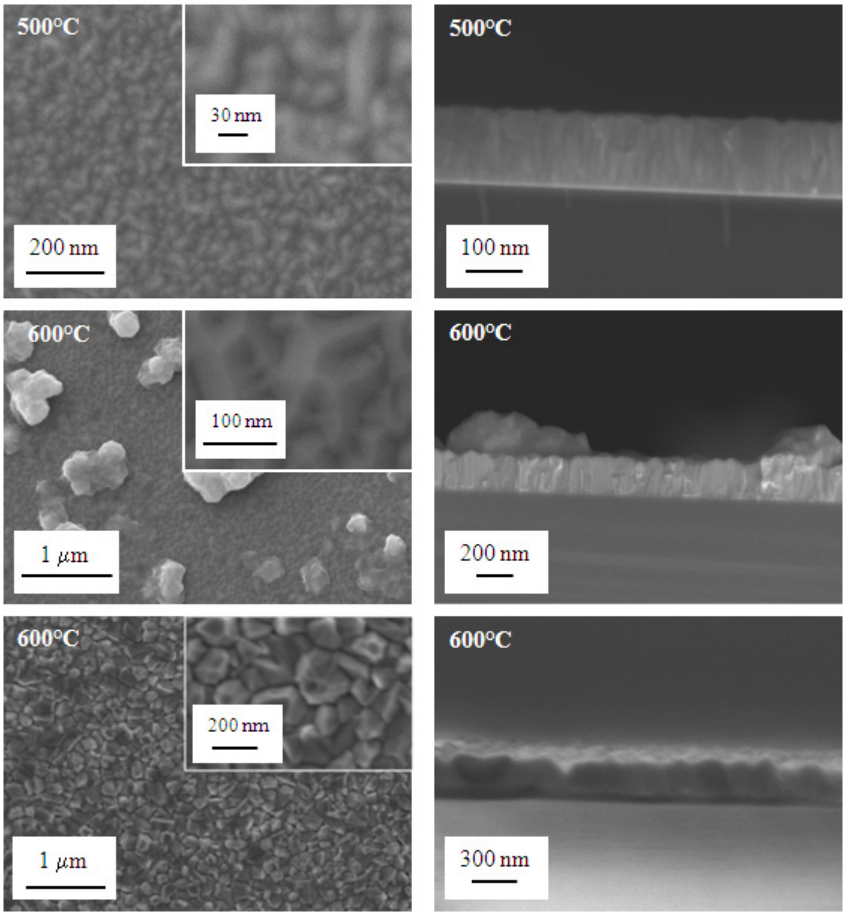

Figure 3.3: Plane-view and cross-sectional FE-SEM micrographs of ZnO films deposited at 500°C and 600°C using: (a) precursor **1**, on Si(100); (b) precursor **2**, on Si(100) and on borosilicate ((b), bottom images). (Insets show higher magnification images.)

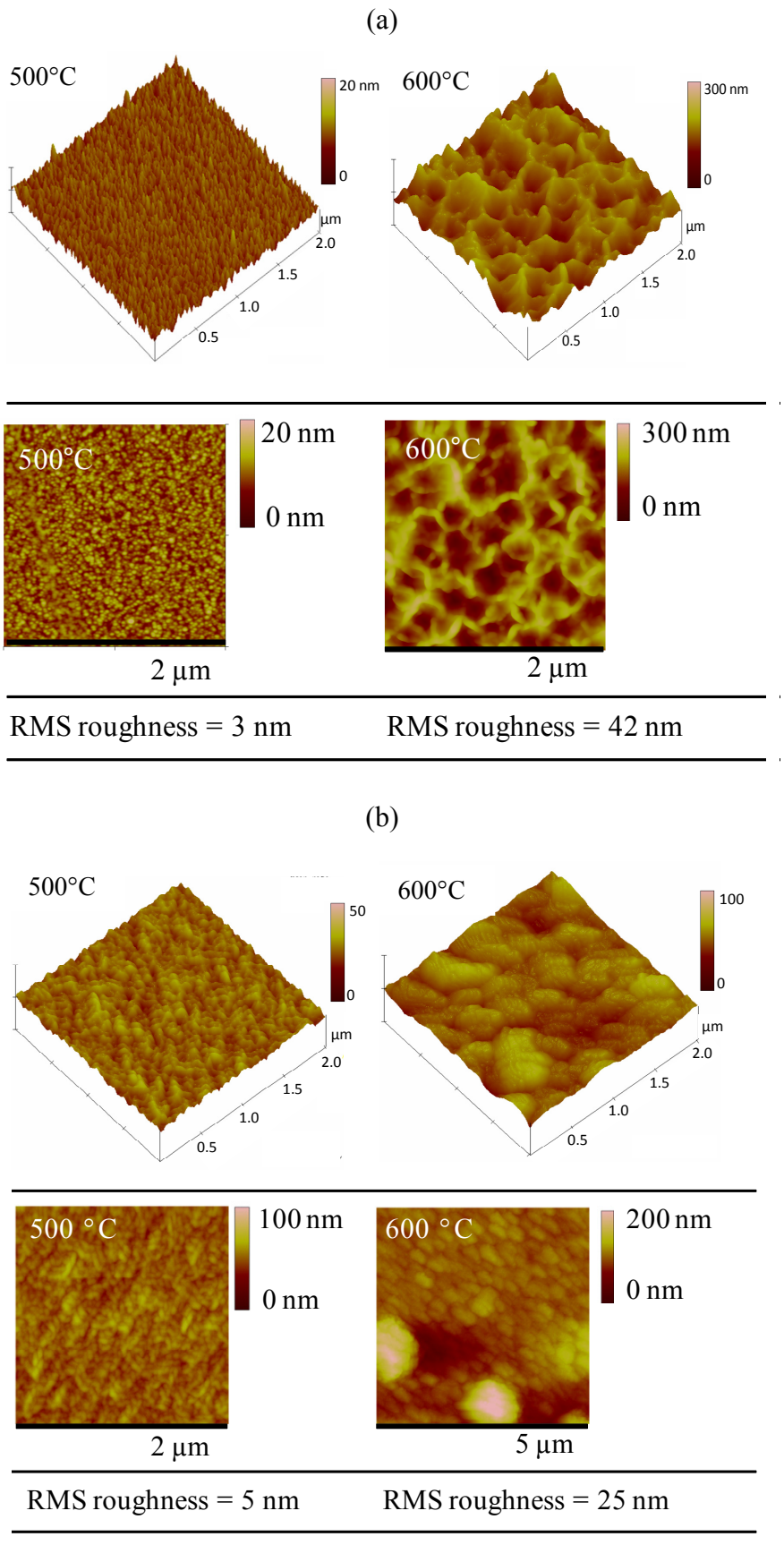

Figure 3.4: AFM micrographs of ZnO films deposited on Si(100) using: (a) precursor **1**; (b) precursor **2**.

❖ 3.3.3 Composition

RBS was employed to determine the film stoichiometry, and the presence of Zn and O in the spectra of a ZnO film grown at 600°C is clearly seen (**figure 3.5**). The thickness of the layer is in agreement with the value determined by the SEM image (**figure 3.3**), taking into account the surface roughness. The recorded spectrum is described by a simulation of a 190 nm thick layer of zinc (41 at. %), oxygen (45 at. %) deposited on a silicon substrate. In comparison to the simulated data, the broadening of the Si edge and of the low-energy Zn edge can be attributed to the surface roughness of the layer (**figure 3.3**). The spectrum indicates the presence of carbon in the range of 5 weight %, proximate to its detection limit, thus indicating that the precursor is able to provide the ZnO material in the right stoichiometry.

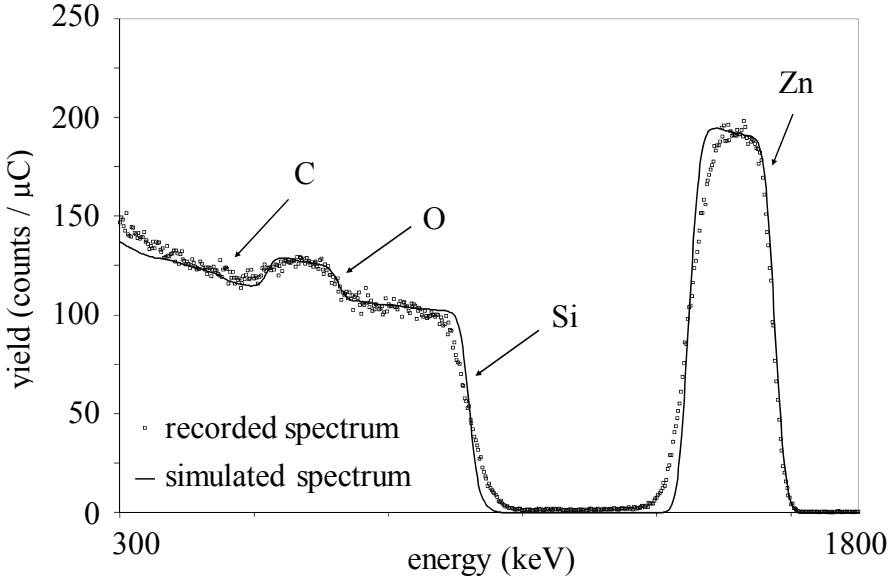

Figure 3.5: Representative RBS spectrum of ZnO grown at 600°C by using compound **1**.

The surface and in-depth chemical composition of the ZnO films were investigated by XPS, yielding very similar results for films obtained from both precursors. Representative XPS spectra of Zn and O peaks are reported in **figure 3.6**, both before and after Ar^+ erosion. Irrespective of the process conditions and the used precursor, the Zn2$p_{3/2}$ and Zn3$p_{3/2}$ spin-orbit components were centered at binding energies (*BE*) = 1021.8 and 88.9 eV, as expected for ZnO. [*Barreca-2007-C*, *Barreca-2003-B*, *Moulder-1992, Nist*] The fingerprint for the presence of the sole zinc(II) oxide was provided by the evaluation of the Auger parameter [α_{Zn} = *BE*(Zn2$p_{3/2}$) + *KE*(Zn*LMM*), where *KE* = kintetic energy], which was 2010.2 eV for all films grown from precursors **1** and **2**. This value is in

excellent agreement with literature data for ZnO. [*Armelao-2006*, *Armelao-2008, Barreca-2007-C, Briggs-1990, Moulder-1992*]

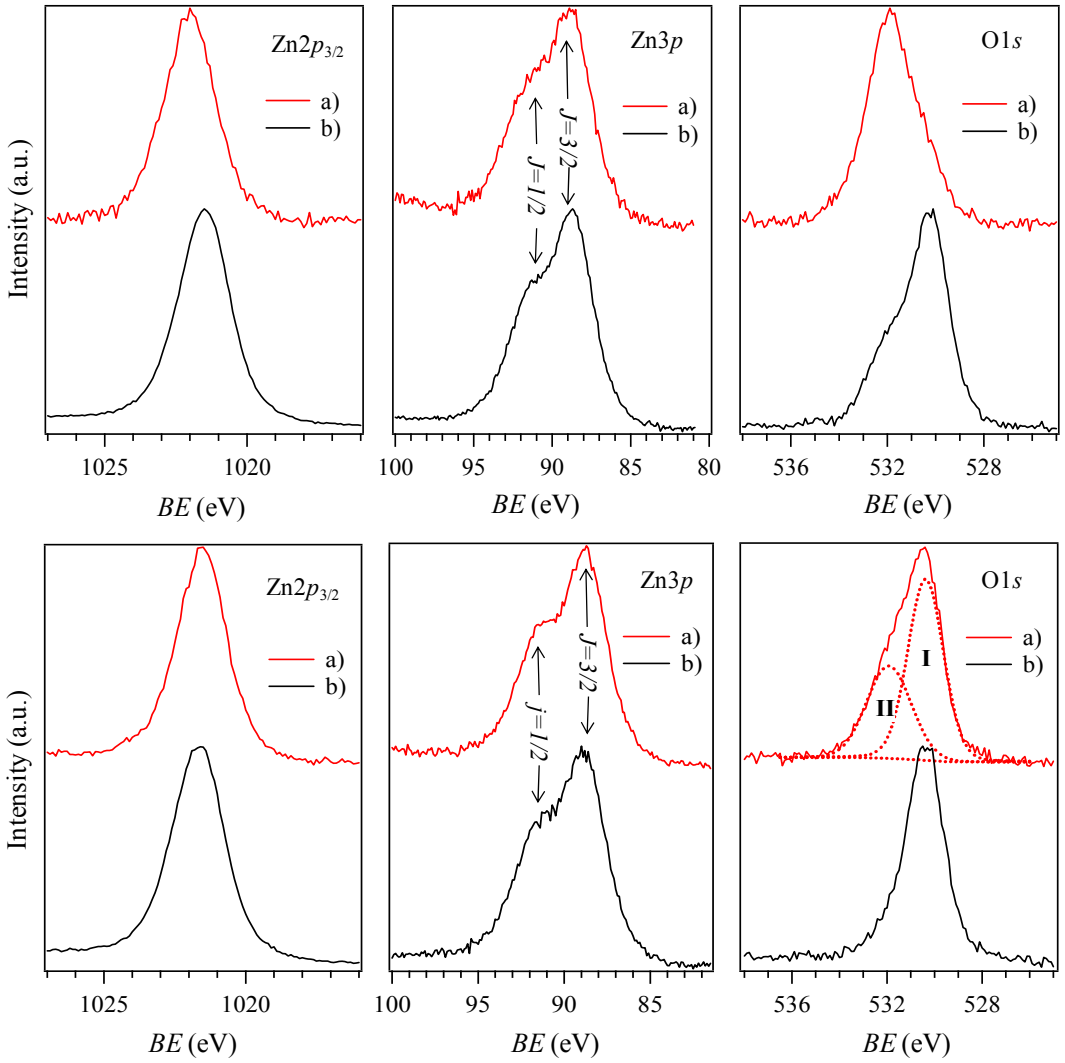

Figure 3.6: Representative XPS zinc and oxygen signals for ZnO samples grown at 600°C from precursor **1** (top) and **2** (bottom): (a) surface; (b) after 8 min Ar^+ erosion. For the second specimen, the fitting components for the surface O1*s* peak are also displayed along with the raw spectrum.

The surface O1*s* signal could be decomposed by means of two contributions (**figure 3.6**). The most intense one (**I**, *BE* = 530.4 eV) was attributed to Zn-O-Zn bondings of the oxide phase, whereas the minor one (**II**), centered at *BE* = 532.0 eV, could be mainly assigned to surface -OH groups, whose presence is frequently observed on a ZnO surface. [*Armelao-2006*, *Armelao-2008*, *Barreca-2007-C*, *Bekermann-2010-B*, *Scalisi-2008*] Contributions to this component from carbonate species arising from air exposure were

also likely to be present, as confirmed from the surface C1*s* line shape (not shown), that displayed a minor component located at *BE* = 288.4 eV. [*Moulder-1992, Nist*] As a result, typical surface O/Zn atomic ratios were higher than the expected value for ZnO (1.8 – 2.0). Nevertheless, the O1*s* **II** component disappeared to noise level after Ar^+ erosion, thus indicating that the above species essentially arose from contact with the outer atmosphere. Correspondingly, the O/Zn ratio nearly approached the stoichiometric value (~ 1.1).

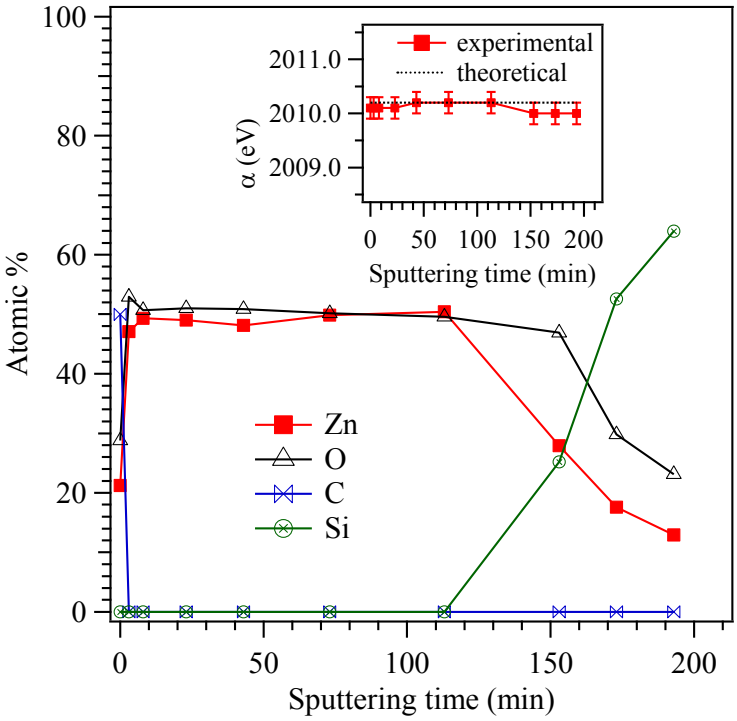

Figure 3.7: XPS depth profile of a ZnO sample grown from precursor **2** at 600°C. In the inset, the dependence of the Auger parameter on the sputtering time is shown. [*Moulder-1992*]

Further insight into the in-depth film composition was gained by XPS profiling (**figure 3.7**). It is noteworthy that the carbon signal completely disappeared after only 3 min Ar^+ sputtering, thus confirming that it arose from the atmospheric contamination of the sample surface. This feature, along with the absence of any nitrogen signal from the precursor ligands, indicates that the precursor decomposition was a clean process, leading to impurity-free ZnO under the adopted conditions. In addition, zinc and oxygen signals had a ratio close to the theoretical value throughout the bulk of the film, apart from an oxygen excess at the interface with the substrate that could be attributed to the presence of a native silica layer on Si(100). The Auger α_{Zn} parameter dependence on depth (**figure**

3.7, inset) confirmed the uniform formation of zinc(II) oxide throughout the sample thickness.

❖ 3.3.4 Optical Properties

Selected UV-Vis transmission spectra recorded for samples obtained from precursor **1** on borosilicate glass are depicted in **figure 3.8**. All the samples exhibited a transmittance > 60% in the visible region, and a sharp UV absorption edge located at λ = 370 nm, related to the characteristic ZnO band-to-band transitions. [*Armelao-2006*, *Malandrino-2005*] The optical band gap E_g was evaluated from the Tauc plot $(\alpha\, h\nu)^2$ vs. $h\nu$ (**figure 3.8**, inset), where α is the absorption coefficient computed from the recorded spectra by extrapolating the trend to zero absorption. [*Periasamy-2002*, *Barreca-2003-B*] For all the analyzed ZnO films, the obtained E_g values were close to 3.3 eV, which is in agreement with the literature for stoichiometric ZnO. [*Armelao-2006*]

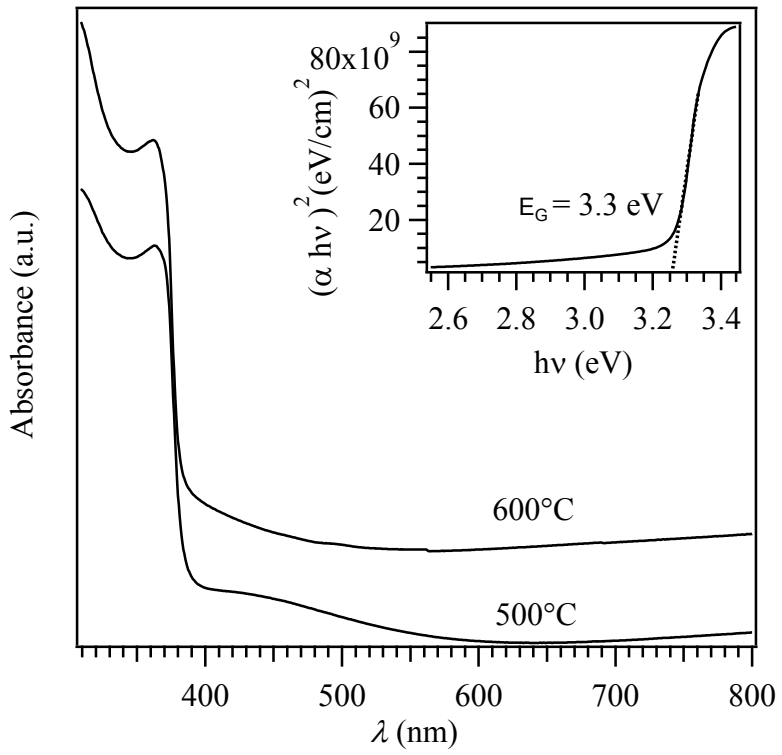

Figure 3.8: Representative optical spectra of ZnO thin films grown on borosilicate substrates from precursor **1**. Inset: Tauc plot of $(\alpha\, h\nu)^2$ vs. $h\nu$ for the specimen grown at 600°C.

The optical properties of the as-deposited ZnO layers were also investigated by means of PL measurements. **Figure 3.9** displays the PL spectra of ZnO films on Si(100) obtained from precursor **2** at 500 and 600°C. At room temperature, the former sample showed a high quality excitonic peak of ZnO at 3.30 eV (376 nm) [*Bekermann-2010-B*, *Li-2007-A*] with a full width at half maximum (FWHM) of 18 nm. The room temperature PL spectrum of the deposit obtained from precursor **2** at 600°C shows an even narrower FWHM of 13 nm. The small FWHM values of the excitonic peaks measured at room temperature demonstrated the high crystalline quality of the ZnO samples. Irrespective of the laser intensity, all samples gave maximum response at 3.30 eV at room temperature (**figure 3.9 (b)** and **(d)**). At 77 K, the maximum was shifted to 3.37 eV (**(a)** and **(c)**), in agreement with previous reports. [*Li-2007-A, Teke-2004*] This so-called Varshni shift arises from shifts in the relative position of E_C (conduction band) and E_V (valence band) (i) due to the temperature dependence of the thermal expansion of the lattice, and (ii) because of temperature-dependent electron/lattice interactions. [*Varshni-1967*] At variance with most literature data, no PL signals due to deep level emission defects (V_O, V_{Zn}, Zn_i, and O_i) in the region 420 - 540nm could be detected. [*Bekermann-2010-B*, *Jeong-2004, Kuang-2005, Liu-2004-A, Mikrajuddin-2001, Park-2006, Wang-2009-A]*

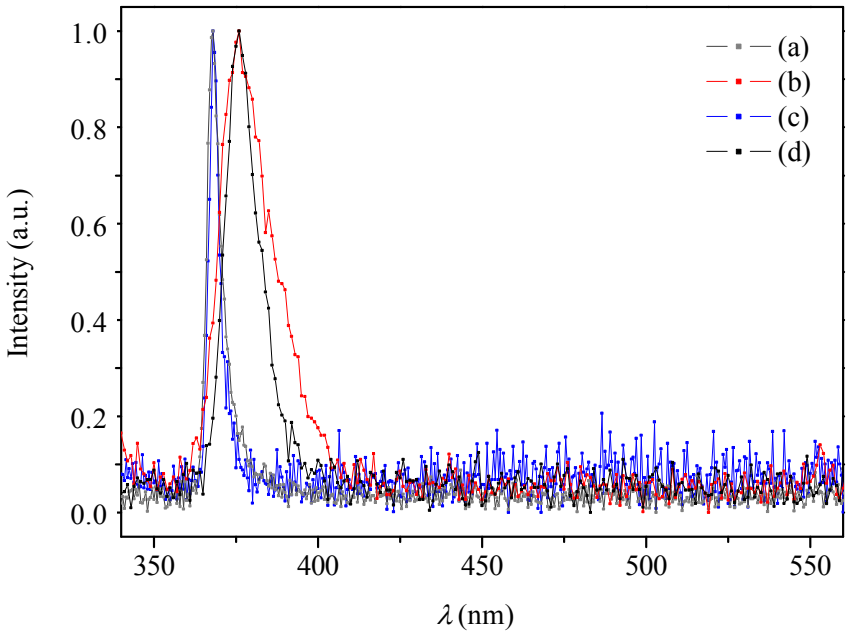

Figure 3.9: Normalized PL spectra of ZnO films on Si(100) grown from precursor **2** at 500°C, (a) 77 K and (b) room temperature; and at 600°C, (c) 77 K and (d) room temperature (excitation power = 20 W / cm^2).

❖ 3.4 PECVD of ZnO Nanostructures on Si(100) and Polycrystalline Al_2O_3

❖ 3.4.1 Deposition Procedure

PECVD of ZnO nanorods from $[Zn\{[(CH_2)_xOCH_3]NC(CH_3)=C(H)C(CH_3)=O\}_2]$ (**1**: x = 2; **2**: x = 3) was carried out by a RF (ν = 13.56 MHz) two-electrode custom-built apparatus (**8.3.3**). Growth experiments (duration = 1 h) were performed under Ar/O_2 plasmas (total Ar (O_2) flow rate = 75 (20) sccm) and at a total pressure of 1.0 mbar. *p*-Type Si(100) substrates were cleaned, without removing the native oxide layer, by iterative dipping in sulfonic detergent and distilled water, distilled water, acetone, and isopropylic alcohol. [*Armelao-1998*, *Bekermann-2010-B*]

Table 3.2: Overview of sample labeling as a function of substrate, precursor, deposition temperature and RF-power. Pressure, deposition time and T_{vap} were 1 mbar, 60 min and 140°C, respectively for all depositions.

Substrate	Si(100)			
Precursor	**1**			**2**
RF-power	40 W	20 W	10 W	20 W
T (°C)				
100	**1_100_40W(Si)**	**1_100_20W(Si)**		**2_100_20W(Si)**
200	**1_200_40W(Si)**	**1_200_20W(Si)**		**2_200_20W(Si)**
300	**1_300_40W(Si)**	**1_300_20W(Si)**	**1_300_10W(Si)**	**2_300_20W(Si)**
400	**1_400_40W(Si)**	**1_400_20W(Si)**		**2_400_20W(Si)**

Substrate	Al_2O_3			
Precursor		**1**		**2**
RF-power		20 W		20 W
T (°C)				
200		**1_200_20W(Al)**		**2_200_20W(Al)**
300		**1_300_20W(Al)**		**2_300_20W(Al)**

The Zn(II) ketoiminate precursors were vaporized in an external vessel maintained at 140°C by means of an oil bath and transported into the deposition zone through an Ar

flow. The gas lines connecting the precursor reservoir and the reactor chamber were maintained at 160°C by means of heating. For all experiments, the deposition time and interelectrode distance were set at 1 h and 6 cm, respectively. The labeling of the present samples is reported in **table 3.2**.

❖ 3.4.2 Morphology and Structure

❖ *3.4.2.1 ZnO Nanorod Growth on Si(100) from **1***

In the case of precursor **1**, the combined influence exerted by the growth temperature and the applied RF-power, both related to the energy supply during the deposition process, was investigated. To this regard, **figure 3.10** provides a comparative FE-SEM morphology overview for samples synthesized from precursor **1** (see **table 3.2**). As can be observed, the use of high RF-power values (40W samples, **1_100_40W(Si)** – **1_400_40W(Si)**) resulted in the obtainment of relatively compact system morphology. In particular, variations of the substrate temperature from 100 to 400°C produced a thickness increase from ≈ 60 nm to ≈ 150 nm (**table 3.3**). While the **1_100_40W(Si)** sample showed the presence of pseudo-globular particles typical for an isotropic growth, the development of a columnar morphology was evidenced for specimens **1_200_40W(Si)** and **1_300_40W(Si)**. In particular, the 300°C sample (**1_300_40W(Si)**) presented the most pronounced anisotropy, with the formation of some faceted tips on the column surface. Conversely, at 400°C (**1_400_40W**), a compact ZnO film characterized by a rather smooth surface was obtained. Even though at 20 W (samples **1_100_20W(Si)** – **1_400_20W(Si)**) a qualitatively similar evolution was observed as a function of the substrate temperature, the system morphology was systematically characterized by a more pronounced 1D growth with respect to specimens synthesized at 40 W (**1_100_40W(Si)** – **1_400_40W(Si)**). This difference could be traced back to an enhanced energy supply to the substrate surface at 40 W, leading to more marked coalescence phenomena between adjacent nanoaggregates and to an increased lateral growth. [*Jeong-2008*, *Park-2006*]
Regarding samples synthesized at 20 W, the most interesting results were obtained at intermediate temperatures, that is, for **1_200_20W(Si)** (200°C) and **1_300_20W(Si)** (300 °C). In fact, under these conditions ordered arrays of NRs aligned perpendicularly to the substrate surface were grown, with an aspect ratio (length/diameter) increasing from 9.5 at 200°C to 12.4 at 300°C. In the case of sample **1_300_20W(Si)**, having the more

pronounced 1D morphology, the density of these nanostructures per unit area, estimated by plane-view images, was ≈ 950 nanorods/μm^2.

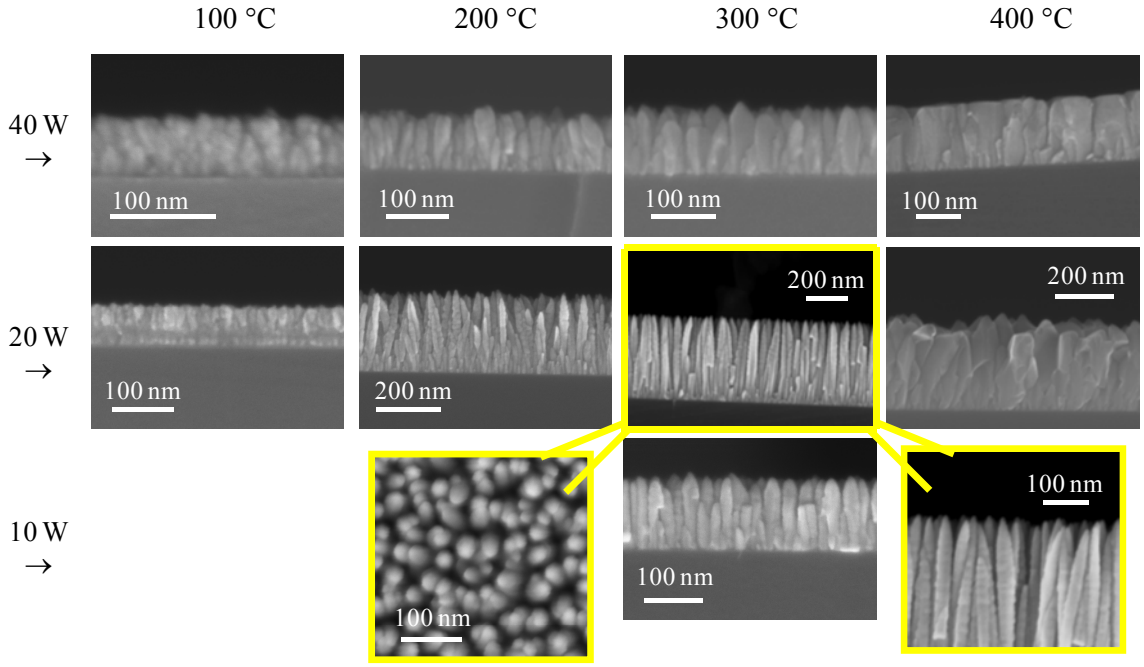

Figure 3.10: Cross-section FE-SEM micrographs of Si(100)-supported ZnO nanodeposits synthesized from precursor **1** as a function of the adopted RF-power and growth temperature (see **tables 3.2** and **3.3**). For sample **1_300_20W(Si)**, representative plane-view and high magnification cross-section images are also reported.

An increase of the growth temperature up to 400°C (sample **1_400_20W(Si)**) resulted in the formation of a relatively compact cross-section texture, although the surface appeared rougher than in the case of **1_400_40W(Si)**. This phenomenon suggested that, at 400°C, a reduction of the applied RF-power produced a progressive transformation from a compact film to a columnar one, [*Park-2006*] accompanied by an enhancement of the overall system thickness (i.e. of the GR, **table 3.3**). A similar effect indicated that the use of more drastic RF-power conditions favored etching phenomena over the competitive deposition ones, [*Li-2003*] whereas the use of a lower RF-power (20 W) had a beneficial influence on the GR and also induced an improvement of the anisotropic 1D morphology. In order to further ascertain the latter effect, PECVD of ZnO from precursor **1** was also undertaken at 300°C and 10 W (**1_300_10W(Si)**). Under these conditions columnar structures were still obtained, but the deposit thickness (130 nm) and aspect ratio (4.9) were appreciably lower than for the corresponding sample (**1_300_20W(Si)**) obtained at 20 W. The above results, in line with previous literature works, [*Falyouni-2009*, *Jeong-*

2007, *Kim-2009*, *Li-2003*] highlight the need for intermediate growth temperatures and RF-power values to obtain anisotropic ZnO NR arrays.

Table 3.3: Film thicknesses (*t*) for Si(100) supported samples obtained from **1** (see **table 3.2**).

Sample	*t* (nm)	Sample	*t* (nm)	Sample	*t* (nm)
1_100_40W(Si)	65	**1_100_20W(Si)**	70		
1_200_40W(Si)	90	**1_200_20W(Si)**	250		
1_300_40W(Si)	105	**1_300_20W(Si)**	405	**1_300_10W(Si)**	130
1_400_40W(Si)	150	**1_400_20W(Si)**	330		

GIXRD analyses on specimens **1_100_40W(Si)** – **1_400_40W(Si)** and **1_100_20W(Si)** – **1_400_20W(Si)** (**figure 3.11**) evidenced the sole reflections expected for the hexagonal ZnO *wurtzite* structure (*zincite*; [*JCPDS-A*]). Nevertheless, both the relative peak amplitudes and the total diffracted intensity were significantly influenced by the synthesis conditions. At 100°C, the recorded patterns were characterized by four well-evident reflections at 2θ = 31.8, 34.4, 36.3, and 47.5°, attributed respectively to ZnO (100), (002), (101), and (102) reflections. [*JCPDS-A*] The relative intensities of the observed peaks suggested the absence of marked preferential orientation effects. This result, in line with the observed globular morphology of both **1_100_40W(Si)** and **1_100_20W(Si)** samples (compare **figure 3.10**), confirmed the occurrence of an isotropic crystallite growth. [*Fu-2007-B*, *Ali-2009*] In a different way, for ZnO nanodeposits synthesized in the 200 - 400°C range, a strong *c*-axis preferential orientation was always observed, as indicated by the remarkable intensity of the (002) peak with respect to the other reflections (**figure 3.11**). The total diffracted intensity for samples synthesized at the same temperature was always higher at 20 W, in agreement with the increased deposit thickness applying 20 W of RF-power (see also **figure 3.16**). It is worthwhile observing that for specimen **1_300_20W(Si)**, characterized by the most anisotropic 1D architecture, the GIXRD pattern was dominated by the (002) reflection. This result, highlighting the occurrence of a direct relationship between the sample structure and morphology, indicated that the observed ZnO NRs were characterized by a <001> growth direction perpendicular to the substrate surface. [*Jeong-2008*, *Lee-2005*, *Li-1999*, *Liu-2004-A, Umar-2006*, *Wang-2005-A*, *Wu-2009*, *Zhang-2006-A*]

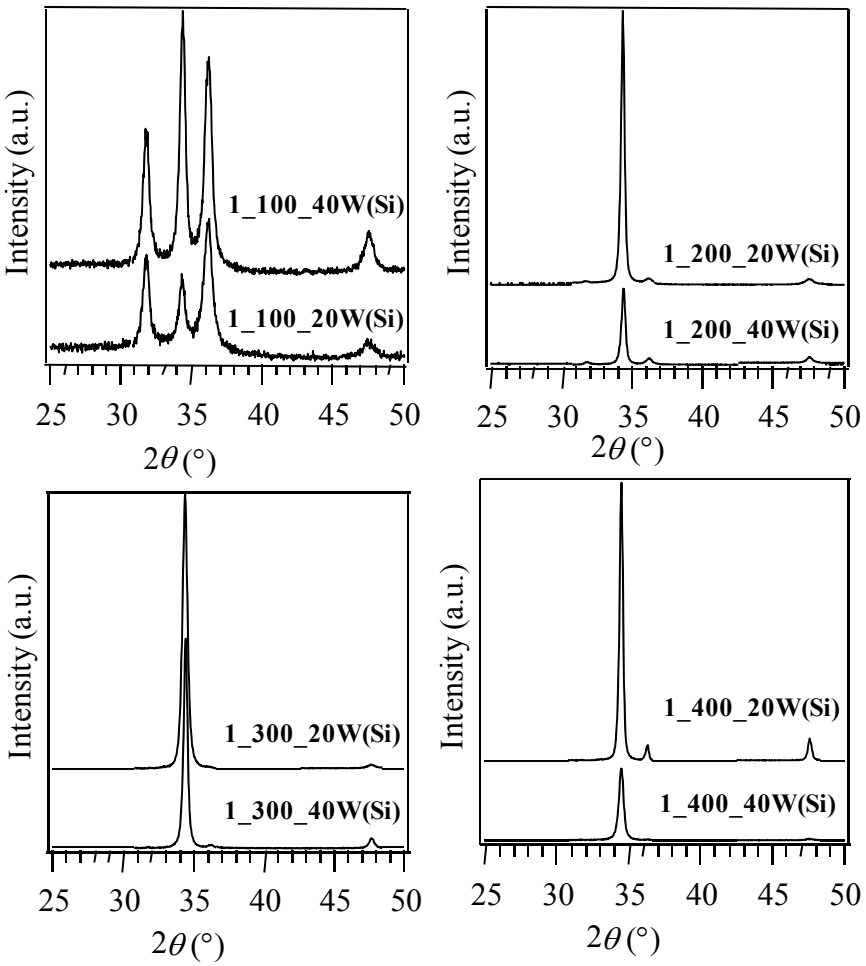

Figure 3.11: GIXRD spectra for samples **1_100_40W(Si)** – **1_400_40W(Si)** and **1_100_20W(Si)** – **1_400_20W(Si)** deposited on Si(100) from precursor **1**.

In order to attain a deeper insight into the structure and morphology of the synthesized ZnO nanosystems, selected specimens were subjected to TEM and high-resolution TEM (HR-TEM) analyses. **Figure 3.12 (a)** and **(b)** display the low magnification cross-section structure of samples **1_200_20W(Si)** and **1_300_20W(Si)**. The observed topological features were in excellent agreement with results provided by FE-SEM investigation (compare **figure 3.10**) and confirmed the formation of uniform NR arrays oriented perpendicularly to the substrate surface, with aspect ratio values directly dependent on the synthesis conditions. As already discussed in **paragraph 3.2.2**, the obtainment of ZnO 1D growth under optimized synthetic conditions is usually related to the non-centrosymmetric hexagonal wurtzite structure, and, in particular, to the divergence of surface energies, resulting in diversified GRs as a function of crystallographic directions. [*Barreca-2007-B, Li-1999*, *Wang-2008-A*, *Wu-2002*, *Wu-2009*] Nevertheless, the sole occurrence of an anisotropic growth regime is not sufficient to ensure the alignment of the

resulting NRs perpendicular to the substrate surface. To this regard, an epitaxial relationship with the Si(100) support cannot explain the obtained results, since a native SiO_2 layer ≈ 2 nm thick was always present at the ZnO/substrate interface (see **figure 3.12 (c)**). [*Lee-2005*, *Liu-2004-A Scalisi-2008*,] In the present case, a reasonable justification for the highly oriented growth of ZnO NRs relies on the intrinsic polarization along the *c*-axis of the wurtzite structure, favoring the rod alignment in the direction of the applied electric field, that is, normal to the substrate surface. [*Li-1999*, *Liu-2009-B*, *Liu-2004-A*, *Wang-2008-A*]

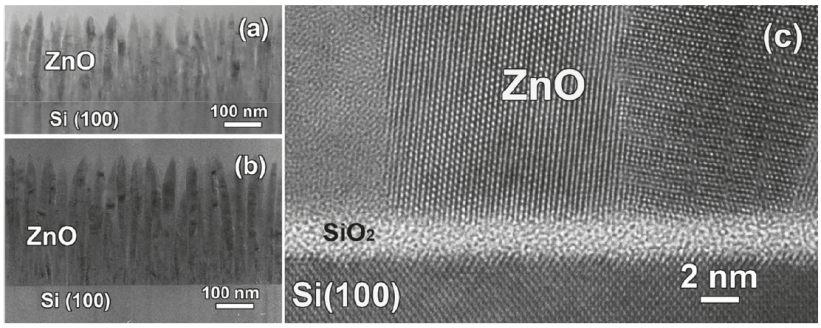

Figure 3.12: Cross-section low magnification TEM images of samples (a) **1_200_20W(Si)** and (b) **1_300_20W(Si)**. (c) Representative HR-TEM image of the ZnO/substrate interface for specimen **1_200_20W(Si)**.

HR-TEM analyses confirmed that ZnO NRs always grew along the <001> direction, that is, with the *c*-axis mainly perpendicular to the substrate surface (see **figure 3.13**). Although this effect was common to all 1D ZnO nanodeposits, other structural features were found to be directly dependent on the specific synthesis conditions. In this regard, **figure 3.13** shows some important differences between samples **1_200_20W(Si)** (200°C) and **1_300_20W(Si)** (300°C) obtained at 20 W RF-power. As can be observed, stacking faults (SF) were the main type of defects in both cases, but their density was appreciably higher for **1_200_20W(Si)**. This phenomenon suggested that an increase of only 100°C in the growth temperature resulted in a more efficient ZnO crystallization. Such an effect, also confirmed for samples synthesized from precursor **2** (**figure 3.15**), was responsible for the different optical properties of the corresponding ZnO NR arrays (see PL results, **paragraph 3.4.4**). The most common type of SF for all samples was found to be the one shown in **figure 3.13 (b)**. As the stacking sequence of 2H-ZnO structure can be represented as ABABAB along the *c* direction, this SF can be described as ABABACAC (I_1 type). [*Stampfl-1998*] The displacement vector R can be determined as 1/3 [100]. Only

in sample **1_200_20W(Si)**, besides the above quoted I_1 SF, some ZnO NRs exhibit a different type of SF sequence - ABABCBACA (**figure 3.13 (a)**). This alternative stacking structure can be described either as a 4H-type structure inserted in 2H-ZnO (AB/ABCBA/CA), or as an I_1 type SF with an additional two-layer insertion, that is, ABAB/CB/ACAC. In this case, the displacement vector R is 2/3 [100].

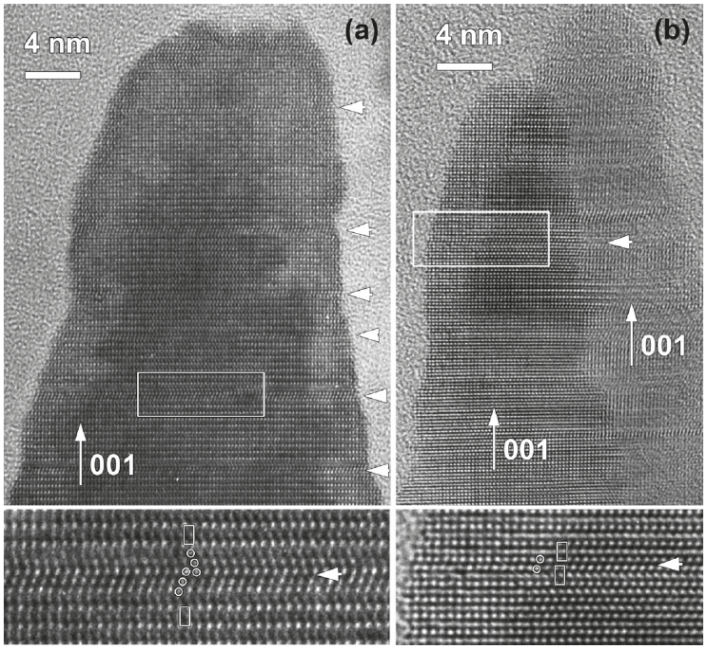

Figure 3.13: Cross-section HR-TEM images of single ZnO NRs in samples (a) **1_200_20W(Si)** and (b) **1_300_20W(Si)**, obtained from precursor **1**. White arrows mark SF along the <001> growth direction. The areas highlighted by white rectangles are enlarged at the bottom of the figure to show different SF types in the two samples. In (b), two adjacent NRs grown with a similar <001> orientation are imaged.

❖ *3.4.2.2 ZnO Nanorod Growth on Si(100) from **2***

On the basis of the results presented so far, the attention was devoted to the use of compound **2** as the PECVD precursor and to a comparative analysis of the resulting ZnO nanosystem properties. In this case, samples were synthesized adopting an applied RF-power of 20W (**table 3.2**), corresponding to the best conditions for the obtainment of ZnO NR arrays in the case of compound **1**. In particular, the influence of the growth temperature on the system morphological evolution was investigated for samples **2_100_20W(Si)** - **2_400_20W(Si)** (**figure 3.14**). Once again, ZnO NRs with the highest

aspect ratio (13.0) and the mostly pronounced anisotropic 1D morphology were obtained at 300°C. Nevertheless, two important differences are worth being highlighted with respect to specimens **1_100_20W(Si)** - **1_400_20W(Si)**, obtained from precursor **1** at the same RF-power (20W) and growth temperatures. First, in this case, even the sample obtained at 400°C (**2_400_20W(Si)**) presented a well-evident 1D morphology, at variance with the homologous **1_400_20W(Si)** grown at the same temperature. In addition, under the same processing conditions, the growth rate from precursor **2** was appreciably higher than in the case of compound **1** (**table 3.4**, **figure 3.16**), in agreement with results from **paragraph 3.2** (**figure 3.1**).

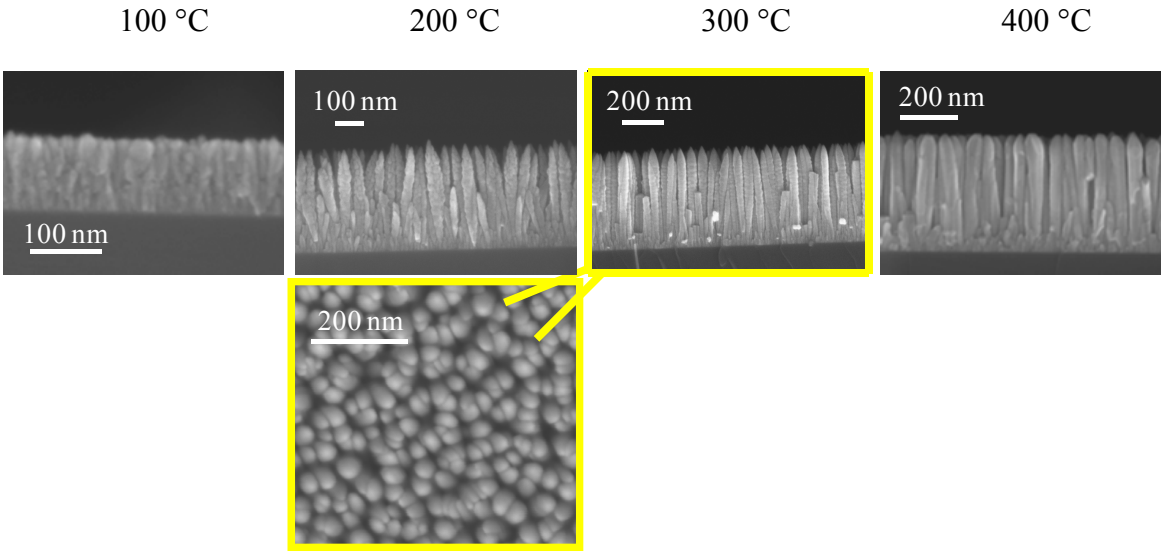

Figure 3.14: Representative cross-section FE-SEM micrographs of Si(100)-supported ZnO specimens synthesized from precursor **2** as a function of the adopted growth temperature (see **tables 3.2** and **3.4**). For sample **2_300_20W(Si)**, a plane-view image is presented.

Also in the case of precursor **2**, ZnO nanosystems possessing the most pronounced 1D morphology were investigated by TEM. Once again, the obtained results, that agreed to a good extent with FE-SEM ones (**figure 3.15**), revealed an appreciable density of SFs and a NR faceting directly dependent on the synthesis conditions. **Figure 3.15** shows HR-TEM images of ZnO NRs obtained from precursor **2** (**2_200_20W(Si)** and **2_300_20W(Si)**). Similar to the corresponding samples obtained from precursor **1** (compare **figure 3.13**), even in this case the SF density was appreciably higher at 200°C than at 300°C. As evidenced by HR-TEM imaging (**figure 3.15 (a)**), SFs perpendicular to the growth direction were clearly related to the nanorod faceting, the main exposed planes

being {101} and {100}. The common <001> growth direction led to a perfect heteroepitaxial intergrowth of adjacent nanorods (**figure 3.15 (b)**), with an atomically sharp boundary free from amorphous or intermediate layers.

Table 3.4: Film thicknesses for Si(100) supported samples obtained from **2** (see **table 3.2**).

Sample	thickness (nm)
2_100_20W(Si)	110
2_200_20W(Si)	355
2_300_20W(Si)	505
2_400_20W(Si)	410

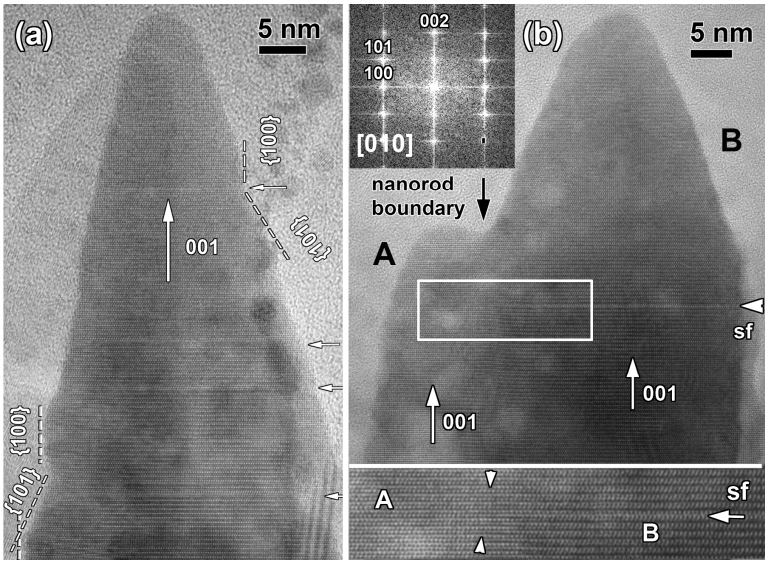

Figure 3.15: Cross-section HR-TEM images of single ZnO NRs in samples (a) **2_200_20W(Si)** and (b) **2_300_20W(Si)**, obtained from precursor **2**. In (a), white arrows mark SFs along the <001> growth direction. Exposed surface planes are also labeled. Figure (b) shows the intergrowth of two adjacent NRs (A and B). The presence of a SF in NR B, that stops at the boundary with A (marked by a black arrow), is also highlighted by the white rectangle and enlarged at the bottom of the figure. The fast Fourier transform (FT) along the [010] zone is reported in the inset.

❖ *3.4.2.3 Summary: ZnO Nanorod Growth on Si(100) from **1** and **2***

On the basis of the above results, a general growth mechanism can be proposed as a function of the adopted synthetic parameters. In this regard, **figure 3.16** summarizes the dependence of the growth rate on the deposition temperature for samples synthesized from compounds **1** and **2**. Interestingly, irrespective of the used precursor, four growth regimes, corresponding to different morphological features, can be identified in the graph. In particular, specimens grown at 100°C are characterized by an isotropic growth, that is, by the formation of pseudo-globular particles (compare **figures 3.10** and **3.14**). Reasonably, at the lowest deposition temperature (100°C), the limited thermal energy supply was the main factor preventing the 1D growth, irrespective of the adopted RF-power (20 or 40 W). Upon increasing the deposition temperature to 200 - 300°C, two growth regimes can be observed, namely, a columnar ("quasi-1D") and a 1D one, corresponding to the formation of ZnO NRs, occurring at higher growth rates. Similar results have also been recently reported in the PECVD of TiO_2 from Ti(IV) isopropoxide. [*Borras-2009*]

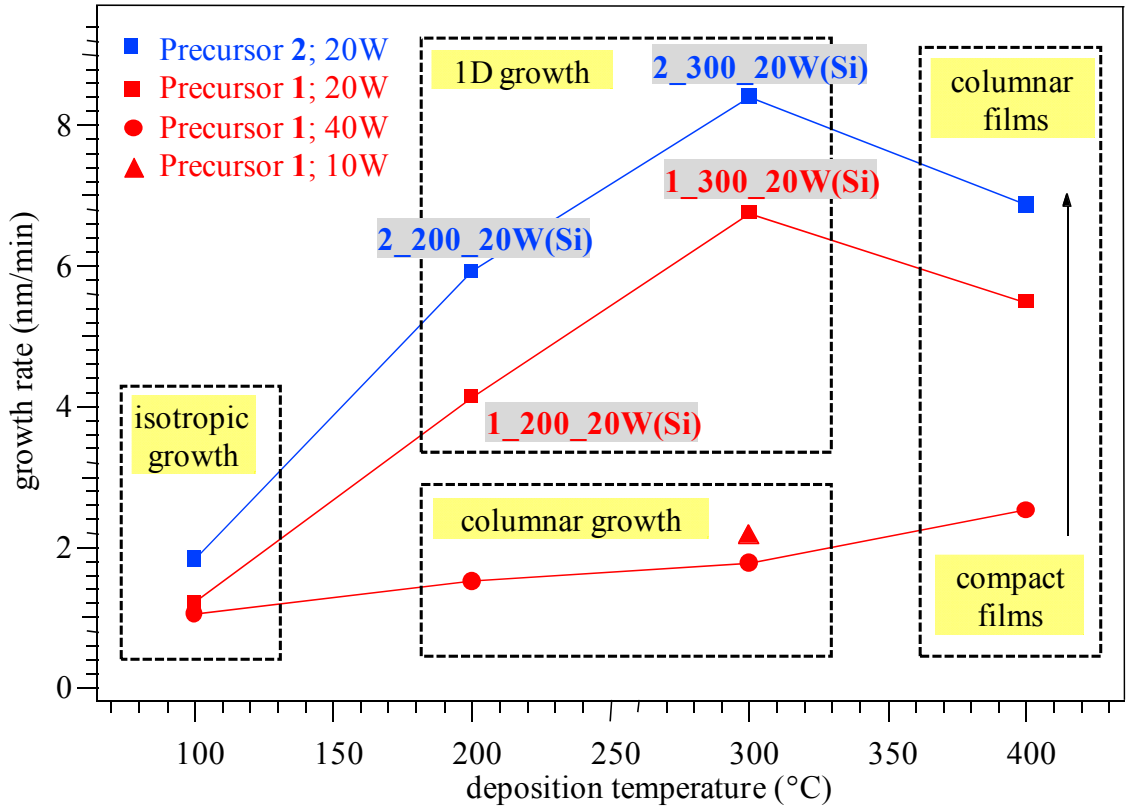

Figure 3.16: Synoptic diagram showing the dependence of the ZnO morphology on PECVD growth parameters. Red and blue markers correspond to ZnO samples synthesized from precursors **1** and **2**, respectively. (See **table 3.2**, **figures 3.10** and **3.14**.)

Furthermore, the morphology of the NR arrays with the most pronounced 1D growth (**2_200_20W(Si)**, **1_300_20W(Si)** and **2_300_20W(Si)**) was investigated by AFM imaging. The RMS roughness, an important parameter in the functionalization of nanostructures (see **paragraph 3.4.5**), was found to depend on the NR length and density, so that **2_300_20W(Si)**, that has the longest and most sparsely grown NRs, showed the highest RMS roughness value of 5.8 (**figure 3.17**).

(a)

Sample	NRs length (nm)	NRs density (NRs/μm^2)	RMS roughness (nm)
2_200_20W(Si)	356	710	3.2
1_300_20W(Si)	405	950	2.6
2_300_20W(Si)	504	620	5.8

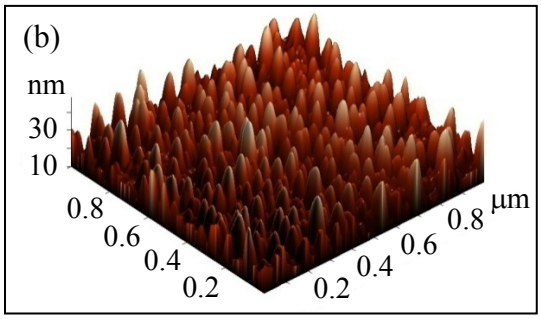

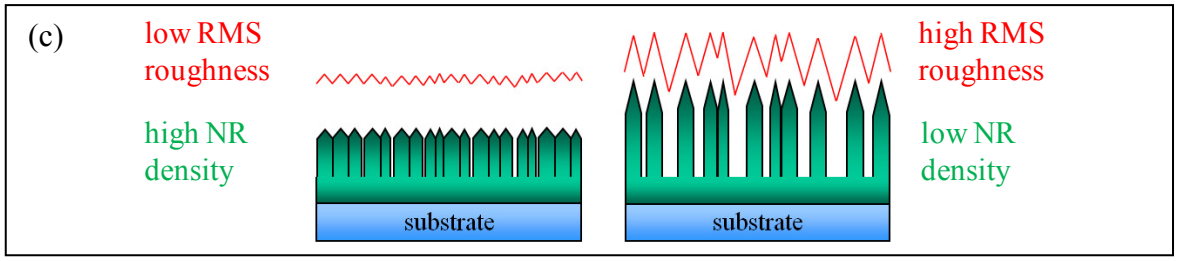

Figure 3.17: (a) RMS roughness values of selected NR arrays; (b) AFM of **2_300_20W(Si)**; (c) Sketch of the morphology of ZnO 1D NR arrays grown at different PECVD parameters (see also **figure 3.16**).

As a whole, the present findings provide a useful guideline for the control of the ZnO system morphogenesis from a phenomenological point of view. In the absence of epitaxial relationships with the substrate, as in the present case, a possible explanation for the obtainment of highly oriented NRs is as follows. At the beginning of the deposition process, the formation of small ZnO seeds takes place. At intermediate temperatures (200 or 300°C) and in the presence of plasma activation, such crystallites mainly grow with {001} planes parallel to the substrate surface since this orientation, characterized by a spontaneous polarization, is favored by the applied electric field. As the growth process proceeds, these ZnO nanoparticles act as self-catalysts for the formation of ZnO anisotropic systems [*Liu-2004-A*, *Wu-2009*, *Wang-2008-A*] and preferentially grow along the <001> direction when a high mass supply to the substrate surface is provided, giving rise to the observed NR arrays. [*Park-2006*, *Wu-2009*, *Wu-2002*] An increase of the

deposition temperature up to 400°C led to the formation of ZnO films maintaining a strong <001> preferential orientation but showing a progressive evolution from compact deposits to columnar ones upon increasing the GR (see **figure 3.17**). Although higher GRs still favored the formation of more anisotropic nanostructures, the increased thermal energy supply at 400°C resulted in an enhanced lateral growth, explaining thus the formation of relatively compact films rather than 1D (or "quasi-1D") systems.

❖ *3.4.2.4 ZnO Nanorod Growth on Al_2O_3 from **1** and **2***

Encouraged by the obtainment of high quality ZnO NRs on Si(100) at relatively low temperatures, and in order to integrate the rough NR arrays into gas sensing devices, the above discussed PECVD procedure using precursors **1** and **2** was applied for the growth of ZnO on polycrystalline Al_2O_3 at 200 - 300°C, resulting in urchin-like 1D ZnO NR arrays with strong *c*-axis orientation, as shown below.

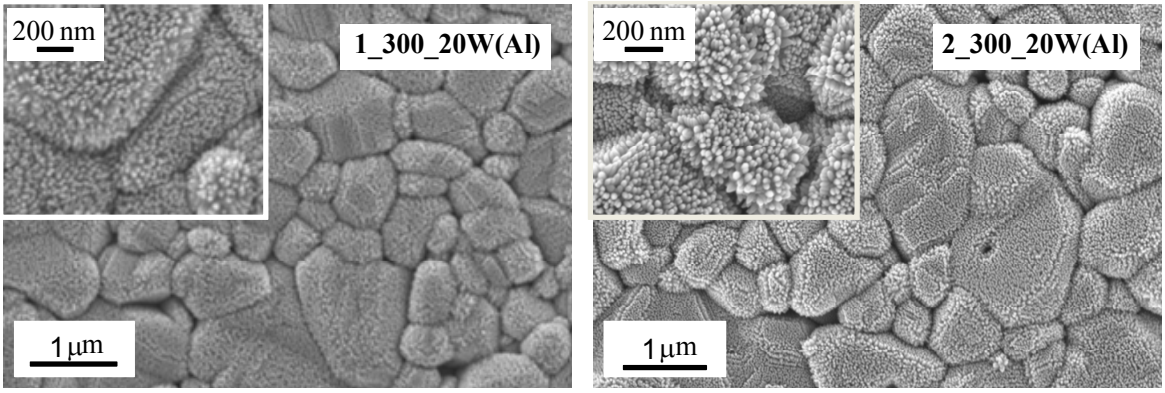

Figure 3.18: Plane-view FE-SEM micrographs of samples **1_300_20W(Al)** and **2_300_20W(Al)** (see **table 3.2**).

The morphology of the obtained ZnO systems was analyzed by FE-SEM, and it was found to be directly dependent on the adopted synthesis conditions. For all samples, plane-view micrographs (**figure 3.18** and **3.19**) evidenced the presence of globular particles typical of the Al_2O_3 substrate, whose dimensions ranged from 400 nm to more than 1 μm. Higher magnification images (see insets in **figure 33.18** and **3.19**) clearly displayed smaller ZnO nanostructures uniformly decorating the substrate surface. ZnO specimens **1_200_20W(Al)** and **2_200_20W(Al)**, grown at 200°C, presented a relatively compact agglomeration of globular ZnO particles (**figure 3.19 (b)**), while a rise of the

temperature (T = 300°C), led to the formation of uniform "3D/1D" urchin-like aggregates extending throughout the substrate surface (**figure 3.18** and **3.19**).

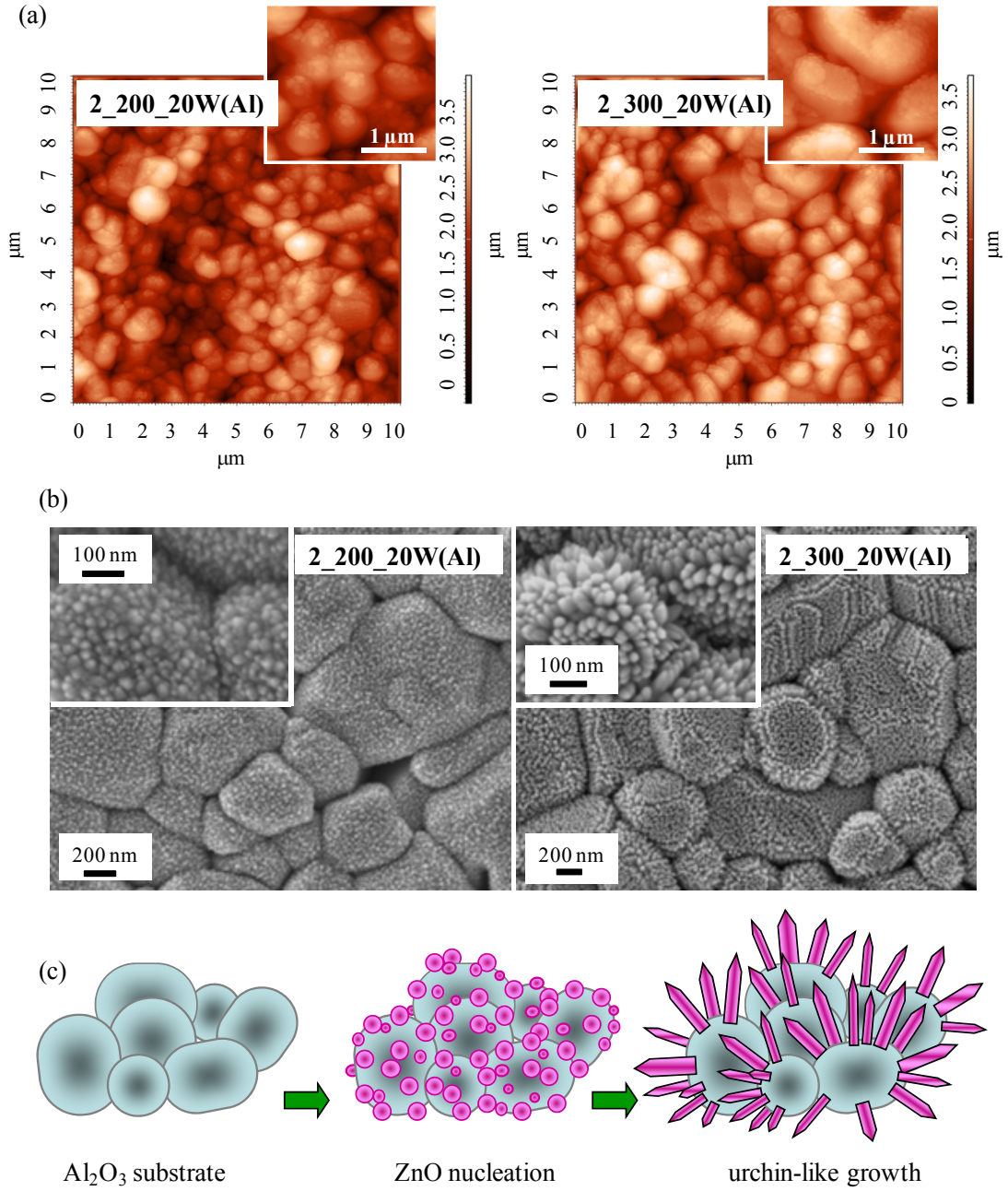

Figure 3.19: 10×10 µm^2 AFM (a) and plane-view FE-SEM (b) micrographs for **2_200_20W(Al)** (78 nm) and **2_300_20W(Al)** (116 nm) are shown (see **table 3.2**). (The film thicknesses are derived from SIMS, see **figure 3.23**.) In the insets, higher magnification images are shown. A schematic view of the formation process of urchin-like ZnO NR arrays is displayed in (c).

ZnO deposits **1_300_20W(Al)** and **2_300_20W(Al)** were characterized by a homogeneous array of 1D like structures (average diameter = 30 ± 5 nm) grown on the surface of individual Al_2O_3 islands, whose surface density was depended on the adopted synthesis conditions. Sample **1_300_20W(Al)** (**figure 3.18 (b)**) showed uniform ZnO arrays with 1800 nano-columns/μm^2, fabricated at 300°C and by use of precursor **1**. By use of precursor **2** at the same temperature (**2_300_20W(Al)**), longer 1D nanostructures with 1450 rods/μm^2 were obtained.

The system morphology was further analyzed by AFM (**figure 3.19 (a)**). The micrographs were dominated by the globular Al_2O_3 particles with a mean diameter of 600 nm. In line with FE-SEM results, higher magnification images showed that ZnO nanograins (see insets of AFM figures) uniformly covered the underlying substrate. All samples displayed a highly rough surface, with a RMS roughness close to 70 nm. Hence, such nanoarchitectures are reasonably characterized by a high surface area, a key factor in view of gas-sensing applications.

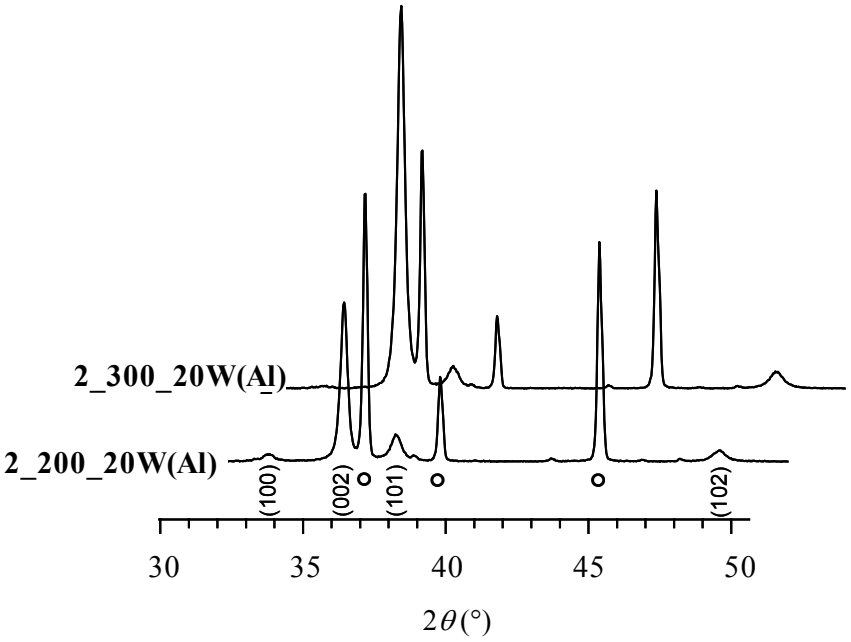

Figure 3.20: GIXRD patterns of **2_200_20W(Al)** and **2_300_20W(Al)** (see **table 3.2** and **figure 3.19**). Reflections of the *wurtzite* phase are directly indexed, whereas diffraction peaks of the Al_2O_3 substrate are marked by circles.

XRD analyses (**figure 3.20**) showed Bragg reflections of the hexagonal ZnO *wurtzite* phase characterized by a strong intensity and narrow width, indicating the formation of high crystalline ZnO. As frequently observed for 1D ZnO nanosystems, [*Bekermann-2010-B*, *Hsueh-2007-B*, *Zeng-2009-A*] a common feature to the synthesized specimens

was the predominance of the (002) ZnO signal, ascribed to the concurrence of a preferential *c*-axis orientation and an anisotropic crystallite growth, as indeed confirmed by FE-SEM investigation.

Basing on the present data, a growth model for the observed urchin-like structures is proposed in **figure 3.19 (c)**. At the beginning of the deposition process, the initial formation of small ZnO seeds takes place. Subsequently, in the presence of plasma activation, such nanoparticles act as a self-catalyst for the development of NRs along the <001> direction, as indicated by XRD measurements. The typical globular morphology of the alumina substrates, is responsible for the formation of the observed urchin-like arrays instead of parallel aligned 1D rods. [*Barreca-2010-A*]

❖ 3.4.3 Composition

The chemical composition of silicon and alumina supported ZnO samples was investigated by the combined use of EDXS, XPS and SIMS. Since all ZnO specimens revealed identical compositional information, irrespective of the substrate and processing conditions, the results are discussed below using selected silicon or alumina based samples as representative examples.

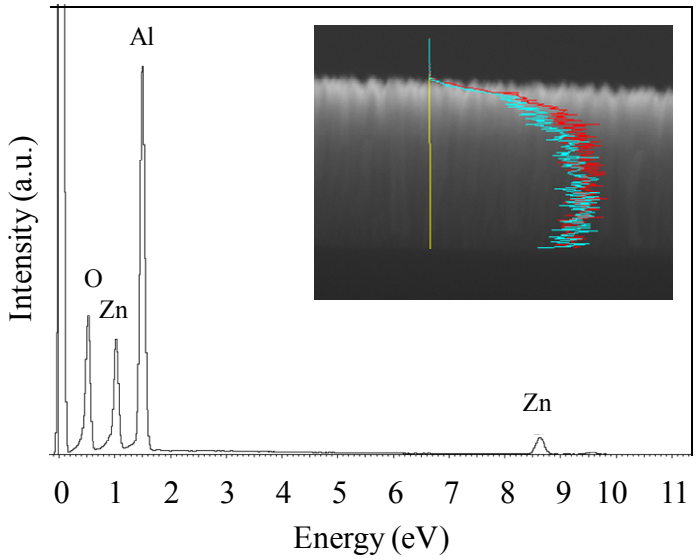

Figure 3.21: Representative EDX spectrum (here for **1_300_20W(Al)**, see **table 3.2**). The inset shows typical EDXS profiles for O Kα1 (red) and Zn Kα1 (blue) X-ray signals along the cross section of **2_300_20W(Si)** (see **table 3.2** and **figure 3.14**).

Preliminary investigation was performed by EDXS analysis. Irrespective of the preparation conditions, EDX spectra (**figure 3.21**) were characterized by the sole lines of oxygen (O Kα at 0.52 keV) and zinc (Lα and Kα peaks located at 1.01 and 8.63 keV), along with the substrate signal (Al Kα at 1.49 keV). No carbon that might arise from the incorporation of undecomposed precursor residuals was detected, suggesting thus a clean decomposition of the used Zn sources under the present PECVD conditions, as further confirmed by the data below. From EDXS cross-section line scans (**figure 3.21** inset) it can be seen that a slight oxygen excess is present on the sample outermost layers, that could be mainly related to the presence of -OH groups (see XPS below) arising from atmospheric exposure (**figure 3.21**).

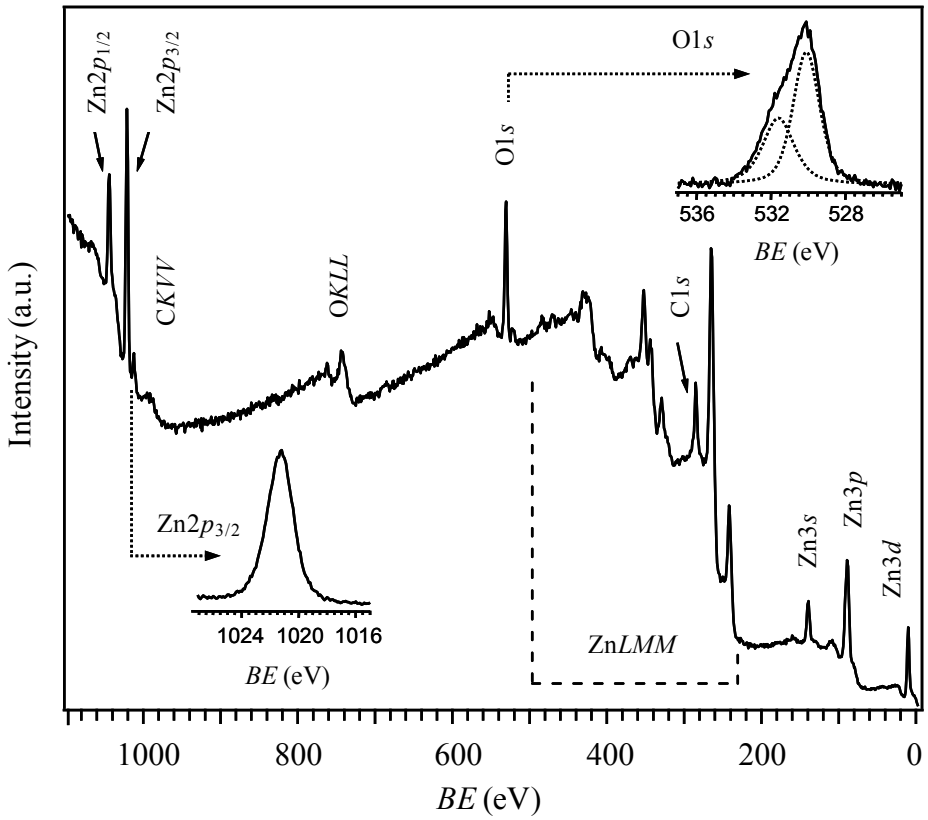

Figure 3.22: Representative surface XPS survey spectrum of ZnO NRs on Si(100) or Al_2O_3 (see **table 3.2**), obtained from **1_200_20W(Al)** (**figure 3.18**). Surface photoelectron peaks for Zn2*p* and O1*s* photopeaks are displayed as insets, along with the two O1*s* components resulting from spectral deconvolution.

To attain a deeper insight into the chemical composition, all the obtained ZnO specimens were analyzed by XPS. To this regard, **figure 3.22** reports the surface wide-scan spectrum of a representative sample, along with the detailed Zn2*p* and O1*s* regions. (Similar XPS

features for ZnO NR arrays (**paragraphs 3.4.2.1 - 3.4.2.4**) have been obtained, see [*Barreca-2010-C*, *Bekermann-2010-A*, *Bekermann-2010-B*].) The survey displayed the expected zinc and oxygen signals, along with the C1*s* and C*KVV* ones. The complete disappearance of the carbon photopeaks after Ar^+ sputtering, as in the case of ZnO by CVD (**paragraph 3.3.3**), confirmed that its presence was limited to the outermost sample layers and that it arose from atmospheric contamination, in agreement with EDXS results. As regards the zinc signals, the Zn2$p_{3/2}$ peak was centred at *BE* = 1021.2 eV ((FWHM) = 2.1 eV). This value, along with the calculation of the Auger parameter (2010.0 eV), confirmed the formation of ZnO free from other zinc-containing phases. [*Barreca-2007-B*, *Briggs-1990*, *Qurashi-2009*] The O1*s* peak presented a broad spectral profile that could be fitted by two contributions (see inset of **figure 3.22**). While the main component at 530.1 eV (FWHM = 1.7 eV; 65 %) was ascribed to lattice oxygen in the ZnO wurtzite structure, the second one (*BE* = 531.6 eV; FWHM = 2.0 eV; 35 %) was mainly related to hydroxyl groups arising from interaction with atmospheric H_2O. [*Barreca-2007-A*, *Barreca-2007-C*, *Liangyuan-2010*, *Li-2007-B*] The presence of such species, commonly revealed on metal oxides, was reasonably enhanced in the present case due to the high surface area of the obtained ZnO nanosystems, and accounted for the O/Zn ratio (≈ 1.3) higher than the stoichiometric value. Such a phenomenon, was reasonably enhanced in the present case due to the high surface-to-volume ratio of the obtained ZnO NR arrays (see **figures 3.10**, **3.14**, **3.18** and **3.19**).

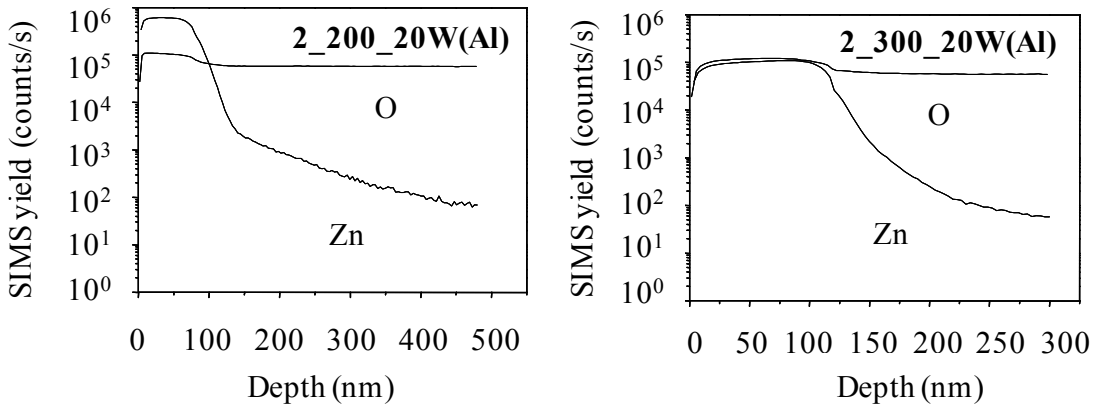

Figure 3.23: SIMS depth profiles for samples **2_200_20W(Al)** and **2_300_20W(Al)** (see **table 3.2** and **figure 3.19**).

The in-depth chemical composition of the present specimens was further investigated by SIMS analyses (**figure 3.23**). As a general rule, the ZnO nanodeposits presented a

uniform and parallel Zn and O distribution up to the interface with the substrate, confirming thus their common chemical origin, in agreement with EDXS and XPS data.

❖ 3.4.4 Optical Properties

To gain further information about the quality of Si(100) supported ZnO NR arrays, the optical properties of two selected ZnO NR arrays (**2_200_20W(Si)** and **2_300_20W(Si)**), characterized by the most pronounced 1D morphology (see **section 3.4.2.3** and **figure 3.16**) were investigated by PL measurements (**figure 3.24**).

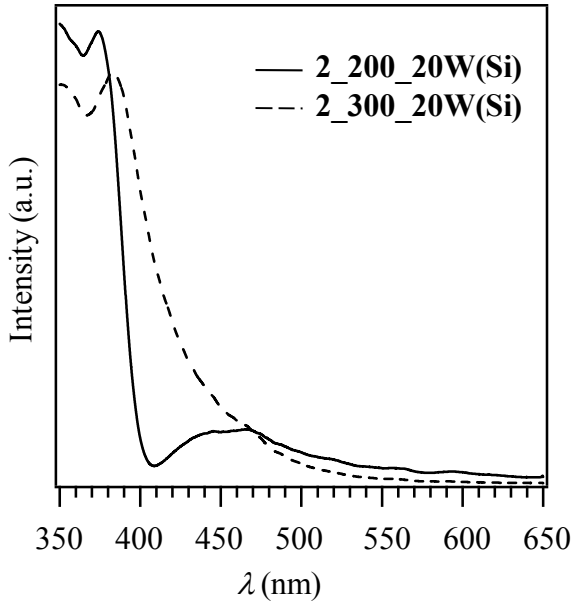

Figure 3.24: PL spectra of sample **2_200_20W(Si)** (200°C) and **2_300_20W(Si)** (300°C) (see **section 3.4.2.2** and **figure 3.16**).

In the case of sample **2_200_20W(Si)**, the PL spectrum presented a strong UV peak centered at 384 nm, displaying an appreciable tailing toward higher wavelengths. This signal was ascribed to the near band-edge emission of ZnO, originated from free exciton recombination. [*Kuang-2005*, *Liu-2004-A*, *Umar-2006*, *Wu-2009*, *Wang-2005-A*] On the other hand, the emission in the visible region could be traced back to the combined contribution of various kinds of defects for NRs synthesized at 200°C, even though their exact nature can be hardly deduced from the present spectrum. [*Rowlette-2009*, *Scalisi-2008*] In a different way, the PL spectrum of sample **2_300_20W(Si)** presented a narrower excitonic band centered at 374 nm. The blue-shift of the UV band with respect

to specimen **2_200_20W(Si)** could be related to the higher surface-to-volume ratio for **2_300_20W(Si)** specimen (see **figure 3.14** and **3.17**). [*Jeong-2008*] In fact, although the average NR diameter was ≈ 40 nm in both cases, their aspect ratio was appreciably different (9.1 for **2_200_20W(Si)** and 13.0 for **2_300_20W(Si)**).

Regarding **2_300_20W(Si)**, an additional structured emission band in the region between 420 and 540 nm was also detected and ascribed to the presence of point defects, such as V_O and Zn_i. [*Kim-2005-B*, *Kuang-2005*, *Liu-2004-A*, *Park-2006*, *Wu-2009*]

❖ 3.4.5 PSH and PCO Properties

For PSH and PCO applications, a high surface-to-volume ratio, like in the case of the above described ZnO NRs (**sections 3.4.2.1 - 3.4.2.3**), is generally considered favorable, since it enables a faster arrival of photo-generated electrons and holes to the surface, reducing detrimental recombination phenomena. [*Wan-2005*, *Zhang-2009-A*] Therefore, in the following, the silicon based ZnO NR arrays of highest aspect ratio and roughness, namely **1_200_20W(Si)**, **1_300_20W(Si)**, **2_200_20W(Si)** and **2_300_20W(Si)** (**figure 3.16** and **3.17**), were investigated regarding PSH and PC. Special attention was devoted to the interrelations between the photo-activity of the obtained 1D ZnO systems and their morphological characteristics.

PSH properties were analyzed by monitoring the evolution of water contact angle (WCA) as a function of the UV irradiation time (**paragraph 8.6.1**). The self-cleaning activity of the synthesized NRs was investigated through a novel quantitative and highly sensitive PCO method (**8.6.2**), based on the determination of the TPA oxidation product HOTPA: [*Černigoj-2010*]

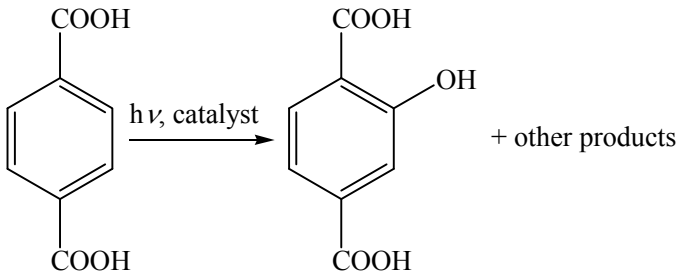

(reaction 3.1)

As regards PSH properties, specimen **1_200_20W(Si)** presented the lowest activity among the analyzed samples. Such an effect was ascribed both to the reduced NR length, responsible for less efficient light absorption, [*Barreca-2007-B*, *Zhang-2009-A*] and to the

relatively compact cross-sectional structure (**figure 3.10**), resulting in a lower active area. In a different way, ZnO NR arrays thicker than 300 nm, namely **1_300_20W(Si)** (**figure 3.10**), **2_200_20W(Si)** and **2_300_20W(Si)** (**figure 3.14**), presented remarkable PSH performances with a very fast hydrophobic-to-superhydrophilic conversion upon UV exposure (**figure 3.25**). The initial hydrophobic WCA value was close to 120° for all samples, in agreement with previous reports. [*Badre-2009*, *Barreca-2009-A*, *Fujishima-2008*, *Liu-2004-B*, *Meng-2005*] This phenomenon was mainly attributed to adventitious carbon contamination, as evidenced by XPS (see **figure 3.22**).

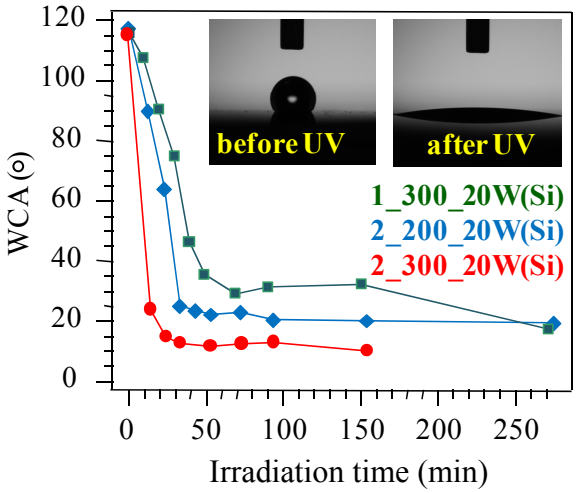

Figure 3.25: PSH behaviour of Si(100) supported ZnO NRs **1_300_20W(Si)**, **2_200_20W(Si)** and **2_300_20W(Si)** (see **section 3.4.2.3**): WCA as a function of irradiation time. Photographs of H_2O droplets on sample **2_300_20W(Si)** before (left) and after 150 min (right) UV irradiation.

Upon UV irradiation, a fast WCA decrease was observed. The present performances were significantly better than those of the standard Pilkington® glass, the benchmark TiO_2 material, and also higher than those of ZnO nanosystems, tested under similar operating conditions. [*Barreca-2009-A*, *Liu-2004-B*, *Fujishima-2008*] It is worth observing that, for specimens **1_300_20W(Si)**, **2_200_20W(Si)** and **2_300_20W(Si)**, the hydrophobic-to-superhydrophilic conversion kinetics did not improve in the same order of the NR length (**figure 3.25**, compare **tables 3.3** and **3.4**). In fact, the performances of the sample with shortest NRs, **2_200_20W(Si)**, were intermediate between those of **1_300_20W(Si)** and **2_300_20W(Si)**. Such results suggest that, although an increase in the NR length may result in more efficient light harvesting, other parameters concur in determining the

system PSH activity, such as surface chemical composition and topography. [*Barreca-2007-B*, *Feng-2004*, *Li-2008-A*, *Meng-2005*]

It is also worthwhile observing that all nanodeposits were characterized by a high surface -OH content, as evidenced by XPS (see **figure 3.22**). [*Badre-2009*, *Barreca-2007-B*] The formation of hydroxyl species could be mainly traced back to the dissociative chemisorption of atmospheric H_2O on surface oxygen vacancies, whose content is reasonably enhanced by plasma bombardment effects during PECVD. [*Meng-2005*, *Bekermann-2010-B*] Upon UV irradiation, photo-generated holes can react with lattice O species to form new V_O. This phenomenon further promotes water chemisorption, increasing the surface -OH amount and resulting in a superhydrophilic behaviour due to an increased wettability. [*Feng-2004*, *Zhou-2008*] For ZnO NR arrays, a RMS roughness increase could be related to a higher active surface area (see **figure 3.17 (c)**). [*Liu-2004-B*] On this basis, it is reasonable to suppose that the overall hydroxyl group content increased in the same order of RMS values, that is, **1_300_20W(Si)** < **2_200_20W(Si)** < **2_300_20W(Si)**, further supporting the PSH trends reported in **figure 3.25 (a)**.

As regards the PCO behaviour, for all ZnO samples a progressive increase of the HOTPA concentration vs. irradiation time was observed (**figure 3.26 (a)**). Under the present conditions, TPA degradation and, consequently, HOTPA formation followed pseudo-zero-order kinetics (rate constant = k_1).

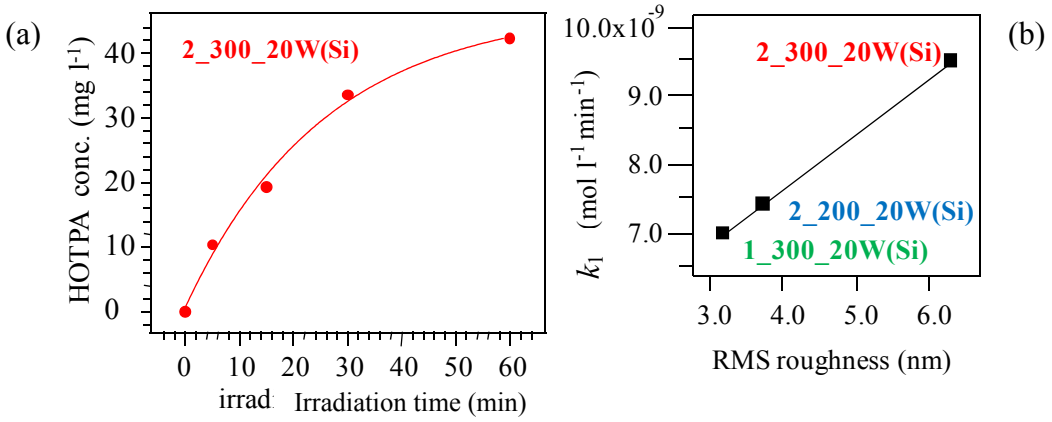

Figure 3.26: (a) PCO behaviour of specimen **2_300_20W(Si)**: HOTPA concentration as a function of irradiation time. (b) Rate constant (k_1) dependence on RMS roughness for samples **1_300_20W(Si)**, **2_200_20W(Si)** and **2_300_20W(Si)** (see **section 3.4.2.3** and **figure 3.17**).

Considering that HOTPA degradation should also be taken into account (rate constant = k_2), HOTPA concentration vs. time dependence could be described by equations 3.1 and 3.2: [*Černigoj-2010*]

$$d[HOTPA] / dt = (k_1 - k_2) [HOTPA] \quad \text{(equation 3.1)}$$

$$[HOTPA] = (k_1 / k_2) (1 - \exp(-k_2 t)) \quad \text{(equation 3.2)}$$

The trend in **figure 3.26 (a)** could be fitted by equation 3.2. Similarly to PSH behaviour, systems with the highest RMS surface roughness also displayed improved PCO performances. In fact, an increase of the k_1 reaction rate constant proportional to RMS roughness was detected for specimens **1_300_20W(Si)**, **2_200_20W(Si)** and **2_300_20W(Si)** (**figure 3.26 (b)**). The reasons explaining this trend are in line with previous considerations on PSH data, as well as with the pictorial model reported in **figure 3.17**. Specifically, on going from sample **1_300_20W(Si)** to **2_200_20W(Si)** and, finally, to **2_300_20W(Si)**, the progressive RMS enhancement and the concomitant increase of the active area have a promotional effect on the PCO processes involved. In particular, the large content of surface oxygen vacancies, acting as capturing centers for photogenerated electrons, minimizes charge-carrier recombination phenomena. As a consequence, photo-generated holes are more readily available for the oxidation of organic pollutants. Furthermore, oxygen vacancies also assist the generation of active species, such as $^{\bullet}OH$ and $O_2^{\bullet-}$, on the surface of ZnO NRs, providing thus a two-fold beneficial contribution to PCO activity. [*Liu-2009_A*, *Wan-2005*, *Wang-2008-C*] For the best-performing sample (**2_300_20W(Si)**), the analyses yielded $k_1 = 9.5\ 10^{-9}$ mol l^{-1} min^{-1}, a value five times higher than that of the Pilkington® glass. This difference is likely dependent on several parameters, including the higher roughness and overall deposit thickness of specimen **2_300_20W(Si)**. [*Černigoj-2010*, *Liu-2004-B*, *Mills-2003*] In conclusion, by tailoring the morphological features of the obtained ZnO NR arrays (RMS roughness, NR length and density), the PSH and PCO properties could be tuned as a function of the system characteristics.

❖ 3.4.6 Gas Sensing Properties

The gas sensing properties of the alumina supported "3D/1D" ZnO assemblies have been tested for the first time in the detection of various analytes, both reducing (CH_3CH_2OH, CH_3COCH_3, CO, H_2, CH_4) and oxidizing (O_3, NO_2) gases. (Technical details and definitions of responses, response and recovery times can be found in **paragraph 8.6.4**.) In general, the obtained urchin-like 1D ZnO NR arrays **1_200_20W(Al)**, **1_300_20W(Al)**, **2_200_20W(Al)** and **2_300_20W(Al)** (see **3.4.2.4**) displayed an appreciable capability to detect different gaseous species. For all analytes, gas sensing tests revealed reproducibility of the electrical responses upon prolonged utilization cycles, an important pre-requisite for practical application.

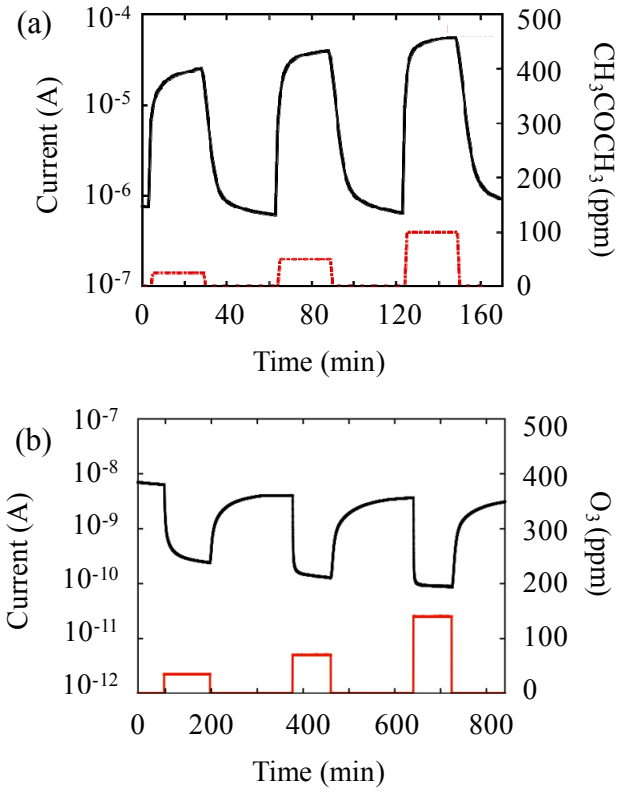

Figure 3.27: Typical dynamic response of urchin-like ZnO NR arrays grown on Al_2O_3 from compound **2** (see **3.4.2.4** and **figure 3.19**) upon exposure to square concentration pulses of: (a) CH_3COCH_3, at 400°C; (b) O_3, at 200°C.

As a prototype for the sensing behaviour toward reducing and oxidizing gases, **figure 3.27** displays the kinetic response to square concentration pulses of CH_3COCH_3 and O_3, using of urchin-like ZnO NR arrays grown on Al_2O_3 from compound **2** (see **3.4.2.4** and **figure 3.19**). As expected for *n*-type semiconductors, exposure to reducing gases (**figure**

3.27 (a)) resulted in an increase of the current, whereas the opposite effect was observed upon reaction with oxidizing analytes (**figure 3.27 (b)**). In both cases, the measured variations increased with the gas concentration and a rapid regeneration of the pristine air current values (typically in 1 - 2 min for CH_3CH_2OH and CH_3COCH_3) was observed. [*Barreca-2007-A*] The almost complete baseline recovery at the end of each gas pulse, observed for all the investigated analytes (CH_3CH_2OH, CH_3COCH_3, CO, H_2, CH_4, O_3, NO_2), revealed a reversible interaction with the sensing elements and excluded appreciable poisoning effects.

For reducing gases, the sensing mechanism usually involves the chemisorption of oxygen molecules on the oxide surface to generate active oxygen species (O_2^-, O^-, O^{2-}, O^- being the dominant and more active [*Zhang-2009-B*]), by capturing electrons from the conduction band. [*Jing-2008*, *Li-2008-B*, *Qi-2008*] The involved processes can be described as follows: [*Chatterjee -1999*, *Hsueh-2007-A*, *Lupan-2010*, *Qurashi-2009*, *Ryu-2003*]

$O_{2\,(g)} \rightleftarrows O_{2\,(ads)}$ (reaction 3.2)

$O_{2\,(ads)} + e^- \rightleftarrows O_2^-{}_{(ads)}$ (reaction 3.3)

$O_2^-{}_{(ads)} + e^- \rightleftarrows 2\,O^-{}_{(ads)}$ (reaction 3.4)

The reducing gas adsorbs at the sensor surface and reacts with chemisorbed O^- (equations 3.5 - 3.9): [*Basu-2008*, *Bie-2007*, *Dayan-1997*, *Gong-2006*, *Hung-2009*, *Jing-2008*, *Kang-2009*, *Lupan-2010*, *Ra-2010*, *Zhang-2009-B, Zeng-2009-B*]

$CH_3COCH_{3(ads)} + 8\,O^-_{(ads)} \rightarrow 3\,CO_{2(g)} + 3\,H_2O + 8\,e^-$ (reaction 3.5)

$CH_3CH_2OH_{(ads)} + 6\,O^-_{(ads)} \rightarrow 2\,CO_{2(g)} + 3\,H_2O + 6\,e^-$ (reaction 3.6)

$CO + O^-{}_{(ads)} \rightleftarrows CO_2 + e^-$ (reaction 3.7)

$H_2 + O^-{}_{(ads)} \rightleftarrows H_2O + e^-$ (reaction 3.8)

$CH_4 + 4\,O^-{}_{(ads)} \rightleftarrows CO_2 + 2\,H_2O + 2\,e^-$ (reaction 3.9)

After sufficient adsorption of oxygen, depletion layers are formed at the surface, inducing a decrease of the carrier concentration and making ZnO surface highly resistive. [*Li-2007-B*, *Martins-2004*, *Zeng-2009-A*] Subsequent exposure to reducing gases decreases the surface density of oxygen species, resulting in an increased electron concentration and

current intensity. [*Hsueh-2007-B*, *Kwak-2008*] Upon exposure to oxidizing target species, such as O_3 and NO_2, the analyte reaction with adsorbed O^-, as well as direct adsorption on the surface of ZnO NRs, may occur. Correspondingly, the electron concentration on the surface of ZnO NRs diminishes and the electron depletion layer is widened. As a consequence, the measured resistance increases, producing, in turn, a decrease in the current intensity. [*Barreca-2010-A*, *Kenanakis-2007*]

$$O_{3(g)} + e^- \rightarrow O_3^-{}_{(ads)} \qquad \text{(reaction 3.10)}$$

$$O_3^-{}_{(ads)} + O^-{}_{(ads)} + 2\ e^- \rightarrow O_{2(g)} + 2\ O^{2-}{}_{(ads)} \qquad \text{(reaction 3.11)}$$

$$NO_{2(g)} + e^- \rightarrow NO_2^-{}_{(ads)} \qquad \text{(reaction 3.12)}$$

$$NO_2^-{}_{(ads)} + O^-{}_{(ads)} + 2\ e^- \rightarrow NO_{(g)} + 2\ O^{2-}{}_{(ads)} \qquad \text{(reaction 3.13)}$$

The responses of ZnO urchin-like arrays (**3.4.2.4** and **figure 3.19**) towards selected concentrations of various analytes is reported in **figure 3.28**. Similarly to previous works, [*Chen-2011-A*, *Chen-2011-B*, *Oh-2009*, *Sadek-2007*] the response towards oxidizing gases underwent a progressive decrease with the operating temperature (from 104.0 (18.0) to 10.0 (1.5) for O_3 (NO_2), on going from 100 to 300°C). The reason is twofold: (i) the O^- ions, that assist the adsorbed oxidizing target gas to take electrons from the ZnO NR arrays, become less stable with increasing working temperature (WT), while O^{2-} adsorption becomes the dominant process; and (ii) desorption of all adsorbed species is generally enhanced by increasing the temperatur. In the case of CH_3CH_2OH and CH_3COCH_3, the highest responses of 180 and 246 were observed at 300°C, in agreement with recent reports. [*Qi-2008*, *Zeng-2009-A*, *Zeng-2009-B*]

Since many types of reducing/oxidizing gases can interact with the sensing material simultaneously, the selective detection of a specific analyte is not easy to be accomplished. In particular, the sensing behaviour of ZnO systems to CH_3CH_2OH and CH_3COCH_3 are similar in most investigations. [*Qi-2008*] Nevertheless, the obtained results indicate that the use of high temperatures (400°C) can ease the discrimination of reducing gases (CH_3CH_2OH, CH_3COCH_3) with respect to oxidizing ones (O_3, NO_2). At 100°C the detection of oxidizing species is favored, since the pertaining responses exceeded the corresponding values towards CH_3CH_2OH and CH_3COCH_3 more than one order of magnitude. Hence, the present 1D ZnO NR arrays can act as multifunctional

selective gas sensors to both reducing and oxidizing species. [*Barreca-2010-A*, *Jing-2008*]

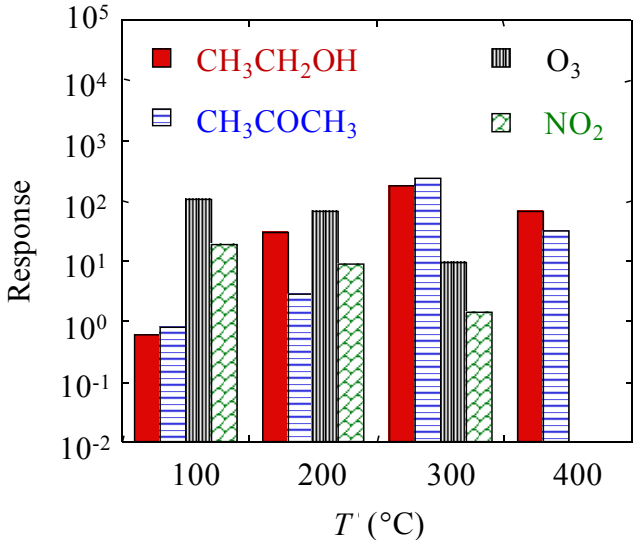

Figure 3.28: Responses of urchin-like 1D ZnO NR arrays grown on Al_2O_3 from compound **2** (**3.4.2.4** and **Figure 3.19**) to selected analyte concentrations (CH_3CH_2OH, 100 ppm; CH_3COCH_3, 100 ppm; O_3, 280 ppb; NO_2 dioxide, 1 ppm) at different operating temperatures.

To the best of our knowledge, the recorded response values for CH_3CH_2OH, CH_3COCH_3, O_3 and NO_2 are the highest ever reported in the detection of the test gases by ZnO NRs, [*Barreca-2007-A*, *Chen-2006*, *Hsueh-2007-B*, *Oh-2009*, *Qi-2008*, *Wu-2008-A*, *Zeng-2009-A*, *Zhang-2009-B*] even when activated by metal nanoparticles (*e.g.* Pd, Au [*Li-2008-B*]), under similar operating conditions. Thus, the present urchin-like ZnO NR arrays are very promising for practical utilization in gas sensors.

As regards the detection of the other flammable and toxic gases, **figure 3.29 (a)** reports a typical response of a ZnO sample to different concentration pulses of CO. The flowing current increased proportionally to the analyte concentration. The response and recovery times were typically of the order of 1 min. [*Hsueh-2007-A*, *Krishnakumar-2009*] **Figure 3.29 (b)** displays the dependence of the response towards 500 ppm of CO as a function of the sensor operating temperature (100 - 400°C). As can be observed, the measured value was maximum at 200°C. A similar behaviour in CO detection by ZnO nanosystems has already been reported in literature. [*Dayan-1997*, *Krishnakumar-2009*, *Liangyuan-2010*] For operating temperatures < 200°C, the measured response is rather low because the adsorbed CO molecules are not sufficiently activated to react with surface oxygen species

(see reaction 3.8). [*Chang-2008*] An increase in the operating temperature up to 200°C enables to overcome the activation energy barrier of the reaction, resulting in the observed response increase. For higher temperatures the decrease in CO gas adsorption is not adequately compensated by the increased extent of the surface reaction, and the sensor response decreases again. [*Gong-2006*, *Krishnakumar-2009*]

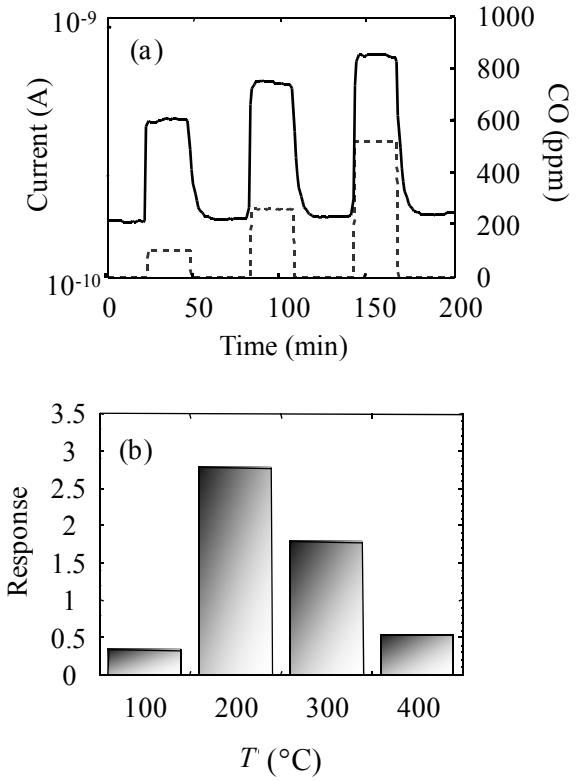

Figure 3.29: (a) Dynamic response of ZnO NR arrays grown on Al_2O_3 from compound **1** (see **3.4.2.4** and **figure 3.18**) to square CO concentration pulses (working temperature = 200°C). (b) Response to 500 ppm CO as a function of the operating temperature.

Figure 3.30 (a) reports the dynamic response of a ZnO sensor to H_2 injection pulses at an operating temperature of 400°C. Upon introduction of H_2 square pulses, the experimental curve increased sharply and subsequently more slowly up to the end of the pulse, a behaviour that appeared to be more marked for H_2 concentrations > 1000 ppm. [*Lupan-2009*, *Tien-2005*] This trend suggested that the chemisorption of molecular H_2 onto ZnO was the rate-limiting step in the resulting current change. [*Wang-2005-B*, *Wright-2010*] Nevertheless, at variance with recent reports, [*Lupan-2010*, *Sadek-2007*, *Wang-2006*] a very good and rapid (≈ 1 min) recovery of the pristine air value was observed at the end of each H_2 pulse, a promising feature for use of the present materials as H_2 sensors.

Unlike CO, the sensing response to H_2 (**figure 3.30 (b)**) underwent a progressive increase with the adopted working temperature, reaching the highest measured value at 400°C. This behaviour agreed to a good extent with that observed by Qurashi *et al*, [*Qurashi-2009*] claiming an enhanced reaction between H_2 and adsorbed oxygen upon increasing the temperature. [*Hazra-2006*, *Stamataki-2009, Hung-2009*, *Sadek-2007*]

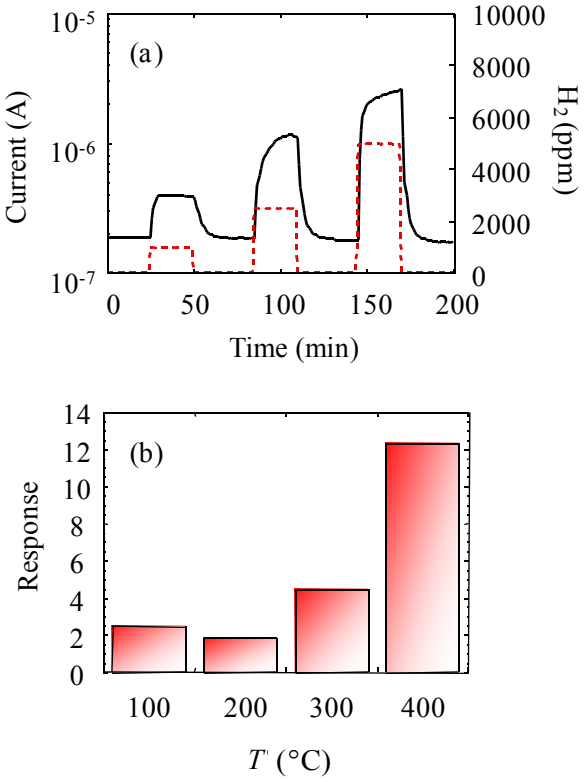

Figure 3.30: (a) Dynamic response of ZnO NR arrays grown on Al_2O_3 from compound **1** (see **3.4.2.4** and **figure 3.18**) to square H_2 concentration pulses (working temperature = 400°C). (b) Response to 5000 ppm H_2 as a function of the operating temperature.

In **figure 3.35** representative data pertaining to CH_4 detection at an operating temperature of 300°C are shown. The obtained results evidenced the possibility of detecting concentrations as low as 100 ppm, a valuable result considering that CH_4 is a scarcely reducing gas. The dynamic response (**figure 3.31 (a)**) revealed that the sensor current increased rapidly upon contact with CH_4 (response times ≈ 1 min), whereas the recovery of air values at the end of the gas pulses was slower (≈ 2 - 3 min). The present kinetic performances compare favourably with previous studies. [*Mitra-2007*] In addition, it is worthwhile observing that the shape of the response curves was appreciably better than those reported for CH_4 sensing by other ZnO systems, [*Bhattacharyy-2006*,

Bhattacharyy-2008-B] indicating a more reversible interaction with the analyte gas in the present case. A significant sensing action for CH_4 began at working temperatures higher than 100°C (**figure 3.31 (b)**), in agreement with literature data. [*Mitra-2007*] In addition, the CH_4 response presented a maximum like behaviour, the best operating temperature being 300°C, in line with previous studies, [*Basu-2008*, *Bhattacharyy-2008-B*, *Dayan-1997*] indicating a steady equilibrium between CH_4 adsorption and desorption at this temperature. Upon further increasing the operating temperature to 400°C, CH_4 desorption phenomena became predominant and the measured response decreased. [*Bhattacharyy-2007*, *Bhattacharyy-2008-A*, *Mukherjee-2009*]

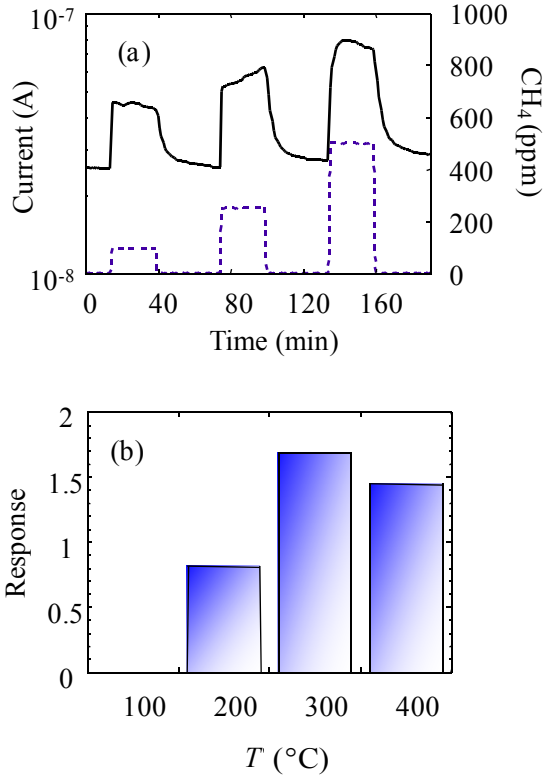

Figure 3.31: (a) Dynamic response of ZnO NR arrays grown on Al_2O_3 from compound **2** (see **3.4.2.4** and **figure 3.19**) to square CH_4 concentration pulses (working temperature = 300°C); (b) Response to 500 ppm CH_4 as a function of the operating temperature.

For all investigated toxic and flammable gases, the present sensor responses were higher than those reported under similar operating conditions for ZnO systems with *e.g.* Pd, Ag, Pt [*Bhattacharyy-2008-B*, *Bhattacharyy-2008-A*, *Wright-2010*] and Au [*Bhattacharyy-2007*, *Chang-2008*, *Kang-2009*]) and without dopants. [*Chen-2008*, *Das-2010*, *Dayan-*

1997, *Kang-2009*, *Mukherjee-2009*, *Sadek-2007*, *Lupan-2009*, *Qurashi-2009*, *Ra-2008*, *Ra-2010*, *Zhang-2009-B*]

The sensor response was also investigated as a function of gas concentration. The experimental trend can be modeled by the following equation: [*Barreca-2007-A*]

$$R = A\,[C]^N \qquad \text{(equation 3.3)}$$

where A is a constant, [C] denotes the target gas concentration and the exponent N depends on the involved reactions and the material morphology. [*Li-2009-B*] In contrast to previous works, [*Bhattacharyy-2008-A*, *Bie-2007*, *Chen-2008*, *Das-2010*, *Dayan-1997*, *Gong-2006*, *Wang-2006*] the experimental trends yielded a linear dependence in the investigated concentration ranges without any evidence of saturation, as shown in **figure 3.32** and **figure 3.33** for some representative measurements. [*Barreca-2007-A*, *Chen-2008*]

Under consideration of **figure 3.32** and the assumption of equation 3.3 even at lower gas concentrations, the detection limit extrapolated for O_3 was estimated to be less than 1 ppb, which is the best value for O_3 detection by ZnO NRs reported so far. [*Kang-2005, Kortidis-2009*] Similarly, the detection limit for NO_2 was lower than 1 ppb, which is significantly better than those recently reported. [*Chen-2011-B*, *Oh-2009*] These results further highlight the significance and validity of the present study in the obtainment of efficient and reliable gas sensing systems.

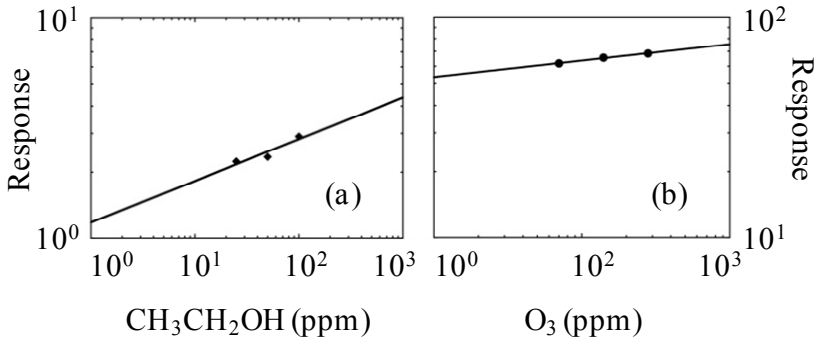

Figure 3.32: Response dependence on CH_3COCH_3 (a) and O_3 (b) concentrations at a fixed working temperature of 200°C, using ZnO NR arrays grown on Al_2O_3 from compound **2** (see **3.4.2.4** and **figure 3.19**).

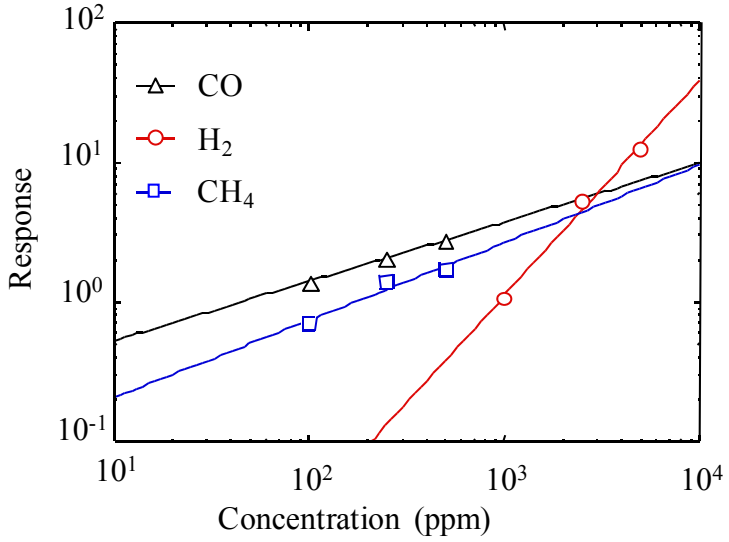

Figure 3.33: Gas sensing response as a function of concentration towards (a) CO (WT = 200°C), (b) H_2 (WT = 400°C) and (c) CH_4 (WT = 300°C), using ZnO NR arrays grown on Al_2O_3 (see **3.4.2.4**).

The improved performances, regarding sensitivity, reversibility and selectivity of the ZnO NR sensors, can be explained by the sensing mechanism, based on the adsorption of the target gas on the ZnO surface, where subsequent reactions with oxygen species take place (reactions 3.2 – 3.13). [*Chang-2008*, *Liangyuan-2010*, *Ra-2008*, *Zhang-2009-B*] This mechanism implies that the gas sensing behaviour is strongly related to the system surface properties. [*Bie-2007*, *Das-2010*, *Krishnakumar-2009*] The fact, that the obtained responses compared favorably with literature ones, was attributed to the synergy of chemical and electronic effects in the present zinc oxide materials. [*Krishnakumar-2009*, *Liangyuan-2010*, *Wang-2006*] The high length-to-diameter and surface-to-volume ratios are considered to be the main reason for the outstanding gas sensing performances of the ZnO NR arrays. [*Kenanakis-2007*] It is well known that the sensing response is strongly dependent on the grain size and can be significantly increased whether the NR lateral size approaches the Debye length L_d (L_d = 7.5 nm for ZnO, [*Chen-2006*, *Li-2009-B*]) a regime in which the sensor functional behaviour is dominated by surface interactions. Since the diameter of the above ZnO NRs is comparable to $2L_d$, a high portion of the 1D cross-section structure can be completely depleted and the sensitivity is controlled by the width of the depletion layer. [*Hsueh-2007-B*, *Li-2008-B*] Thus, the improved performances of 1D-like nanosystems with respect to traditional spherical particles can be ascribed to the fact that most of the nanostructure lateral section is completely depleted, generating this

way enhanced current modulations upon injection of the target chemicals. [*Dayan-1997*, *Li-2007-B*, *Lupan-2010*, *Ra-2010*, *Sadek-2007*, *Wang-2006*] On the other hand, the high aspect ratio of the present ZnO nano-assemblies likely results in an increased content of oxygen vacancies and in a more efficient gas uptake with respect to conventional systems. [*Bie-2007*, *Das-2010*, *Hung-2009*, *Krishnakumar-2009*, *Lupan-2009*, *Qurashi-2009*, *Ra-2008, Tien-2005*, *Zhang-2009-B*]

❖ 3.5 Conclusions

In summary, the present chapter reports on the development of ZnO nanostructures as improved photo-active and gas sensing materials. **Paragraph 3.3** documents the potential of the precursors, $[Zn\{[(CH_2)_xOCH_3]NC(CH_3)=C(H)C(CH_3)=O\}_2]$ (**1**: $x = 2$; **2**: $x = 3$) (see also **2.7** and **8.1**) for the CVD of pure ZnO of high crystalline quality by CVD, as evidenced by XRD, RBS, XPS and PL analyses. Subsequently, the use of **1** and **2** was extended to the PECVD of ZnO NR arrays on Si(100) and polycrystalline Al_2O_3 (**3.4**). As a result, the herein presented PECVD process allowed the catalyst-free growth of *c*-axis oriented 1D ZnO nanosystems under milder conditions (200 – 300°C, 20 W) compared to previously reported plasma assisted ones, involving elevated temperatures, powers, use of catalyst and/or pyrophoric precursors (see **3.2**). The high purity, crystalline quality at low temperatures, and strong alignment has been attributed to clean precursor decomposition (**8.1**), activation by the Ar/O_2 plasmas (**paragraph 2.4**) and to the electric field, promoting <001> oriented growth of wurtzite ZnO. The perpendicular growth of ZnO NRs on Si(100) and rough alumina substrates resulted in vertically aligned arrays and urchin-like structures, respectively. The ZnO deposits high surface areas and nano-organization showed to be favorable for functional applications.

PSH and PCO testing of silicon supported ZnO NR arrays grown under optimum conditions (200 – 300°C, 20 W, see **section 3.4.2.3**) revealed improved photo-active system performances with increasing RMS roughness (see **figures 3.17**, **3.25** and **3.26**), owing to efficient light trapping and electron/hole separation. This observation can be attributed to the fact, that long and sparsely grown rods (i) improve light harvesting and (ii) expose a higher active surface, leading to an enhanced hydrophilicity by –OH adsorption, and favoring PCO by the generation of active radical species and capturing electrons at surface defects. Accordingly, the measured PSH performances followed the

order **1_300_20W(Si)** < **2_200_20W(Si)** < **2_300_20W(Si)** (see **section 3.4.2.3** and **figure 3.17**), and were superior to those of the benchmark material (Pilkington® glass) and higher than those of ZnO nanosystems, tested under similar operating conditions. [*Barreca-2009-A*, *Fujishima-2008*, *Liu-2004-B*] Also for the PCO of TPA, **2_300_20W(Si)** was the best-performing sample, yielding a value five times higher than that of the Pilkington® glass.

The use of urchin-like ZnO nanostructures on Al_2O_3 (see **section 3.4.2.4**) in gas sensing devices toward reducing (CH_3CH_2OH, CH_3COCH_3, CO, H_2 and CH_4) and oxidizing (O_3, NO_2) analytes provided superior gas sensing properties in a reversible process compared to literature. Specifically, improvements were obtained in terms of (i) response values, (ii) kinetics, (iii) selectivity and (iv) sensitivity.

(i) Response values for all target analytes higher than reported ones by ZnO systems, [*Barreca-2007-A*, *Chen-2006*, *Dayan-1997*, *Das-2010*, *Hsueh-2007-B*, *Mukherjee*-2009, *Oh-2009*, *Qi-2008*, *Qurashi-2009*, *Kang-2009*, *Sadek-2007*, *Lupan-2009*, *Chen-2008*, *Ra-2010*, *Ra-2008*, *Wu-2008-A*, *Zeng-2009-A*, *Zhang-2009-B*] even when activated by metal nanoparticles (*e.g.* Pd, Ag, Pt, Au [*Bhattacharyy-2007*, *Bhattacharyy-2008-A*, *Bhattacharyy-2008-B*, *Chang-2008*, *Kang-2009*, *Li-2008-B*, *Wright-2010*), under similar operating conditions.

(ii) Recovery time for H_2 detection shorter (≈ 1 min) than recently reported. [*Lupan-2010*, *Sadek-2007*, *Wang-2006*]

Recovery and response times for CH_4 sensing (≈ 1 min and ≈ 2 - 3 min) favourable compared to previous studies. [*Mitra-2007*]

(iii) Discrimination between oxidizing and reducing analytes as a function of working temperature.

(iv) Recorded detection limit for O_3 (< 1 ppb) lower than by ZnO NRs reported so far. [*Kang-2005, Kortidis-2009*]

Recorded detection limit for NO_2 (< 1 ppb) lower than reported values. [*Chen-2011-B*, *Oh-2009*]

As a whole, the successful improvement of ZnO PSH, PCO and gas sensing performances along with a softening of CVD processing conditions was enabled by choice of precursors with clean and controlled decomposition pattern and exploitation of the advantages of plasma processing, paving the way to multifunctional ZnO based materials.

4. Co_3O_4

❖ 4.1 Abstract

In this chapter, the PECVD of pure and in-situ fluorine-doped Co_3O_4 using [$Co(dpm)_2$] (**3**) and [$Co(hfa)_2$·TMEDA] (**4**) (see **paragraphs 2.8** and **8.2**.) is presented. The Co_3O_4 nanomaterials were deposited on single crystals (MgO(100), $MgAl_2O_4$(100), Si(100)) and polycrystalline substrates (Al_2O_3) and analyzed by a multi-characterization technique.[1,2,3,4] The silicon and alumina supported deposits have been tested in photocatalytic H_2 production[2,3] and detection of ethanol and acetone. [2,4] In this context, key efforts were dedicated to study the impact of F-doping on the systems performances.

Paragraph 4.3 is focused on the PECVD of Co_3O_4 thin films on MgO(100) and $MgAl_2O_4$(100),[1] which have a lattice mismatch with Co_3O_4 of 4.2 and <0.01%, respectively. [*Klepper-2007*, *Mane-2002*, *Vaz-2009-A*] Deposition experiments were performed from **3** in Ar/O_2 plasmas with an input power of 20 W at temperatures between 100 and 400°C (**4.3.1**). The morphology, structure (**4.3.2**) and composition (**4.3.3**) of the Co_3O_4 systems were thoroughly analyzed by FE-SEM, bidimensional XRD (XRD^2), XPS/XE-AES and SIMS.

The synthesis procedure was transferred to the growth of Co_3O_4 on Si(100),[2,3] silica and polycrystalline Al_2O_3 (**paragraph 4.4**),[2,4] in order to tailor the material as a photocatalyst and gas sensing material, respectively. All growth experiments (**4.4.1**) were carried out at 100 - 400°C with an input power of 20 W from the two CVD cobalt (II) sources **3** and **4**, never utilized in plasma-assisted routes to obtain cobalt oxides before. [$Co(hfa)_2$·TMEDA] (**4**) was used for the preparation of fluorine-doped Co_3O_4 species (**4.4.1**). (F-)Co_3O_4-based deposits were characterized by the use of FE-SEM, TEM,

[1] [*Barreca-2011-D*] D. Barreca, A. Devi, R.A. Fischer, D. Bekermann, A. Gasparotto, M. Gavagnin, C. Maccato, E. Tondello, E. Bontempi, L.E. Depero, C. Sada, CrystEngComm 13 (2011) 3670.

[2] [*Gasparotto-2011*] A. Gasparotto, D. Barreca, D. Bekermann, A. Devi, R.A. Fischer, C. Maccato, E. Tondello, J. Nanosci. Nanotechnol. 11 (2011) 8206.

[3] [*Gasparotto-2011-A*] A. Gasparotto, D. Barreca, D. Bekermann, A. Devi, R.A. Fischer, P. Fornasiero, V. Gombac, O.I. Lebedev, C. Maccato, T. Montini, G. Van Tendeloo, E. Tondello, J. Am. Chem. Soc. 133 (2011) 19362.

[4] [*Barreca-2011-C*] D. Barreca, D. Bekermann, E. Comini, A. Devi, R.A. Fischer, A. Gasparotto, M. Gavagnin, C. Maccato, C. Sada, G. Sberveglieri, E. Tondello, Sens. Actuators, B 160 (2011) 79.

GIXRD (**4.4.2**), XPS/XE-AES and SIMS (**4.4.3**). UV-Vis absorption spectroscopy was carried out on silica-supported samples (**4.4.4**).

The *p*-type Co_3O_4 nanostructured films grown on Si(100) were tested in the photocatalytic production of H_2 from water/ethanol solutions under both near-UV and solar irradiation (**4.4.5**).[2,3] It is demonstrated that the introduction of fluorine into *p*-type Co_3O_4 results in a 5-fold increase of hydrogen production (213 000 μmol h^{-1} g^{-1}) with respect to the corresponding undoped oxide under UV-illumination (45 000 μmol h^{-1} g^{-1}). The obtained yields were among the best ever reported for similar semiconductor based photocatalytic processes.

As regards alumina supported (F-)Co_3O_4, the systems performances in the detection of acetone and ethanol at various concentrations and working temperatures have been studied (**4.4.6**).[2,4] It is shown that with increasing F-doping level higher responses could be achieved. In addition, the use of F-doped Co_3O_4 resulted in reversible sensing processes, and low ethanol detection limit (3 ppm).

❖ 4.2 Introduction

Co_3O_4 is attracting increasing interest for diverse applications exploiting their promising electronic, chemical and magnetic properties. [*Barreca-2010-B*, *Barreca-2010-D*, *Barreca-2010-E*, *Barreca-2010-F*, *Casas-Cabanas-2009*, *Fujii-1995*, *Mane-2002*, *Pasko-2004*, *Patil-1998*, *Rooth-2006*, *Shalini-2001*, *Shim-2008*, *Vaz-2009-A*, *Wöllenstein-2003*]

To this regard, the choice of the support material onto which Co_3O_4 is deposited plays a strategic role. Indeed, the substrate nature strongly affects the nucleation and growth of the forming system and its chemico-physical properties, leading, in turn, to diversified functional performances as a function of specific target applications. To date, the growth of Co_3O_4 films by different fabrication methods has been performed on several polycrystalline or amorphous substrates. [*Barreca-2001*, *Barreca-2010-B*, *Barreca-2010-D*, *Barreca-2010-E*, *Barreca-2010-F*, *Fujii-1995*, *Gulino-2003*, *Mane-2002*, *Pasko-2004*, *Patil-1998*, *Rooth-2006*, *Shim-2008*, *Shalini-2001*, *Tyczkowski-2007*, *Wöllenstein-2003*]

In contrast, only a few papers devoted to Co_3O_4 growth on single crystals can be found in the literature. [*Carson-1996*, *Kennedy-1995*, *Klepper-2007*, *Langell-1999*, *Meyer*-2008,

Pasko-2004, *Rooth-2006*, *Shalini-2001*, *Vaz-2009-A*, *Vaz-2009-B*] On this basis, the development of synthetic strategies to control Co_3O_4 deposition and the thorough understanding of its growth on single crystals are of great importance. [*Kennedy-1995*, *Klepper-2007*, *Mane-2002*, *Rooth-2006*, *Wöllenstein-2003*] In addition, the deposition of strongly oriented/epitaxial films typically requires high temperatures and/or harsh conditions in terms of energy supply, ultra-high vacuum or toxic/reactive reagents. [*Fujii-1995*, *Kennedy-1995*, *Mane-2002*, *Shalini*-2001, *Shim-2008*, *Tyczkowski-2007*] In view of eventual practical utilizations, the availability of milder synthesis conditions, while maintaining a good control over film texture and morphology on the nanoscale, is highly desirable. To this regard, the low-temperature growth of highly oriented Co_3O_4 on single-crystal substrates has been investigated in the framework of this thesis.

Furthermore, the present chapter demonstrates the importance for the development of Co_3O_4 based nanomaterials in view of photocatalytic and gas sensing applications. In this context, a key issue of present chapter was to investigate to which extent F content in Co_3O_4 could be tailored by a proper choice of the processing conditions, with particular regard to its impact on the functional performances.

As regards photocatalytic production of H_2 from water-containing solutions, [*Abe-2010*, *Barreca-2010-F*, *Chen-2010-B*, *Kim-2004*] a great deal of effort has been devoted to the design and development of *n*-type semiconducting photocatalysts, such as TiO_2 and ZnO, and to their chemical modification aimed at obtaining improved functional performances. [*Abe-2010*, *Chen-2010-B*, *Czoska-2008*, *Shet-2011*, *Sun-2010*, *Wang-2009-B*] In particular, anion-doping of the oxide phase has attracted a considerable interest for the possibility of achieving an optimal solar light absorption and an enhanced surface reactivity, together with an efficient exploitation of photo-generated e^-/h^+ pairs. [*Chen-2009*, *Czoska-2008*, *Kim-2004*, *Liu-2009-C*, *Sun-2010*, *Wang-2004-A*, *Xu-2008*, *Zhao-2010*, *Zuo-2010*] Nevertheless, its potential has been scarcely investigated for photocatalytic processes over *p*-type materials and never reported for photoassisted H_2 production. At variance with *n*-type SC*s*, in *p*-type systems cation vacancies and/or anion interstitials are considered the main kind of intrinsic defects and, as a consequence, a different surface reactivity can be foreseen upon adsorption of reactants on the catalyst surface. [*Arora-1998*, *Boumaza-2009*] Furthermore, the presence of sub-surface defects in *p*-type SCs, acting either as recombination centers or as beneficial promoters of redox

processes, might also affect the fate of photo-generated electrons and holes. [*Arora-1998*, *Chen-2010-B*, *Chen-2009*] To this aim, extrinsic anion doping of *p*-type SC*s* represents a valuable mean to achieve improved photocatalytic performances.

As concerns gas sensing, *p*-type SCs, offering an opposite conduction behaviour and much different gas sensing patterns than the well investigated *n*-type systems, [*Barreca-2009-B*, *Barreca-2010-B*, *Li-2009-C, Liu-2010-B*, *Patil-2010*, *Park-2009*] are highly demanded for various applications, such as arrays for electronic noses, [*Comini-2000*, *Liu-2010-B*, *Wisitsoraaat-2009*] because they promise an enhanced sensitivity/selectivity in the detection of several reducing gases. [*Comini-2005*, *Wöllenstein-2003*, *Xie-2009*] In SC sensor devices, it is generally assumed that various forms of chemisorbed oxygen are the active species directly involved in the mechanism of gas detection. [*Hoa-2009*, *Hübner-2010*, *Patil-2010*] A possible explanation for the oxidizing activity of *p*-type SCs is that, whereas *n*-type metal oxides only chemisorb as much oxygen as necessary to compensate their deficiencies, *p*-type SCs can uptake a higher oxygen amount, resulting in a ready surface coverage by chemisorbed oxygen. [*Aroutiounian-2007*, *Choi-2010*] These properties are extremely attractive for the possibility of achieving low temperature operation with limited power dissipation, a key challenge for eventual integration into portable systems (see also **paragraph 3.2**). [*Choi-2001*, *Hernandez-Ramirez-2009*, *Kärkkänen-2009*] Improved gas sensing performances were reported for the F-doping of *n*-type SC oxide, attributed to an enhanced chemisorption of the target species arising from the increased Lewis acidity of surface sites. [*Chen-2010-A*, *Zhao-2010*] Investigations on F-doping of *n*-type SCs for photocatalysis, revealed a decrease of electrical resistivity [*Ghosh-2005*, *Pawar-2008*] due to an increase of carrier concentration/mobility, since fluorine concomitantly acted as an effective dopant and a passivation agent of surface defects, reducing carrier trapping. [*Liu-2010-A*, *Xu-2006-B*] F-doping is not common for *p*-type SCs and has never been investigated up to date in the case of Co_3O_4 materials.

❖ 4.3 PECVD of Co_3O_4 on Mg(100) and $MgAl_2O_4$(100)

❖ 4.3.1 Deposition Procedure

Co_3O_4 depositions were performed on as-received MgO(100) and $MgAl_2O_4$(100) single crystals (Crystal GmbH®, Berlin, Germany) using a two-electrode PECVD apparatus powered by a RF generator (**8.3.3**). After preliminary experiments aimed at the process optimization, the input power was fixed at 20 W. Electronic grade argon and oxygen were used as plasma sources. The [$Co(dpm)_2$] (**3**) precursor was placed in an external vessel heated at 90°C and transported into the deposition zone by a 60 sccm Ar flow. Two further auxiliary gas-lines were used to introduce Ar (15 sccm) and O_2 (20 sccm) directly into the reactor. The gas lines connecting the precursor reservoir and reaction chamber were heated at 120°C. For all experiments the deposition time, total pressure and inter-electrode distance were 1 h, 1 mbar and 6 cm, respectively. Specimens were grown at temperatures between 100 and 400°C, as summarized in **table 4.1**.

Table 4.1: Labelling of the Co_3O_4 samples analyzed in the present work as a function of the used growth temperature and substrate. Pressure, RF-power, deposition time and T_{vap} (precursor **3**) were 1 mbar, 20 W, 60 min and 90°C, respectively for all depositions.

Sample	Substrate	Deposition temperature (°C)
3_100(Mg)	MgO(100)	100
3_200(Mg)		200
3_300(Mg)		300
3_400(Mg)		400
3_100(MgAl)	$MgAl_2O_4$(100)	100
3_200(MgAl)		200
3_300(MgAl)		300
3_400(MgAl)		400

❖ 4.3.2 Morphology and Structure

The morphological evolution of Co_3O_4 films as a function of the adopted growth temperature was investigated by FE-SEM. In the case of MgO(100) single crystals (**figure 4.1**), **3_100(Mg)**, synthesized at 100°C, was characterized by a uniform distribution of low-sized particles, with a mean diameter of 8 nm. As explained below, XRD^2 results evidenced that such crystallites were not randomly oriented. At 200°C, the Co_3O_4 layer displayed a rather smooth surface characterized by the presence of small holes (**figure 4.1**, **3_200(Mg)**). As previously reported, [*Pasko-2004*, *Rooth-2006*] a similar flat and regular morphology is in line with an oriented film growth. In addition, the formation of holes, that was even more evident for the specimens synthesized at 300 (**3_300(Mg)**) and 400°C (**3_400(Mg)**, not reported), could be at least partially related to the different structural parameters of Co_3O_4 and MgO(100) (lattice mismatch = 4.2%) and to the release of thermal stress, in particular at the highest adopted deposition temperatures. [*Gelfi-2004*, *Mane-2002*] A more accurate quantification of residual stress effects by XRD^2 was hindered by the strong film orientation (see below).

For samples grown on $MgAl_2O_4$(100) (**figure 4.1**), at 100°C the system morphology closely resembled the one observed for growth on MgO(100) at the same temperature. Particles forming **3_100(MgAl)** had an average diameter of 12 nm. XRD^2 results (see below) indicated that these crystallites were not randomly oriented, pointing out to a significant structural influence of the substrate on Co_3O_4 growth. An increase of the deposition temperature to 200°C **3_200(MgAl)** resulted in the formation of well-evident cubic particles uniformly protruding from an underlying Co_3O_4 layer. Such structures appeared mainly oriented along the two directions indicated by arrows in the figure inset, evidencing a relation with the substrate and a mixed 2D-3D growth, leading to the formation of plate-like crystallites. [*Klepper-2007*, *Pasko-2004*, *Rooth-2006*] At 300°C, a flat topography characterized by a high density of holes could be observed (**figure 4.1**, **3_300(MgAl)**). Although, similarly to **3_300(Mg)**, their formation could be related to the accommodation of thermal stress, these holes appeared preferentially aligned along two main directions. Such a difference between the two homologous samples deposited on MgO(100) and $MgAl_2O_4$(100) was traced back to the lower lattice mismatch in the

second case (see above), suggesting a stronger structural relationship between the Co_3O_4 layer and the underlying single-crystal substrate.

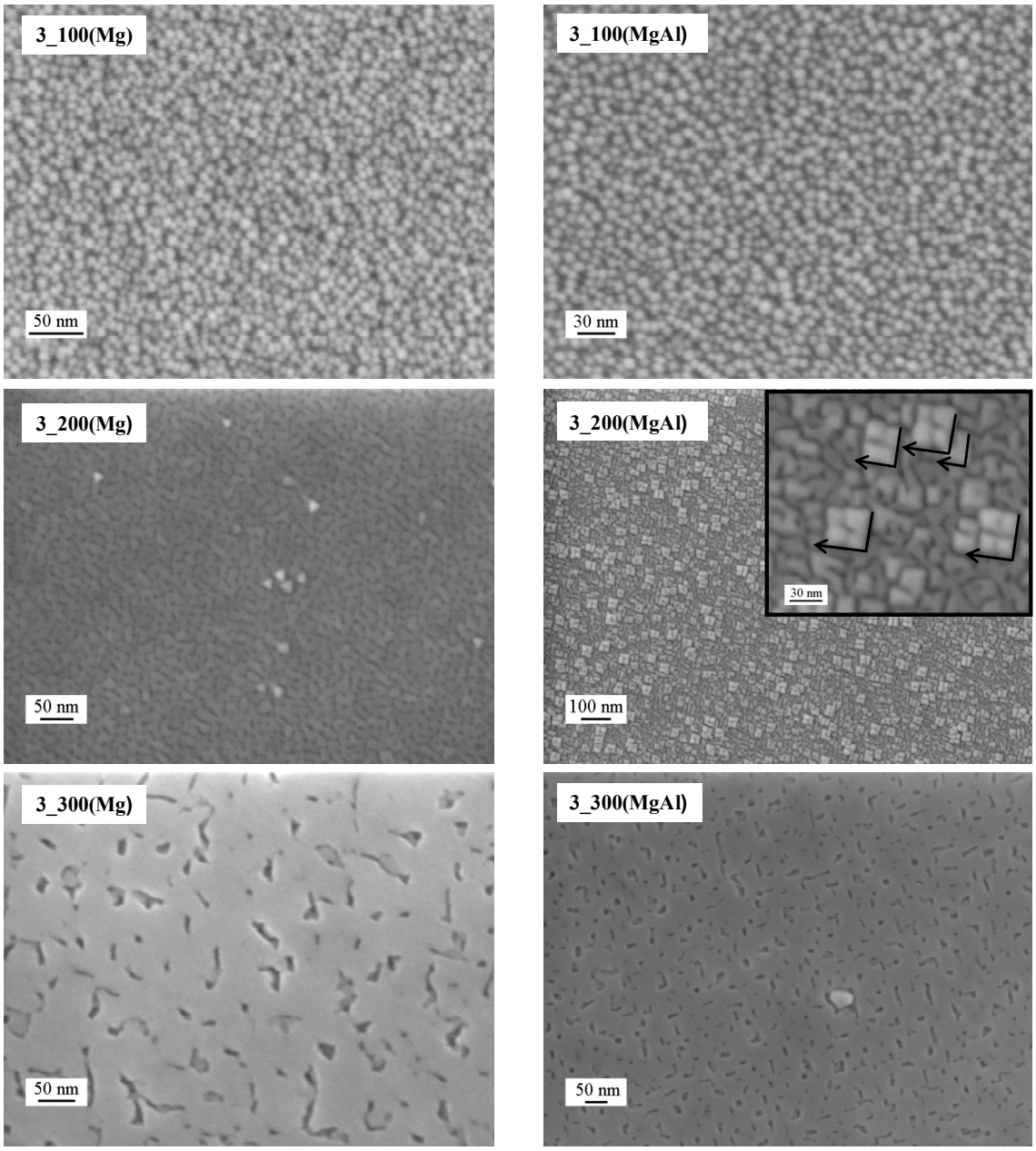

Figure 4.1: Plane view FE-SEM images of Co_3O_4 samples deposited on MgO(100) and on $MgAl_2O_4$(100) at temperatures 100 - 300°C (**table 4.1**).

Despite all samples were analyzed by XRD[2], in many cases contributions from the Co_3O_4 phase in 2D images could not be appreciated, due to the high orientation of the deposited films. As concerns sample **3_100(Mg)** grown on MgO(100), a careful alignment and the higher lattice mismatch with respect to $MgAl_2O_4$(100) allowed to discriminate the film

structural features. As can be observed in **figure 4.2**, some intense diffraction peaks were evident in the 2D image. In particular, the strong reflections at 105.7 and 127.3° (marked by *) can be attributed to the single crystal substrate. Despite XRD peaks of single crystals are generally very intense and sharp; the spots displayed in **figure 4.2** were broadened along β and 2θ, since the patterns were acquired during sample rotation. Interestingly, the two less intense reflections at 36.8 and 77.3° could be ascribed to the Co_3O_4 film. This attribution was confirmed not only by the fact that MgO does not show any reflection at 77.3°, [*JCPDS-B*] but also by the higher 2θ broadening of these signals with respect to the previous ones. As a matter of fact, these spots correspond to the (311) and (533) reflections of Co_3O_4, the first one being the most intense peak of this phase. [*JCPDS-C*] Since the growth of highly oriented films usually requires higher deposition temperatures than 100°C, [*Mane-2002*, *Rooth-2006*] it is reasonable to suppose that an oriented/epitaxial growth was favored not only by the process thermal activation, but also by the continuous plasma bombardment, providing an additional energy supply and promoting specific texturing effects, hardly attainable by conventional approaches. [*Dittmar-2004*, *Mane-2002*, *Shalini-2001*]

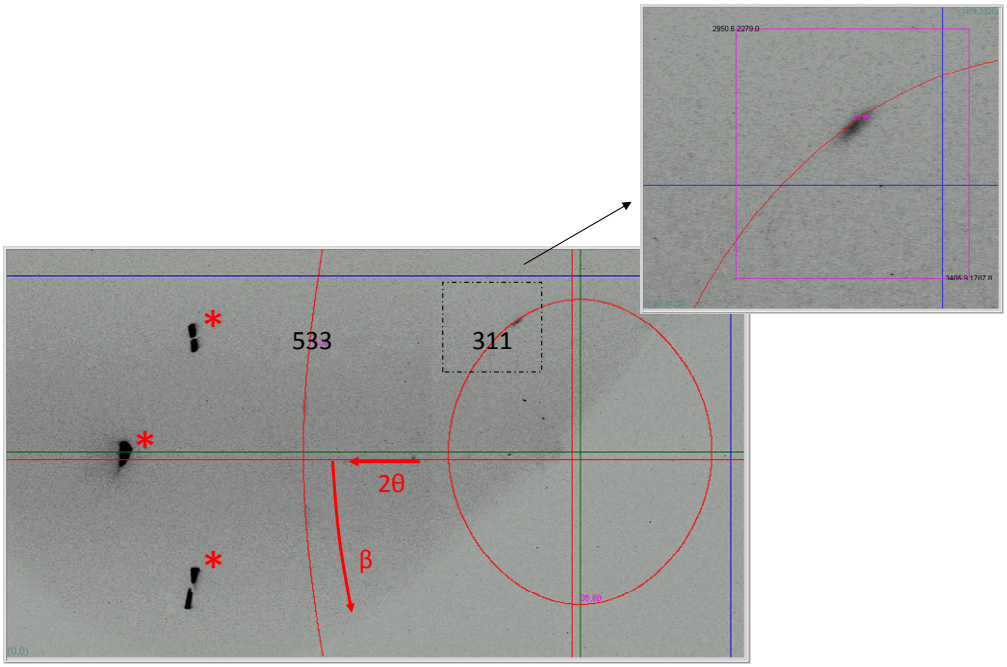

Figure 4.2: XRD^2 image of sample **3_100(Mg)** (see **table 4.1**). Rings indicate peaks attributed to the film (a magnification of the Co_3O_4 (311) reflection is evidenced in the upper box). Stars mark reflections ascribed to the MgO(100) substrate.

❖ 4.3.3 Composition

The surface and in-depth chemical composition of the synthesized Co_3O_4 films was characterized by the combined use of XPS and SIMS analyses.

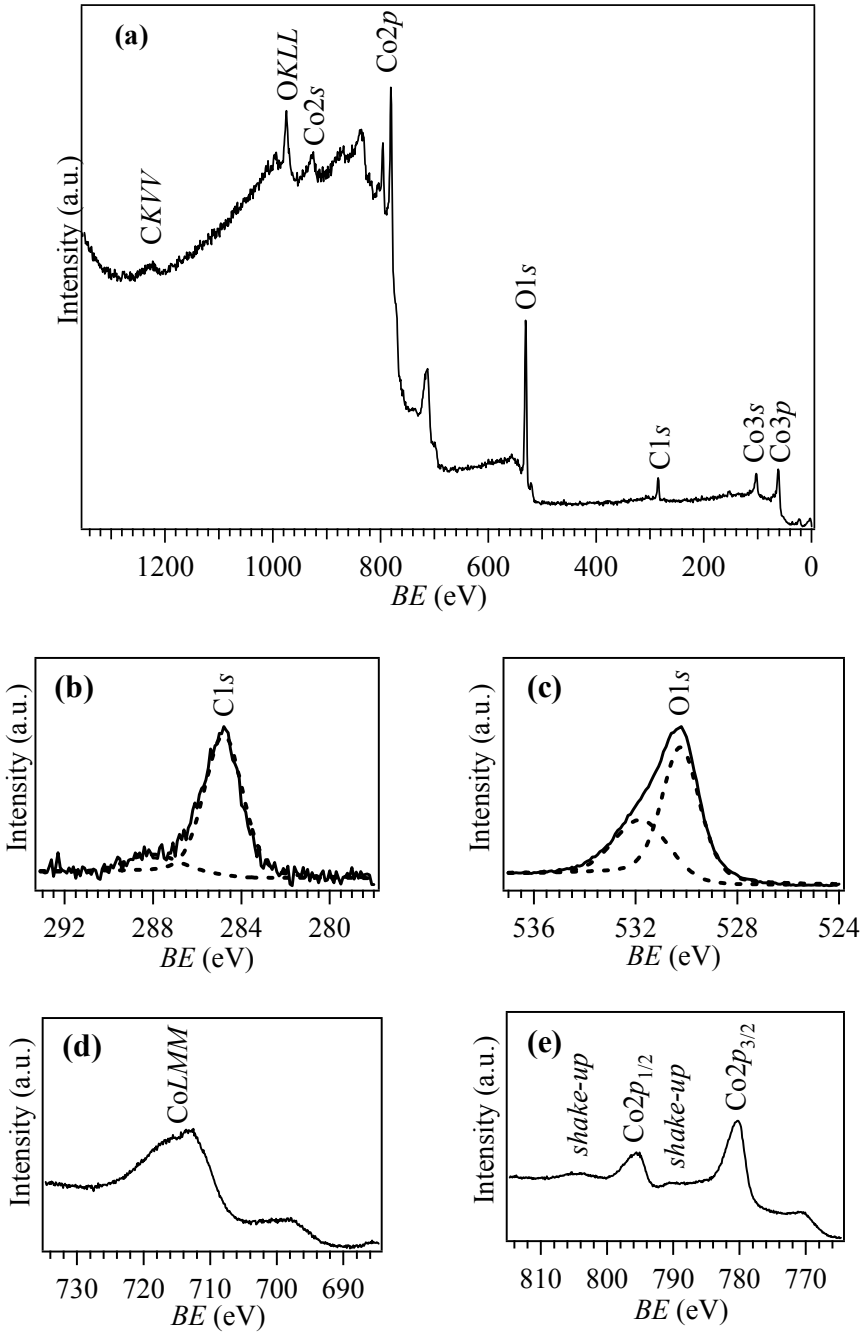

Figure 4.3: (a) Surface wide-scan XP spectrum of a representative Co_3O_4 sample (**3_100(MgAl),** see **table 4.1**). The detailed C1*s* (b), O1*s* (c), Co2*p* (d) and Co*LMM* (e) regions are also displayed.

Figure 4.3 (a) displays the wide-scan XP spectrum of a representative system that was dominated by cobalt and oxygen photopeaks. Although carbon presence was detected, its rapid disappearance after 2 min Ar^+ erosion indicated that it mainly arose from atmospheric exposure, in agreement with SIMS results (see below). Indeed, the surface C1*s* signal (**figure 4.3 (b)**) was characterized by two distinct contributions at *BE* = 284.8 (typically 90 % of the total C1*s* peak) and 288.0 eV (10 % of the C1*s* signal), related to adventitious carbon and carbonate groups, respectively. [*Barreca-2010-B*, *Cong-2009*] As a general rule, the C, O and Co percentages were typically 20, 48 and 32 at.-%, respectively. The obtainment of an O/Co ratio close to 1.5, slightly higher than the one expected for stoichiometric Co_3O_4, was justified by the presence of surface carbonate and/or hydroxyl species arising from air exposure, as already reported for CVD Co_3O_4 deposits. [*Barreca-2010-B*, *Pasko-2004*] Accordingly, the O1*s* spectrum (**figure 4.3 (c)**) was fitted by two main bands at *BE* = 530.2 and 531.9 eV, ascribed to lattice oxygen (65 % of the total O1*s* peak) in the Co_3O_4 phase, and to surface carbonates and/or hydroxyls species (35 % of the O1*s* signal). [*Barreca-2001*, *Gulino-2003*, *Hagelin-Weaver-2004*, *Petitto-2008*, *Shim-2008*] The position of the Co2*p* signal (**figure 4.3 (d)**; *BE* (Co2$p_{3/2}$) = 780.3 eV) was in agreement with literature values for Co_3O_4. [*Pasko-2004*, *Barreca-2001*, *Carson-1996*, *Langell-1999*] Its presence as the only cobalt oxide phase was further confirmed by the energy separation between spin-orbit components (ca. 15.3 eV), the low intensity of *shake-up* satellites and the position of the Co*LMM* peak (**figure 4.3 (e)**), yielding a value of 1552.3 eV for the cobalt Auger parameter. [*Barreca-2010-D*, *Barreca-2010-F*, *Carson-1996*, *Cong-2009*, *Dittmar-2004*, *Gulino-2003*, *Hagelin-Weaver-2004*, *Langell-1999*, *Petitto-2008*, *Vaz -2009-B*]

In order to investigate the in-depth chemical composition, SIMS measurements were performed on both MgO(100) and $MgAl_2O_4$(100) supported samples (**figure 4.4**). Irrespective of the used substrate, very similar profiles were recorded on different areas of the same specimen, indicating a good lateral homogeneity. Notably, for all Co_3O_4 deposits, carbon content was lower than < 60 ppm, pointing out to a clean precursor decomposition. Apart from the transient regime observed in the outermost sample regions (corresponding to a thickness of ca. 5 nm), Co and O ionic yields presented a correlated trend throughout film thickness, suggesting their common chemical origin. On both single crystals, Co_3O_4 films were characterized by a quite sharp interface with the substrate,

despite an apparent magnesium segregation was evidenced at the film-MgO interface (**figure 4.4**, samples **3_200(Mg)** and **3_400(Mg)**). This effect could be mainly related to an enhancement of Mg sputtering yield in proximity of the substrate, due to matrix effects. [*Wilson-1989*] The long Co tailing observed for **3_200(MgAl)** could be related to the rough morphology of the film, in line with FE-SEM analyses (see above).

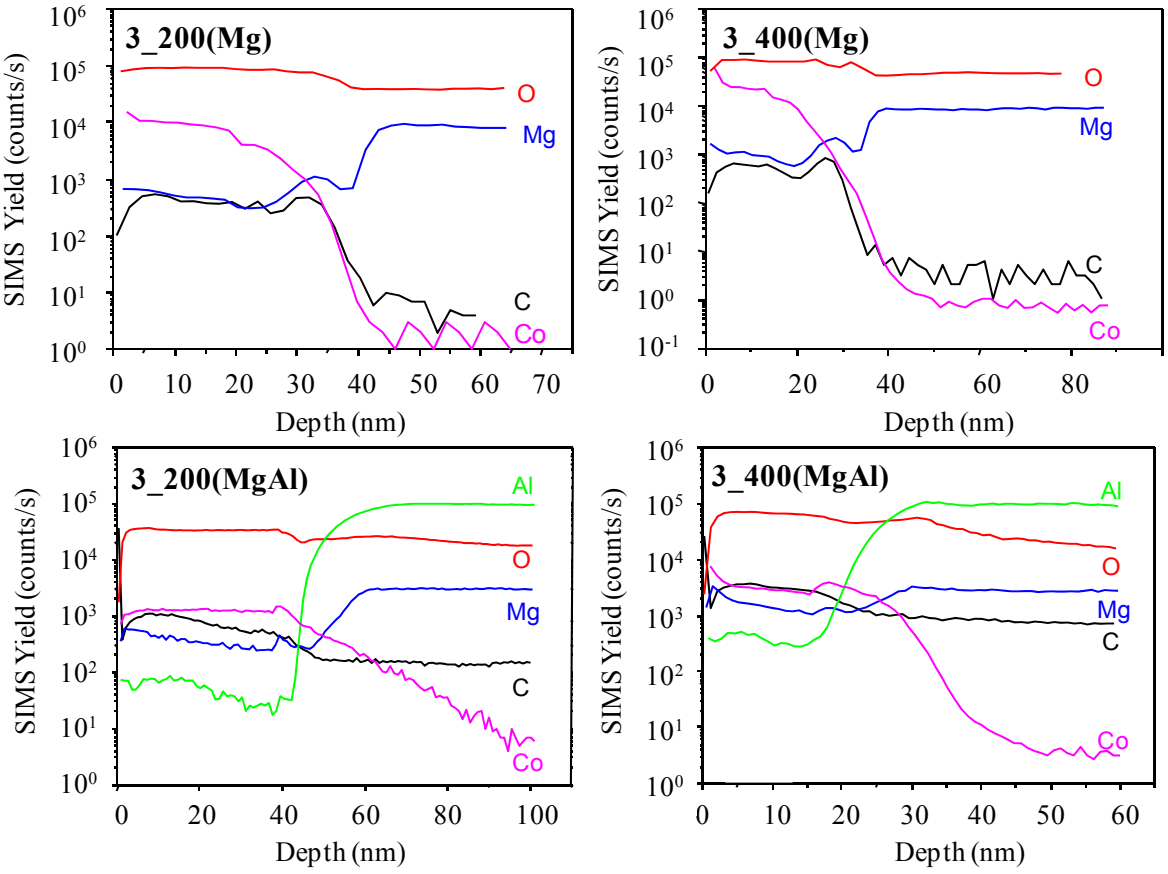

Figure 4.4: SIMS depth profiles for **3_200(Mg)**, **3_400(Mg)** and **3_200(MgAl)**, **3_400(MgAl)** (see **table 4.1**). The corresponding film thickness values are 41±7, 31±7, 57±9 and 37±7 nm, respectively.

❖ 4.4 PECVD of (F-)Co_3O_4 on Si(100) and Polycrystalline Al_2O_3

❖ 4.4.1 Deposition Procedure

Pure and F-doped Co_3O_4 nanostructured films were synthesized on Si(100) and Al_2O_3 *via* PECVD from both fluorinated and fluorine-free *β*-diketonate cobalt derivatives, **3** and **4**

respectively, using a two-electrode RF PECVD apparatus (**8.3.3**). Co_3O_4-based systems for photoassisted H_2 generation were deposited on 1.5 × 2.0 cm^2 Si(100) substrates and Herasil® silica slides pre-cleaned by standard procedures (**8.3.3**). Co_3O_4 growth for gas sensing applications was performed on polycrystalline alumina slides (3×3 mm^2; thickness = 250 μm), that were suitably cleaned prior to each experiment (**8.3.3**). Electronic grade argon and oxygen were used as plasma sources. The respective precursor was placed in an external reservoir heated by an oil bath and transported into the reaction chamber by an Ar flow (60 sccm). Compounds **3** and **4** were evaporated at 90°C and 60°C, respectively. Additional O_2 and Ar flows (15 and 20 sccm, respectively) were directly introduced in the reactor. The gas lines connecting the precursor vessel and reaction chamber were heated at 120°C (**3**) and 80°C (**4**). Depositions were performed at temperatures between 100 and 400°C and a total pressure of 1.0 mbar, using an RF-power of 20 W and an interelectrode distance of 6 cm (duration = 1 h). The processing conditions for the specimens analyzed in the present work are summarized in **table 4.2**.

Table 4.2: Synthesis conditions and sample labelling of silicon and alumina supported Co_3O_4 materials obtained from **3** and **4** at different substrate temperatures. Pressure, RF-power, deposition time, T_{vap} (precursor **3**) and T_{vap} (precursor **4**) were 1 mbar, 20 W, 60 min, 90°C and 60°C for all depositions.

Substrate	Si(100)		Al_2O_3	
Precursor	**3**	**4**	**3**	**4**
T (°C)				
100	**3_100(Si)**	**4_100(Si)**		
200	**3_200(Si)**	**4_200(Si)**	**3_200(Al)**	**4_200(Al)**
300	**3_300(Si)**	**4_300(Si)**	**3_300(Al)**	**4_300(Al)**
400	**3_400(Si)**	**4_400(Si)**	**3_400(Al)**	**4_400(Al)**

❖ 4.4.2 Morphology and Structure

Important information on the interrelations between the system morphology and the synthesis parameters was gained by FE-SEM analyses (**figure 4.5** and **figure 4.9**). As a general rule, the use of [$Co(hfa)_2$·TMEDA] (**4**) enabled the obtainment of a higher nanodeposit thickness with respect to [$Co(dpm)_2$] (**3**). This feature was ascribed to a higher mass supply of the former precursor to the growth surface under the adopted experimental conditions (see **8.2.3**). [*Bandoli-2009*, *Barreca-2001*]

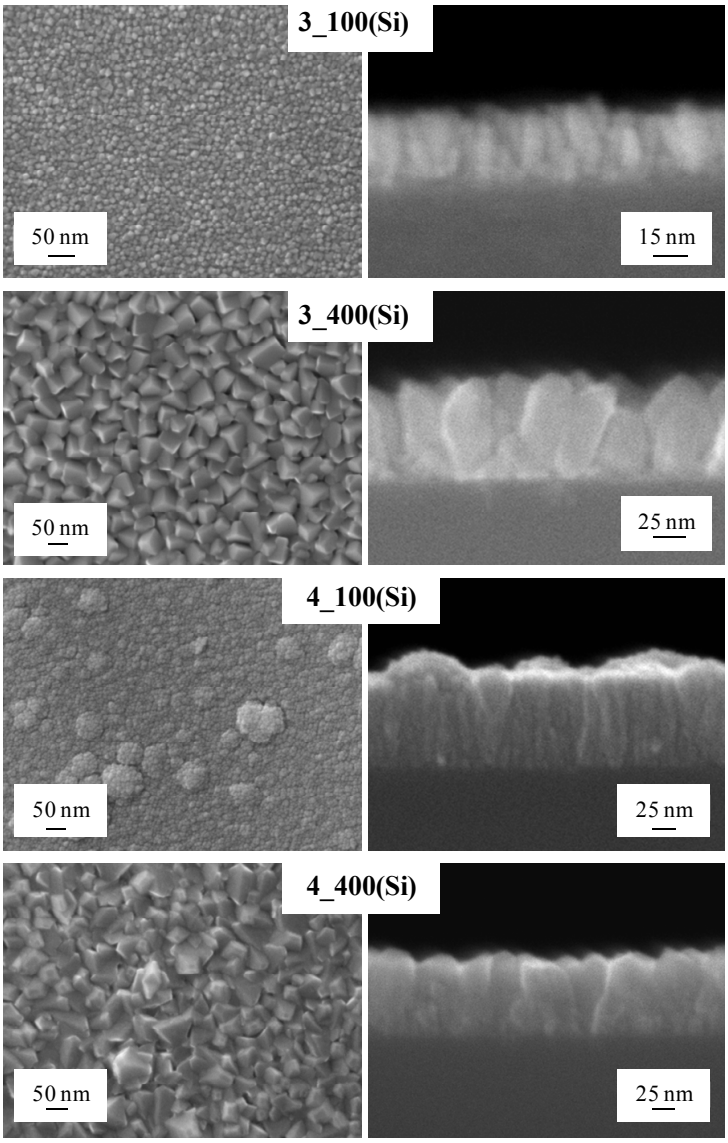

Figure 4.5: Representative FE-SEM cross-sectional and plane-view micrographs of Co_3O_4-based nanodeposits obtained from **3** and **4** at 100 and 400°C of substrate temperature. For sample indexing, see **table 4.2**.

At 100°C, Si(100)-supported samples (**3_100(Si)** and **4_100(Si)**) were formed by small interconnected globular particles, resulting in rather compact deposits (**figure 4.5**). At higher deposition temperatures, an enhanced particle size and a more pronounced faceting became evident. In particular, at 400°C **3_400(Si)** (**figure 4.5**) was dominated by well-defined pyramidal aggregates, likely due to the preferential exposure of low surface energy {111} crystallographic planes (**figure 4.6**). [*Barreca-2010-D*] For **4_400(Si)** (**figure 4.5**), such a faceting was less evident, consistently with the absence of any appreciable texturing effect (compare **figure 4.7**). HR-TEM measurements (**figure 4.6**) showed that the growth directions of the obtained columnar structures were <311> and <100> for undoped and F-doped Co_3O_4, respectively.

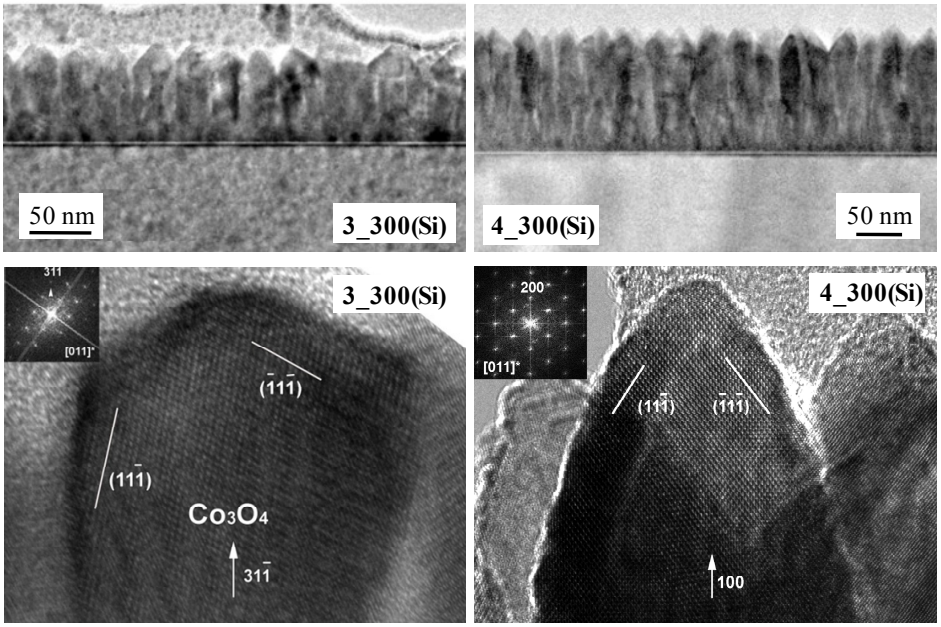

Figure 4.6: Cross-section TEM and HR-TEM images of undoped (left, **3_300(Si)**) and F-doped (right, **4_300(Si)**) Co_3O_4 samples (see also **table 4.2**). The Fourier Transform (FT) patterns of HR-TEM images are given as insets in (c).

In the case of Si(100)-supported specimens, the average nanoparticle dimensions underwent an increase from ≈ 10 nm, at 100°C, to ≈ 30 nm, at 200 - 400°C, irrespective of the used precursor. The initial size increase with deposition temperature (from 100 to 200°C) can be ascribed to a higher supply of thermal energy to the depositing system, progressively favoring the nanocrystal growth. On the other hand, the dimension constancy above 200°C could be related to the competition between deposition and

ablation processes characterizing the used plasmas, which plays a key role in the obtainment of materials with a controlled nanostructured organization. [*Barreca-2003-A*] A comparison of the above grain sizes with the values evaluated by the Scherrer equation suggested that the majority of particles observed in **figure 4.5** and were single-domain crystallites

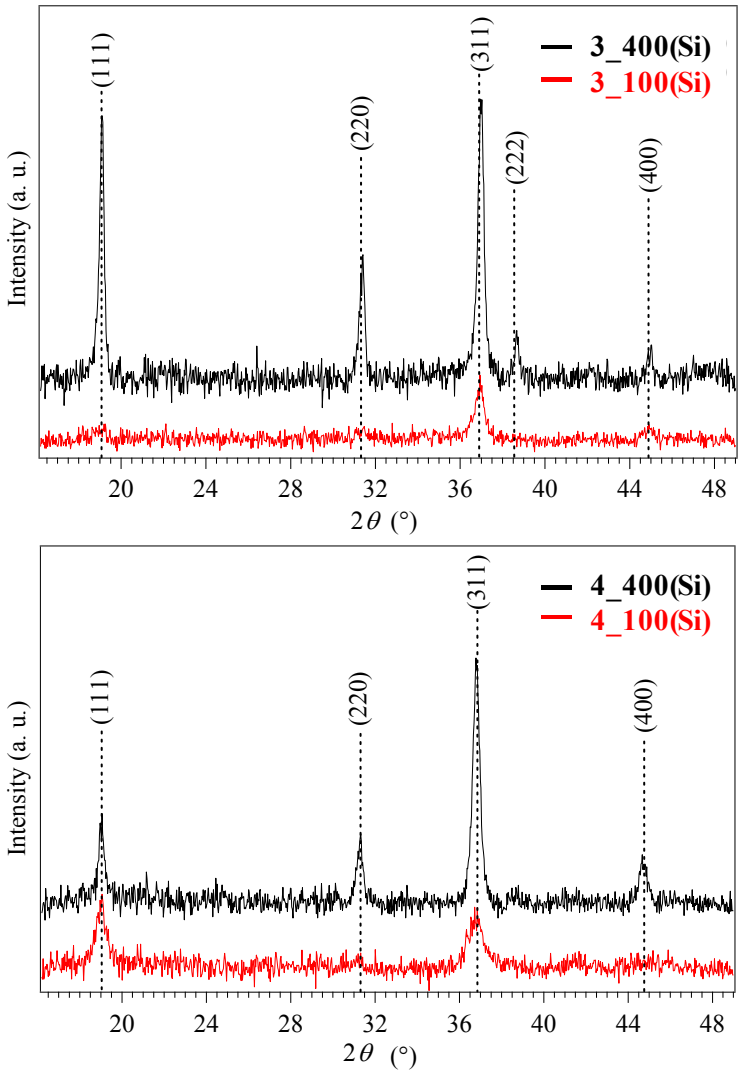

Figure 4.7: GIXRD patterns for **3_100(Si)**, **3_400(Si)**, **4_100(Si)** and **4_400(Si)**, deposited on Si(100) from **3** and **4** at 100 and 400°C (see **table 4.2** and **figure 4.5**).

Figure 4.7 displays GIXRD patterns for selected systems deposited on Si(100). As a general trend, all the spectra were in agreement with the formation of the spinel-type cubic Co_3O_4 phase, [*JCPDS-C*] but the relative intensity of the observed reflections was directly influenced by the growth temperature and the adopted precursor. Regarding

3_100(Si), only the signal of the (311) planes at $2\theta = 36.9°$ was present, which is the most intense even in the powder reference pattern. It is worth highlighting that the obtainment of crystalline deposits under such mild conditions is a peculiar effect of plasma activation, since in conventional thermal CVD analogous results were obtained for deposition temperatures not lower than 350°C. [*Barreca-2001*, *Barreca-2010-D*] At 400°C, well-developed diffraction peaks could be clearly observed (**3_400(Si)**). Furthermore, the intensity ratio between the (111) reflection (centered at 2θ = 19.0°) and the above mentioned (311) one was higher than that of the powder spectrum, [*JCPDS-C*] suggesting the possible occurrence of anisotropy/texturing effects. A qualitatively similar situation in terms of relative diffracted intensities was present for **4_100(Si)**, whereas for **4_400(Si)** the pattern was in line with that expected for polycrystalline Co_3O_4. Overall, these features indicate that the precursor nature and decomposition pattern directly influenced the deposit structural characteristics.

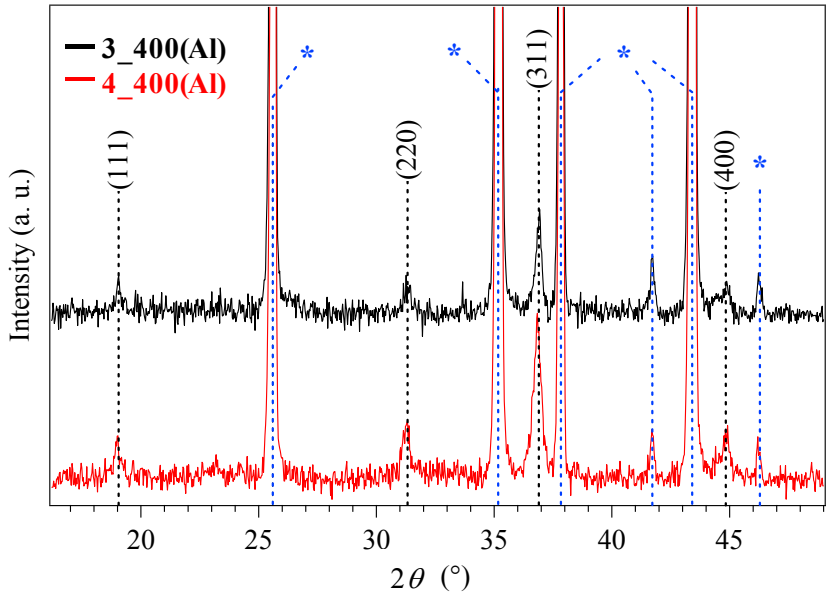

Figure 4.8: GIXRD patterns for **3_400(Al)** and **4_400(Al))**, deposited on Al_2O_3 from **3** and **4** at 100 and 400°C (see **table 4.2**).

In the case of Al_2O_3-supported systems, all observed diffraction peaks could be readily assigned to cubic Co_3O_4 (**figure 4.8**), irrespective of the adopted precursor and growth temperature. In particular, the recorded Bragg reflections at $2\theta = 19.0°$, 31.3°, 36.9° and 44.8° corresponded to the (111), (220), (311) and (400) Co_3O_4 planes, respectively, and

their relative intensities matched those of the powder patterns, indicating the absence of significant texturing effects. [*JCPDS-C*] This phenomenon could be traced back to the polycrystalline nature and high roughness of this substrate, resulting in an isotropic growth of the deposited specimens. The nanocrystal diameters had average values of ≈ 30 nm for Co_3O_4 systems obtained from both precursors.

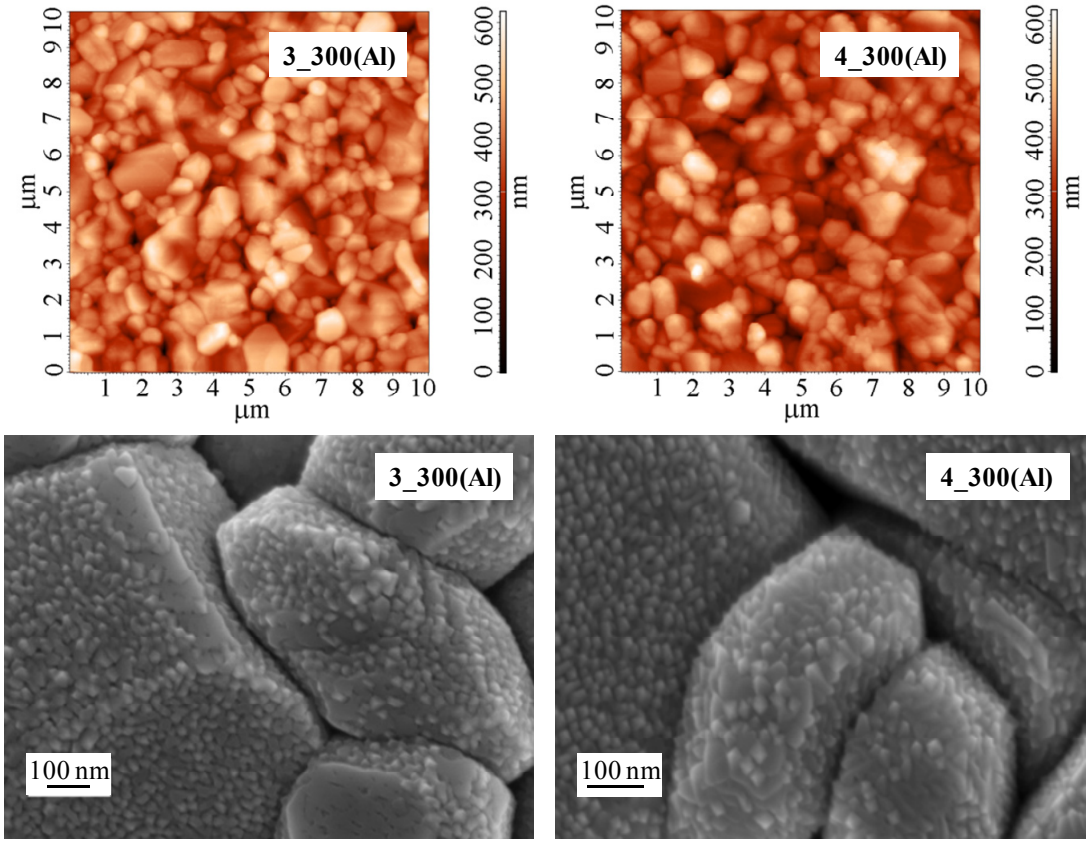

Figure 4.9: Representative AFM (top) and plane-view FE-SEM (bottom) micrographs of **3_300(Al)** and **4_300(Al)**, deposited on Al_2O_3 from **3** and **4** at 300°C (see **table 4.2**).

The system morphology of alumina-supported samples was analyzed by AFM and FE-SEM, and representative micrographs are displayed in **figure 4.9**. All specimens presented a very rough surface (typical RMS roughness = 75 nm), mainly due to the underlying alumina substrates, characterized by globular particles with sizes ranging from 300 to 1000 nm. Plane-view FE-SEM micrographs showed that polycrystalline Al_2O_3 substrates were conformally decorated by Co_3O_4 nanoaggregates, with an average dimension of 30 nm for both the used precursors. A comparison with crystallite sizes obtained from GIXRD analyses suggested that the observed aggregates were mainly

single-crystal domains and that, under the adopted experimental conditions, nucleation was predominant on the subsequent aggregate growth. Overall, the uniform distribution of Co_3O_4 nanoparticles on the underlying Al_2O_3 grains resulted in high surface-area materials, an attractive feature in view of sensing applications. [*Barreca-2010-A*, *Barreca-2010-C*, *Li-2009-C*]

❖ 4.4.3 Composition

An insight in the system chemical composition was obtained by XPS and SIMS. All Co_3O_4 specimen revealed very similar compositional information, irrespective of the substrate and processing conditions used. Compositional results are discussed below using representative examples.

The system chemical composition, investigated by XPS, was almost identical to the one described in **4.3.3**. As evidenced by **figure 4.10**, wide-scan spectra clearly displayed Co and O photopeaks, together with a weak C and F contribution (the latter for the sole trace **(b)**), whose origin is explained below. As a general rule, surface contamination arose from adventitious carbon (*BE* = 284.8 eV; 85% of total C), as well as from carbonates/bicarbonates due to air exposure (*BE* = 288.0 eV; 15% of total C) [*Cong-2009*, *Li-2009-C*, *Moulder-1992*] and precursor residuals (see below). Accordingly, the O/Co atomic ratio (1.5) was slightly higher than the stoichiometric value expected for Co_3O_4. The Co2*p* peak position [*BE*(Co2$p_{3/2}$) = 780.3 eV, with an energy separation between spin-orbit components of 15.3 eV], along with the low intensities of *shake-up* satellites, agreed with the formation of cobalt (II,III) oxide, irrespective of the growth conditions. [*Briggs-1990*, *Li-2009-C, Li-2009-A*, *Patil-2010*]

The main difference upon using **3** or **4** as starting sources was the presence of the F1*s* signal in the latter case (**figure 4.10**, upper panel, **4_200(Si)**). Such photopeak had the maximum intensity at a growth temperature of 100°C (**figure 4.10**, lower panel) and could be fitted by means of two different components, located at 688.0 (**I**) and 684.5 (**II**) eV, respectively. While the latter contribution was consistent with the presence of lattice fluorine in the oxide network arising from the incorporation of radical F species (see also EI-MS data above), the high *BE* one could be traced back to CF_2/CF_3 moieties. [*Gulino-2000*, *Ni-2007-B*] Upon increasing the deposition temperature from 100 to 400°C, F-

content was progressively reduced from ≈ 16 to ≈ 1 at. % and, correspondingly, component (**I**) disappeared, suggesting thus an improved precursor decomposition at higher temperatures. Notably, component (**I**) rapidly disappeared upon Ar^+ sputtering (**figure 4.11**), indicating that lattice fluorine was the only important species contributing to the in-depth F distribution. Furthermore, in-depth analyses (**figure 4.12**) indicated an almost constant fluorine concentration from the surface to the inner specimen regions. Such observations indicate that the presence of undecomposed precursor fragments was limited to the system surface.

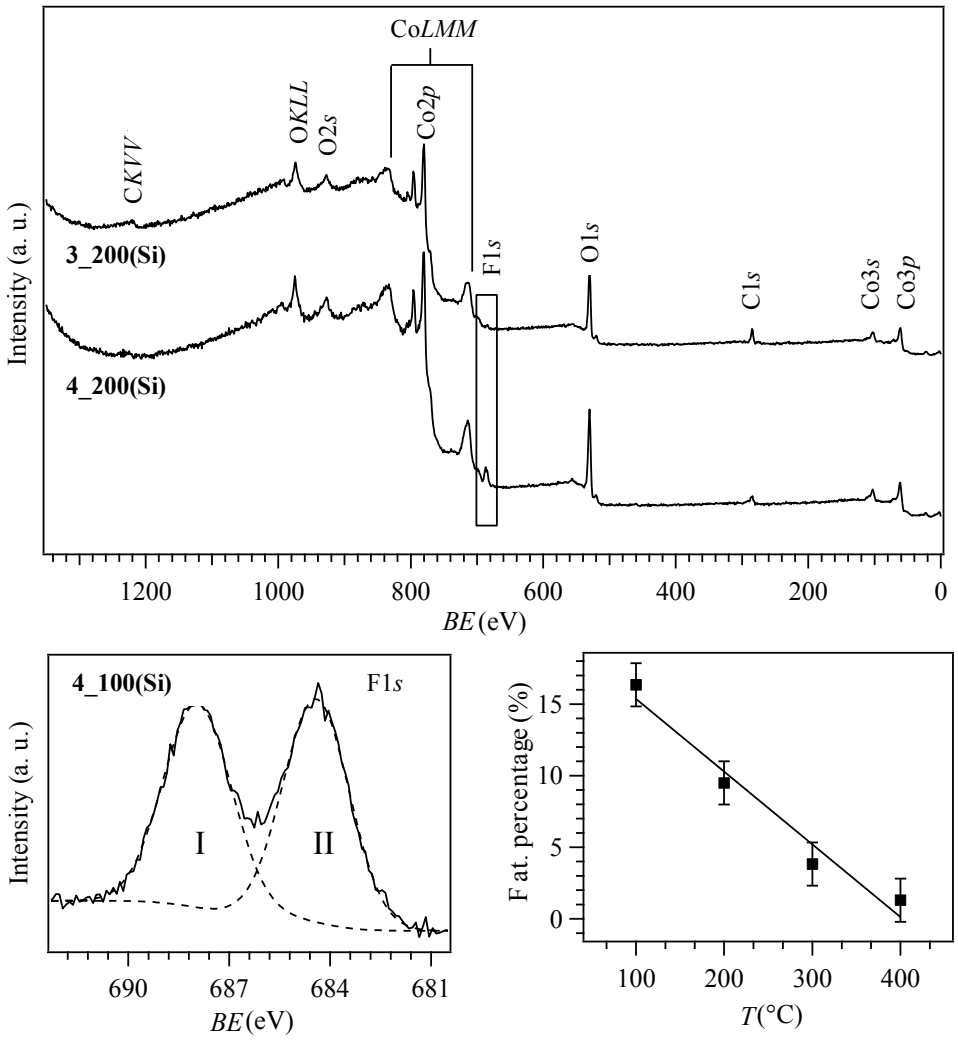

Figure 4.10: Top: Surface XPS wide-scan spectrum for **3_200(Si)** and **4_200(Si)** (**table 4.2**). Bottom: Deconvolution of surface F1*s* peak for **4_100(Si)** (**table 4.2**) and dependence of surface F content on the deposition temperature for Si(100)-supported samples obtained from **4**.

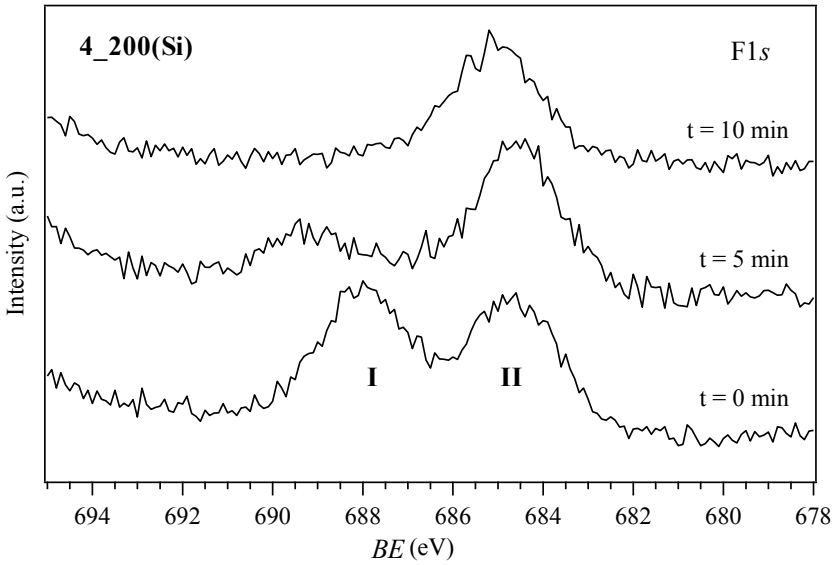

Figure 4.11: Evolution of the F1*s* XPS peak of sample **4_200(Si)** as a function of Ar^+ sputtering time. (See also **figure 4.12** and **table 4.2**.)

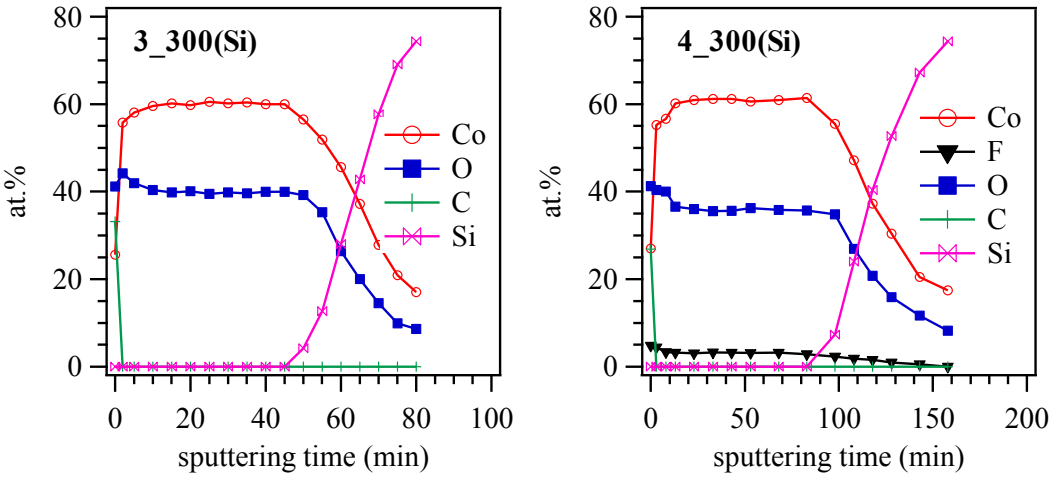

Figure 4.12: (a) XPS depth profiles of undoped (left, **3_300(Si)**) and F-doped (right, **4_300(Si)**) Co_3O_4 specimens. (See also **figures 4.10** and **4.11**.)

Figure 4.13 displays representative in-depth SIMS profiles for Co_3O_4-based systems. In all cases, the higher C yields in the outermost ≈ 5 nm region could be assigned to surface contamination, in agreement with XPS analyses (**figures 4.10** and **4.12**). The overall carbon content in Co_3O_4 deposits was estimated to be around ppm, indicating a clean precursor decomposition into the target material. The similar trend of Co and O ionic yields throughout the deposit thickness was in line with the presence of Co_3O_4 as the only cobalt-containing phase, as already pointed out by GIXRD data (**figures 4.7** and **4.8**).

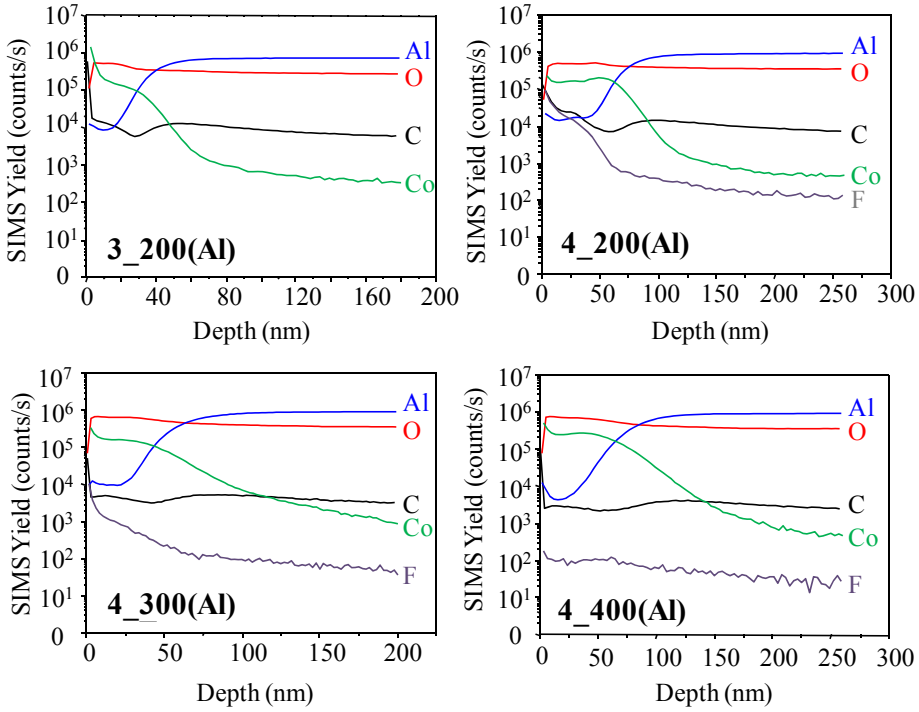

Figure 4.13: SIMS depth profiles for samples **3_200(Al)**, **4_200(Al)**, **4_300(Al)** and **4_400(Al)** (see **figures 4.10** and **4.12**). The corresponding thickness values were 40±6, 79±10, 65±9 and 85±11 nm, respectively.

For all samples obtained from precursor **4**, an important feature was the presence of fluorine throughout the investigated depth. In particular, F-yield followed a trend similar to Co and O signals, indicating a common chemical origin of these species. Such an observation indicated that the use of **4**, bearing F atoms in the hfa ligands, was effective in achieving an homogeneous fluorine-doping of Co_3O_4 nanodeposits. To date, a similar result has been never documented in the literature. Interestingly, an increase in the growth temperature from 200 to 400°C led to a progressive decrease of the mean F-yield (**figure 4.13**), suggesting thus a parallel variation of the corresponding F-doping level.

❖ 4.4.4 Optical properties

In order to elucidate the impact of fluorine doping on the material optical properties, UV-Vis absorption measurements were performed. Band-gap estimation from the Tauc plots of **figure 4.14** yielded values of 1.4 - 1.5 (E_{g1}) and 2.0 - 2.1 (E_{g2}) eV for both undoped and doped systems, indicating a negligible influence of fluorine-doping. [*Barreca-2001*]

A comparison of the left and right figures clearly reveals an increase of the absorption coefficient for F-doped Co_3O_4, an important goal for efficient light harvesting and subsequent generation and exploitation of e^-/h^+ pairs. [*Murphy-2007*, *Zolfagahri-2007*] In fact, since the diffusion length of charge carriers in SC oxides is small (typically a few nm), it is important that photons are largely absorbed in the near-surface layers, so that photo-generated e^- and h^+ species can effectively reach the catalyst surface and participate to the target chemical processes.

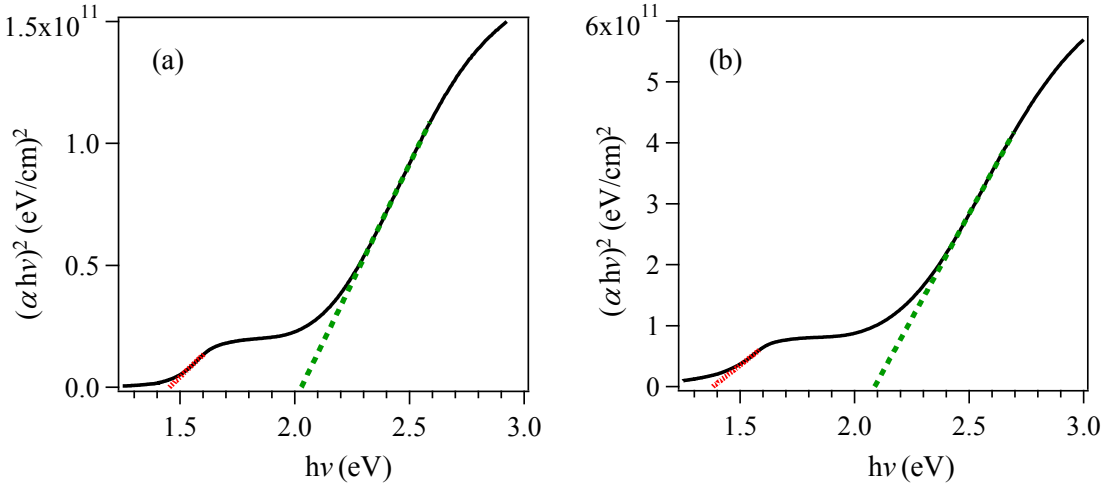

Figure 4.14: Tauc plots of undoped (a) (**3_400(Si)**) and F-doped (b) (**4_400(Si)**) Co_3O_4 specimens, obtained from **3** and **4**, respectively (**table 4.2**).

❖ 4.4.5 Photocatalytic H_2 Production

Photo-assisted experiments were carried out at 20°C in 1:1 water/ethanol mixtures using the discontinuous batch reactor described in the experimental section (**paragraph 8.6.3**). All tests were carried out in the presence of O_2, resulting from an initial air bubbling (15 ml/min for 10 min) in the water/ethanol solution. According to Cargill, [*Cargill-1976*] the initial concentration of oxygen was ≈ 9 mg/l. No appreciable evolution of gaseous products was observed when illumination and photocatalyst were not simultaneously present. Furthermore, only a weak and transient reactivity was revealed on de-aerated water/ethanol solutions, due to the surface formation of inactive CoO, as previously reported for bare Co_3O_4. [*Barreca-2010-F*]

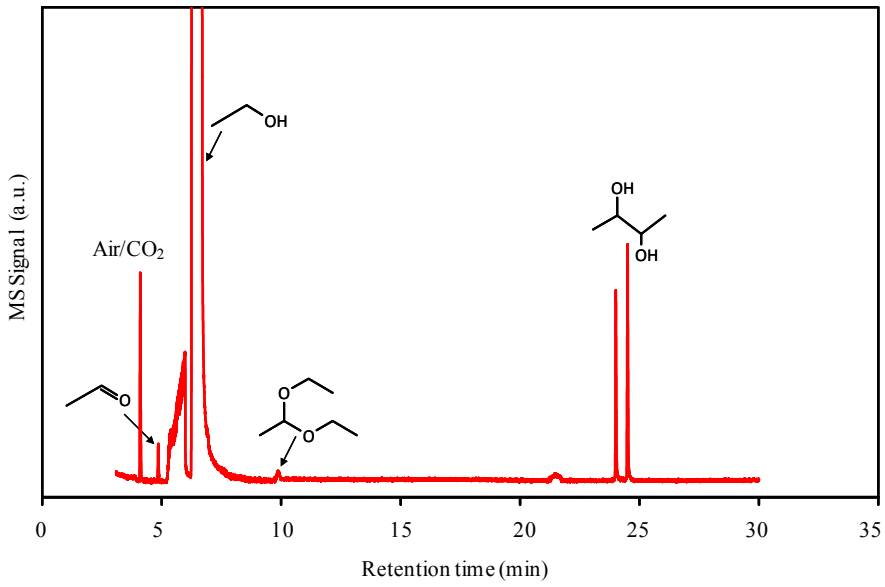

Figure 4.15: GC-MS analysis of a water/ethanol solution after the photocatalytic tests upon near-UV irradiation of F-doped Co_3O_4 (**4_400(Si)** , see **table 4.2**).

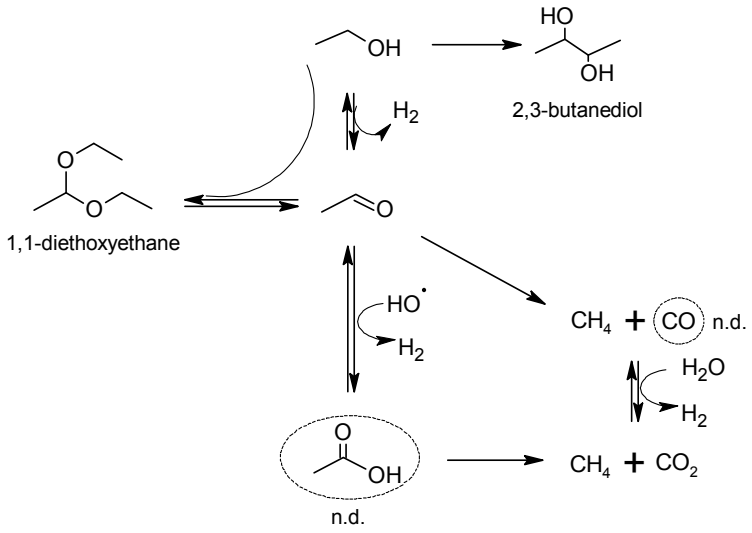

Figure 4.16: Possible reaction pathway for H_2 formation and ethanol by-products. n.d. = not detected.

Ethanol photo-reforming can proceed through ethanol dehydrogenation with the production of equimolar quantities of hydrogen and acetaldehyde. While hydrogen solubility in the liquid phase is low, the concentration of acetaldehyde is indeed remarkable, due to the establishment of a gas-liquid equilibrium. CH_3CHO could decompose to CH_4 and CO, followed by light-promoted water gas shift reaction.

[*Millard-2002*] Although no acetic acid or its esters are detected by GC-MS analysis (**figure 4.15**), their presence cannot be completely ruled out based on the observation of strong adsorption of acetic acid on some oxides. [*Mattsson-2010*] A consequence of the presence of both ethanol, acetaldehyde and surface acidic sites of Co_3O_4 is the formation of 1,1-diethoxyethane (**figure 4.16**).

Under near-UV irradiation and in the presence of O_2 (**figure 4.17**), undoped Co_3O_4 showed an average hydrogen production of ~3 µmol h^{-1} cm^{-2}, whereas in the presence of fluorine the H_2 evolution rate was 5-fold increased. For the latter sample, an estimation of the catalyst amount based on film thickness and Co_3O_4 bulk density led to an activity of 213 000 µmol h^{-1} g^{-1} (45 000 µmol h^{-1} g^{-1} for undoped Co_3O_4). Notably, this is one of the best values ever reported in the literature for SC-based photocatalytic hydrogen generation, also taking into account that no co-catalysts (e.g., Rh, Pd, Pt) were used in this work. [*Chen-2010-B*]

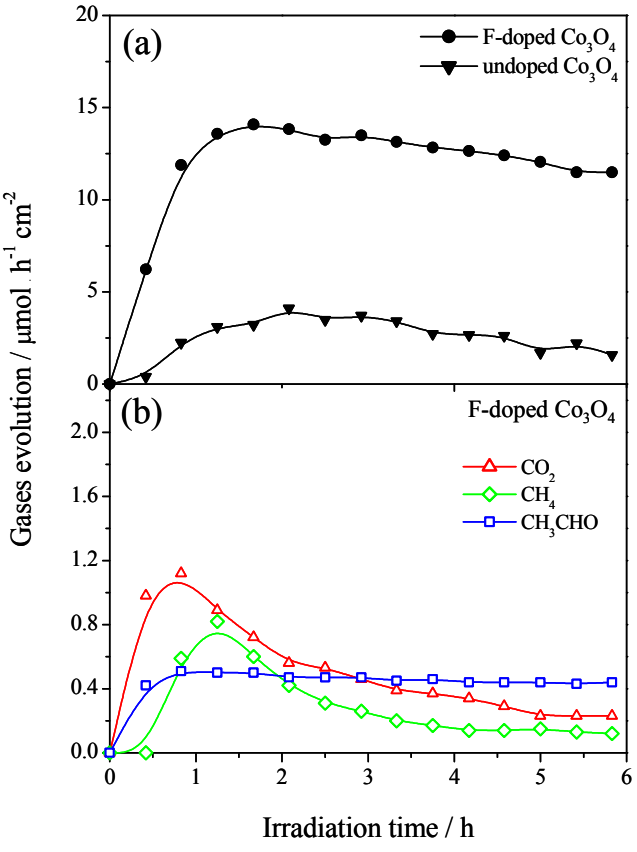

Figure 4.17: (a) H_2 evolution from a water/ethanol solution upon near-UV irradiation of undoped and fluorine-doped Co_3O_4 catalysts **3_400(Si)** and **4_400(Si)** (**table 4.2**). (b) Evolution of C-containing gaseous products for the F-doped sample reported in (a).

The parallel evolution of CO_2 and CH_3CHO, resulting from ethanol oxidation, over F-doped Co_3O_4 (**figure 4.17 (b)**), suggested the occurrence of two parallel reaction pathways, involving adsorbed ethanol and liquid-phase reactions between CH_3CH_2OH and free $OH^{\bullet}$, respectively. [*Chen-1999*] The slight decrease of the H_2 yield and the more evident rate reduction for CO_2 and CH_4 could be mainly associated to CoO formation, attributed, in turn, to a progressive oxygen depletion in the reaction medium. Notably, acetaldehyde evolution was almost constant (**figure 4.17 (b)**), suggesting thus the establishment of a gas-liquid equilibrium ensuring a buffering condition. As regards liquid-phase products (see **figure 4.15**), an interesting effect revealed over F-doped Co_3O_4 is the photo-assisted generation of 2,3-butanediol, a useful precursor for the industrial production of methylethylketone and 1,3-butadiene. [*Syu-2001*, *Xiu-2008*]

Figure 4.17 (a) also displays the presence of an initial induction period (duration *ca.* 75 min) characterized by a progressive increase of hydrogen evolution rate. This phenomenon suggested the occurrence of a light-induced surface activation, followed by the establishment of an equilibrium between the by-products adsorbed on the catalyst surface and in the liquid/gas phase.

The 5-fold increase of hydrogen production yield observed for the fluorinated catalyst can be explained by the synergistic combination of various beneficial phenomena. Specifically, it has been reported that replacement of surface OH groups by fluorine can lead to: (i) an increase of free $OH^{\bullet}$ radicals in the liquid-phase, resulting in a faster ethanol oxidation and in a concomitant enhancement of $H^+ \rightarrow H_2$ reduction; [*Oh-2004*, *Minero-2000*] (ii) inhibition of e^-/h^+ recombination; [*Montoya-2010*] (iii) modification of band-gap/absorption properties and/or tuning of band position. [*Sun-2010*, *Yu-2002*] As already discussed, the presence of fluorine does not significantly change band gap values. As a consequence, the improved performances of F-doped Co_3O_4 could be mainly traced back to (i) and (ii) and, in particular, to the larger availability of $OH^{\bullet}$ radicals. In addition, F-doping could induce a favourable shift of Co_3O_4 flat-band potentials, making photo-generated electrons more available for H_2 production. [*Hu-2009*] Finally, fluorine presence on the catalyst surface might enhance the Lewis acidity of cobalt centers, as also observed for TiO_2-based photocatalysts, beneficially affecting the system activity. [*Chen-2009*, *Sun-2010*, *Zhao-2010*]

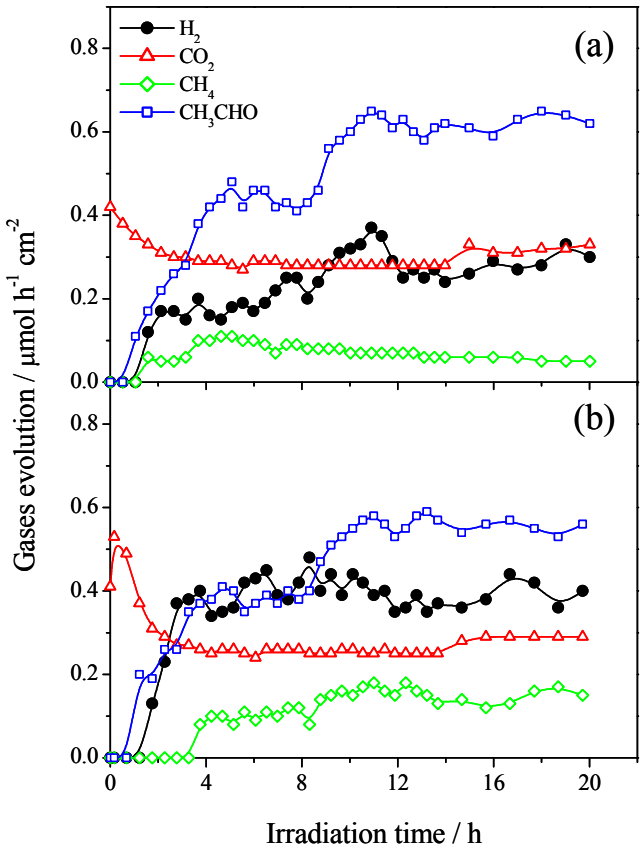

Figure 4.18: Evolution of gases from a water/ethanol solution upon Vis irradiation of an undoped (a) and a fluorine-doped (b) Co_3O_4 samples **3_400(Si)** and **4_400(Si)** (see **table 4.2**).

Differently from the case of UV illumination (**figure 4.17**), the use of less energetic Vis light (**figure 4.18**) enabled to perform photocatalytic experiments up to 20 h of irradiation without significantly altering the water/ethanol molar ratio. In fact, variation in the concentration of sacrificial agent could affect hydrogen production. [*Kondarides-2010*] Under these more sustainable conditions, a lower, though appreciable, hydrogen evolution was still observed (**figure 4.18**). Compared to bare Co_3O_4, the fluorinated specimen showed only a 2-fold increase in H_2 production, along with a slightly more abundant methane evolution, as a result of acetic acid degradation or CO_2 hydrogenation (see **figure 4.16**). The relatively high initial CO_2 evolution is in line with the presence of carbonate traces on the catalyst surface, [*Barreca-2010-D*] that are progressively decomposed under the present reaction conditions. Nevertheless, after 2 h of irradiation, a constant CO_2 production was observed indicating the occurrence of ethanol photo-

reforming involving a C-C bond cleavage. Notably, at variance from the case of UV light, no appreciable decrease of the hydrogen evolution rate was revealed during Vis irradiation, even after 20 hours of reaction. Such an improved system stability was ascribed to several possible contributing effects. First, the lower conversion of ethanol into H_2 and other C-containing by-products with respect to the case of **figure 4.17** implies a lower surface coverage/poisoning by partially oxidized species. In addition, the lower H_2 yield minimizes the reaction between hydrogen and the oxygen present in solution, thus decreasing the formation of inactive CoO surface species. [*Barreca-2010-F*]

❖ 4.4.6 Gas Sensing Properties

Gas sensing of ethanol and acetone using alumina supported (F-)Co_3O_4 specimens (**table 4.2**) was performed by flow-through technique as described in **paragraph 8.6.4**, along with definitions of responses, response and recovery times. Preliminary gas sensing tests yielded almost negligible responses (≤ 0.1) towards CO, CH_4 (10 – 100 ppm) and NO_2 (1 – 5 ppm), in agreement with previous literature reports. [*Aroutiounian-2007*, *Barreca-2010-B*, *Cao-2006*, *Choi-2010*, *Li-2009-A*, *Kärkkänen-2009*, *Wöllenstein-2003*] The main attention in electrical tests was subsequently devoted to systematic studies on two conventional analytes, CH_3CH_2OH and CH_3COCH_3, with particular focus on the interrelations between the chemico-physical properties of the synthesized systems and their functional performances.

Figure 4.19 reports typical dynamic responses to acetone square concentration pulses for undoped and F-doped Co_3O_4 nanodeposits obtained from precursors **3** and **4**, respectively. In both cases, upon contact with the target gas the measured current displayed a decrease proportional to CH_3COCH_3 concentration, without any significant saturation effect. The stability and reversibility of Co_3O_4 sensors was evidenced by the good recovery of the baseline upon purging with synthetic air after each gas pulse. The observed current decrease can be examined in more detail in relation to the possible gas sensing mechanism. As already discussed in the introduction, Co_3O_4 is a *p*-type semiconductor, whose surface is readily covered by chemisorbed oxygen in air: [*Choi-2010*, *Patil-2010*, *Wang-2008-D*]

$$\tfrac{1}{2}\, O_{2\,(g)} \rightleftarrows O^-_{(ads)} + h^+ \qquad \text{(reaction 4.1)}$$

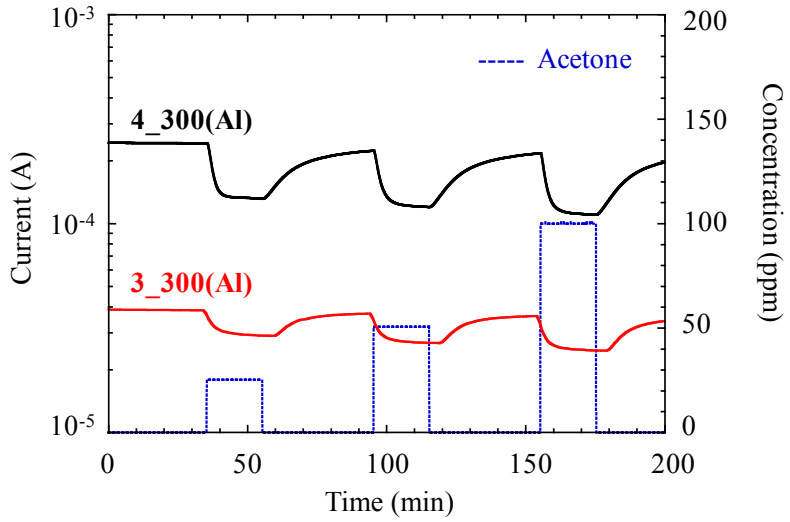

Figure 4.19: Dynamic responses of Co_3O_4 nanodeposits **3_300(Al)** and **4_300(Al)** (see **figure 4.9** and **table 4.2**) to square concentration pulses of acetone, recorded at a fixed working temperature of 200°C.

In the presence of the target analytes, the occurring oxidation processes could be expressed as: [*Park-2009*, *Hübner-2010*, *Kärkkänen-2009*]

$$CH_3CH_2OH + 6O_{(ads)} + 6h^+ \rightleftarrows 2CO_{2\,(g)} + 3H_2O_{(g)} \qquad \text{(reaction 4.2)}$$

$$CH_3COCH_3 + 8O_{(ads)} + 8h^+ \rightleftarrows 3CO_{2\,(g)} + 3H_2O_{(g)} \qquad \text{(reaction 4.3)}$$

The latter reactions involve a decrease in the concentration of holes, the majority carriers, in the surface charge accumulation layer, producing, in turn, a conductance drop-off, [*Barreca-2009-B*, *Hoa-2009*] *i.e.* a decrease of the measured current, as indeed observed. The current variations occurring upon contact with the analytes were more rapid than the recovery of air values at the end of the gas pulses. Typical response and recovery times for acetone detection were estimated to be ≈ 2 and 15 min, respectively. This difference suggested that the processes involving the analytes in-diffusion and their subsequent oxidation according to reactions 4.2 and 4.3 were generally faster than recovery processes involving the counter-diffusion of oxidized gases, [*Choi-2010*] as previously reported for reducing gases over *p*-type gas sensors. [*Barreca-2010-B*]

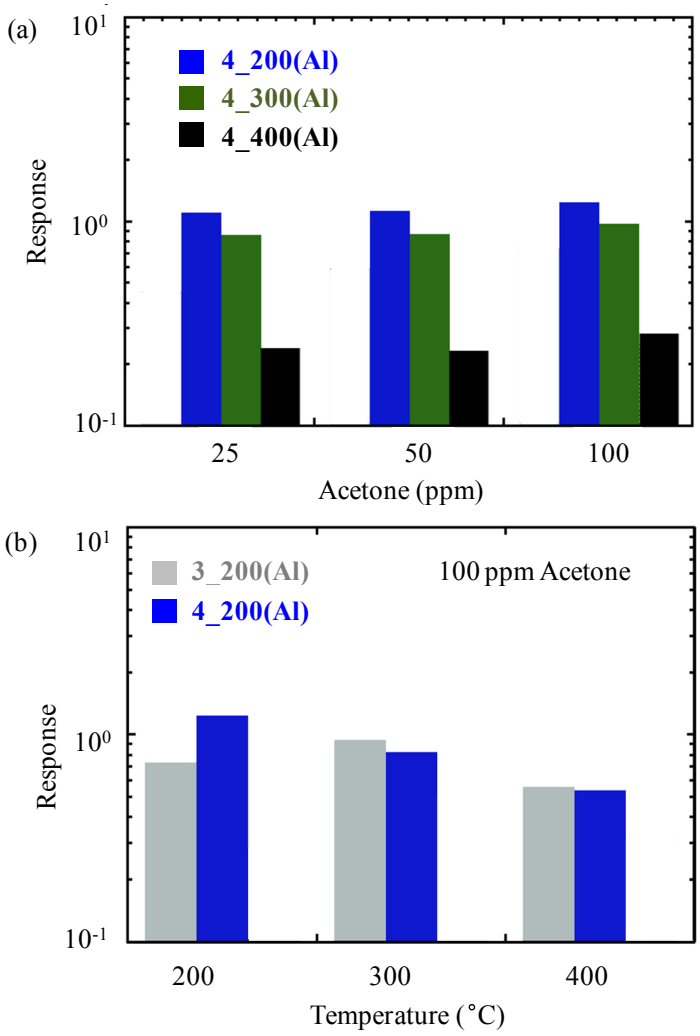

Figure 4.20: (a) Responses of Co_3O_4 nanodeposits obtained from precursor **4** to various acetone concentrations (working temperature = 200°C). (b) Responses of Co_3O_4 sensors deposited at 200°C from **3** and **4** (**4_300(Al) and 4_300(Al)**, see **table 4.2**) to 100 ppm of acetone at different operating temperatures.

Figure 4.19 shows that the current variations experienced by the F-containing specimen (**4_300(Al)**) were systematically higher than for the fluorine-free system deposited at the same temperature, suggesting a beneficial effect of F-doping on the sensing performances. In order to attain a deeper insight into this phenomenon, **figure 4.20 (a)** compares the responses to different acetone concentrations for samples obtained from precursor **4**. As already discussed (see **4.4.3**), the main difference between these materials is the total F-content, which progressively decreased from **4_200(Al)** to **4_400(Al)**. The obtained data demonstrated that, for each analyte concentration, the response followed the

same trend as the fluorine amount in the oxide phase. This behaviour, which is unprecedented for Co_3O_4-based gas sensors, can be explained taking into account that, due to the high fluorine electronegativity, F centres can attract electron density from Co ones, enhancing, in turn, the Lewis acidity (*i.e.*, the Co_3O_4 *p*-type character) and further promoting the corresponding catalytic activity. [*Zhao-2010*] In addition, the presence of fluorine might be effective in saturating dangling bonds at the Co_3O_4 surface, whose presence is detrimental for trapping of the free carriers and consequent lowering of the system performances. [*Liu-2010-A*, *Xu-2006-B*] In other words, F-introduction can prevent undesired free carrier annihilation, increasing the concentration of h^+ species involved in reactions 4.2 and 4.3, thus producing enhanced responses towards the analyte gases.

Figure 4.20 (b) illustrates the influence of the working temperature on the responses to acetone of undoped (**3_200(Al)**) and F-doped (**4_200(Al)**) Co_3O_4 sensors. Whereas for the former the best response was registered at 300°C, for the latter specimen the measured values decrease monotonically in the range 200 - 400°C, and the maximum value was obtained at 200°C. This behaviour indicated a change in the sensing pattern attributable to the effective catalytic action of fluorine centres, paving the way to efficient gas detection at lower operating temperatures. The downward temperature shift is of great interest in order to decrease the energy consumption and enhance the suitability of the sensor for specific technological applications. [*Park-2009*] Despite F-doping revealed to be the main factor governing the sensing intensity, a careful inspection of **figure 4.20** evidenced comparable responses at 300 and 400°C, irrespective of fluorine presence. This observation suggested that other factors, like the effective surface area or grain boundary and connectivity, could influence the system behaviour, and that the actual sensing properties are the outcome of a concurrence of various factors. Indeed, a thorough insight into the problem requires more detailed investigations.

The favourable influence of F-doping on the system performances was also confirmed by examining response data pertaining to ethanol detection, as displayed in **figure 4.21 (a)**. As a matter of fact, the responses for the **4_200(Al)** specimen were systematically higher than those of the **4_400(Al)** one, indicating that the higher fluorine amount of the former had a beneficial effect even in the detection of this analyte. At variance with a recent report on sensors based on Co_3O_4 hollow nanospheres, [*Park-2009*] no marked saturation

was present for these samples. This effect could be better appreciated by an inspection of **figure 4.21 (b)**, clearly showing a linear behaviour in the log–log scale throughout the whole investigated concentration range. Such a result can be traced back to the availability of a sufficiently high number of sensing sites capable of interacting with the target gases. [*Patil-2010*] Assuming the validity of the linear relation even at lower gas concentrations, the detection limit was estimated for a fixed response of 0.5, yielding a value of 3 ppm. This particular value is lower than the detection limit of commercial breath analyzers (200 ppm), [*Barreca-2007-D*, *Cao-2006*, *Li-2009-C*] confirming thus the validity and impact of the present sensors in view of large-scale practical applications.

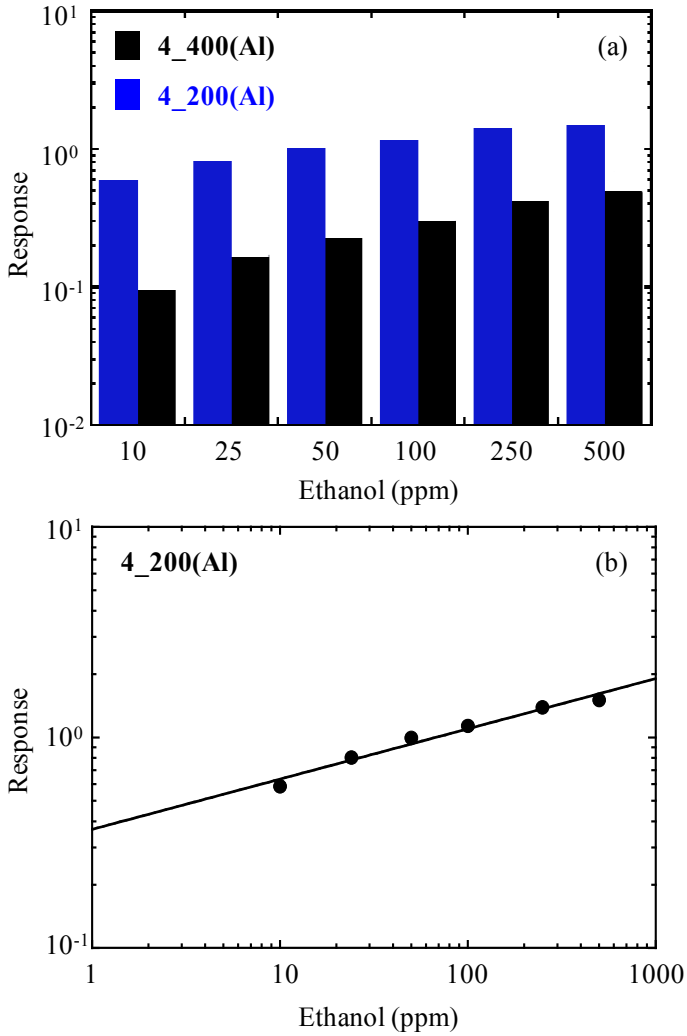

Figure 4.21: (a) Gas sensing responses of **4_200(Al)** and **4_400(Al)** (see **table 4.2**) as a function of ethanol concentration (working temperature = 200°C). (b) Dependence of response values for sample **4_200(Al)** on ethanol concentration and corresponding fit.

Overall, the response values for the detection of acetone and ethanol reported in this work were comparable to those of other oxide-based systems exhibiting a *p*-type behaviour, such as TiO_2/NiO, CuO/TiO_2, Au/CuO/TiO_2, Cu_xO (x=1,2) and Au/Co_3O_4. [*Barreca-2009-B*, *Barreca-2010-B* , *Barreca-2011-A*, *Wisitsoraaat-2009*]

Although the sensing mechanism of the present systems is different with respect to the case of *n*-type semiconductors, the effective sensor resistance is also determined by the system nano-organization, and, in particular, by the active surface area and the dimensions of the obtained nanostructures. [*Cao-2006*, *Cong-2009*, *Choi-2010*, *Li-2009-A*] In fact, nanoparticles as small as ≈ 10 - 30 nm tend to become completely depleted, producing thus an enhancement of sensing performances. [*Li-2010*] Such features, that, in turn, result in a higher defect density, giving thus an enhanced interaction of the analytes with the sensing surface, can be considered reponsible for the superior responses with respect to those previously reported for various kinds of Co_3O_4 materials. [*Cao-2006*, *Li-2005*, *Park-2009*, *Patil-2010*, *Li-2009-C*]

❖ 4.5 Conclusions

In this chapter, it was demonstrated, that the use of PECVD enabled the low-temperature growth (100 – 400°C) of pure and fluorine-doped Co_3O_4 based materials, whose physico-chemical features and hence functional properties could be tailored as a function of growth temperature and precursor.

Highly pure and oriented Co_3O_4 thin films on MgO(100) and $MgAl_2O_4$(100) single crystals were obtained from [$Co(dpm)_2$] (**3**) at temperatures as low as 100°C (**figures 4.1** and **4.2**). Despite the growth of highly oriented films usually requires higher deposition temperatures than 100°C (see **4.2**), it is likely that an oriented/epitaxial growth was further promoted by continuous plasma bombardment, providing an additional energy supply and promoting texturing effects, hardly attainable by conventional approaches. [*Dittmar-2004*, *Shalini-2001*, *Mane-2002*]

Based on these results, Co_3O_4-based nanomaterials were grown by this PECVD procedure on Si(100) and polycrystalline Al_2O_3 substrates in view of their applications in photocatalytic H_2 generation and gas sensing. Whereas the use of precursor **3** resulted in

pure Co_3O_4 deposits, the use of [Co(hfa)$_2$·TMEDA] (**4**) enabled an *in-situ* fluorine-doping of the nanosystems, which has never been reported for *p*-type Co_3O_4 before. The fluorine-incorporation level was controlled by variation of substrate temperature (see **4.4.3**)

F-doping of the Si(100) supported Co_3O_4 deposits resulted in a remarkable performance improvement in the photocatalytic production of H_2. Upon near-UV irradiation (**figure 4.17**) of F-doped Co_3O_4, a 5-fold hydrogen yield increase was evidenced with respect to the corresponding undoped oxide. Notably, the obtained yields of 213 000 μmol h^{-1} g^{-1} and 45 000 μmol h^{-1} g^{-1} for F-doped and pure Co_3O_4, respectively, were among the best ever reported for similar semiconductor based photocatalytic processes, even upon comparison with metal-functionalized catalysts. In the case of Vis light (**figure 4.18**), a lower activity in H_2 evolution, was observed, but the appreciable time stability of the response candidates this material as an attractive photocatalyst for the sustainable generation of hydrogen activated by sunlight.

In the detection of acetone and ethanol by Al_2O_3 supported (F-)Co_3O_4 materials, F-doping resulted in higher responses, enhanced reversibility and lowered working temperature (200°C) (**figures 4.20** and **4.21**), attractive features in view of technological applications. The response values reported in this work were comparable to those of other *p*-type oxide-based systems. Improvements achieved by use of F-Co_3O_4 were the absence of saturation effects, observed for Co_3O_4 systems reported in literature, and the detection limit of 3 ppm in the sensing of ethanol, being considerably lower than the one for commercial breath analyzers (200 ppm), confirming thus the validity and impact of the present sensors in view of large-scale practical applications.

Overall, the presented results add novel information to the research for improved functional *p*-type materials. Key open issues that still must be properly addressed concern a deeper understanding of the electronic and chemical effects induced by F presence. It is also worthwhile noting that the synthetic strategy reported herein for the preparation of F-doped Co_3O_4 can be regarded as a general and versatile route for the tailored anion doping of oxide SC nanosystems.

5. Ag/ZnO

❖ 5.1 Abstract

This chapter deals with the growth, characterization and functional validation of Ag/ZnO nanocomposites by a plasma-assisted approach.[1] Basing on the studies on single-component ZnO and Ag nanosystems, [*Barreca-2005*, *Bekermann-2010-B*] an innovative plasma-assisted route to synthesize supported Ag/ZnO nanocomposites with tailored features is proposed, consisting of two subsequent steps: (i) growth of columnar ZnO arrays by PECVD (see **3.4.1**); (ii) deposition of Ag NPs by RF-sputtering, tuning the overall metal amount by variation of the sputtering time (**paragraph 5.3.1**). The morphological organization, structure and composition of the resulting composites, both as-prepared and after annealing in air, were investigated by GIXRD, FE-SEM, TEM, (**paragraph 5.3.2**) EDXS and XPS (**paragraph 5.3.3**). The silver NP density, size and dispersion was dependent on the overall Ag amount, i.e. sputtering time, and annealing.
For the first time, the above systems have been used as catalysts in the production of hydrogen by photo-reforming of alcoholic solutions, yielding a stable H_2 evolution (~ 0.3 - 4 $\mu mol^{-1}\ h^{-1}\ cm^{-2}$) under both UV-Vis and simulated solar radiation (**paragraph 5.3.4**). The dependence of the photocatalytic performances on the silver amount, distribution and oxidation state is discussed. In addition, the sensing performances of Ag/ZnO nanocomposites in hydrogen detection were tested (**paragraph 5.3.5**), yielding improved response values with respect to pure ZnO (see **3.4.6**) and Ag/ZnO systems reported in literature.

❖ 5.2 Introduction

Since Ag/ZnO features are strongly dependent on size, shape, and mutual distribution of the components, the development of controllable synthetic strategies is highly demanded to tune their functional performances. Up to date, Ag/ZnO nanosystems have been

[1] [*Simon-2011*] Q. Simon, D. Barreca, D. Bekermann, A. Gasparotto, C. Maccato, E. Comini, V. Gombac, P. Fornasiero, O.I. Lebedev, S. Turner, A. Devi, R.A. Fischer, G. Van Tendeloo, Int. J. Hydrog. Energ. 36 (2011) 15527.

prepared both as powders and supported materials by liquid, [*Lin-2009*, *Roy-2004*] vapor, [*Prokes-2007*, *Tan-2008*] and hybrid liquid-vapor phase routes. [*Deng-2009*] Nevertheless, in spite of various studies, a thorough understanding of Ag/ZnO interactions is still an open question, especially due to the high reactivity of silver NPs towards oxidation. [*Kibis-2010*, *Qi-2010*] Furthermore, beyond the use of powdered materials, [*Arabatzis-2003*, *Lin-2009*] a current challenge concerns the development of organized Ag/ZnO assemblies onto suitable substrates, enabling their direct integration into functional devices. As a consequence, in the present chapter, this issue has been addressed by developing Ag/ZnO nanomaterials on different substrates to be applied for the photocatalytic generation and sensing of hydrogen.

The importance of hydrogen as an appealing energy vector, due to its high efficiency and environment-friendly combustion, is nowadays well recognized and documented. [*Alenzi-2010*, *Miwa-2010*, *Muradov-2008*, *Wu-2008-B*, *Zheng-2010-B*] Nevertheless, in spite of several research activities in this field, the large-scale production and detection of H_2, an odorless, colorless and flammable gas, remain challenging issues and require the development of suitable materials acting as multifunctional platforms for the sustainable generation and sensing of hydrogen. Among the possible candidates, ZnO has been the object of several studies regarding photocatalysis and gas sensing utilization (see **paragraphs 3.4.5 and 3.4.6**). [*Özgür-2010*] Its functional properties for such applications can be improved by the synergistic combination of nanostructured ZnO with metallic NPs, which, beside their inherent catalytic activity, promote an enhancement of charge carrier separation due to the formation of a Schottky barrier at the metal/oxide interface. [*Barreca-2011-E*, *Fu-2007-A*, *Zeng-2008*]

Among the different metals, silver has demonstrated a great potential to improve ZnO antibacterial/pollutant degradation activity [*Height-2006Lin-2009*, *Lu-2008*, *Tan-2008*,] and optical properties, [*Deng-2009*, *Irimpan-2008*, *Roy-2004*, *Prokes-2007*, *Zhang-2007*] whereas H_2 production from Ag/ZnO nanomaterials is still rather unexplored. In particular, whereas few reports devoted to H_2 production by methanol reforming over Ag/ZnO catalysts are available, [*Mo-2004*, *Pérez-Hernández-2010*] photo-induced reforming of aqueous solutions to yield H_2, a promising route for its clean and sustainable generation, [*Yao-2011*] has never been attempted on such systems.

As regards gas sensing applications, the dispersion of metallic aggregates into the oxide matrix can advantageously modify the surface reactivity of the SC phase, yielding improved performances. [*Basu-2009*, *Comini-2009-B*] Yet, in spite of numerous studies devoted to the impact of Au, Pt and Pd NPs on ZnO sensing performances, [*Hongsith-2008*, *Hsueh-2007-C*, *Rout-2006*] only few reports have been focused on Ag/ZnO systems, [*Xiang-2010*, *Zong-2010*] and only one paper on sensing by Ag/ZnO composites is available in the literature. [*Xiang-2010*]

❖ 5.3 PECVD and Sputtering of Ag/ZnO on Si(100) and Polycrystalline Al_2O_3

❖ 5.3.1 Deposition Procedure

Columnar ZnO arrays were grown by PECVD using precursor $[Zn\{[(CH_2)_3OCH_3]NC(CH_3)=C(H)C(CH_3)=O\}_2]$ (**2**), as described in **3.4.1**. The precursor was vaporised at 150°C and transported into the reaction chamber by a 60 sccm Ar flow. The temperature of the lines was maintained at 170°C. Additional Ar (15 sccm) and O_2 (20 sccm) flows were introduced into the reactor. All ZnO growth processes were carried out for 1 h at 300°C, at a total pressure of 1 mbar, and using a RF-power of 20 W. Depositions were performed onto Si(100) substrates (MEMC®, Merano, Italy; dimensions = 2 cm × 1 cm × 1 mm), for hydrogen production, and polycrystalline Al_2O_3, dimensions = 3 mm × 3 mm × 250 μm) for sensing application. The substrates were suitably pre-cleaned using procedures described in **paragraph 8.3.3**.

Subsequently, Ag NPs were deposited on the obtained ZnO arrays by RF-sputtering from Ar plasmas, using a RF-power of 5 W and a total pressure of 0.3 mbar. The process was performed at a temperature as low as 60°C to prevent undesired modifications of the pristine ZnO matrices. Different sputtering times were used to vary the overall silver amount in the resulting composites (**table 5.1**). The effect of *ex-situ* thermal treatment in air at 400°C for 1 h was investigated for silicon supported samples. The deposits on alumina were annealed in air (400°C, 1 h), in order to stabilize the system for gas sensing.

Table 5.1: Sample labeling for as-prepared and thermally annealed Ag/ZnO on Si(100) and Al_2O_3[2] as a function of Ag sputtering time. All other processing parameters for ZnO growth (p = 1 mbar, P = 20 W, t = 60 min, substrate temperature T = 300°C and T_{vap} (precursor **2**) = 150°C) and Ag sputtering (p = 0.3 mbar, P = 5 W, T = 60°C) were kept constant.

Ag sputtering time (min)	Sample on Si(100), as-prepared (**A**)	Sample on Si(100), Annealed (**T**)	Sample on Al_2O_3, annealed
0	**ZnAg0_A(Si)**	**ZnAg0_T(Si)**	
10	**ZnAg10_A(Si)**	**ZnAg10_T(Si)**	**ZnAg10_T(Al)**[2]
30	**ZnAg30_A(Si)**	**ZnAg30_T(Si)**	
90	**ZnAg90_A(Si)**	**ZnAg90_T(Si)**	
150	**ZnAg150_A(Si)**	**ZnAg150_T(Si)**	

❖ 5.3.2 Morphology and Structure

Cross-section FE-SEM investigations (**figure 5.2**) showed that the initial ZnO columnar morphology (compare **figure 5.1**) did not undergo significant alteration upon silver deposition, apart from a systematic reduction of the column length from 180 to 120 nm. This effect could be ascribed to the occurrence of ablation phenomena, competitive with deposition ones in the used plasmas. [*Barreca-2011-F*]

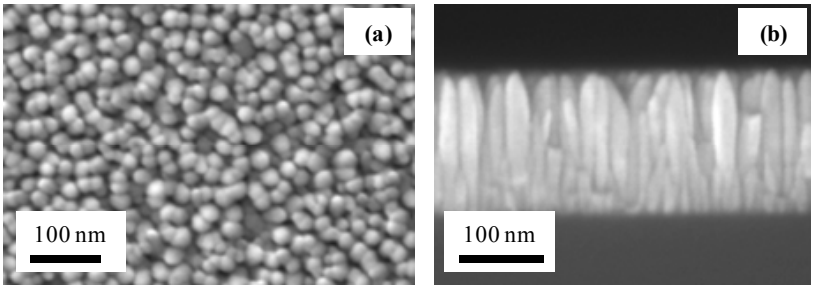

Figure 5.1: Plane-view (a) and cross-section (b) FE-SEM micrographs of **ZnAg0_A(Si)** (see **table 5.1**).

[2] Note that only one alumina based sample (**ZnAg10_T(Al)**), used to present representative gas sensing data, is considered in the following paragraphs. Discussions on the effects of Ag sputtering time on morphology, structure, overall Ag loading and dispersion are mainly focused on silicon supported samples due to the similarity of results of Si(100) and Al_2O_3 based Ag/ZnO composites, avoiding thus redundancy.

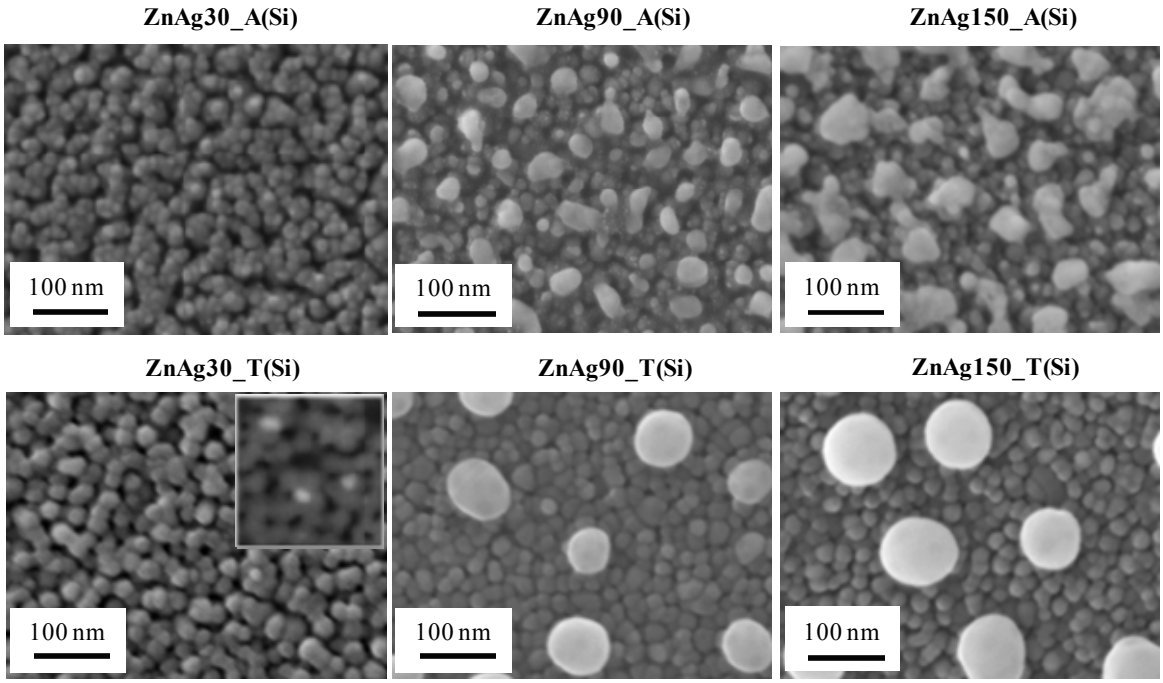

Figure 5.2: Plane-view FE-SEM micrographs of as-prepared and annealed Ag/ZnO nanocomposites on Si(100) with Ag sputtering times t = 30 - 150 min (**table 5.1**). The presence of Ag particles for sample **ZnAg30_T(Si)** is highlighted by a backscattered electron image (same scale bar) in the inset.

Table 5.2: Silver particle sizes for as-prepared and annealed Ag/ZnO nanocomposites on Si(100) with Ag sputtering times t = 30 - 150 min (see **figure 5.2** and **table 5.1**). Surface silver molar fractions ($\boldsymbol{x}_{Ag}$ = [Ag/(Ag+Zn+O)]×100) were determined from XPS analyses.

Sample name	Ag particle size (nm)	$\boldsymbol{x}_{Ag}$
AgZn30_A(Si)	10	15.5
AgZn90_A(Si)	35	32.6
AgZn150_A(Si)	60	44.6
AgZn30_T(Si)	10	1.6
AgZn90_T(Si)	80	8.3
AgZn150_T(Si)	100	14.7

Plane-view images of as-prepared Ag/ZnO nanosystems (**figure 5.2**) clearly evidenced the presence of Ag particles localized on the top of the columns, with morphological features directly dependent on the adopted sputtering time. The mean Ag NP size progressively increased on going from sample **ZnAg30_A(Si)** (30 min Ag sputtering) to **ZnAg150_A(Si)** (150 min Ag sputtering), with a concomitant shape evolution from spherical to island-like aggregates. Upon annealing (**figure 5.2**), the formation of large spherical Ag aggregates took place, due to thermally-induced agglomeration of the pristine NPs (see also **table 5.2**), a phenomenon particularly evident for sputtering times ≥ 90 min.

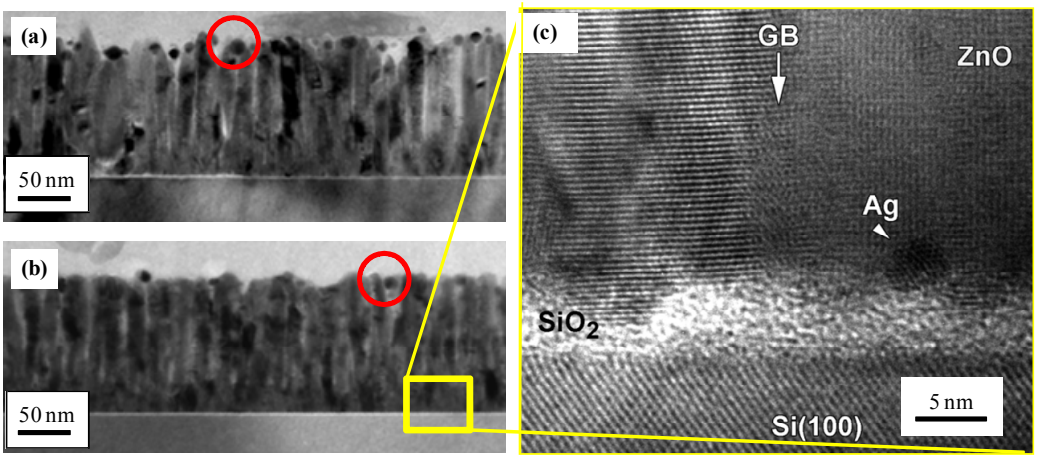

Figure 5.3: Cross-section bright field TEM images of nanocomposites **ZnAg30_A(Si)** (a) and **ZnAg30_T(Si)** (b) (see **table 5.1** and **figures 5.1** and **5.2**). Red circles mark the location of Ag NPs. (c) HR-TEM of the deposit/Si(100) interface region highlighted by the yellow rectangle in (b). Note that Ag NPs are present even at the interface with the substrate, where an amorphous SiO_2 layer is also detected.

To obtain a deeper insight into the system nanostructure, with particular regard to the spatial distribution of the Ag NPs inside the ZnO matrix, TEM analyses were carried out. Representative cross-section TEM images of specimens **ZnAg30_A(Si)** and **ZnAg30_T(Si)** are shown in **figures 5.3 (a)** and **(b)**, respectively. At variance with powdered ZnO (*zincite*), *c*-oriented zinc oxide systems with (001) preferential orientation were obtained (see also XRD, **figure 5.5**), as often observed for ZnO nanostructures. [*Deng-2009*, *Lin-2009*, *Lu-2008*, *Pérez-Hernández-2010*, *Wang-2004-B*, *Xiang-2010*] As already discussed in **paragraphs 3.3.2** and **3.4.2**, in the present case, this [001] growth,

leading to columns perpendicular to the substrate surface, was further enhanced by the sheath electric field. [*Bekermann-2010-B*, *Romero-Gómez-2010*] In line with FE-SEM analyses, sample **ZnAg30_A(Si)** showed small silver particles mainly dispersed into the outermost ZnO region (**figure 5.3 (a)**). Conversely, for specimen **ZnAg30_T(Si)** (**figure 5.3 (b)**) only a few Ag particles were present at the surface, in agreement with the Ag in-depth distribution evidenced by EDXS (**paragraph 5.3.3**, **figure 5.7**). Accordingly, HR-TEM images of sample **ZnAg30_T(Si)** revealed the presence of small Ag NPs diffused through the grain boundaries (GB) of the ZnO deposit, down to the interface with the Si substrate (**figure 5.3 (c)**). Such results unambiguously confirm the in-depth penetration of silver along the whole ZnO deposit, favoured by the porous ZnO morphology and the typical infiltration power of RF-sputtering, and further promoted by thermal treatment in air.

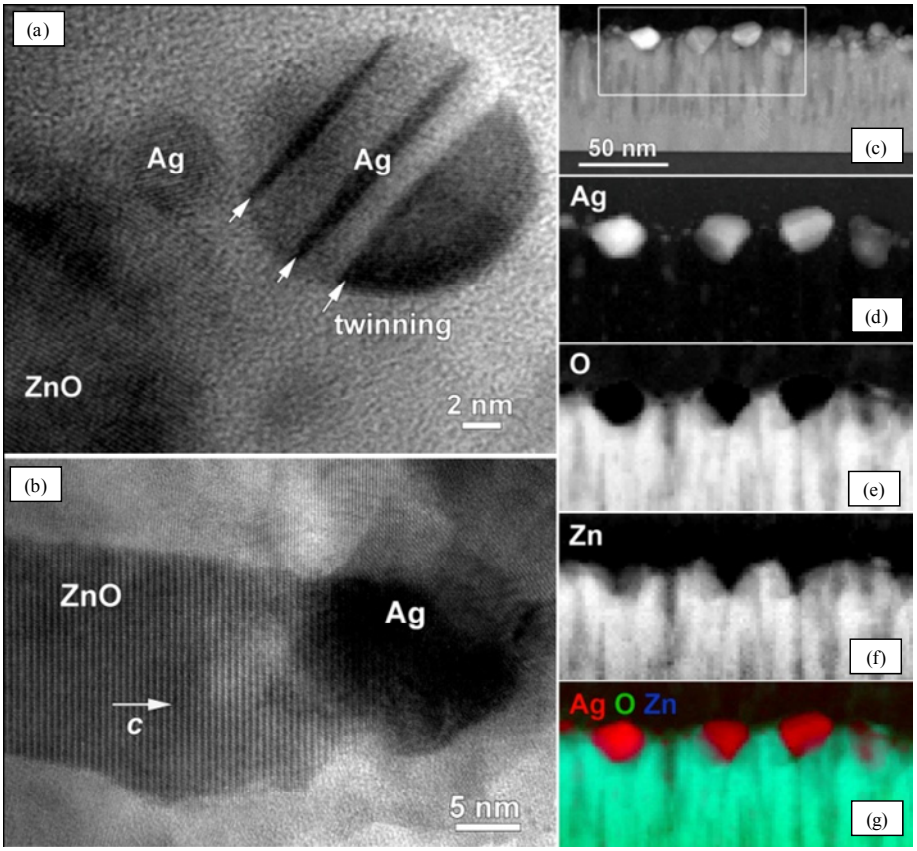

Figure 5.4: Cross-section TEM observations of specimen **ZnAg90_T(Si)** (see **table 5.1** and **figure 5.2**): (a - b) HR-TEM micrographs; (c) HAADF-STEM image and corresponding elemental maps (d - g) extracted from STEM-EELS experiments. Color codes: Ag = red, O = green, Zn = blue.

Figure 5.4 displays typical HR-TEM **(a - b)** and high angle annular dark field (HAADF)-STEM **(c)** images for specimen **ZnAg90_T(Si)**. Beside the large silver aggregates evidenced also by FE-SEM and EDXS (compare **figures 5.2** and **5.7**), even smaller Ag NPs, with typical diameters between 5 and 20 nm, could be observed. Low-sized Ag NPs were single crystalline and defect free, while larger ones showed the presence of {111}-type twins (marked by white arrows in **figure 5.4 (a)**). **Figure 5.4 (b)** displays a ZnO column grown along the *c*-axis in contact with a silver NP. Spatially resolved EELS measurements were also performed on the region highlighted by the box in **figure 5.4 (c)**. As revealed by **figure 5.4 (d – g)**, elemental maps confirmed the presence of large silver particles segregated in the outermost ZnO region.

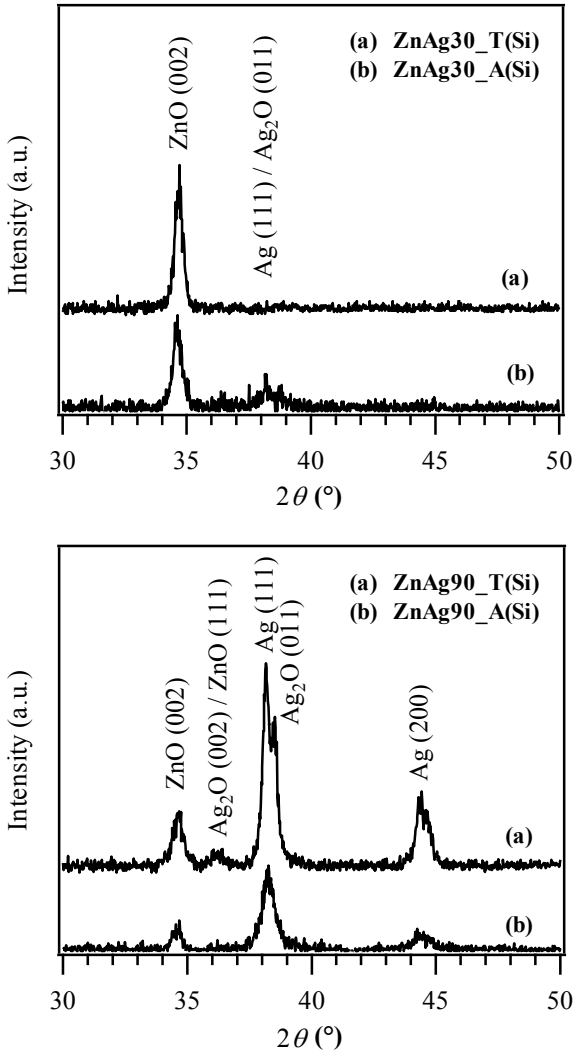

Figure 5.5: GIXRD patterns of representative Ag/ZnO nanocomposites on Si(100) before and after thermal treatment (Ag sputtering times t = 30 and 90 min, see **table 5.1**).

Representative GIXRD patterns of Ag/ZnO systems are presented in **figure 5.5**. Although no significant variation of ZnO peak positions were observed with respect to the bare oxide nanosystems (compare **paragraph 3.3.2**), the system structural features were influenced by both the annealing process and the Ag deposition. In fact, the appearance of additional diffraction peaks related to the presence of metallic silver [*JCPDS-D*] or silver(I) oxide [*JCPDS-E*] took place, whose intensity increased with Ag sputtering time (compare patterns for **ZnAg30_A(Si)** and **ZnAg90_A(Si)**). On going from sample **ZnAg30_A(Si)** to **ZnAg30_T(Si)**, the peak at 2θ = 38.1° ascribed to silver-containing phases disappeared, in line with the enhanced silver particle dispersion into the ZnO matrix evidenced by EDXS and TEM (compare **figures 5.3** and **5.7**) . Conversely, an appreciable intensity increase of silver-related signals was detected upon passing from specimen **ZnAg90_A(Si)** to **ZnAg90_T(Si)**, due to the previously discussed Ag segregation in the outermost system regions (**figure 5.4 (d – g)**). Furthermore, the appearance of peaks attributed to hexagonal Ag_2O [*JCPDS-E*] highlighted the occurrence of silver oxidation during thermal treatment. At variance with the results reported by Ramesh *et al.* for annealed Ag_2O films, [*Ramesh-2007*] no evidence of the Ag_2O cubic phase was obtained.

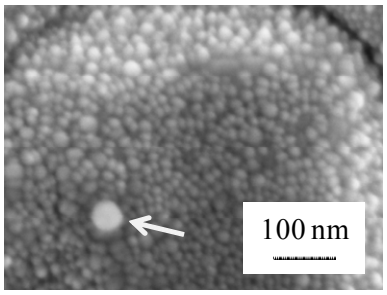

Figure 5.6: Plane-view FE-SEM micrograph of an annealed Ag/ZnO deposited on polycrystalline Al_2O_3 sample (**ZnAg10_T(Al)**, see **table 5.1**). A silver particle is highlighted by an arrow.

GIXRD analyses (not shown) of alumina-supported Ag/ZnO nanocomposites revealed the presence of hexagonal ZnO, with peaks of silver-containing phases detectable only for sputtering times above 90 min. At variance with Si(100) supported specimens, the system morphology was characterized by an urchin-like structure (**figure 5.6**, see also **paragraph 3.4.2.4**), [*Barreca-2010-C*] produced by a uniform conformal coverage of

globular Al_2O_3 grains with ZnO nanoparticles (mean lateral size = 20nm). In addition, the presence of silver NPs on the oxide matrix could be observed (**figure 5.6**).

❖ 5.3.3 Composition

Since all Ag/ZnO specimens revealed very similar compositional information, irrespective of the nature of the underlying substrate, the results discussed below are based on Ag/ZnO/Si(100) samples as representative examples.

The system composition of Ag/ZnO/Si(100) specimens as a function of the processing conditions was investigated by EDXS along the deposit cross-sections (**figure 5.7**). For all the analyzed samples, the intensities of O and Zn X-ray signals were always overlapped throughout the sample depth, in line with the uniform and homogeneous formation of zinc(II) oxide. In as-prepared samples, silver was not only present on the top of ZnO columns, but also in the sub-surface layers. Same was observed also for **ZnAg150_A(Si)**, characterized by the highest silver loading, though in this case the strong intensity of the Ag signal in the proximity of the surface suggested a metal segregation in this region.

Upon annealing, two different behaviors depending on the silver content were observed for Ag redistribution. For **ZnAg30_T(Si)**, the dominant phenomenon was an in-depth silver diffusion into ZnO. For **ZnAg90_T(Si)** and **ZnAg150_T(Si)**, characterized by a progressively higher silver content, the amount of silver diffused into the inner system layer underwent an appreciable increase. In addition, excess Ag segregated in the outermost region, forming spherical particles on the sample surface. A similar behavior has also been observed upon annealing of Ag-implanted ZnO samples. [*Rita-2003*, *Sakaguchi-2010*]

The surface chemical composition as a function of silver content was investigated by photoelectron spectroscopy. Irrespective of Ag sputtering time and annealing process, Zn Auger parameter was 2010.0 eV, the value expected for ZnO. [*Barreca-2007-C*] Surface quantitative data (**table 5.2**) showed that Ag content underwent a remarkable decrease after thermal treatment due to the concurrence of two different phenomena: (i) for **ZnAg30_T**, silver partially diffused into the inner ZnO layers; (ii) for **ZnAg90_T(Si)** and

150_T(Si) specimens, the re-organization of smaller Ag NPs into larger ones led to a higher ZnO surface exposed to XPS probing.

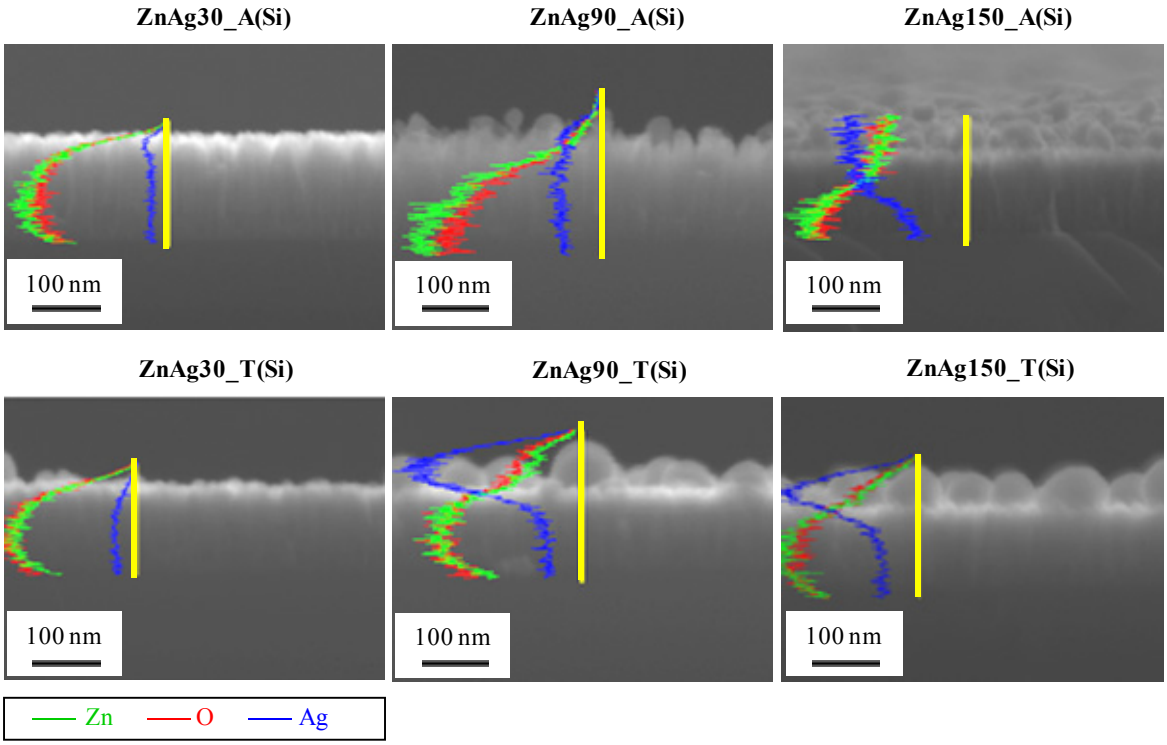

Figure 5.7: Cross-section EDXS line-scans for as-prepared and annealed Ag/ZnO nanocomposites on Si(100) with Ag sputtering times t = 30 - 150 min (see **table 5.1**, compare also **table 5.2** and **figures 5.1, 5.3** and **5.4**). The red, green and blue lines correspond to O, Zn, and Ag signals, respectively.

Surface XPS Ag3*d* and XE-AES Ag*MVV* spectra of a representative Ag/ZnO nanocomposite are displayed in **figure 5.8 (a)**. For all the investigated specimens, the Ag3$d_{5/2}$ photopeak was centered at a mean *BE* = 368.0 eV. Due to the very close *BE* values for Ag(0) and Ag(I) species, [*Barreca-2005*, *Kibis-2010*, *Liu-2011*, *Michaelides-2005*, *Sen-2005*, *Waterhouse-2001*] silver Auger parameters were evaluated to obtain a finger print of silver oxidation state. [*Waterhouse-2001*] For as-prepared samples, the obtained values [α_1 (Ag) = 724.3 eV; α_2 (Ag) = 718.8 eV] revealed the presence of Ag(I) oxide as the main silver species. [*Armelao-2009*, *Barreca-2005*, *Waterhouse-2001*]

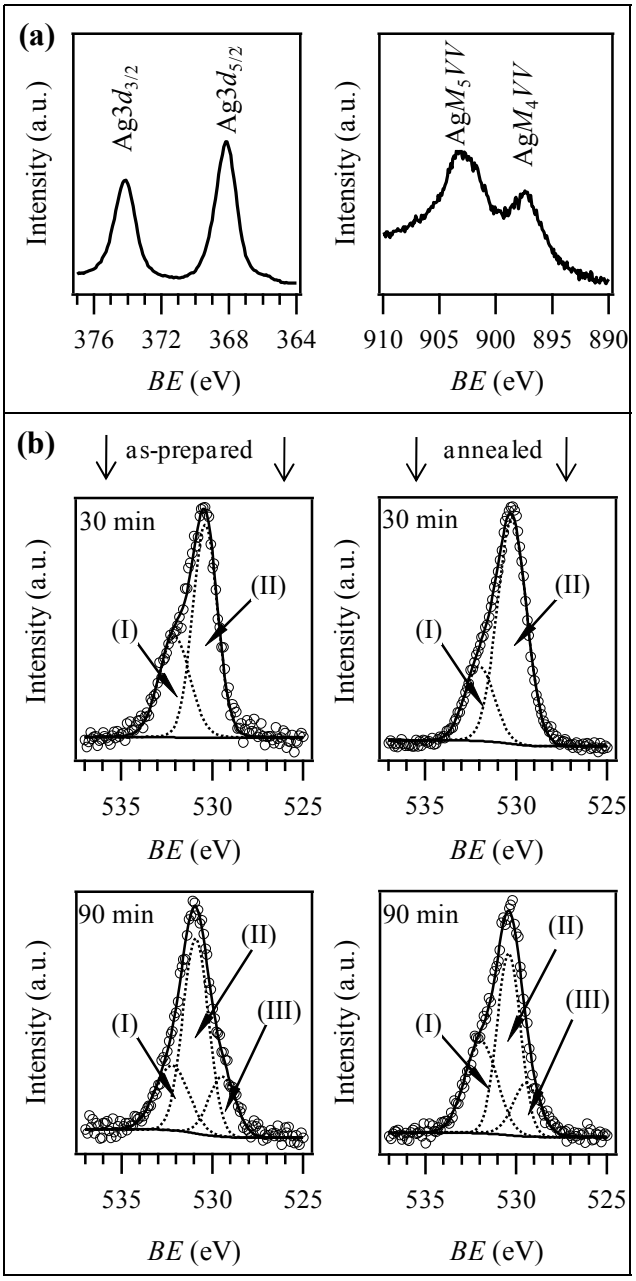

Figure 5.8: (a) Surface Ag3*d* and Ag*MVV* signals for an as-prepared (**A**) Ag/ZnO nanocomposite on Si(100). (b) Surface O1*s* photopeaks for various Ag/ZnO nanocomposites (**ZnAg30_A(Si)**, **ZnAg30_T(Si)**, **ZnAg90_A(Si)**, **ZnAg90_T(Si)**, see **tables 5.1** and **5.2**).

In a different way, the increase of these values to α_1 (Ag) = 726.2 eV and α_2 (Ag) = 720.3 eV upon annealing suggested the occurrence of an Ag(I) reduction to Ag(0) [*Barreca-2005*, *Waterhouse-2001*]. This evolution could be related both to the thermal instability of

Ag(I) oxide and to the morphological reorganization of silver aggregates, as highlighted by FE-SEM and EDXS observations (**figures 5.2** and **5.7**). In fact, Ag NPs underwent a significant size increase upon annealing. It is reasonable to suppose that the smaller Ag particles in as-prepared samples had a higher contact area with both ZnO matrices and the outer atmosphere, which was responsible for a more marked silver oxidation. [*Kibis-2010*, *Qi-2010*] Conversely, the NP size increased. The Ag segregation in the outermost ZnO region revealed upon thermal treatment could explain the predominance of Ag(0) at the sample surface. These results suggested that the Ag_2O phase observed in the GIXRD pattern of annealed samples (**figure 5.5**) should be mainly localized in the inner ZnO layers.

At variance with the case of pure ZnO samples (**paragraphs 3.3.3** and **3.4.3**), three bands contributed to the O1*s* signal for Ag sputtering times higher than 30 min (**figure 5.8 (b)**). The average *BE* of the three components were: (**I**) 532.0 eV, (**II**) 530.5 eV, and (**III**) 529.4 eV. Whereas peak (**I**) could be ascribed to surface absorbed carbonate and hydroxyl groups, [*Barreca-2007-C*] the position of peak (**II**) was in agreement with the values reported for lattice oxygen in ZnO. [*Barreca-2007-C*, *Bekermann-2010-B*] Component (**III**) could be attributed to the presence of silver(I) oxide, [*Gao-2010*, *Kibis-2010*, *Waterhouse-2001*] since its intensity increased with silver content.

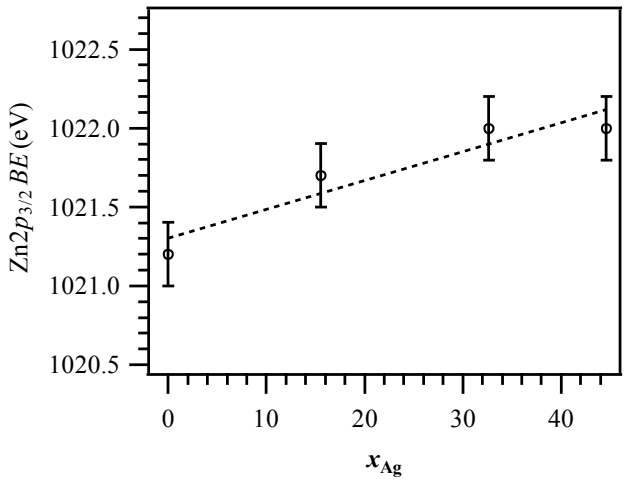

Figure 5.9: Evolution of surface Zn2$p_{3/2}$ *BE* of as-prepared samples on Si(100) (**table 5.1**) as a function of silver molar fraction (defined in **table 5.2**).

Interestingly, a linear increase of the surface Zn2$p_{3/2}$ *BE*s with Ag content took place for as-prepared samples (**figure 5.9**), highlighting the occurrence of electronic interactions between silver and zinc oxide. Also for annealed samples, surface Zn2$p_{3/2}$ *BE*s were systematically higher than 1021.4 eV, the value expected for ZnO. [*Barreca-2007-C*] This observation could be related both to charge transfer events from ZnO to Ag/Ag_2O NPs, [*Lin-2009*, *Lu-2008*] and to the surface oxidation of Ag NPs to *p*-type Ag_2O, [*Gao-2010*] resulting in Ag_2O-ZnO *p*/*n* junctions generating a depletion layer at the interface.
The obtainment of Ag_2O-ZnO and Ag-ZnO interfaces with tunable features appears very promising for a possible improvement of the system functional properties in photocatalytic H_2 generation and gas sensing.

❖ 5.3.4 Photocatalytic H_2 production

Photocatalytic H_2 production from methanol/water solutions (for experimental details see **8.6.3**) was carried out under UV-Vis and simulated solar irradiation using silicon supported Ag/ZnO composites. In order to prevent the occurrence of undesired alterations upon functional testing, hydrogen production measurements were performed on *ex-situ* annealed specimens.
Figure 5.10 displays the rate of H_2 photo-production *vs*. UV-Vis irradiation time for Ag/ZnO nanocomposites obtained under different processing conditions. Whereas pure ZnO specimens did not show any significant activity, an appreciable H_2 evolution was measured for Ag/ZnO systems, highlighting the key role of silver NPs in promoting the photo-reforming of methanol/water solutions under UV-Vis irradiation. Under these conditions, the process is likely to proceed through the direct photo-excitation of electrons from the valence to the conduction band of ZnO, followed by their transfer to Ag NPs. [*Liu-2011*] Subsequently, H^+ reduction on the metal particles results in H_2 generation, whereas alcohol oxidation is promoted by holes in ZnO valence band. Beside the Schottky junction between ZnO and Ag NPs, preventing electron/hole recombination, [*Primo-2011*] a further promotion of the observed process might result from the formation of Ag_2O-ZnO *p/n* junctions. A similar effect has recently been reported for CuO-SnO_2 nanocomposites. [*Zheng-2010-B*]

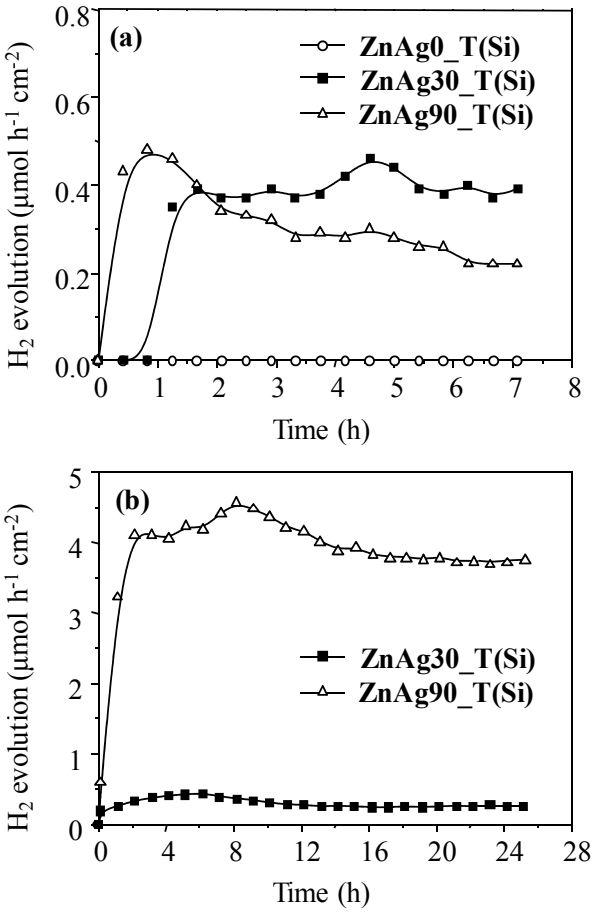

Figure 5.10: H_2 evolution rate per unit area as a function of illumination time on Ag/ZnO/Si(100) nanocomposites (Ag sputtering times t = 0, 30 and 90 min, see **table 5.1**) from H_2O/CH_3OH solutions under: (a) UV-Vis light; (b) simulated solar irradiation.

H_2 production rate was not directly proportional to silver content, and the best performances were obtained for **ZnOAg30_T(Si)**. This observation could be explained by the necessity of a sufficiently high fraction of uncovered ZnO surface to enable efficient radiation absorption. Nonetheless, Ag presence was essential for photo-assisted H_2 evolution. For a relatively low Ag NP density and size, such as for sample **ZnOAg30_T(Si)** (see **figure 5.2**), the good photocatalytic performances can be attributed both to an intimate contact between Ag and ZnO and to a large exposed ZnO surface. In addition, the highly dispersed Ag NPs in sample **ZnOAg30_T(Si)** (compare SEM and TEM results, **figures 5.2 – 5.4**) may favourably act as electron capturing centres to generate H_2. In a different way, for specimen **ZnOAg90_T(Si)**, the increased coverage of

the ZnO matrix by larger Ag particles (compare **table 5.2** and **figures 5.2 – 5.3**) along with the less intimate Ag-ZnO contact resulted in a lowered radiation absorption, explaining the trend in **figure 5.10 (a)**. Upon increasing the silver deposition time to 150 min, a similar behavior was observed (**ZnOAg150_T(Si)**, data not shown).

The above results are consistent with those obtained for Au/TiO_2 nanosystems, whose optimal photocatalytic performances were obtained for intermediate metal loading due to a compromise between gold NPs reactivity and their covering of titanium oxide surface. [*Armelao-2007*]

From **figure 5.10 (a)** can be seen that for **ZnOAg30_T(Si)** a stable activity was obtained, with an average H_2 production rate of 0.4 μmol^{-1} h^{-1} cm^{-2}. Conversely, specimen **ZnOAg90_T(Si)** presented a decrease of H_2 production after 1 h of irradiation. Such an effect could be related to the reduction of Ag_2O upon illumination, [*Kudo-2009*] a process which is expected to be less pronounced for smaller silver NPs, explaining thus the good stability of sample **ZnOAg30_T(Si)**.

A remarkable photo-reforming activity was observed under illumination with simulated solar light (**figure 5.10 (b)**), an important result in view of practical utilization. Very interestingly, H_2 production rate over sample **ZnOAg90_T(Si)** was more than one order of magnitude higher than for use of more energetic radiation (**figure 5.10 (a)**). At variance with data obtained under UV-Vis illumination, a net performance enhancement was obtained upon passing from **ZnOAg30_T(Si)** to **ZnOAg90_T(Si)**. Once again, no further improvement was observed by increasing the deposition time to **ZnOAg150_T(Si)** (data not shown). These phenomena can be interpreted basing on the combination of different effects. An increase of the metal NP content can lead to a more efficient Vis light absorption due to Surface Plasmon Resonance (SPR) of silver aggregates. [*Barreca-2005*, *Liu-2011*, *Chuang-2011*] Indeed, Ag SPR band centered at $\lambda \approx 410$ nm was observed for particles with diameters in the 5 - 100 nm range, with a red-shift upon increasing metal NP size. [*Zielinska-2009*] In addition, the presence of Ag_2O species can positively affect the system reactivity. This observation is consistent with previous findings for TiO_2 based systems. In fact, Lalitha *et al.* showed that pure TiO_2 and Ag_2O, or even Ag/TiO_2 nanosystems, did not present high performances in photo-assisted H_2 production. [*Lalitha-2010*] Conversely, Ag_2O/TiO_2 nanocomposites yielded an improved efficiency, due to both a beneficial interaction between Ag(I) species and

TiO_2 and an enhanced radiation absorption in the Vis range. Therefore, the presence of large silver aggregates and the low accessibility of ZnO due to its high degree of coverage justify the poorer reactivity of the **ZnOAg150_T(Si)** sample with respect to the **ZnOAg90_T(Si)** sample.

❖ 5.3.5 Gas Sensing Properties

The sensor responses of the alumina supported Ag/ZnO systems to hydrogen were investigated at temperatures between 100 - 400°C. Technical details and definitions of responses, response and recovery times are provided in **paragraph 8.6.4**. The H_2 concentration pulses were varied between 1000 and 5000 ppm. The maximum recorded deviations for Ag/ZnO system responses were lower than 10%, indicating a good reproducibility. As an example, typical variations for two subsequent response scans to hydrogen (1000 - 5000 ppm concentrations, 200°C; see **figure 5.11**) were approximately 5%, a value within the response uncertainty.

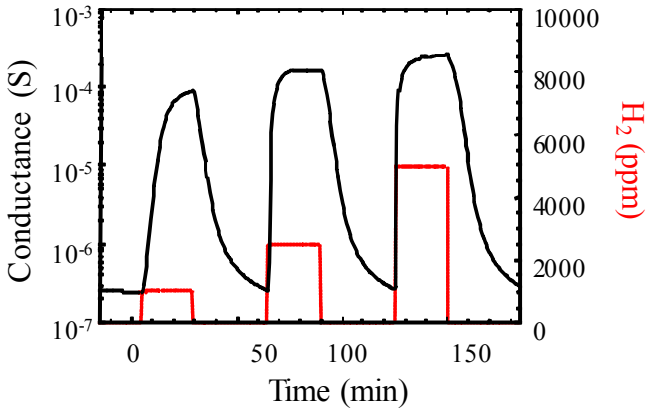

Figure 5.11: Representative dynamic response for a $Ag/ZnO/Al_2O_3$ nanocomposite (**ZnAg10_T(Al)**, see **figure 5.6** and **table 5.1**) to square H_2 concentration pulses (working temperature = 200°C).

Isothermal dynamic responses of Ag/ZnO nanomaterials to square concentration pulses of H_2 revealed a conductance increase upon interaction with the target gas, a behavior typical for an *n*-type semiconductor. It is worth emphasizing that, irrespective of the preparative conditions, the conductance variations upon injection of the target gas were

proportional to the H_2 concentration, without displaying any appreciable saturation effect. This behavior, along with the good recovery of the conductance baseline value upon switching off the analyte pulse, indicated a reversible H_2 interaction with the Ag/ZnO system, an important prerequisite for the sensor technological application (see also previous **chapters 3** and **4**).

The present system responses were considerably high (370 - 960 as the H_2 concentration increased from 1000 to 5000 ppm) despite the moderate working temperature (200 °C), and exceeded by far previous literature data for hydrogen sensing by Ag/ZnO nanosystems. [*Xiang-2010*] The fast response and recovery times (≈ 3 min) were also promising in view of practical applications. These performances can be related to the morphology of ZnO nanoaggregates, presenting a high surface-to-volume ratio, together with an average size close to the zinc oxide Debye length, [*Barreca-2010-C*] enabling their total depletion under the test conditions (compare **figure 5.11** and **paragraph 3.4.6**). Furthermore, Ag nanoparticles can exert a catalytic promotion of the chemical processes involved in the sensing mechanism, and improve charge separation at the interface with ZnO (see **5.2**). [*Xiang-2010*]

❖ 5.4 Conclusions

The work of the present chapter was focused on a two-step approach to supported Ag/ZnO nanocomposites combining PECVD, for the growth of columnar ZnO arrays (according to **3.4.1**), and RF-sputtering, for the dispersion of Ag NPs in the oxide matrices. Various sputtering times (from 10 to 150 min) were used to tailor the overall silver amount. The typical infiltration power of RF-sputtering in combination with the porous ZnO morphology allowed a good silver dispersion into ZnO matrices, and the simultaneous control of Ag NPs size by variations of the sputtering time. In addition, silver distribution in the ZnO systems could be controlled by thermal treatments which, in turn, governed the Ag(0)-Ag(I) inter-conversion leading to an electronic interplay between the different phases. A fine tuning of Ag/ZnO nanocomposite physico-chemical properties was thus enabled by control of the process parameters, and directly impacted the system functional properties in H_2 photo-production and sensing.

In this work, for the first time, Ag/ZnO nanocomposites have been studied as catalysts in the production of hydrogen by photo-reforming of alcoholic solutions. Notably, pure ZnO revealed to be inactive under both UV-Vis and solar illumination. Functionalization with Ag NPs resulted in stable and appreciable H_2 evolution rates (~ 0.3 - 4 $\mu mol^{-1}\ h^{-1}\ cm^{-2}$), competing well with most values reported for similar semiconductor based photocatalytic processes (see **paragraphs 4.2**, **4.4.5** and **4.5**). The best photocatalytic performances were obtained using Ag/ZnO systems characterized by a low ZnO coverage, an intimate Ag/ZnO contact and the presence of Ag_2O.

Due to Ag-ZnO interactions, very good responses with a long-term stability were also obtained in the gas-phase detection of H_2. In fact, even at mild working temperatures (200°C), the response values (370 - 960 as the H_2 concentration increased from 1000 to 5000 ppm) were considerably higher compared to pure ZnO (see **3.4.6**, **figure 3.30**) and Ag/ZnO nanosystems reported in literature.

Overall, the results provided herein pave the way to engineering of the present nanosystems as multifunctional platforms for both hydrogen generation and reliable sensing, two main issues of critical importance in view of large-scale H_2 manipulation.

6. Co_3O_4/ZnO

❖ 6.1 Abstract

The present chapter deals with the design, characterization and functional tests of quasi-1D *p*-Co_3O_4/*n*-ZnO nanocomposites. Based on the PECVD procedures of ZnO and pure Co_3O_4 described in the previous chapters (see **3.4.1** and **4.4.1**), arrays of <001> oriented ZnO nanoparticles were grown on Si(100) or Al_2O_3 substrates at 300°C from $[Zn\{[(CH_2)_3OCH_3]NC(CH_3)=C(H)C(CH_3)=O\}_2]$ (**2**), followed by the deposition of Co_3O_4 at 200°C from precursor **3** (**6.3.1**). Structure and morphology have been investigated by XRD and FE-SEM (**paragraph 6.3.2**), compositional information was gained from EDXS, FT-IR, SIMS and XPS/XE-AES measurements (**paragraph 6.3.3**). The analyses evidenced the successful formation of pure and high-area nanocomposites with a tailored dispersion of Co_3O_4 into ZnO and an intimate contact between the two oxides.

Preliminary investigations on the PCO oxidation and PH performances of the silicon supported Co_3O_4/ZnO heterostructures revealed their activity for light-activated functional applications, such as antifogging or self-cleaning materials (**paragraph 6.3.4**). In addition, functional tests for the detection of CH_3COCH_3, CH_3CH_2OH and NO_2 indicated promising sensing responses and the possibility of discriminating between reducing and oxidizing species as a function of the operating temperature (**paragraph 6.3.5**).[1] The dependence of the sensor responses on the overall Co_3O_4 content has been investigated.

❖ 6.2 Introduction

Nanocomposites based on the combination of *p*-type and *n*-type semiconducting oxides have come under intense scrutiny for the possibility of joining the intrinsic properties of individual components with the multi-functional behaviour exhibited by low-dimensional materials (see **chapter 1**). In this regard, *p*/*n* oxide-based nanocomposites have been

[1] [*Bekermann-2012*] D. Bekermann, A. Gasparotto, D. Barreca, C. Maccato, E. Comini, C. Sada, G. Sberveglieri, A. Devi, R.A. Fischer, ACS Appl. Mater. Interfaces 4 (2012) 928.

investigated for various technological applications, such as magnetism, optoelectronics, photocatalysis and gas sensing. [*Hong-2008*, *Hsieh-2008*, *Hwang-2009*, *Kanjwal-2011*, *Kim-2005-A*, *Martín-González-2008*, *Na-2011*, *Shifu-2009*, *Zhang-2010*]

The superior functional performances of these systems in comparison to the corresponding single-phase SC oxides [*Hong-2008*, *Kim-2005-A*, *Martín-González-2008*, *Shifu-2009*] are mainly ascribed to the build-up of an inner electric field at the *p*/*n* junction interface. [*Hsieh-2008*, *Kim-2005-A*, *Na-2011*, *Vanaja-2008*, *Zhang-2010*, *Zhuge-2010*] For instance, such a phenomenon is beneficial for optoelectronics, thanks to the resulting rectifying effects, and photocatalysis, due to the enhanced separation of photo-generated electron/hole carriers. [*Hsieh-2008*, *Kim-2005-A*, *Shifu-2009*, *Vanaja-2008*, *Zhang-2010*, *Zhuge-2010*] As regards gas sensing applications, the combination of *p*- and *n*-type nanomaterials can provide higher sensitivities and faster responses due to the formation of a more extended depletion layer. [*Chowdhuri-2002*, *Na-2011*]

In this context, the present chapter of the thesis is focused on *p*-Co_3O_4/*n*-ZnO nanocomposites, whose attractive performances have been recently demonstrated for a broad perspective of utilizations. [*Kanjwal-2011*, *Martín-González-2008*, *Na-2011*, *Rubio-Marcos-2010*, *Uriz-2011*] The choice of such oxides is motivated by the high technological importance of *n*-type ZnO, an extremely versatile workhorse for various applications (see **chapter 3**), [*Barreca-2010-A*, *Barreca-2010-C*, *Hong-2008*, *Huang-2001*, *Kanjwal-2011*, *Tak-2008*, *Wang-2010*] whereas *p*-type Co_3O_4 is well known for its high catalytic activity, in particular in oxidation reactions (see **4.2**). [*Barreca-2011-C*, *Kanjwal-2011*, *Ma-2010*, *Na-2011*, *Tak-2008*, *Yu-2009*]

A key problem for the development of efficient photo-active materials is the fast recombination rate of photo-generated e^-/h^+ pairs. [*Shifu-2009*, *Zheng-2009*] Recently, it was shown, that the carrier separation in ZnO photocatalysts can be significantly enhanced by its coupling with a *p*-type SC oxide. [*Shifu-2009*, *Zhang-2010*] In spite of these promising attempts, limited information is available on the preparation and properties of *p*/*n* junction photocatalyst, and only one work on the photo-activity of Co_3O_4/ZnO can be found in the literature. [*Kanjwal-2011*, *Shifu-2009*]

Furthermore, the synergistic combination of these two SCs paves the way to the development of gas sensors characterized by improved sensitivity/selectivity and mild working temperatures. These issues, along with the long-term stability and limited power

dissipitation, are the main challenges to be overcome in order to develop efficient and reliable devices for large scale utilization (see **3.2**). [*Barreca-2010-C*, *Barreca-2011-C*, *Na-2011*]

It is worth noting that only few studies on the photocatalytic and gas sensing properties of Co_3O_4/ZnO nanocomposites are available in the literature up to date. [*Kanjwal-2011*, *Na-2011*]

❖ 6.3 PECVD of Co_3O_4/ZnO on Si(100) and Polycrystalline Al_2O_3

❖ 6.3.1 Deposition Procedure

Basing on the previous results on single-phase ZnO (**chapter 3**) and Co_3O_4 (**chapter 4**) nanosystems, *p*-Co_3O_4/*n*-ZnO nanocomposites were synthesized under optimized preparative conditions, with particular attention on the obtainment of suitably porous ZnO deposits in order to perform the over-dispersion of Co_3O_4. $[Zn\{[(CH_2)_3OCH_3]NC(CH_3)=C(H)C(CH_3)=O]\}_2]$ (**2**) and $[Co(dpm)_2]$ (**3**) were selected as zinc and cobalt precursors, respectively (see **8.1** and **8.2**). *p*-type Si(100) and polycrystalline Al_2O_3 slides were used as substrates and suitably cleaned prior to each deposition (see **8.3.3**). Electronic grade Ar and O_2 were used as plasma sources in a two-electrode custom-built RF PECVD apparatus (**8.3.3**). The zinc and cobalt precursors were vaporized at 150 and 100°C, respectively, in reservoirs heated by an oil bath, and transported into the reaction chamber by an Ar flow (60 sccm) through heated gas lines to prevent undesired condensation phenomena. Additional O_2 and Ar flows (15 and 20 sccm, respectively) were directly introduced in the reactor. All experiments were performed at a total pressure of 1.0 mbar, using a RF-power of 20 W and an interelectrode distance of 6 cm. For the initial deposition of ZnO, the growth temperature and deposition time were fixed at 300°C and 60 min, respectively, keeping constant the ZnO materials amount and morphological features for all specimens prepared. In the subsequent process step, the amount of Co_3O_4 was tailored as a function of the process duration (10 - 120 min, growth temperature = 200°C). Finally, the resulting Co_3O_4/ZnO composites were thermally stabilized by annealing at 400°C for 60 min in air. In the

following, samples will be labelled according to the Co_3O_4 deposition time as shown in **table 6.1**.

Table 6.1: Overview of sample labelling as a function of Co_3O_4 deposition time. All other processing parameters for ZnO growth (p = 1 mbar, P = 20 W, t = 60 min, substrate temperature T = 300°C and T_{vap} (precursor **2**) = 150°C) and Co_3O_4 deposition (p = 1 mbar, P = 20 W, T = 200°C and T_{vap} (precursor **3**) = 100°C) were kept constant.

Co_3O_4 deposition time (min)	10	30	60	120
Si(100)	**ZnCo_10(Si)**	**ZnCo_30(Si)**	**ZnCo_60(Si)**	**ZnCo_120(Si)**
Al_2O_3	**ZnCo_10(Al)**	**ZnCo_30(Al)**	**ZnCo_60(Al)**	**ZnCo_120(Al)**

❖ 6.3.2 Morphology and Structure

The morphological and structural characterization of the Co_3O_4/ZnO composites has been performed by FE-SEM and XRD analyses. For the growth of Co_3O_4/ZnO on Si(100), first ZnO NR arrays with average length and diameter of 120 nm and 18 nm, respectively, were synthesized. After the subsequent deposition Co_3O_4, two separate materials could be appreciated from FE-SEM cross-sectional images, as indicated by the different image contrast (**figure 6.1**). Co_3O_4 grew following the ZnO morphology, forming an axial heterostructure. For 10 min of Co_3O_4 deposition (**ZnCo_10(Si)**) plane-view FE-SEM images revealed spherically topped nanoparticles with an average diameter (d) of 18 nm. Upon increasing Co_3O_4 deposition time, the NP diameters progressively increased, and triangularly shaped nanoparticles (d = 30 nm) were formed for **ZnCo_120(Si)** (t = 120 min) (**figure 6.1**). The evolution of triangular faceting, exposing Co_3O_4 low surface energy planes, is typical for face-centered cubic systems. [*Barreca-2010-D*] The observed morphology and, in particular the low particle sizes in combination with the close contact between *p*- and *n*-type metal oxide can result in advantageous photocatalytic performances. [*Shifu-2009*, *Zhang-2010*] The overall system thickness progressively increased with Co_3O_4 deposition time from 145 nm (**ZnCo_10(Si)**) to 215 nm

(**ZnCo_120(Si)**). Correspondingly, the Co_3O_4 deposit thickness varied proportionally with the deposition time, i.e. Co_3O_4 overall loading.

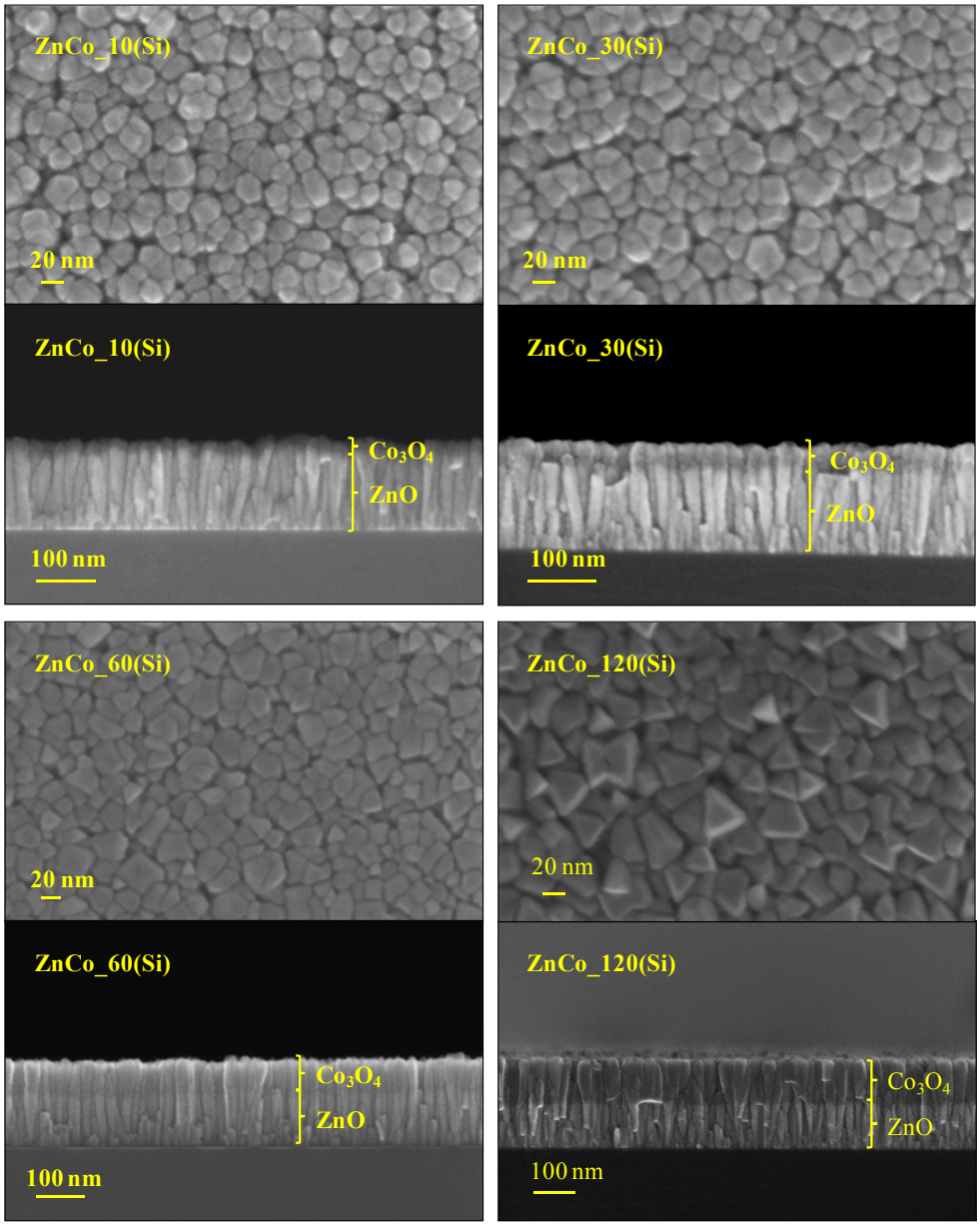

Figure 6.1: FE-SEM plane-view and cross-section images of **ZnCo_10(Si)**, **ZnCo_30(Si)**, **ZnCo_60(Si)** and **ZnCo_120(Si)** (see **table 6.1**).

GIXRD patterns for Si(100) supported specimens are displayed in **figure 6.3**. In general, ZnO systems were strongly <001> oriented, the pattern showing only the (002) reflection of ZnO at $2\theta = 34.4°$ (FWHM = 0.3°). [*JCPDS-A*] The reflections at $2\theta = 19.0°$ and 36.8° were assigned to the (111) and (311) Bragg reflections of Co_3O_4, respectively. [*JCPDS-*

C] The ZnO (002) reflection showed a similar intensity for all specimens, as expected due to the constant ZnO growth parameters (**paragraph 6.3.1**). In contrast, the intensity of the Co_3O_4 reflections clearly followed a trend dependent on its deposition time (**figure 6.2**). In particular, for 10 min of Co_3O_4 deposition (**ZnCo_10(Si)**) no Co_3O_4 reflection could be detected according to the low amount of Co_3O_4. For **ZnCo_30(Si)** the (111) and (311) reflections appeared weak and broad and were significantly sharper for **ZnCo_60(Si)**. Finally, for the composite with the highest Co_3O_4 loading (**ZnCo_120(Si)**), as seen from FE-SEM, the Co_3O_4 (111) and (311) signals have the highest intensities with respect to the other specimens. In line with FE-SEM observations, the intensity (*I*) ratio I_{111}/I_{311} was higher than for powder Co_3O_4, [*JCPDS-C*] indicating anisotropic growth, exposing {111} surface sites. (TEM measurements for confirmation are under way.) No additional peak shifts, that could indicate the formation of a ternary phase, were detected. In this context, it is worthwhile noting that the formation of Zn-Co-O ternary phases through solid state reactions between Co_3O_4 and ZnO could be reasonably excluded, since it usually requires harsh conditions in terms of both temperature and/or applied RF power. [*Bhargava-2010*, *Sudakar-2008*, *Wei-2009*, *Yang-2002*, *Zhuge-2010*]

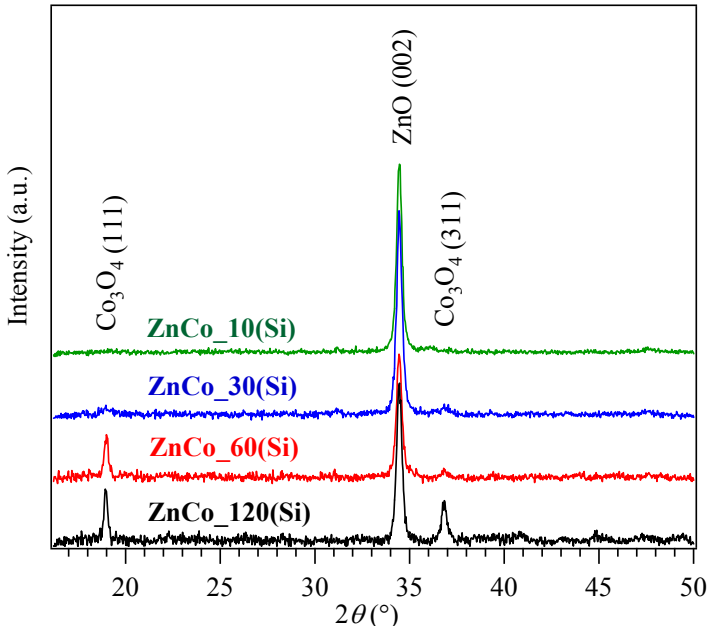

Figure 6.2: GIXRD patterns of **ZnCo_10(Si)**, **ZnCo_30(Si)**, **ZnCo_60(Si)** and **ZnCo_120(Si)** (see **table 6.1**).

In the case of alumina supported Co_3O_4/ZnO species, GIXRD patterns (**figure 6.3**) displayed very similar features for the whole samples set, irrespective of the Co_3O_4

loading. Beside the reflections of the alumina substrate, the (002) signal of the ZnO *zincite* phase at 2θ = 34.4° [*JCPDS-A*] was the only detectable one, suggesting the occurrence of a strong <001> preferential orientation, as in the case of the Si(100) supported specimens. At variance from the latter, the absence of clearly detectable Co_3O_4 signals suggested a high dispersion of this oxide into the ZnO matrix, and/or low crystallite size. These features likely arose from the high roughness (~ 70 nm) of the used polycrystalline Al_2O_3 substrates.

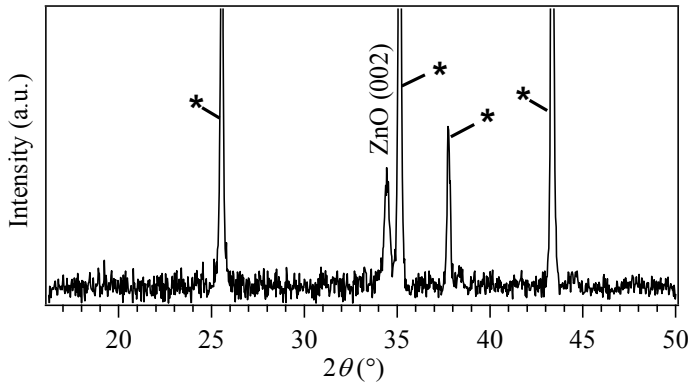

Figure 6.3: GIXRD pattern for a representative Co_3O_4/ZnO specimen (**ZnCo_30(Al)**, see **table 6.1**). Stars (*) indicate the reflections of the Al_2O_3 substrate.

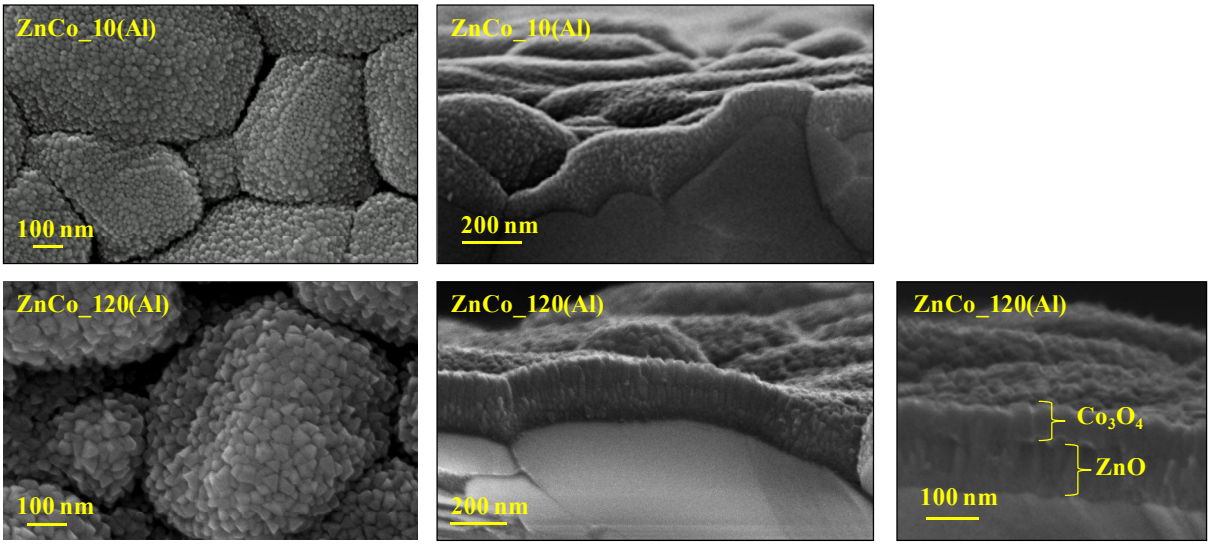

Figure 6.4: Selected FE-SEM micrographs for **ZnCo_10(Al)** and **ZnCo_120(Al)** (**table 6.1**) plane-view and cross-section. A higher magnification image for the **ZnCo_120(Al)** cross-section is also shown.

The morphology of the alumina supported composites was investigated by FE-SEM analyses (**figure 6.4**). In the absence of Co_3O_4, the globular Al_2O_3 substrate particles (0.3 - 1 μm) were conformally covered by ZnO grains with average lateral and vertical dimensions of 20 and 100 nm, respectively. After Co_3O_4 deposition for 10 min (**ZnCo_10(Al)**), plane-view micrographs showed more faceted and slightly bigger particles (≈ 30 nm), while according to cross-section investigations the overall deposit thickness raised to 120 nm. Upon increasing the Co_3O_4 deposition time up to 120 min (**ZnCo_120(Al)**), the observed nanograins possessed an average size of ≈ 40 nm and exhibited well-evident pyramidal-like morphology, as often reported for face-centered cubic systems like Co_3O_4. [*Barreca-2010-B*, *Barreca-2010-D*] The mean deposit thickness was found to be 180 nm. The corresponding cross-sectional analyses suggested the existence of two separated phases, attributed to a Co_3O_4 deposit (≈ 80 nm thick) on a ZnO matrix of approximately 100 nm. The high roughness and reduced particle size characterizing the present Co_3O_4/ZnO/Al_2O_3 composites suggested a high active area, anticipating attractive gas sensing performances. In addition, the over-dispersion of Co_3O_4 on ZnO results in an intimate contact between the two oxides, enabling a favorable exploitation of their mutual electronic interactions. [*Barreca-2011-A*]

❖ 6.3.3 Composition

The system composition was investigated by EDXS, XPS and SIMS analyses. Since all Co_3O_4/ZnO specimens revealed similar compositional information, irrespective of the underlying substrate, the results are discussed below using selected silicon or alumina based samples as representative examples.

Figure 6.5 shows the EDXS line-scan spectra for samples **ZnCo_10(Si)** – **ZnCo_120(Si)** along the thickness: the O Kα1, Zn Kα1 and Co Kα1 signals were measured as a function of film thickness. In line with FE-SEM data (compare **figure 6.1**), the Co Kα1 signal had a maximum in the outermost layer and underwent a progressive decrease towards the substrate interface, while the Zn Kα1 line followed an opposite trend. In a different way, in all samples the O Kα1 signal is constantly present throughout the whole film thickness. The part of the outermost sample region, where Co is predominant over Zn, increases

parallel to the Co_3O_4 deposition time. In particular, for **ZnCo_10(Si)**, the Co accumulation at the surface is the least pronounced, and Zn and O are prevailing after the outermost ~ 30 nm. For **ZnCo_120(Si)** Zn Kα1 remains at the noise level along approximately half of the outer sample thickness, whereas the evolutions of the Co Kα1 and O Kα1 signals are almost parallel in this region. In addition, a progressive increase of the Co:Zn weight ratio as a function of the Co_3O_4 deposition time was evidenced. The Co:Zn ratio averaged over the entire composite thickness was 4:96 for **ZnCo_10(Si)**, 13:87 for **ZnCo_30(Si)**, 21:79 for **ZnCo_60(Si)**, 37:63 for **ZnCo_120(Si)**. These results, in accordance with FE-SEM cross-sectional data, further supported the presence of the two single-phase oxides.

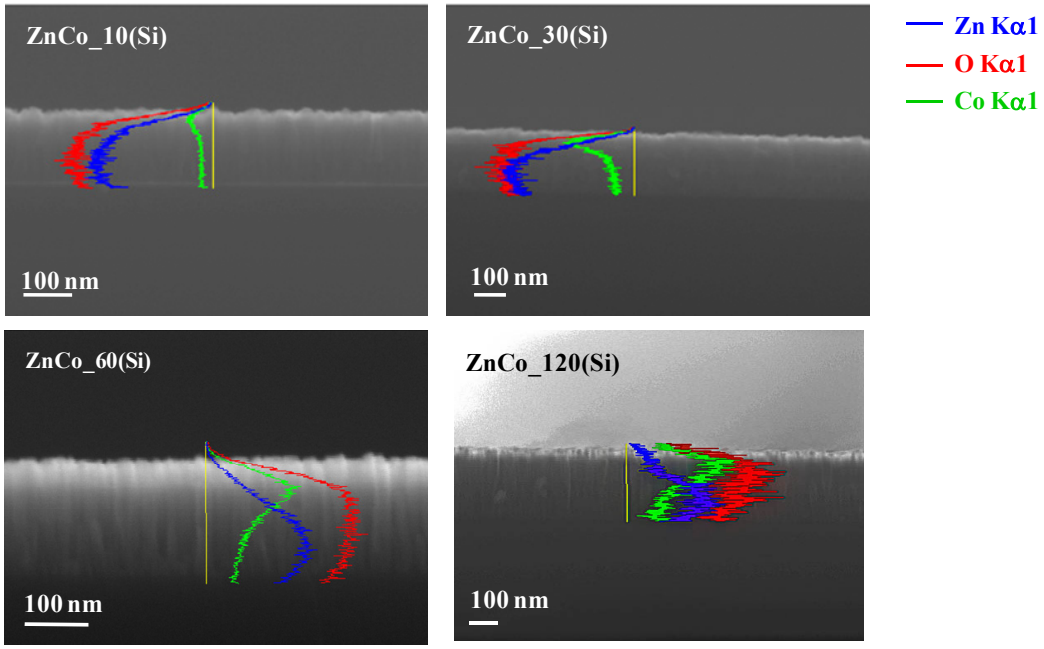

Figure 6.5: EDXS cross section of **ZnCo_10(Si)**, **ZnCo_30(Si)**, **ZnCo_60(Si)** and **ZnCo_120(Si)** (see **table 6.1** and **figure 6.1**).

In order to obtain further compositional information, FT-IR spectra were recorded (**figure 6.6**). The band at 411 cm^{-1} can be ascribed to the E_1 transverse optical mode of ZnO. [*Demyanets-2011*, *Morkoç-2009*, *Zou-2011*] The two absorption bands at ν_1 = 560 and ν_2 = 660 cm^{-1} were attributed to Co-O stretching modes. Whereas the former was associated to B–O vibrations in the spinel lattice, with B indicating Co(III) centers in octahedral sites, the latter could be attributed to ABO_3 vibration modes, where A is a Co(II) center in

a tetrahedral environment. [*Jiu-2002*, *Lai-2008*, *Li-2008-C*, *Lu-2009*] Notably, the bands v_1 and v_2 have not been observed for **ZnCo_10(Si)**, and their intensities increased as a function of Co_3O_4 deposition time by going from **ZnCo_30(Si)** to **ZnCo_120(Si)**. In line with the previous results, FT-IR data suggested the co-presence of ZnO and Co_3O_4 in the synthesized systems.

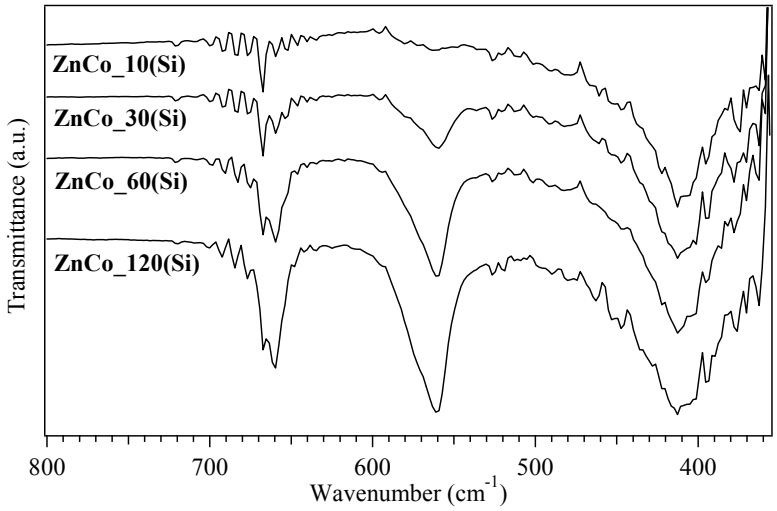

Figure 6.6: FT-IR spectra of **ZnCo_10(Si)**, **ZnCo_30(Si)**, **ZnCo_60(Si)** and **ZnCo_120(Si)** (see **table 6.1**). The spectra have been vertically shifted for clarity.

Information on the Co_3O_4 and ZnO vertical distribution for alumina supported samples was obtained by in-depth compositional analyses. **Figure 6.7 (a)** displays a cross-sectional EDXS line-scan of **ZnCo_120(Al)**, showing a net predominance of cobalt over zinc in the outermost sample region. Conversely, the Zn Kα1 intensity underwent a progressive increase in the inner system region at expenses of the Co Kα1 one. (For compositional trends as a function of Co_3O_4 deposition time, see **figure 6.5** and pertaining discussion.) A deeper insight into the system composition was obtained by SIMS, and a representative in-depth profile is shown in **figure 6.7 (b)**. In general, the negligible C content (< 35 ppm) evidenced the high purity of the obtained materials. In line with the above discussed results, Co_3O_4 was mainly confined to the outermost deposit region, and the corresponding estimated thickness from the analysis of the Co SIMS profile was ≈ 80 nm, as also derived from FE-SEM. Below this layer, the Zn ionic yield underwent a progressive increase and a subsequent intensity reduction in the proximity of the Al_2O_3 substrate, *i.e.* upon increasing the Al signal. These data, in line with EDXS

results, pointed out to the obtainment of bi-layered composites, with zinc oxide being confined in the inner system region. The corresponding ZnO thickness was estimated to be 100 nm, in good agreement with FE-SEM results (see **figure 6.4** and related discussion).

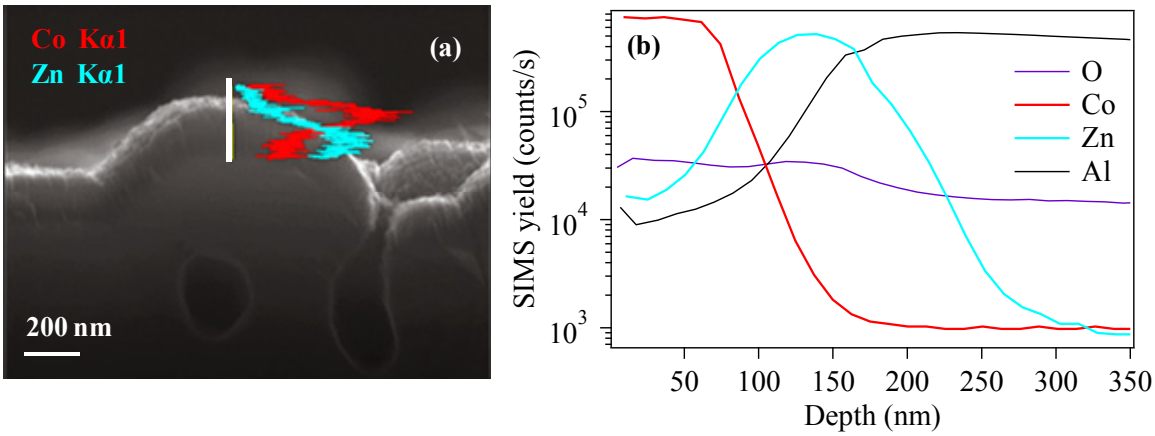

Figure 6.7: Cross-sectional EDXS line-scan (compare also **figure 6.5**) (a) and SIMS depth profile (b) for sample **ZnCo_120(Al)** (see **table 6.1** and **figure 6.4**)

In order to investigate the possible surface co-presence of both the single oxides [*Martín-González-2008*, *Wei-2009*] and the exposure of different sites, XPS and XE-AES analyses were undertaken. For all samples, spectra evidenced the presence of C and O signals. Surface XPS and XE-AES analyses were carried out to study in detail the O1*s*, Zn2$p_{3/2}$, Zn3*p* and Co2*p* core levels, as well as the Zn and Co Auger peaks, of the composite material and to evaluate the pertaining Auger parameters (α_{Zn} and α_{Co}).

The main C1*s* component (**figure 6.8**) centered at binding energy (*BE*) = 284.8 eV was ascribed to adventitious hydrocarbon contamination, whereas the shoulder at *BE* = 287.8 eV was related to the presence of carbonate containing species at the sample surface, [*Barreca-2011-C*, *Moulder-1992*, *Nist*, *Wei-2009*] likely arising from air exposure. The strong decrease of the C1*s* signal after 5 min Ar^+ erosion indicated that it mainly arose by contact with the outer atmosphere. The O1*s* surface peak (**figure 6.8**) was decomposed by means of two different bands, located at *BE* = 529.7 eV (≈ 58% of the total oxygen) and at *BE* = 531.5 eV. The low *BE* contribution was assigned to lattice oxygen. [*Moulder-1992*, *Nist*] The component centered at *BE* = 531.5 eV corresponded to the presence of surface hydroxyl groups and carbonate species, in line with the C1*s* peak shape,

[*Barreca-2010-C*, *Moulder-1992*] and underwent a net intensity decrease after 5 min of Ar^+ erosion.

The surface presence of zinc demonstrated the dispersion of Co_3O_4 particles in the ZnO matrix, without a complete coverage of the latter. In fact, irrespective of the Co_3O_4 deposition time, Zn and Co signals were always detected on the sample surface, with a Co/Zn atomic ratio increasing from 1.7 (**ZnCo_10(Si)**) to 2.0 (**ZnCo_120(Si)**). This result indicated that, despite the conformal coverage of ZnO by Co_3O_4, a residual porosity was still present at the interface between the two phases. Such a feature, together with the formation of nanosized *p*-Co_3O_4/*n*-ZnO heterojunctions, is promising for eventual functional applications. [*Chowdhuri-2002*]

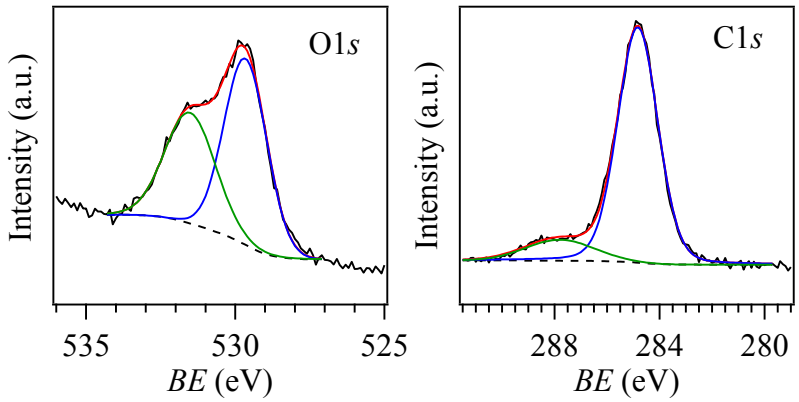

Figure 6.8: Surface XPS peaks for carbon and oxygen for **ZnCo_10(Si)** (see **table 6.1**). The two components and the background resulting from the least-squares fitting are plotted together with the raw spectrum.

The Zn2$p_{3/2}$ spin-orbit component (**figure 6.9**) possessed a position (*BE* = 1021.4 eV) and a shape typically observed for zinc(II) oxide. [*Barreca-2010-C*, *Barreca-2007-C*] This attribution was supported by the Auger parameter, whose value (2010.2 eV) was in agreement with the reported one for ZnO (**paragraphs 3.3.3** and **3.4.3**). [*Barreca-2010-C*, *Barreca-2007-C*] The Co2$p_{3/2}$ and Co2$p_{1/2}$ components (**figure 6.9**) had positions (*BE*(Co2$p_{3/2}$) = 780.2 eV, *BE*(Co2$p_{1/2}$) = 795.5 eV) and a spin-orbit splitting (15.3 eV) typically observed for spinel-type cobalt oxide, that, along with the low *shake-up* satellites intensity confirmed the presence of Co_3O_4 as such in the analyzed systems. [*Barreca-2011-D*, *Martín-González-2008*] This attribution is supported by α_{Co}, whose value (1552.1 eV) was in agreement with the reported values for Co_3O_4 (**paragraph**

4.3.3). [*Barreca-2011-D*, *Barreca-2010-D*] These results, along with the absence of any *BE* shift for the Co and Zn signals as a function of the Zn/Co ratio, suggested the formation of composite systems under the adopted processing conditions, excluding thus the presence of Co-Zn-O ternary phases. [*Barreca-2011-C*, *Barreca-2011-D*, *Martín-González-2008*]

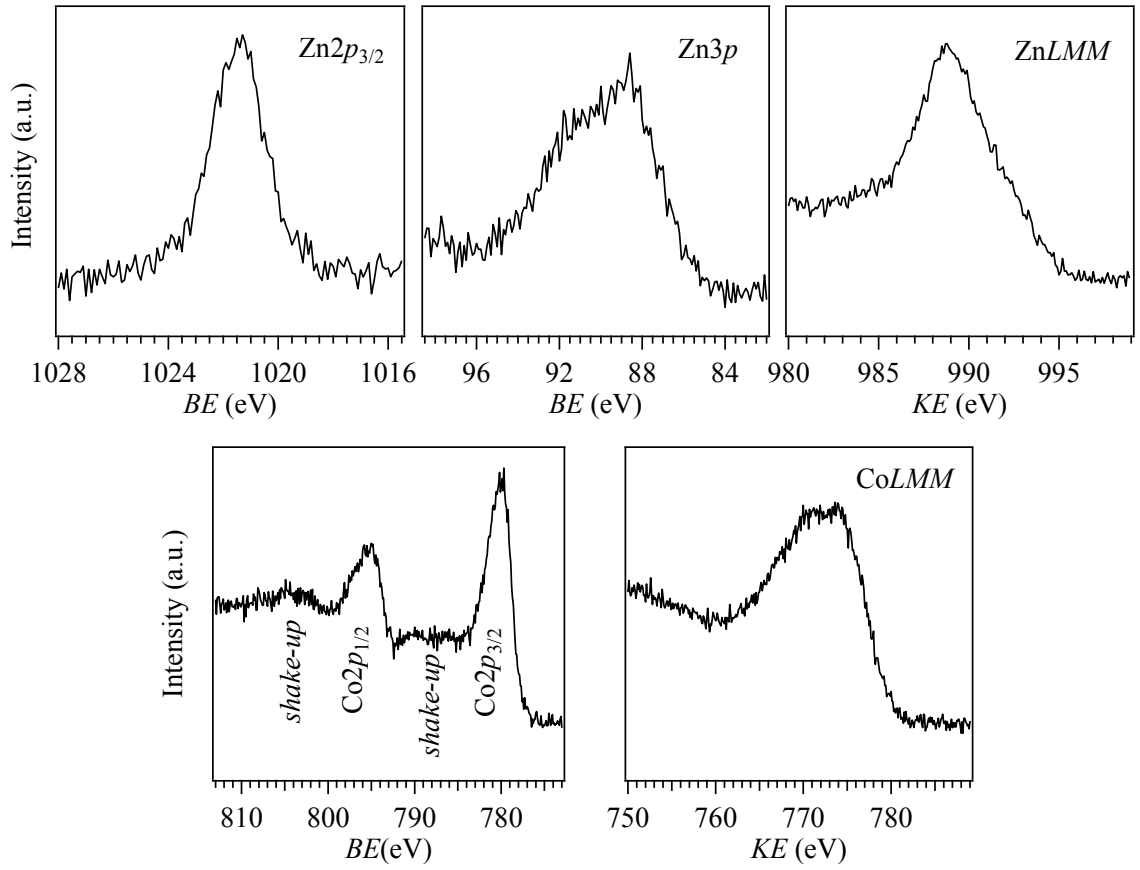

Figure 6.9: Representative XPS and XE-AES surface peaks for zinc and cobalt taken from sample **ZnCo_10(Si)** (see **table 6.1**).

❖ 6.3.4 PH and PCO Properties

The photo-activity of the *p*-Co_3O_4/*n*-ZnO on Si(100) was preliminary tested by photo-induced hydrophilicity (PH) measurements and photocatalytic oxidation of TPA (for experimental details see **8.6.1** and **8.6.2**).

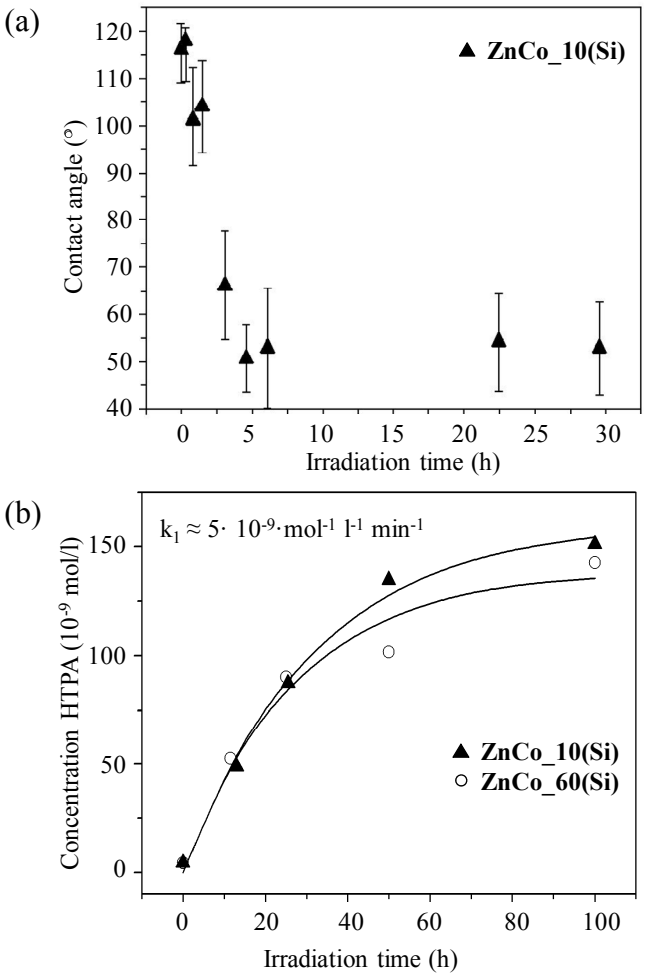

Figure 6.10: (a) Water contact angle as a function of irradiation time obtained from sample **ZnCo_10(Si)**. (b) HOTPA concentration as a function of irradiation time taken from samples **ZnCo_60(Si)** and **ZnCo_10(Si)**. For sample assignments see **table 6.1**.

PH properties were analyzed by measuring the water contact angle as a function of the UV irradiation time (**figure 6.10 (a)**). In the absence of UV light, the hydrophobic WCA was close to 120°, as also observed for non-activated pure ZnO (**3.4.5**), [*Barreca-2009-A*, *Bekermann-2010-A*] which can be explained by: (1) the relative rough composite surface; [*Barreca-2009-A*] (2) the presence of aliphatic carbon, arising from surface contamination (see XPS data). [*Badre-2009*, *Barreca-2007-B*, *Bekermann-2010-A*, *Feng-2004*] Upon UV-light irradiation the WCA decreased, reaching half of its initial value after four hours and a minimum value of 50° after five hours, indicating to an enhanced surface wettability. [*Feng-2004*, *Zhou-2008*] The latter originates from the formation of oxygen vacancies by the reaction of photo-generated holes with lattice O, ultimately

resulting in the dissociative adsorption of H_2O. [*Barreca-2009-A*, *Bekermann-2010-A*] It is also worth noting, that upon prolonged UV irradiation the hydrophilic surface properties were maintained for at least 24 hours, an interesting aspect in view of eventual technological applications.

The self-cleaning activity of Co_3O_4/ZnO has been tested by the photocatalytic oxidation of TPA to HOTPA (**8.6.2**). [*Černigoj-2010*] Consequently, the HOTPA concentration was monitored as a function of the UV-irradiation time (**figure 6.10 (b)**). As a general rule, a progressive increase with illumination time was observed, following a pseudo-zero-order kinetics (rate constant = k_1). The obtained data points could be fitted according to the model introduced in **paragraph 3.4.5**, yielding a kinetic constant of $k_1 = 5 \cdot 10^{-9}$ mol·l^{-1}, a value comparable to that of the bench mark material (Pilkington® Active glass). [*Bekermann-2010-A*, *Mills-2003*]

Despite being prelimary, the present results demonstrate the potential of such nanocomposites for self-cleaning and anti-fogging surfaces. [*Kansal-2007*, *Kuo-2007*, *Sun-2001*]

❖ 6.3.5 Gas Sensing Properties

Investigation of the composite gas sensing performances was addressed at the detection of acetone, ethanol and nitrogen dioxide, and selected dynamic responses are displayed in **figures 6.11 (a-c)**. (Technical details and definitions of responses, response and recovery times can be found in **paragraph 8.6.4**.) As can be observed, the measured conductance underwent an increase in the presence of reducing gases (CH_3COCH_3, CH_3CH_2OH, **figures 6.11 (a-b)**), whereas the opposite phenomenon was revealed upon contact with NO_2, an oxidizing analyte (**figure 6.11 (b)**). Such a behavior, typical for *n*-type SCs, [*Barreca-2010-A*, *Hwang-2009*] was related to the higher overall content of the ZnO phase with respect to Co_3O_4 (see **6.3.2** and **6.3.3**). Furthermore, for all the tested analytes the conductance variation progressively increased with the gas concentration, enabling to rule out appreciable saturation effects under the adopted conditions. The almost complete recovery of the baseline conductance values at the end of each pulse indicated a reversible interaction between the sensing element and the target analytes.

The generally accepted sensing mechanism for similar SC systems is based on the initial dissociative chemisorption of oxygen at the sensor surface, resulting in the formation of negatively charged oxygen species (see also **paragraph 3.4.6**). [*Barreca-2010-C*, *Barreca-2010-A*, *Barreca-2011-C*, *Hwang-2009*, *Kim-2010*, *Na-2011*] Upon adsorption of CH_3CH_2OH or CH_3COCH_3, oxygen species promote their oxidation to CO_2 and H_2O and the concomitant release of electrons into the system conduction band, increasing thus the concentration of main charge carriers and, hence, the measured conductance. In a different way, upon sensing of an oxidizing gas, such as NO_2, electrons are withdrawn from the SC surface, resulting in a conductance decrease. Irrespective of the target gas, the sharp conductance variation observed on the analyte injection, followed by a slower increase up to the end of the pulse, suggested that the analyte chemisorption was the rate-determining step for the overall process. [*Barreca-2010-C*, *Barreca-2011-A*]

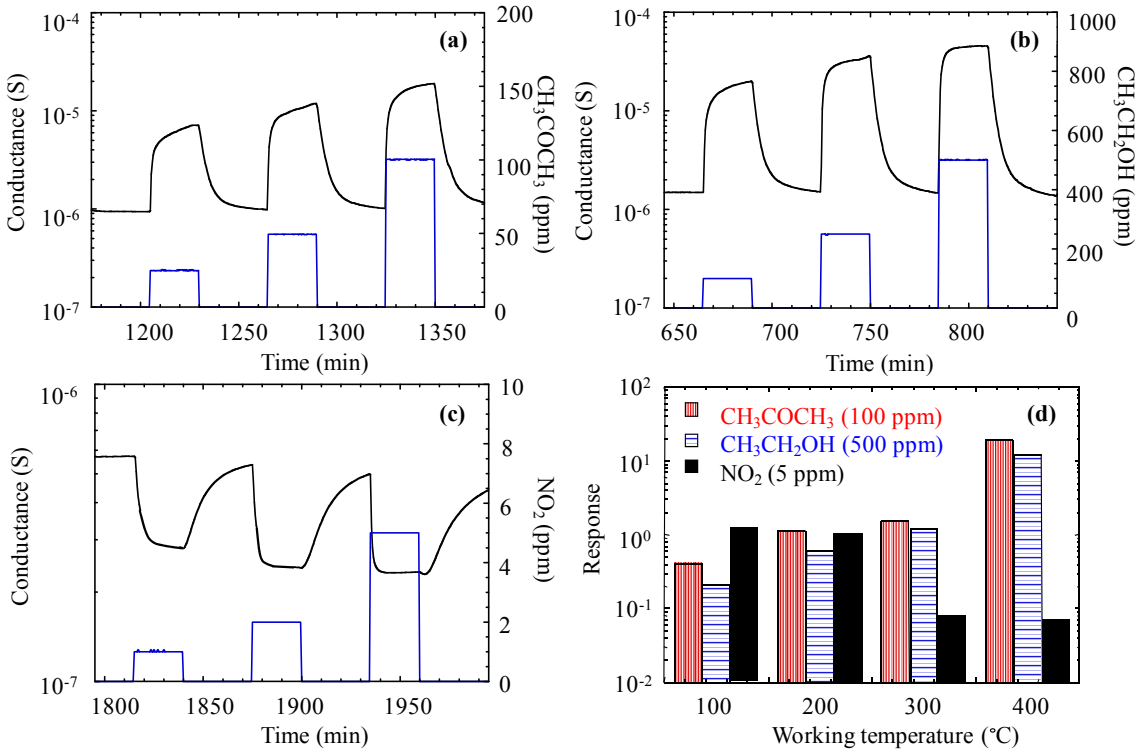

Figure 6.11: Gas sensing responses (black) of a Co_3O_4/ZnO sensor (**ZnCo_10(Al)**, see **table 6.1** and **figure 6.4**) toward square concentration pulses (blue) of (a) CH_3COCH_3, (b) CH_3CH_2OH, and (c) NO_2. Working temperatures = (a, b) 400 and (c) 200 °C. (d) Dependence of the response on the operating temperature for selected analyte concentrations (specimen **ZnCo_10(Al)**).

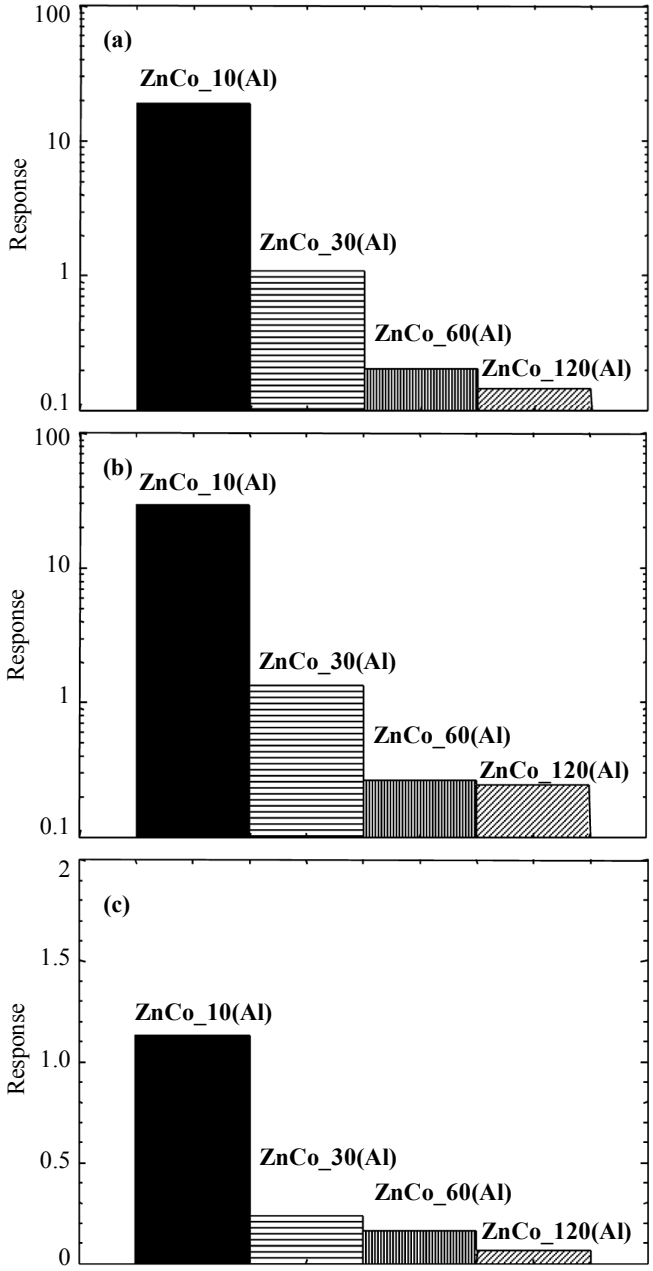

Figure 6.12: Responses toward (a) 100 ppm CH_3COCH_3, (b) 500 ppm CH_3CH_2OH, and (c) 5 ppm NO_2 for nanocomposites characterized by a different Co_3O_4 deposition time (see **table 5.1**). Working temperatures = (a, b) 400 and (c) 200 °C.

In view of practical applications, the sensor selectivity is a key concern and, at the same time, an open problem still far from being completely solved. [*Barreca-2011-A*, *Na-2011*] In the present work, the selectivity towards reducing or oxidizing gases could be controlled as a function of the sensor working temperature (**figure 6.11 (d)**). Indeed, at 100°C the measured responses to NO_2 (> 1) were higher than the corresponding values

for CH_3COCH_3 and CH_3CH_2OH. Conversely, for working temperatures higher than 200°C, the response to nitrogen dioxide progressively lowered, and a net increase of the responses to reducing gases was detected at 400°C, yielding values higher than 10. These results are of interest in view of technological application of the current sensors in the presence of gas mixtures under real-world conditions.

The responses of nanocomposites characterized by different Co_3O_4 deposition times toward fixed concentrations of CH_3COCH_3, CH_3CH_2OH, and NO_2 are displayed in **figure 6.12**. As can be observed, irrespective of the target analyte, the system performances decreased on going from sample **ZnCo_10(Al)** to **ZnCo_120(Al)**. This result can be likely ascribed to the concurrence of two main factors, i.e. the increased Co_3O_4 particle size and the partial reduction of the system porosity for the highest cobalt oxide loadings (see also comments to **figure 6.13**). These findings indicate that the best performances correspond to a Co/Zn ratio ensuring, at the same time, an efficient interfacial contact between ZnO and Co_3O_4 and a high surface area available for gas adsorption.

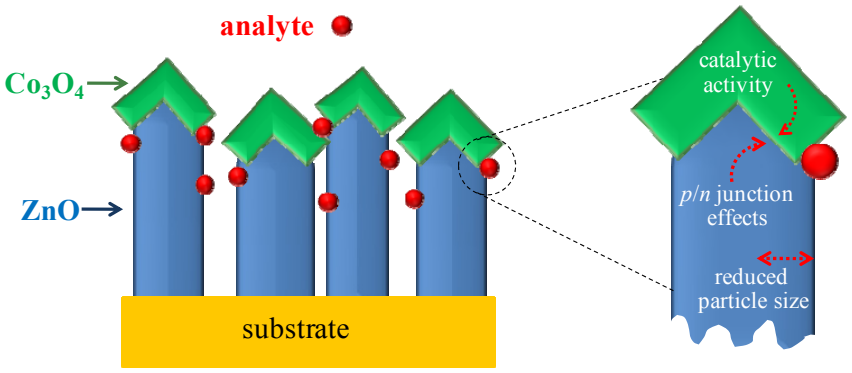

Figure 6.13: Schematic representation of the main phenomena beneficially affecting the gas sensing behaviour of the present Co_3O_4/ZnO nanocomposites.

In the case of specimen **ZnCo_10(Al)**, where such conditions are likely fulfilled, the sensor performances result appreciably better than those of our previous studies on pure, Au-doped or F-doped Co_3O_4 (see also **4.4.6**), [*Barreca-2010-C*, *Barreca-2011-C*] and comparable to the results obtained by Na et al., [*Na-2011*] the only work on Co_3O_4/ZnO gas sensors reported so far. Such results can be explained by considering that *p*-Co_3O_4/*n*-ZnO junctions produce an improved charge separation at the interface between the two

oxides, generating, in turn, an enhanced conductance modulation upon interaction with the target gases (**figure 6.13**).

In this context, the reduced particle size and the well-known catalytic activity of cobalt oxide are believed to play a further beneficial role on the functional behavior. [*Na-2011*] It is worth observing that whereas *n*-type metal oxides only chemisorb as much oxygen as necessary to compensate their deficiencies, the concentration of surface oxygen on *p*-type SCs is significantly higher (see also **4.2**). [*Barreca-2011-C*, *Kim-2010*] As a consequence, the co-presence of Co_3O_4 and ZnO, with an intimate contact between them, can further contribute to the improvement of the composite sensor performances.

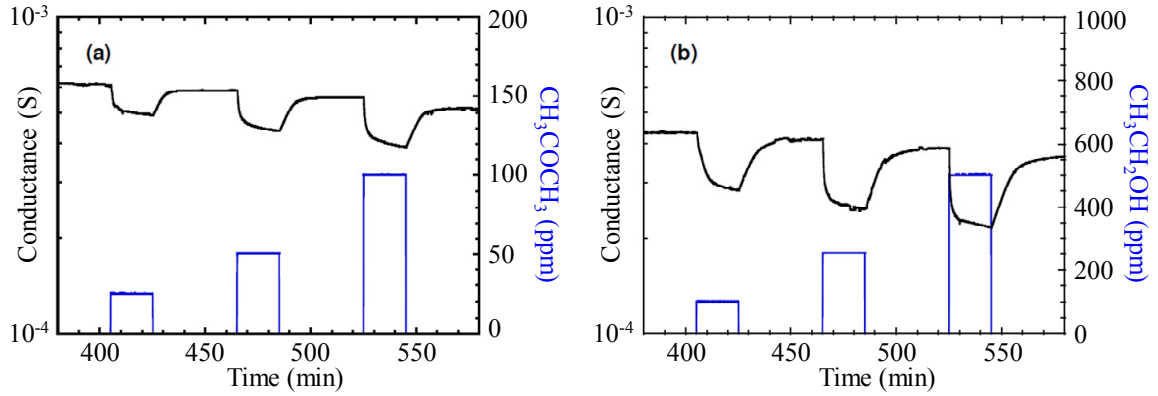

Figure 6.14: Dynamic response (black) of a bare Co_3O_4 film towards square concentration pulses (blue) of CH_3COCH_3 (a) and CH_3CH_2OH (b). Working temperature = 400°C.

To validate the above observations, a bare Co_3O_4 film was grown directly on Al_2O_3 adopting the same synthesis conditions used for cobalt oxide in specimen **ZnCo_10(Al)**. As expected, upon exposure to reducing gases such as acetone or ethanol (see **figure 6.14**), Co_3O_4 displayed a conductance reduction, in line with its *p*-type behaviour. [*Barreca-2011-C*] Apart from this difference with respect to sample **ZnCo_10(Al)**, the response values extrapolated by **figure 6.14** were more than one order of magnitude lower than the ones obtained for the corresponding Co_3O_4/ZnO composite under the same testing conditions (see also **figures 6.11** and **6.12**). As previously discussed, these findings highlight beneficial synergistic effects originating from Co_3O_4/ZnO coupling. Similar results were also observed for the detection of NO_2. In this case, whereas

Co_3O_4/ZnO possessed a remarkable sensitivity for such analyte, bare Co_3O_4 displayed an almost negligible response, in line with results presented in **4.4.6**.

In the literature, ZnO deposits with thickness comparable to the zinc oxide layer of the present Co_3O_4/ZnO nanocomposites have been reported to display gas sensing performances both higher or lower that the ones reported above. [*Al-Hardan-2010*, *Barreca-2010-A*, *Kakati-2010*, *Trinh-2011*] Such issue indicates that, beside film thickness, gas sensing performances are also affected by other parameters (e.g., crystallite size, surface area, defect content,...), evidencing thus the importance of both material design and morphological/ structural control.

❖ 6.4 Conclusions

The work presented in this chapter was focused on the deposition of *p*-Co_3O_4/*n*-ZnO nanocomposites by a two-step PECVD process, consisting in the growth of Co_3O_4 crystallites on the tips of 1D-like ZnO under relatively mild processing conditions (20 W, 200 – 300°C). An extensive characterization of the system structure, morphology and composition unambiguously evidenced the co-existence of the two single-phase oxides and an increasing Co_3O_4 overall loading on top of the ZnO with increasing Co_3O_4 deposition time. The obtained systems were highly pure and characterized by an intimate Co_3O_4/ZnO contact.

Since such axial nanoheterostructures are promising candidates for the exploitation of the *p*/*n* interface for potential functional applications, we tested the Co_3O_4/ZnO material in PH and PCO, revealing activity for light-activated functional applications, such as antifogging or self-cleaning materials. Despite being preliminary, the measured PCO activities are competitive with the current bench mark material (Pilkington® Active glass). Furthermore, tests of the alumina based composites in the detection of reducing (CH_3CH_2OH, CH_3COCH_3) and oxidizing (NO_2) gases revealed *n*-type behavior, due to the higher overall content of the ZnO phase. Gas sensing interactions with all target analytes were reversible, a key issue in view of eventual technological applications. The sensing performances were dependent on the Co/Zn ratio, i.e. the interfacial contact between ZnO and Co_3O_4 and the systems porosity. As a consequence, the best

performances were obtained using **ZnCo_10(Al)**, characterized by the lowest Co_3O_4 loading, being superior compared to pure, Au- or F-doped Co_3O_4 sensors (see also **4.4.6**) and comparable to the results obtained by Na et al., the only work on Co_3O_4/ZnO gas sensors reported so far. [*Na-2011*] Such results can be attributed to the co-presence of several beneficial phenomena: (i) the reduced particle size, enabling enhanced conductance modulations upon interaction with the target analytes; (ii) *p*/*n* junction effects at the Co_3O_4/ZnO interface, inducing an extension of the electron depletion layer; (iii) the Co_3O_4 catalytic activity, promoting the chemical reactions taking place during the sensing process.

Overall, the growth strategy adapted in this work paves the way to fabricate metal oxide nanocomposites with axial alignment under mild processing conditions and opens intriguing perspectives for the design of *p*/*n* composite nanoarchitectures for different kinds of applications, from heterogeneous catalysis to photo-induced pollutant degradation and ferromagnets in spintronic devices.

7. Summary and Perspectives

This PhD thesis has been devoted to the development of innovative vapor-phase routes to the synthesis of multifunctional metal oxide nanostructures.

In particular, the attention has been devoted to the use of Chemical Vapor Deposition processes (CVD, PECVD), versatile means for the obtainment of nanosystems with tailored features. The most attractive characteristics of such techniques are the possibility of obtaining a conformal coverage of complex-shaped substrates and of achieving prescribed material features by a proper choice of the precursor compound and its activation pathway. In this context, PECVD enables to obtain supported nanomaterials under mild conditions thanks to the unique features of non-equilibrium plasmas. Furthermore, the concurrence between growth and ablation, as well as electric field effects, offer peculiar degrees of freedoms in the tailoring of metal oxide systems.

Another promising vapor-phase process is sputtering, enabling the bottom-up synthesis of nanostructures with well defined composition and at low substrate temperatures, down even to the room one. These characteristics, in combination with a high infiltration power, candidate sputtering as an amenable route for the development of hybrid processes in the synthesis of composite materials.

Basing on the above considerations, the main aim of the thesis was the development of versatile synthesis procedures for the obtainment of multifunctional zinc and cobalt oxide based nanostructures by CVD, PECVD, sputtering and their synergistic combinations. A relevant part of research efforts has been devoted to the synthesis and characterization of suitable metal organic precursors, endowed with high volatility and clean decomposition patterns, as required for CVD application. Composition, morphology, microstructure and optical properties of the obtained nanosystems were investigated by means of a multi-technique approach, involving FE-SEM, AFM, GIXRD, (HR)TEM, EDXS, RBS, XPS/XE-AES, SIMS, FT-IR, UV-Vis and PL measurements. Functional validation was aimed at investigating the material functional performances in:

- energetics, with particular regard to light-induced H_2 production from aqueous solutions;
- photo-induced hydrophilicity and photocatalytic performances in pollutant oxidation;
- gas sensing of flammable/toxic gases.

The key results of the research activity are briefly summed up in the following.

❖ Zinc Oxide Nanostructures (Chapter 3)

The two novel volatile bis(ketoiminato) zinc compounds with clean decomposition pattern, $[Zn\{[(CH_2)_xOCH_3]NC(CH_3)=C(H)C(CH_3)=O\}_2]$ (**1**: $x = 2$; **2**: $x = 3$), have been tested in the thermal CVD of ZnO, yielding very pure and <001> oriented ZnO films of high crystalline quality. Encouraged by these results and in order to achieve a better control of the ZnO nanostructure growth at lowered deposition temperatures, PECVD using **1** and **2** was carried out. Pure and strongly <001> oriented ZnO nanorod arrays with a tailored spatial organization have been grown in Ar/O_2 plasmas under mild conditions (optimal 200 - 300°C). These results have been attributed to the beneficial effects arising from cold plasma activation, that enabled a fine-tuning of the system structure and morphology, from continuous films to oriented nanorods. This control had a key importance for the PSH and PCO properties of Si(100) supported NR arrays, since a direct dependence of the performances on the ZnO structure and morphology was observed. The highest PSH and PCO activity was obtained for long and sparse ZnO nanorods, exhibiting a high surface area and enabling an improved light trapping.

3D-1D urchin-like structures were obtained upon depositing ZnO NR arrays on polycrystalline Al_2O_3 substrates, and their potential for the detection of various oxidizing and reducing gases has been studied. Very high responses were obtained, along with the possibility to discriminate between reducing and oxidizing gases as a function of the operation temperature. These promising features were related to the high surface-to-volume ratio of the urchin-like ZnO and to their reduced lateral dimensions, enabling improved conductance modulation upon interaction with the analytes.

❖ Co_3O_4 (Chapter 4)

Pure and fluorine-doped Co_3O_4 nanodeposits were obtained by the PECVD from $[Co(dpm)_2]$ (**3**) and $[Co(hfa)_2{\cdot}TMEDA]$ (**4**) in Ar/O_2 plasmas at temperatures from 100 – 400°C. The use of **3** and **4** as CVD Co sources was motivated by their air-stability, volatility and clean decomposition pattern. A proper choice of the PECVD processing parameters allowed to synthesize Co_3O_4-based nanomaterials with tailored properties on diverse substrates.

In particular, pure and strongly oriented Co_3O_4 thin films were grown on MgO(100) and $MgAl_2O_4$(100) at temperatures as low as 100°C, an outstanding results, since the

synthesis of expitaxial/strongly oriented usually involves harsh conditions in terms of energy supply.

This successful synthesis strategy was further adopted for the growth of Co_3O_4 on Si(100) and Al_2O_3 substrates, in view of their functional tailoring for photocatalytic H_2 generation and gas sensing applications, respectively. In this context, key efforts were dedicated to F-doping and its impact on the physico-chemical and functional features of Co_3O_4. In fact, the use of [$Co(hfa)_2$·TMEDA] (**4**) in the plasma process led to the generation of fluorine radicals and thus allowed to achieve a homogeneous and controllable fluorine-doping of the Co_3O_4 systems.

Interestingly, UV-Vis measurements showed that the fluorine incorporation led to an increase of the absorption coefficient and to a 5-fold activity increase in photocatalytic H_2 generation under UV illumination. These improved performances with respect to pure Co_3O_4 were ascribed to an enhanced light absorption and the role of F as a passivation agent, resulting in a reduced carrier trapping.

As regards gas sensing, F-Co_3O_4 yielded higher responses for the detection of acetone and ethanol than the corresponding pure Co_3O_4 specimens. In addition, fluorine-introduction led to enhanced responses and higher reversibility of the sensing processes, as well as to decreased working temperature. The observed attractive sensing properties of F-Co_3O_4 were mainly related to an enhanced Lewis acidity of Co surface sites, promoting the system catalytic activity.

- **Ag/ZnO (Chapter 5)**

An innovative plasma-assisted route for the growth and functional tailoring of Ag/ZnO nanocomposites has been presented, based on ZnO NR synthesis by PECVD (**chapter 3**) and the subsequent over-dispersion of different Ag amounts by variation of the sputtering time. Under mild conditions a high dispersion of Ag nanoparticles on the ZnO matrices was achieved. In particular, the Ag NPs distribution and size could be controlled as a function of the sputtering time and post-annealing, the latter also affecting Ag(0)-Ag(I) inter-conversion.

The physico-chemical features of the Ag/ZnO systems had a direct impact on the functional performances. In the photocatalytic H_2 generation by photo-reforming, the use of the Ag/ZnO materials resulted in very promising and stable responses under both UV

and Vis irradiation, whereas pure ZnO was not active. This behaviour, enabled by the intimate Ag/ZnO contact was related to the formation of Ag/ZnO Schottky or Ag_2O-ZnO *p*/*n* junctions, improving charge carrier separation. Further contributions arose from the co-presence of Ag(0)-Ag(I), the latter possessing a favourable catalytic activity. For the H_2 detection, Ag loading on ZnO NR arrays, led to very high responses without any saturation at moderate operation temperatures (200°C). These attractive performances were related to the synergy of the peculiar ZnO morphology with the catalytic properties of Ag NPs.

Overall, by the combined approach of PECVD and sputtering multifunctional platforms for the sustainable generation and sensing of hydrogen were both prepared and operated under mild conditions, beneficial in terms of cost- and energy dissipitation.

- **Co_3O_4/ZnO (Chapter 6)**

A novel two-step PECVD synthesis has been developed for the growth of Si(100) and Al_2O_3 supported *p*-Co_3O_4/*n*-ZnO nanocomposites, consisting of the PECVD of ZnO NR arrays followed by over-growth of Co_3O_4 from [$Co(dpm)_2$] (**3**) at 200°C in Ar/O_2 plasmas. The Co_3O_4 loading was varied as a function of its deposition time (10 min – 120 min). The composite morphological, structural and compositional evolution with increasing Co_3O_4 loading, i.e. deposition time, were systematically investigated. The co-existence of both single-phase oxides with a close contact of Co_3O_4 grains with the underlying ZnO matrices, were clearly evidenced.

Preliminary PH and PCO studies showed a change of the surface properties from hydrophobic to hydrophilic upon UV irradiation, with a stable hydrophilicity for at least 24 hours. Furthermore, the activity of the Co_3O_4/ZnO materials in the photo-activated oxidation of TPA was competitive to that of the bench-mark Pilkington® material. As regards gas detection, Co_3O_4/ZnO showed to be sensitive towards reducing and oxidizing analytes, namely CH_3CH_2OH, CH_3COCH_3 and NO_2, and a certain selectivity depending on the working temperature, has been observed. These promising functional properties can be traced back to a reduced particle size, *p*/*n* junction effects at Co_3O_4/ZnO interfaces and the catalytic activity by Co_3O_4.

Due to the encouraging results, more detailed investigations of the Co_3O_4/ZnO structure (TEM) and systematic studies on the interrelationships between the composite physico-chemical properties and functional behaviour will be undertaken

❖ Perspectives

In conclusion, the presented work has concerned the development of oxide nanomaterials as multifunctional platforms by innovative vapour-phase routes. The unique versatility of the adopted approaches will enable to transfer the presented synthesis strategies for the growth of different metal oxide systems (like Fe_xO_y/ZnO, Fe_xO_y/Co_3O_4, ...), as well as their modification by doping or composite formation. In particular, the possibility of in-situ anion-doping in PECVD will be further exploited, one near aim being the fluorine-doping of ZnO by use of [$Zn(hfa)_2$·TMEDA], for the subsequent development Fe_xO_y/F-ZnO systems. Using sputtering processes, it is also planned to functionalize the obtained systems with metal particles (Cu, Ag, Au,...). In this regard, the attention will be devoted to obtain improved performances in sensing and photo-activated applications, but also to design of nano-electrodes to be integrated into lithium-ion batteries.

8. Experimental

In this chapter, synthesis and characterization of the metal organic compounds **1** - **4**, and the deposition experiments along with the reactor set-ups are presented. Basic principles and experimental details of the analysis methods used for the characterization of the precursors and nanodeposits are also provided. **Paragraphs 8.1** and **8.2** deal with the syntheses of the zinc and cobalt precursors, respectively. Since the metal organic compounds play a crucial rule in CVD processes, their composition, structure, thermal properties and fragmentation patterns have been investigated. The corresponding results are briefly discussed in **paragraph 8.1** and **8.2**. The set-ups of the CVD and sputtering instruments are presented in **paragraph 8.3**, and an overview of all depositions performed in this thesis is given. In **paragraph 8.4**, precursor characterization techniques are described. The obtained nano materials were analyzed by a combination of advanced characterization techniques with respect to their morphology, composition, structure and optical properties (**paragraph 8.5**). In **paragraph 8.6**, the experimental details of the functional characterizations performed are provided. In particular, photo-induced superhydrophilicity, photocatalytic oxidation, photocatalytic H_2 production and gas sensing behaviour were investigated.

❖ 8.1 Synthesis and Characterization of Bis(ketoiminato)zinc (II) Complexes 1 and 2

❖ 8.1.1 Synthesis of **1** and **2**

The zinc ketoiminates were obtained by the stoichiometric reaction of DEZ with the neutral ketoiminate in hexane (**scheme 8.1**). Compounds **1** and **2** were characterized by EA, ^{1}H-NMR and ^{13}C-NMR spectroscopy, Single Crystal X-ray Diffraction and EI-MS. [*Bekermann-2010-C*] As both the compounds are very similar (with a small change in the ligand skeleton), the synthesis procedure, structural, and precursor properties of $[Zn\{[(CH_2)_2OCH_3]NC(CH_3)=C(H)C(CH_3)=O\}_2]$ (**1**) will be discussed in detail as a representative example.

All manipulations of air- and moisture-sensitive compounds were performed in a conventional vacuum/argon line by using standard Schlenk techniques. Pure DEZ was purchased from ABCR and used as received. Preparations of samples for further analysis

were carried out in argon-filled glove boxes (MBraun, Lab-Master). All solvents were purified by an MBraun solvent purification system and stored over molecular sieves (4 Å).

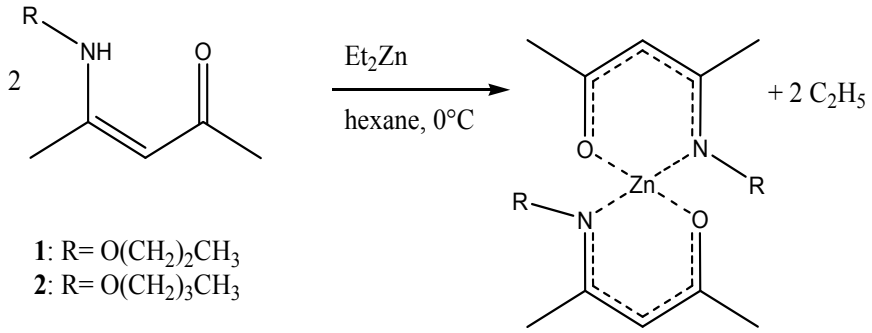

1: R= $O(CH_2)_2CH_3$
2: R= $O(CH_2)_3CH_3$

(reaction 8.1)

Scheme 8.1: Reaction scheme for the synthesis of **1** and **2**.

For the synthesis of **1**, DEZ (3 ml, 29.39 mmol) was dissolved in dry hexane (150 ml). The solution was stirred for 12 h and cooled down to –15°C. To this mixture $(CH_3OCH_2CH_2)N(H)C(CH_3)=C(H)C(CH_3)=O$ (7.11 ml, 58.78 mmol) was added by syringe. The reaction was heated at reflux for 1.5 h and afterwards stirred for 12 h at room temperature. The solvent was removed in vacuo at room temperature. The solid residue was washed with dry pentane (3 × 5 ml) and dried again. The product was obtained as a light yellow powder (8.81 g, 23.43 mmol, 79.7 %). Its chemical composition was determined to be C 51.02, H 7.48, N 7.48 by EA, as theoretically expected for the sum formula $C_{16}H_{28}N_2O_4Zn$ (377.80) (C 51.07, H 7.45, N 7.45). The synthesis procedure of **2** was similar to that adopted for **1**. DEZ (3 ml, 29.39 mmol) was treated with $(CH_3OCH_2CH_2CH_2)N(H)C(CH_3)=C(H)C(CH_3)=O$ (7.68 ml, 58.78 mmol). The product $C_{18}H_{32}N_2O_4Zn$ (405.85) was obtained as a light-yellow powder (8.00 g, 19.80 mmol, 67.3 %) and had the composition C 53.51, H 7.93, N 6.86 (calculated: C 53.47, H 7.92, N 6.93).

❖ 8.1.2 NMR of **1** and **2**

In the ^{1}H-NMR of compound **1** (**figure 8.1**), the two singlets at δ = 1.57 and 1.97 ppm correspond to the methyl groups attached to the chelate ring, whereas those shifted low field to δ = 3.05 ppm can be attributed to the methyl group of the ether arm. The singlet at δ = 4.78 ppm corresponding to one proton can be attributed to the hydrogen atom at the chelate ring. At δ = 3.25 and 3.46 ppm two broad signals appear with an integration

corresponding to four protons; these signals are assigned to the ether side chain. Below, tables of all NMR signals can be found.

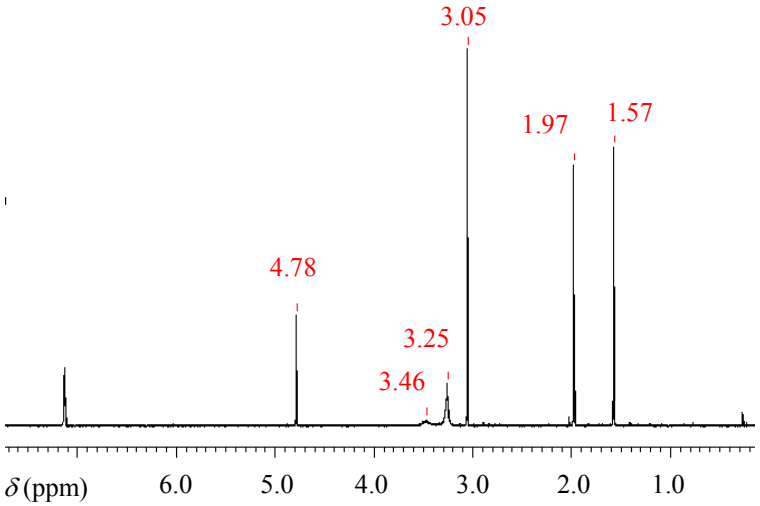

Figure 8.1: ^{1}H NMR of **1**.

Table 8.1: NMR data of **1**.

^{1}H NMR (250 MHz, C_6D_6, 25 °C)

δ [ppm]			attribution
1.57	s	3 H	-NC(C**H**$_3$)
1.97	s	3 H	-OC(C**H**$_3$)
3.05	s	3 H	N(CH$_2$)$_2$OC**H**$_3$
3.25 and 3.46	2 m	4 H	-N(C**H**$_2$)$_2$CH$_3$
4.78	s	1 H	OC(CH$_3$)C(**H**)C(CH$_3$)N

^{13}C NMR (100.6 MHz, C_6D_6, 25 °C)

δ [ppm]	attribution
22.02	NC(**C**H$_3$)
27.84	OC(**C**H$_3$)
50.51	N(**C**H$_2$)$_2$O(CH$_3$)
58.45	N(CH$_2$)$_2$O(**C**H$_3$)
96.87	OC(CH$_3$)**C**(H)C(CH$_3$)N
172.48	OC(CH$_3$)C(H)**C**(CH$_3$)N
183.47	O**C**(CH$_3$)C(H)C(CH$_3$)N

Table 8.2: NMR data of **2**.

^{1}H NMR (250 MHz, C_6D_6, 25 °C)

δ [ppm]			attribution
1.61	s	3 H	-NC(C**H**$_3$)
1.86	quint.	2 H	NCH$_2$C**H**$_2$CH$_2$OCH$_3$
2.01	s	3 H	-OC(C**H**$_3$)
3.02	s	3 H	N(CH$_2$)$_3$OC**H**$_3$
3.16	t	2 H	NCH$_2$CH$_2$C**H**$_2$OCH$_3$
3.32	t	2 H	NC**H**$_2$CH$_2$CH$_2$OCH$_3$
4.80	s	1 H	OC(CH$_3$)C(**H**)C(CH$_3$)N

^{13}C NMR (100.6 MHz, C_6D_6, 25 °C)

δ [ppm]	attribution
21.40	NC(**C**H$_3$)
27.77	OC(**C**H$_3$)
31.36	NCH$_2$**C**H$_2$CH$_2$OCH$_3$
48.06	NCH$_2$CH$_2$**C**H$_2$OCH$_3$
58.15	N(CH$_2$)$_3$O(**C**H$_3$)
70.17	N**C**H$_2$CH$_2$CH$_2$OCH$_3$
96.87	OC(CH$_3$)**C**(H)C(CH$_3$)N
172.48	OC(CH$_3$)C(H)**C**(CH$_3$)N
183.47	O**C**(CH$_3$)C(H)C(CH$_3$)N

❖ 8.1.3 Single Crystal X-ray Diffraction of **1**

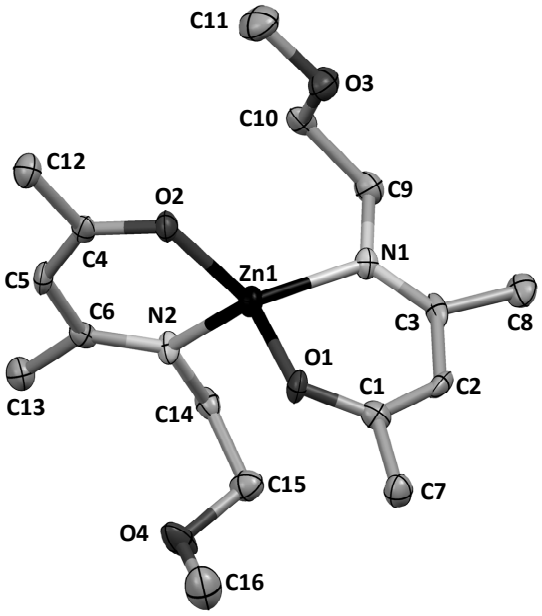

Figure 8.2: Molecular structure of **1** (see also reaction 8.1). Hydrogen atoms are removed for clarity. Ellipsoids are shown with 50 % of probability level.

Single crystals of **1** suitable for X-ray structural analysis were obtained from a saturated solution of the compound in toluene at –30°C over a period of 24 h. Molecule **1** crystallizes in the orthorhombic space group $Pca2_1$. The solid state structure of **1** with an atom-numbering scheme is shown in **figure 8.2**. Molecule **1** is a monomer and it consists of a distorted tetrahedral Zn center with two bidentate ketoiminate ligands. The coordination environment around the zinc is completed by the oxygen and nitrogen atoms of two ketoiminato ligands orthogonal to each other. The six-membered $ZnONC_3$ units are puckered. The oxygen atoms (O3 and O4) of Me–O–CH_2–CH_2–N are far away from the coordination sphere of the zinc center. The crystal structure indicates that the electrons are not completely delocalized in the six membered ring, for the following reasons: (i) The bite angles of the chelating ligands are 97.3 and 97.1°, respectively, and the angles O2–Zn1–N1, O1–Zn1–N2, O1–Zn1–O2, and N1–Zn1–N2 vary between 108.5 and 125.4°, deviating from those expected for an ideal tetrahedron. (ii) As expected, the Zn–O bonds with lengths of 1.955 and 1.939 Å are longer than those for the Zn–N bonds [1.990(2) Å and 1.984(2) Å]. (iii) The torsion angles indicate a non-planar six-membered ring. For a more detailed description of the crystal structure, crystal and structure refinement data see [*Bekermann-2010-C*].

❖ 8.1.4 EI-MS of **1** and **2**

The fragmentation mechanism of the bis(ketoiminato) precursors **1** and **2** was examined by EI-MS (**table 8.3**). Both compounds were clearly identified by their $M^{+\cdot}$ signals at *m*/*z* = 376 and 404 for **1** and **2**, respectively. Typical primary fragments were generated by the cleavage of methyl or ether groups from the remaining chelating ring. All recorded mass spectra strongly supported the complete cleavage of the whole ligand under EI-MS conditions. The decomposition pattern gave no evidence due to formation of fragments, containing Zn-C bonds, thus indicating, that the precursors might not incorporate C upon their use in ZnO CVD.

Table 8.3: EI-MS data for **1** and **2**.

1 fragments	mass [*m* /*z*]	relative intensity [%]	**2** fragments	mass [*m* /*z*]	relative intensity [%]
$M^{+\cdot}$	376	2.0	$M^{+\cdot}$	404	13.8
$M^{+\cdot}$ - $CH_3^{\cdot}$	361	1.6	$M^{+\cdot}$ - $CH_3^{\cdot}$	389	2.0
$M^{+\cdot}$ - $OCH_3^{\cdot}$	345	9.8	$M^{+\cdot}$ - $OCH_3^{\cdot}$	373	0.3
361 - C_2H_6 or - $CH_2O^{\cdot}$	331	13.8	$M^{+\cdot}$ - $C_3H_5^{\cdot}$	363	1.0
or $M^{+\cdot}$ - $CH_2OCH_3^{\cdot}$			$M^{+\cdot}$ - 58	346	1.0
$M^{+\cdot}$ - 1 ligand	220	100	$M^{+\cdot}$ - 1 ligand	234	100
			$OC_3H_6^{\cdot}$ or NC_3H_8	58	

❖ 8.1.5 Thermal Characterization of **1** and **2**

The melting points of **1** and **2** are 57 and 60°C, respectively. Both **1** and **2** can be quantitatively vaporized at 110 and 115°C, respectively, at 5 mbar, without any decomposition. Thermal analysis reveals a nearly one-step decomposition for both compounds (**figure 8.3**), which is desirable for CVD precursors. The temperature window between vaporization and decomposition is sufficiently large. The onset of volatilization for **1** is at 70°C, whereas in the case of **2** it is at 90°C. For **1**, a strong mass loss occurs between 130 and 280°C, whereas the main mass loss for compound **2** starts around 150°C. This shows that a marginal variation in the ligand structure has a distinct influence on the volatilization temperature. The sublimation behavior of the ketoiminato precursors was further investigated by isothermal TG experiments carried out at 120 and 140°C. In all cases, a linear weight loss was observed (**figure 8.3**), indicating that the precursors can

sublime at the set temperature with constant rates for a long period of time. The sublimation rates at 120°C were determined to be 9.3 µg min^{-1} for **1** and 20.1 µg min^{-1} for **2**. The linear trends in the isothermal curves show clean vaporization processes with no signs of premature decomposition.

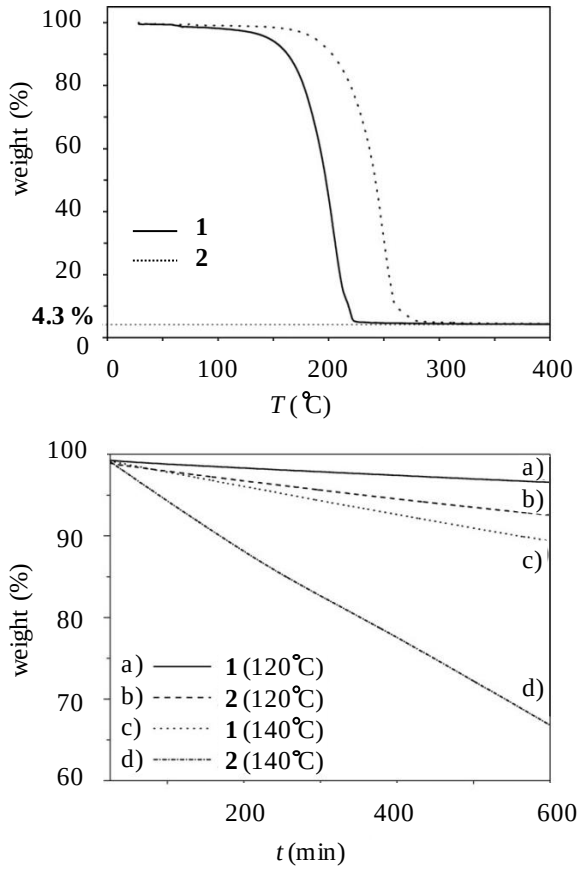

Figure 8.3: Thermal analysis of **1** and **2**. Top: TG (5 K min^{-1}, 300 ml min^{-1}); bottom: isothermal vaporization studies of **1** and **2** at two different temperatures.

❖ 8.2 Synthesis and Characterization of [$Co(dpm)_2$] (3) and [$Co(hfa)_2$·TMEDA] (4)

❖ 8.2.1 Synthesis of **3** and **4**

Both precursors, [$Co(dpm)_2$] **(3)** and [$Co(hfa)_2$·TMEDA] **(4)**, have already been reported and were synthesized according to the corresponding literature procedures. [*Bandoli-2009*, *Barreca-2001*] In order to gain a more thorough insight into their fragmentation and thermal properties, EI-MS and isothermal TG studies were carried out, prior to their use in PECVD.

❖ 8.2.2 EI-MS of **3** and **4**

Precursors **3** and **4** were characterized by EI-MS, since the ionization conditions used for EI-MS analyses are analogous to those adopted in PECVD processes. Thus it is reasonable to suppose that a similar fragmentation process also occurred during the plasma-assisted growth of Co_3O_4-based systems, explaining the effective fluorine-incorporation into the deposited material (see **paragraph 4.4.3**).

In the case of [Co(dpm)$_2$], the EI-MS spectrum (**figure 8.4**) was dominated by several species originating from the loss of the *β*-diketonate ligand and of the *tert*-butyl group, whose presence was also directly detected. [*Barreca-2001*] For [Co(hfa)$_2$·TMEDA] (**figure 8.4**), the detachment and fragmentation of both the TMEDA and hfa moieties were revealed. In particular, ions containing the *β*-diketonate ligand were involved in the elimination of CF_2/CF_3 species, whose formation was in agreement with compositional data on Co_3O_4 based deposits (see [*Gasparotto-2011-A*] and **paragraph 4.4.3**). A careful analysis of EI-MS results also revealed a mass loss of 19 a.m.u. from several ionic species (see for instance m/z = 589 → 570; m/z = 473 → 454). These results pointed out to the formation of fluorine radicals, accounting for the efficient Co_3O_4 fluorine-doping under the present PECVD conditions.

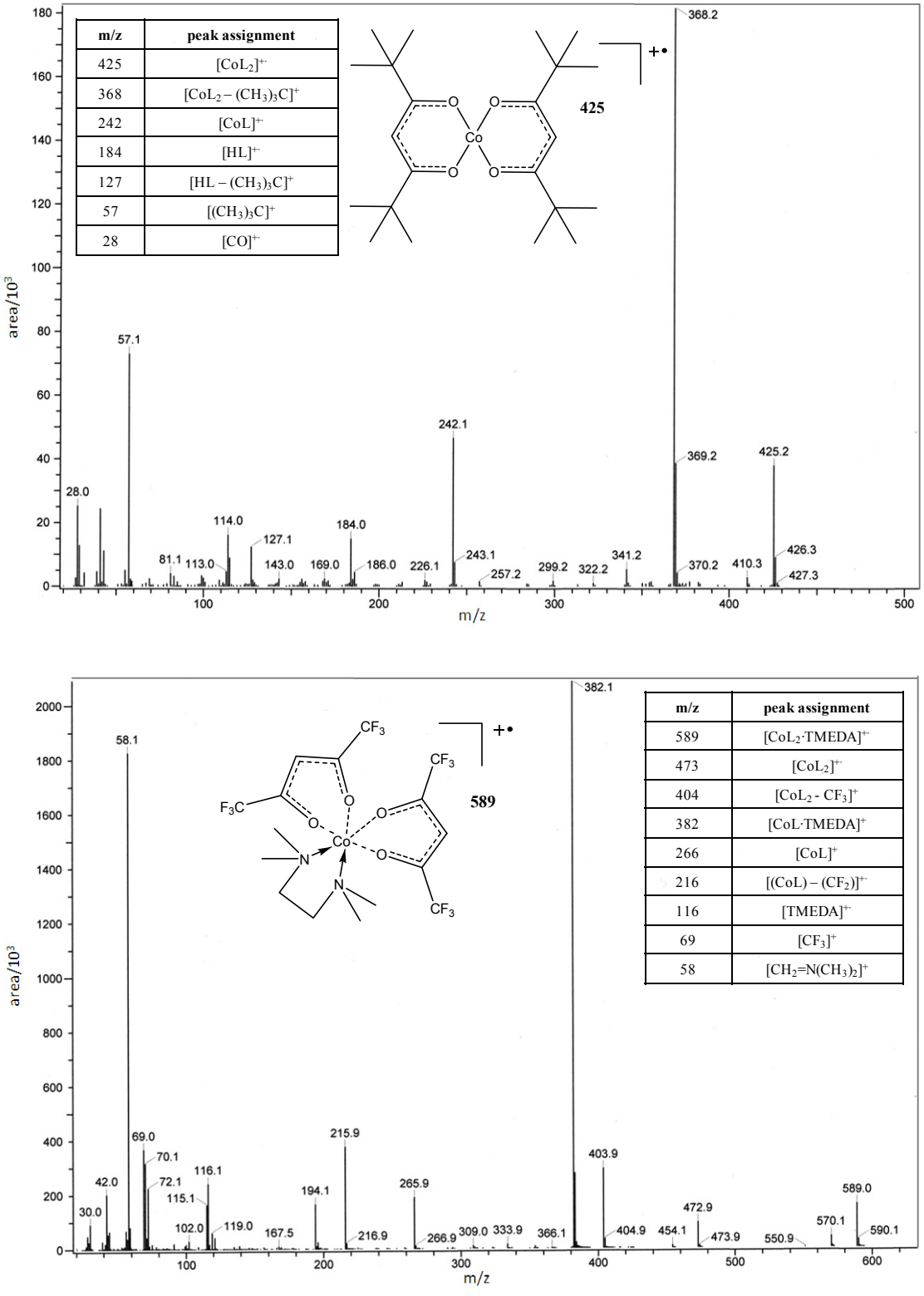

Figure 8.4: EI-MS spectrum of precursors **3** and **4**. The assignment of the main peaks is reported in the tables, where the symbol L indicated the dpm or the hfa ligand, respectively. The structure of the molecular ions is also sketched.

❖ 8.2.3 Thermal Characterization of **3** and **4**

The vaporization behaviours of **3** and **4** were further investigated by isothermal TG experiments. Both precursors revealed a linear weight loss at the set temperatures, 90 and 120°C (**figure 8.5**), indicating that they can sublime with constant rates for a long period of time. The vaporization rates at 90 °C (120 °C) were estimated to be 0.2 µg min^{-1} (2.9 µg min^{-1}) for **3** and 13.6 µg min^{-1} (100.0 µg min^{-1}) for **4**. The linear trends in the isothermal curves indicate clean vaporization processes with no signs of premature decomposition, a key point in view of the eventual compound applications in CVD and PECVD processes.

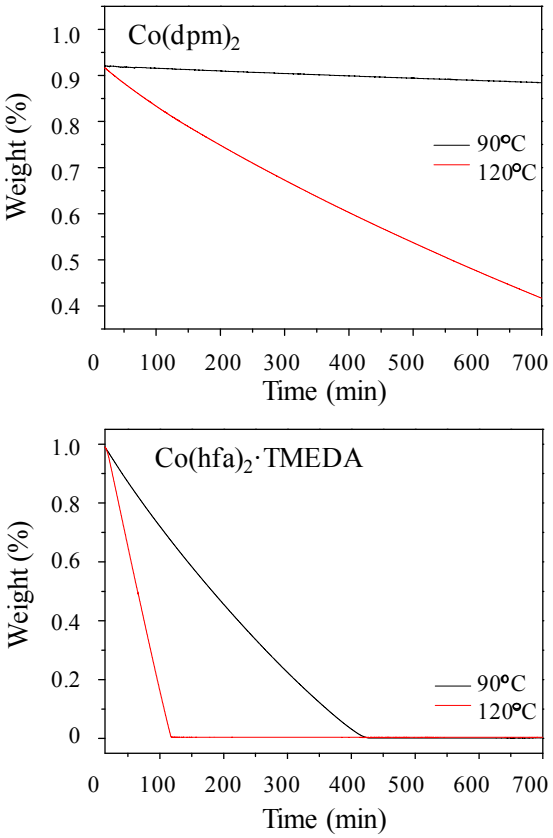

Figure 8.5: Isothermal vaporization studies of **3** and **4** at two different temperatures.

❖ 8.3 Reactor Set-ups and Applied Deposition Parameters

❖ 8.3.1 CVD Reactor Set-up

The self-built horizontal cold wall reactor used in this work is shown in **figure 8.6**. It is made up of a quartz tube, which is surrounded by a hollow glass cylinder, serving as

cooling mantle. In the inner quartz tube a horizontally placed graphite susceptor is inductively heated by high frequency. The substrate is positioned on a Si/C susceptor. Substrate temperature is measured by a pyrometer focused on its surface. The decomposition products are trapped into a nitrogen-cooled glass container. Beyond the cooling trap there are two pressure gauges and an electronic needle valve. The rotary pump serves as forepump for the turbo molecular pump (TMP). An electronic needle valve, connected to pressure readers, is positioned in front of the TMP to control the reactor pressure during deposition.

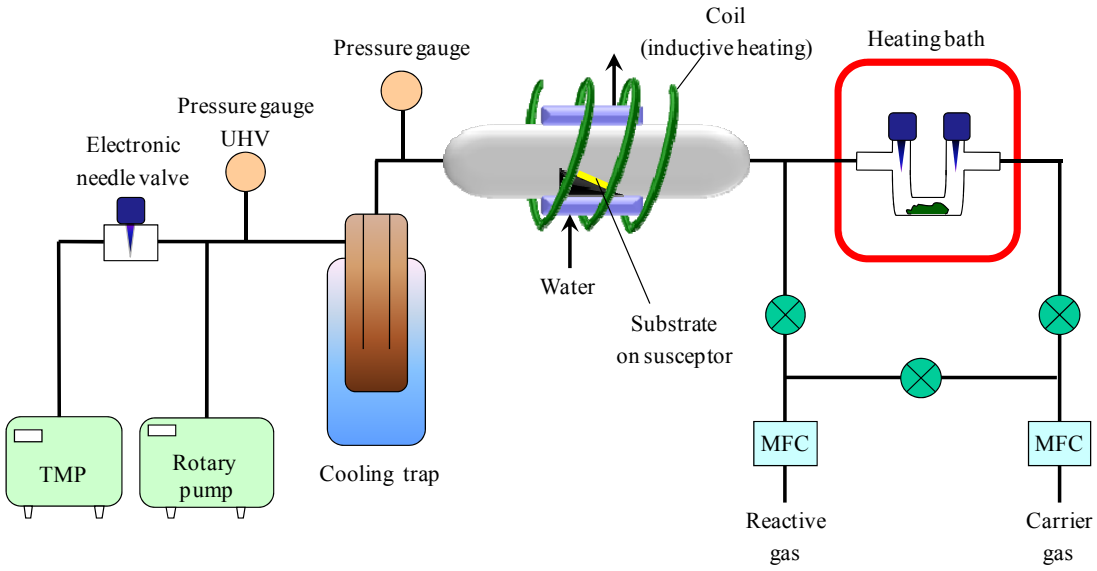

Figure 8.6: Scheme of the CVD reactor used (Ruhr-University Bochum).

The bubblers are u-form type glass tubes that are connected to the CVD system by two flanges. The carrier gas flow is led through the bubbler, taking the precursor gas into the reactor. The bubbler is heated by an air bath, and the temperature can directly be measured on the bubbler itself. The lines between air bath and reactor are heated by heating tapes to avoid precursor condensation. The system has a bypass through which direct introduction of a reactive gas into the deposition chamber is possible. All gas flows are controlled by mass flow controllers (MFCs). For the deposition of zinc oxide films, electronic grade nitrogen and oxygen were used as carrier gas and reactive gas, respectively.

Prior to each deposition, the substrates were ultrasonically cleaned in ethanol (10 min), distilled water (10 min), and dried in air. At the beginning of each deposition experiment the whole system was evacuated for one hour at 10^{-5} mbar to ensure removal of residual gases.

❖ 8.3.2 Deposition Parameters for CVD of ZnO (**3.3.1**)

Deposition of ZnO from $[Zn\{[(CH_2)_xOCH_3]NC(CH_3)=C(H)C(CH_3)=O\}_2]$ (**1**: $x = 2$; **2**: $x = 3$) was carried out using the self-built CVD reactor described in **8.3.1**. Total pressure (p), deposition time (t), N_2 and O_2 flow rates and vaporization temperature (T_{vap}) were maintained at 10.0 mbar, 90 min, 50 sccm and 130°C. The investigated range of substrate temperature (T) was 400 - 700°C. **Table 8.4** lists all applied deposition parameters. For sample indexing see **paragraph 3.3.1**.

Table 8.4: Deposition parameters for CVD of ZnO from **1** and **2**. For sample indexing see **paragraph 3.3.1**.

Material **Paragraph**	ZnO **3.3.1**
Precursor	$[Zn\{[(CH_2)_xOCH_3]NC(CH_3)=C(H)C(CH_3)=O\}_2]$ (**1**: $x = 2$; **2**: $x = 3$)
Precursor amount	0.15 g
T_{vap}	130°C
Substrate	Si(100), borosilicate
T	400 – 700°C
N_2 flow rate	50 sccm
O_2 flow rate	50 sccm
p	10 mbar
t	90 min

❖ 8.3.3 Plasma Reactor Set-up

For the PECVD experiments performed in the framework of this thesis, a two-electrode custom-built apparatus was used. [*Barreca-2003-A*] The instrumental set-up is sketched in **figure 8.7**. The apparatus, equipped with both rotary pump and TMP, consisted of a vacuum metal chamber with a first electrode powered by an RF generator and a second one electrically grounded, to which the substrates were fixed with metallic clips. In each experiment, the ground electrode was resistively heated and its temperature was measured by a thermocouple. The diameter of each electrode was 9 cm and the inter-electrode distance was fixed at 6 cm. Prior to each deposition, the system was evacuated to a base pressure lower than 10^{-5} mbar, as measured by an inverted magnetron gauge. Flow rate

values were controlled by flowmeters with ±1 sccm accuracy, whereas the deposition pressure was monitored by barocel-capacitance manometers. A RF generator is connected to one of the parallel electrodes, the RF electrode, by a matching system, while the second electrode serves as ground electrode (**figure 8.7**). The matching system, basically a condensator of tunable capacity, serves to optimize the energy transfer to the plasma, minimizing the reflected power.

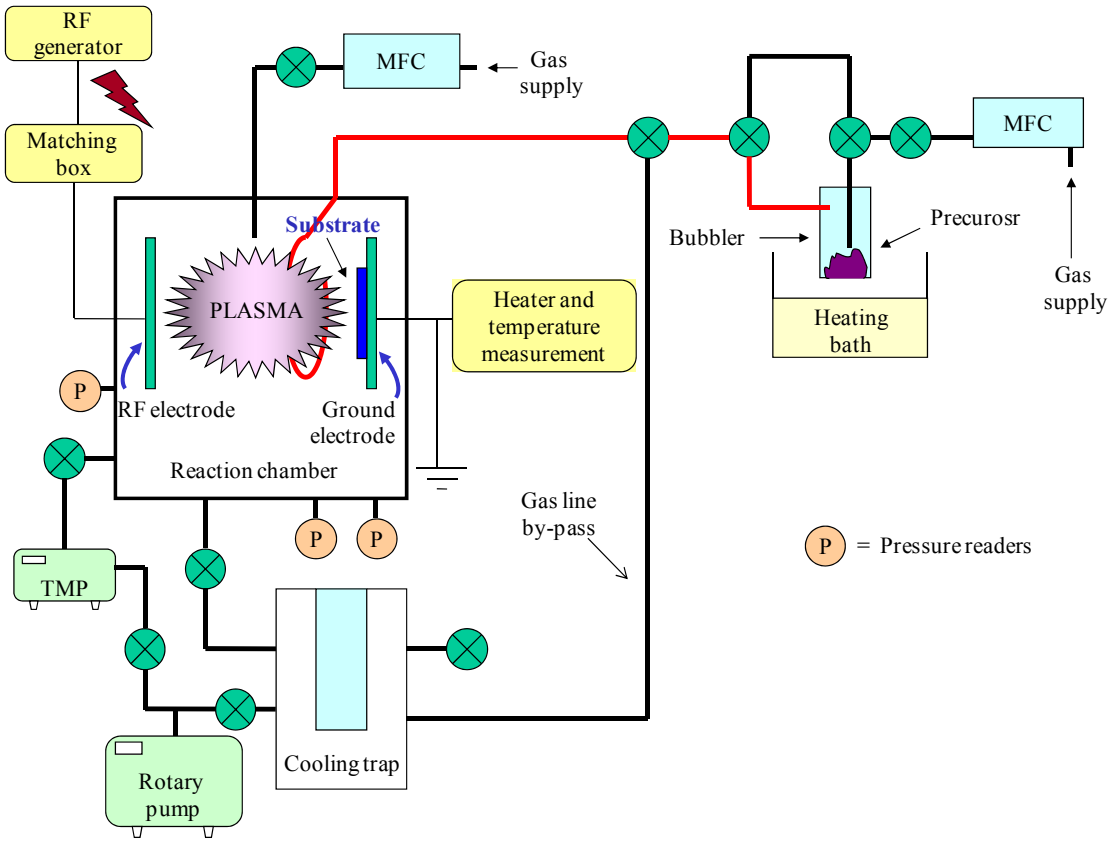

Figure 8.7: Representative scheme of the PECVD reactor used (Padova University).

Depositions were performed on *p*-type Si(100) substrates and polycrystalline Al_2O_3 slides. The former were cleaned without removing the native oxide layer, by iterative dipping in sulfonic detergent and distilled water, distilled water, acetone, and isopropylic alcohol. [*Armelao-1998*] The Al_2O_3 substrates were cleaned in dichloromethane and isopropanol by ultrasonification. Electronic grade Ar and O_2 were used as plasma sources. The precursor was placed in an external vessel heated by an oil bath and transported towards the deposition zone by an Ar flow. Two further auxiliary gas-lines were used to introduce Ar and O_2 gases directly into the reactor. To avoid undesired condensation phenomena, the gas lines connecting the precursor vessel and reaction chamber were heated.

Silver sputtering on ZnO deposits was carried out in the same plasma reactor, used for PECVD, described in this paragraph. The supported ZnO specimen and silver source were fixed on the ground electrode and RF electrode, respectively.

❖ 8.3.4 Deposition Parameters for PECVD of ZnO (**3.4.1**)

Depositions of ZnO from $[Zn\{[(CH_2)_xOCH_3]NC(CH_3)=C(H)C(CH_3)=O\}_2]$ (**1**: $x = 2$; **2**: $x = 3$) were carried out using the PECVD reactor described in **8.3.3**. Total pressure, deposition time, vaporization temperature, Ar (carrier) and Ar/O_2 flow rates were maintained at 1.0 mbar, 60 min, 140°C, 60 and 20/15 sccm. The ZnO systems have been studied as a function of precursor, substrate temperature and RF-power (P) used (**table 8.5**). For sample indexing see **paragraph 3.4.1**.

The ZnO matrices used for the composite materials (see **paragraphs 5.3.1** and **6.3.1**) were grown under optimized conditions (**table 8.5**).

Table 8.5: Deposition parameters for PECVD of ZnO from **1** and **2**. For sample indexing see the corresponding paragraphs assigned in this table.

Material **Paragraph**	ZnO **3.4.1**		ZnO for Ag/ZnO **5.3.1**	ZnO for Co_3O_4/ZnO **6.3.1**
Precursor	**1**	**2**	**2**	
Precursor amount	0.3 g		0.3 g	
T_{vap}	140°C		150°C	
Substrate	Si(100), Al_2O_3		Si(100), Al_2O_3	
T	100 – 400°C		300°C	
P	10 – 40 W	20 W	20 W	
Ar (carrier) flow rate	60 sccm		60 sccm	
Ar/O_2 flow rate	15/20 sccm		15/20 sccm	
p	1 mbar		1 mbar	
t	60 min		60 min	

❖ 8.3.5 Deposition Parameters for PECVD of Co_3O_4 (**4.3.1** and **4.4.1**)

Depositions of Co_3O_4 from $[Co(dpm)_2]$ (**3**) and $[Co(hfa)_2 \cdot TMEDA]$ (**4**) were carried out using the PECVD reactor described in **8.3.3**. Total pressure, RF-power, deposition time, T_{vap}(**3**), T_{vap}(**4**), Ar (carrier) and Ar/O_2 flow rates were maintained at 1.0 mbar, 20 W, 60 min, 90°C, 60°C, 60 and 20/15 sccm. The Co_3O_4 systems have been studied as a function of substrate and deposition temperature in **4.3.1** (**table 8.6**). In **4.4.1**, the influence of precursor and substrate temperature (**table 8.6**) on the morphology and composition of the (F-)Co_3O_4 deposits were investigated. For sample indexing see **4.3.1** and **4.4.1**.

Table 8.6: Deposition parameters for PECVD of Co_3O_4 from **3** and **4**. For sample indexing see the corresponding paragraphs assigned in this table.

Material **Paragraph**	Co_3O_4 **4.3.1**	(F-)Co_3O_4 **4.4.1**	
Precursor	**3**	**3**	**4**
Precursor amount	0.3 g	0.3 g	
T_{vap}	90°C	90°C	60°C
Substrate	Mg(100), $MgAl_2O_4$(100)	Si(100), Al_2O_3	
T	100 – 400°C	100 – 400°C	
P	20 W	20 W	
Ar (carrier) flow rate	60 sccm	60 sccm	
Ar/O_2 flow rate	15/20 sccm	15/20 sccm	
p	1 mbar	1 mbar	
t	60 min	60 min	

❖ 8.3.6 Deposition Parameters for PECVD/Sputtering of Ag/ZnO (**5.3.1**)

Initial PECVD of ZnO (from **2**) and subsequent sputtering of Ag were carried out using the plasma reactor described in **8.3.3**. Based on studies presented in **paragraph 3.4**, the ZnO matrices were grown under optimized condition (see **table 8.5**). Sputtering of Ag was performed at p = 0.3 mbar, P = 5 W, T = 60°C and Ar flow rates of 10 sccm. The Ag/ZnO systems have been studied as a function of silver sputtering time and annealing (see **table 8.7**). For sample indexing see **5.3.1**.

Table 8.7: Parameters for sputtering of Ag on ZnO (see **table 8.5** and **5.3.1**).

Material **Paragraph**	Ag for Ag/ZnO **5.3.1**
Target	Ag
Substrate	ZnO/Si(100), ZnO/Al_2O_3
T	60°C
P	5 W
Ar flow rate	10 sccm
p	0.3 mbar
t	10 - 150 min
Annealing	400°C in air

❖ 8.3.7 Deposition Parameters for PECVD of Co_3O_4/ZnO (**6.3.1**)

Depositions of Co_3O_4/ZnO from precursors **2** and **3** were performed using the PECVD reactor described in **8.3.3**. Based on studies presented in **paragraph 3.4**, the ZnO matrices were grown under optimized condition (see **table 8.5**). Subsequently, Co_3O_4 was grown at p = 1 mbar, P = 20 W, T = 200°C, T_{vap}(**3**) = 100°C and Ar (carrier) and Ar/O_2 flow rates of 60 and 20/15 sccm. The Co_3O_4/ZnO systems have been studied as a function of Co_3O_4 deposition time (see **table 8.8**). For sample indexing see **6.3.1**.

Table 8.8: Deposition parameters for PECVD of Co_3O_4 on ZnO (see **table 8.5** and **6.3.1**).

Material **Paragraph**	Co_3O_4 forCo_3O_4/ZnO **6.3.1**
Precursor	**3**
Precursor amount	0.3 g
T_{vap}	100°C
Substrate	ZnO/Si(100), ZnO/Al_2O_3
P	20 W
T	200°C
Ar (carrier) flow rate	60 sccm
Ar/O_2 flow rate	15/20 sccm
p	1 mbar
t	10 - 120 min

❖ 8.4 Precursor Characterization Techniques

❖ 8.4.1 Elemental Analysis (EA)

Elemental Analysis, also known as C, H, N analysis, was used for determining the elemental composition of the metal-organic compounds presented in this thesis. In practice, 2 - 3 mg of the test substance is weight, placed into a tin crucible and burned at 990°C under oxygen atmosphere. The gaseous products pass through a WO_3 catalyst to guarantee complete oxidation into CO_2, H_2O and NO_x and to eliminate O_2 from the gas mixture. Afterwards, a heated column containing copper granulates serves to reduce NO_x to N_2. Ultrapure helium (5.0) is used as carrier gas. Finally, the gases are brought to a defined pressure/volume and separated by gas-chromatography. Quantification is provided by use of a thermal conductivity detector. The accuracy of measurement for N and C is around 0.05 weight % (500 ppm).
In this work, elemental analysis was performed by the Analytical Service Centre of the Chemistry Department, Ruhr-University Bochum, using a CHNSO Vario EL 1998 instrument.

❖ 8.4.2 Nuclear Magnetic Resonance Spectroscopy (NMR)

Solution NMR measurements were performed to obtain structural information about the precursor compounds used in this work. [*Hesse-2005*] NMR spectroscopy exploits the magnetism of certain nuclear isotopes. A sample placed in a magnetic field B_0 develops a macroscopic magnetization, which is the origin of the spectroscopic signal. The application of electromagnetic waves in the measured radiofrequency region (1 - 600 MHz) generates a magnetic moment μ of the nucleus.
The energy that can be absorbed or emitted by the system can be described by the Larmor frequency ω:

$$\Delta E = (\gamma\, h\, B_0 / 2\,\pi) = h\,\nu = \omega\, h / 2\pi \;\longrightarrow\; \omega = \gamma\, B_0 \qquad \text{(equation 8.1)}$$

h is Planck constant; γ is the magnetogyric constant and characteristic for the nuclear isotope studied. The resonance frequency of a nucleus is not solely dependent on γ, but also on the "electron shielding" σ, related to the density of electrons that shield B_0.

[*Williams-1975*] Taking into account σ, the effective resonance frequency has to be expressed as:

$$\omega = \gamma B_0 (1 - \sigma) \qquad \text{(equation 8.2)}$$

Since ω is a function of B_0, absolute values of the resonance frequency of a nucleus cannot be measured. Therefore a reference, usually tetramethylsilane, is used and relative "chemical shifts" of the resonance frequency can be obtained for comparison: [*Hesse-2005*]

$$\sigma_1 \text{ [ppm]} = (\omega_1 - \omega_{ref}) \text{ [Hz]} / \textit{spectrometer frequency} \text{ [MHz]} \qquad \text{(equation 8.3)}$$

where σ_1 and ω_1 are attributed to the sample and ω_{ref} is the resonance frequency of tetramethylsilane.

High or low electron densities thus result in high-field shifted (low σ_1) or low-field shifted (large σ_1) NMR signals, whose integrated area corresponds to the number of equivalent nuclei. The splitting of the NMR signals, spin-spin couplings, result from the impact of the spin orientation from a nucleus on the magnetic field of the neighbor atom and vice versa. The spin-spin coupling, together with the signal integrated areas and the chemical shifts, make NMR spectrometry a useful tool for structural analyses of molecular compounds. [*Atkins-2006*, *Hesse-2005*]
In this work, ^{1}H and ^{13}C NMR spectra were recorded with a Bruker Advance DPX- 250 instrument (operator: Daniela Bekermann, Ruhr-University Bochum), referenced to internal solvents (residual proton signals) and corrected to the TMS standard values.

❖ 8.4.3 Single Crystal X-ray Diffraction

Single Crystal X-ray Diffraction enables to determine the structure of a single crystal exploiting the diffraction of X-rays in its crystal lattice. [*Warren-1990*] The geometric requirements are expressed by the Bragg equation, see also **figure 8.8**. [*Brundle-1992*]

$$n \lambda = 2 d \sin\theta \qquad \text{(equation 8.4)}$$

where n is an integer number, λ the wavelength and d the specific distance between the crystal planes.

Laue's procedure is based on the use of continuous X-ray radiation. Within certain limits, in every fixed crystal there is a wavelength of the X-ray beam corresponding to a lattice plane distance obeying Bragg law and thus resulting in the so-called Laue-reflections. Upon rotation of the crystal, it is as well possible to satisfy Bragg law by the use of monochromatic radiation.

In this work, Single Crystal X-ray Diffraction experiments were carried out at 112 K with an Oxford Xcalibur 2 CCD/PD diffractometer with monochromatic Mo *Kα* radiation (0.71073 Å) (operators: Daniela Bekermann and Manuela Winter, Ruhr-University Bochum). The structure was solved by direct methods and refined anisotropically with the SHELXL-97 program suite. [*Sheldrick-1997*] CCDC-752098 contains the crystallographic data for the structure of **1** (see **8.1.3**) These data can be obtained from The Cambridge Crystallographic Data Centre via www.ccdc.cam.ac.uk/ data-request/cif.

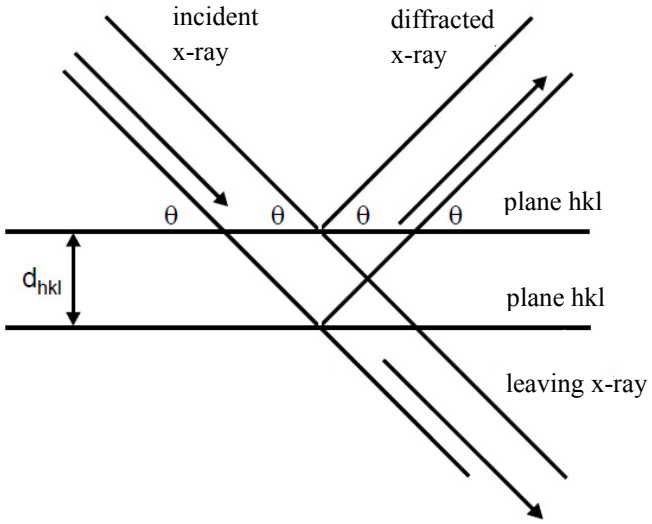

Figure 8.8: Scheme for Bragg conditions.

❖ 8.4.4 Electron Impact-Mass Spectrometry (EI-MS)

In conventional EI-MS, [*Hesse-2005*] the test compound is vaporized in vacuum, ionized, then accelerated through an electric field and finally separated by a magnetic field. The most important information that can be obtained from EI-MS are the molecular mass, or, more specifically, the ratio of the molecule mass to the ion charge (*m/z*), and the interpretation of the sample fragmentation behavior by electron impact. The latter is of

particular importance for PECVD processes in which vaporized precursors undergo inelastic collisions with electrons.

In this work, EI-MS spectra were recorded at 70 eV by using a Varian MAT spectrometer (operator: Sabine Bendix, Ruhr-University Bochum). Data were given as specific masses (*m*/*z*) based on the most abundant isotopes ($^{1}_{1}$H, $^{12}_{6}$C, $^{14}_{7}$N, $^{12}_{8}$O, $^{19}_{9}$F, $^{59}_{27}$Co, $^{64}_{30}$Zn).

❖ 8.4.5 Thermogravimetry/Differential Thermal Analysis (TG/DTA)

Both, thermogravimetry (TG) and differential thermal analysis (DTA) belong to the group of thermo analyses. In TG analysis, the weight loss of the sample as a function of temperature due to vaporization, dehydration and decomposition is recorded, which is of special importance for CVD processes to evaluate precursor thermal stability and volatility. [*Bekermann-2010-C*, *Zhang-2009-C*] During the measurement, the temperature in the sample chamber is raised with a heating rate of $\beta = dT/dt$. The use of TG enables thus the observation of the following processes taking place in certain temperature regions: (i) vaporization, sublimation and dissociation, (ii) desorption/decomposition and (iii) oxidation/reduction. The obtained data are finally shown in a thermogram as mass loss as a function of temperature. Detected changes can also indicate melting, phase transitions or structural changes and are accompanied by characteristic energy variations that can be followed by DTA, by registering the heat change taking place in endothermic or exothermic processes as a function of the oven temperature.

For the precursors used in this thesis, simultaneous thermogravimetric and differential thermal analysis (TG/DTA) was carried out by using a Seiko TG/DTA 6300S11 (operators: Daniela Bekermann and Ke Xu, Ruhr-University Bochum) at ambient pressure (sample weight ≈ 10 mg), with a heating rate of 5 °C min^{-1} (N_2 flow rate = 300 ml min^{-1}).

❖ 8.5 Materials Characterization Techniques

Chemical and physical properties of the materials obtained in this thesis were thoroughly investigated by various analytic techniques. Their morphology was analyzed by AFM and SEM (**8.5.1** and **8.5.2**), their composition determined by EDXS, RBS, XPS/XE-AES and SIMS (**8.5.3** - **8.5.6**); the structural features were studied by XRD and TEM (**8.5.7** -

8.5.8). Finally, the optical techniques used for the materials analysis included FT-IR, UV-Vis and PL (**8.5.9 - 8.5.11**).

❖ 8.5.1 Atomic Force Microscopy (AFM)

AFM is particularly suitable to obtain information at atomic level concerning the surface topography not only for conductors, but also of insulators and semiconductors. [*Brundle-1992*] This method allows an insight into the material textural features, which, in turn, can strongly affect their reactivity and properties. [*Binnig-1986*] In this thesis, AFM was used to characterize the material surfaces from a morphological point of view and to evaluate their surface roughness. The technique probes the surface of a sample with a sharp tip, a couple of microns long and often less than 100 Å in diameter. The tip is located at the free end of a cantilever of 100 to 200 µm length. Forces between the tip and the sample surface cause the cantilever to bend, or deflect. A detector measures the cantilever deflection, as the tip is scanned over the sample, or the sample is scanned under the tip. The measured cantilever deflections allow a computer to generate a map of surface topography (**figure 8.9**).

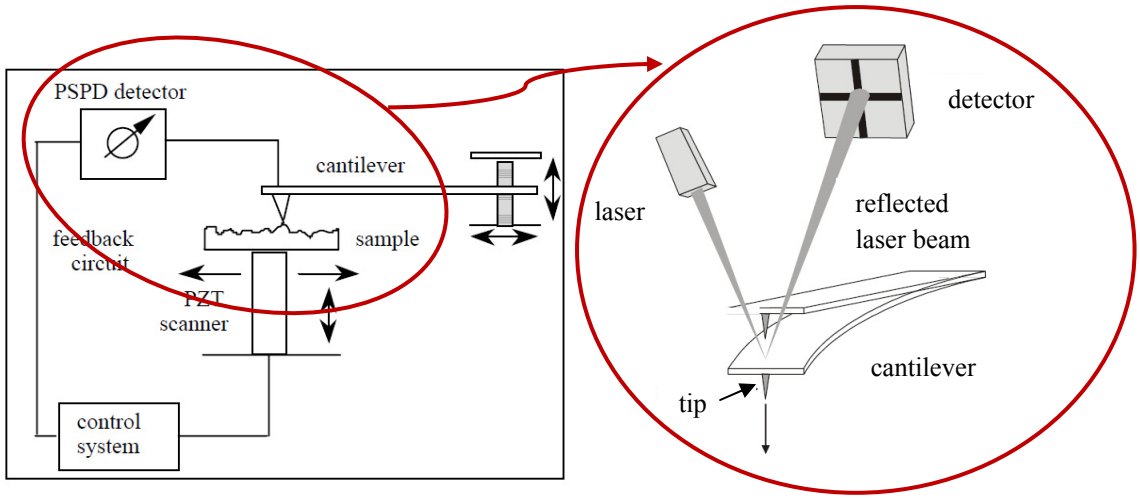

Figure 8.9: Sketch of the AFM acquisition equipment.

Atomic force microscopes can be designed to operate in either contact and non-contact modes. In *contact mode*, also known as repulsive mode, the AFM tip makes soft "physical contact" with the sample. The tip is attached to the end of a cantilever with a spring constant lower than the effective spring constant holding the atoms of the sample together. As the scanner traces the tip across the sample, the contact force causes the

cantilever to bend and to accommodate changes in topography. In *non-contact mode*, also known as attractive mode, the AFM monitors attractive van der Waals forces between the tip and the sample. The tip-to-sample distance is generally in the range of 50 to 100 Å. At this distance, a weak attraction results and the atoms will move closer together until the strong electrostatic repulsion takes over. In non-contact mode, AFM monitors the resonant frequency of the cantilever and keeps it constant via a feedback system that moves the scanner up and down. In this way, the system keeps the average tip-to-sample distance constant.

In this thesis, AFM measurements were performed on two different instruments, either a Nanoscope Multimode III apparatus from Digital Instruments or a NT-MDT SPM Solver P47HPRO instrument, both operating in tapping mode and in air (operators: Teodor Toader, Ruhr-University Bochum; Chiara Maccato, Padova University). The micrographs have been recorded in different areas of each sample, in order to test the system homogeneity.

❖ 8.5.2 Scanning Electron Microscopy (SEM)

SEM is a powerful tool for the investigation of nanomaterial morphology, with a resolution considerably higher compared to conventional optical microscopy. [*Brundle-1992, Eberhart-1991*] In this technique, the incident beam consists of highly energetic electrons of typically 1 - 50 keV. Upon striking the sample, different types of signals are generated that serve constructing sample images. Interactions with the sample may be either elastic, resulting in the backscattering of primary electrons (PE), or inelastic, when the primary beam causes the ejection of secondary electrons (SE), along with characteristic photon radiation. Since the PEs come from a deeper region of the interaction volume (down to ≈ 1 μm), they do not provide morphological information, but their emission yield, which depends on the atomic number of the sample atoms, can be used for contrast imaging of the sample composition. In contrast, the lower energetic SEs are easily and rapidly absorbed by the sample itself and thus only measured if generated near to the sample surface. This permits the obtainment of direct morphological information.

In this work, Field Emission SEM (FE-SEM) measurements were performed. A field emission source is based on the extraction of electrons from a suitable material (generally

W/ZrO_2) by the tunnel effect through application of a strong electric field. The advantage of FE-SEM is the generation of a well stabilized electron beam enabling the obtainment of high resolution, down to some nm, even at low acceleration voltages (< 10 kV), so that electrostatic charging effects can be minimized and the surface sensitivity increased. Thus, in the case of inorganic materials, sample preparation can be avoided.

The sample surface morphology of the films obtained by thermal CVD was determined by SEM by using a LEO 1530 Gemini instrument (Zeiss) (operator: Rolf Neuser, Ruhr-University Bochum). All other FE-SEM measurements were performed at primary beam acceleration voltages between 5 and 20 kV by a Zeiss SUPRA 40 VP instrument, equipped with an Oxford INCA x-sight X-ray detector for EDXS analyses (operator: Chiara Maccato, Padova University).

❖ 8.5.3 Energy Dispersive X-ray Spectroscopy (EDXS)

Upon electron bombardment of a sample, among various interactions between the primary and sample electrons (see **paragraph 8.5.2**), also emission of element characteristic X-ray radiation is induced, that can be exploited for the analysis of the sample chemical composition. [*Zhang-2009-C*] The corresponding spectroscopy is called EDXS, that permits local compositional analysis, compositional depth profiles (complementary to XPS) and mapping of selected regions of interest.

Light elements with $Z \leq 4$ cannot be detected, since the liquid nitrogen cooled semiconducting detector is separated by a Be window from the SEM and thus strongly absorbs the $K\alpha$ lines of these lighter elements. Due to the primary beam diameter and the propagation of scattered electrons, the lateral sampling diameter is about 1 μm with a depth resolution of 1 – 5 μm.

In this thesis, EDXS measurements were performed by a Zeiss SUPRA 40 VP FE-SEM instrument, equipped with an Oxford INCA x-sight X-ray detector (operator: Chiara Maccato, Padova University).

❖ 8.5.4 Rutherford Backscattering Spectroscopy (RBS)

In RBS measurements, monoenergetic ions (H^+ or He^+) with energy of a few MeV strike the sample and are backscattered as a result of elastic collisions with the matrix sample

atoms. The backscattered ions are analyzed and separated by their respective energies. This technique enables the qualitative and quantitative analysis of chemical composition without the need of standards and is non-destructive. [*Brundle-1992*]

For the interpretation of this technique the Rutherford atomic model is used. The incident ions are backscattered upon meeting the nucleus of a sample atom, which allows the identification of the element, while interactions with the electrons lead to an energy loss, revealing in-depth information about the respective elemental distribution. In practice, the number of counts per Coulomb are traced as a function of the energy of the backscattered ion. A proper fitting of the curves and the integration of the peak areas allows the determination of the qualitative and quantitative elemental composition and the film thickness. RBS is an especially suitable tool for the investigation of heavy elements on a substrate composed of lighter elements. [*Alford-2005, Brundle-1992*]

The RBS measurements have been performed at the Dynamitron-Tandem-Laboratory at the University of Bochum by using a singly charged He beam with the energy of 2 MeV and a beam current of 20 – 40 nA. A silicon surface barrier detector was placed at an angle of 160° with respect to the beam axis. The solid angle of the detector was 1.911 msrad. The spectra were analyzed with the program RBX.

❖ 8.5.5 X-ray Photoelectron Spectroscopy and Auger Electron Spectroscopy (XPS/XE-AES)

XPS is powerful tool for the qualitative and quantitative compositional analysis of a materials surface and, upon erosion, also for its in-depth investigation. Its primary importance derives (i) from the extent of chemical bonding and compositional details obtainable from peak position analysis, (ii) from the possibility to analyze the in-depth distribution and (iii) from the low level of radiation damage introduced into the sample by soft x-ray excitation.

XPS is based on the photoelectric effect, the emission of an electron from an inner atomic shell with a binding energy *BE* relative to the Fermi level E_F by an incident X-ray quantum $\hbar\upsilon$. [*Briggs-1983, Briggs-2003*] Leaving the sample surface, the electron has to overcome the work function Φ and has a kinetic energy *KE*. The kinetic energy distribution of the emitted photoelectrons can be measured using any appropriate electron

energy analyzer, and a photoelectron spectrum (the difference of the work function between sample and electron detector) can thus be recorded.

$KE = h\nu - BE - \Phi$ (equation 8.5)

For each element, there is a characteristic *BE* associated with each core atomic orbital, i.e. each element gives rise to a characteristic set of peaks in the photoelectron spectrum at *KE*s determined by the incident photon energy and by the respective *BE*s. The presence of peaks at particular energies therefore indicates the presence of a specific element in the investigated sample. Furthermore, the intensity of the peaks is related to the concentration of the element within the sampled region. XPS is sensitive to as low as 0.5 atomic percent and detects almost all elements except H and He. The most commonly employed x-ray sources are Mg *Kα* radiation (h ν = 1253.6 eV) and Al *Kα* radiation (h ν = 1486.6 eV). Accordingly, the emitted photoelectrons have *KE*s in the range of ca. 0 - 1250 eV or 0 - 1480 eV. Since such electrons have very short mean free paths in solids (tenths of angstroms), [*Atkins-2006*] the technique is necessarily surface sensitive.

Since the occupied energy levels are quantized, the photoemission distribution is characterized by a discontinuous pattern with different peaks and its investigation of this energy distribution represents the basis of the analytical method. Emission from some levels (*p, d*) gives rise to closely spaced doublets due to spin-orbit coupling.

The *BE* of an electron depends not only upon the level from which photoemission is occurring, but also upon (i) the formal atom oxidation state and (ii) the local chemical and physical environment. Changes in either (i) or (ii) give rise to small (chemical) shifts in the peak positions in the spectrum. This ability to discriminate between oxidation states and chemical environments is one of the major advantages of the XPS technique.

Photoelectron spectra of conducting or semiconducting materials generally display one or several weaker satellite peaks on the low-energy side of photoelectron peaks, due to plasmon excitation. Additional effects due to multiple excitations may generate further peaks or modify line profiles; these effects include the "*shake-up*" (second electron raised from the valence band to the conduction band), and the "*shake-off*" effect (second electron ejected from the valence band into the continuum). [*Briggs-1983, Briggs-2003*]

During photo ionization process, holes are formed in the core levels. [*Atkins-2006*, *Briggs-1983*] They decay through a recombination with an electron coming from higher energy states according to two competitive processes:

1) X-ray fluorescence, in which the excess energy is emitted as photons (radiative decay);

2) Auger emission, in which the excess energy is released to an electron (Auger electron), which is emitted (non radiative decay).

Also the Auger peaks show a chemical shift, even though, in this case, the interpretation is more complex than in the case of XPS. To this regard, the Auger α parameter is used, which is characteristic for every oxidation state of the investigated species and therefore used as a "finger print": [*Briggs-1983*]

$$\alpha = BE\ (XPS) + KE\ (Auger) \qquad \text{(equation 8.6)}$$

The area under the photoelectron bands contains quantitative information about the sample composition. To this regard, a simplified formula can be used, putting in relation the area *A* of a peak with the corresponding sensitivity factor *Sj*, the latter depending on the investigated species and instrument:

$$C_i = 100\ \frac{A_i}{S_i}\left(\sum_j \frac{A_j}{S_j}\right)^{-1} \qquad \text{(equation 8.7)}$$

For the investigation of the underlying layers of the supported nanosystems, the analysis of the atomic percentages as a function of depth is of great importance. The method used in this work implies the controlled erosion of the sample layers with an Ar^+ ion beam of a known energy (sputtering) and the measurement of the photoelectron peaks after each sputtering cycle. This way, a depth profile can be obtained displaying the variation of the respective atomic percantages contained in the sample as a function of sputtering time.

In this work, XPS/XE-AES investigations of this work were carried out at a Perkin Elmer Ø 5600 Multi Technique System with a double anode as X-ray source Mg–Al (operators: Davide Barreca, Daniela Bekermann, Marco Gavagnin and Alberto Gasparotto, Padova University). The *BE*s (standard deviation = ± 0.2 eV) were corrected for charging effects by assigning to the adventitious C1*s* line a *BE* of 284.8 eV. The analysis involved Shirley-type background subtraction and, whenever necessary, spectral deconvolution, carried out by nonlinear least-squares curve fitting adopting Gaussian-Lorentzian sum functions. The atomic composition was calculated by peak integration, using sensitivity factors provided by Φ V5.4A software. Ar^+ sputtering was carried out at 4×10^{-8} mbar and 4.5 kV, with a raster size of 2×2 mm^2.

❖ 8.5.6 Secondary Ion Mass Spectrometry (SIMS)

Among compositional analysis methods, SIMS displays a high sensitivity to all the elements of the periodic tables, [*Brundle-1992*, *Grasserbauer-1986*] including the lightest ones, and allows to discriminate different isotopes due to the high signal-to-noise (S/N) ratio related to the absence of an intrinsic background. Detection limits can easily reach one ppb. Another advantage of this technique is that with respect to other methods, e.g. XPS, no lower atomic number limit occurs.

In SIMS analysis, the surface of the sample is bombarded by a focused beam of primary ions accelerated with an energy ranging between 0.5 and 20 keV. If submitted to a non-reactive ion beam of a few kV, a solid undergoes various interaction effects. The impinging ions can:

1) lose kinetic energy due to nuclear and electronic stopping (i.e. ballistic collisions and electronic excitations),

2) cause a collision cascade,

3) stop and remain implanted,

4) induce a series of ionization-excitation processes followed by relaxation and emission processes,

5) determine sputtering phenomena,

6) lead to amorphization or epitaxial regrowth of the material.

A fraction of the ejected atoms is ionized, thus producing a secondary flux, of both positive and negative ions.

In addition to surface analysis, SIMS is also used to establish concentration profiles as a function of depth. [*Wilson-1989*] Through ion milling, successive atomic layers are removed. During this progressive erosion, surface compositional analysis is performed. Preferential sputtering, which produces a variation of the original composition of the material, has to be taken into account. The erosion efficiency of the elements can be different, so that selective enrichments can result. Even the composition and the structure of the matrix can affect the sputtering yield. All these factors have to be carefully considered for a correct interpretation of experimental data.

In this work, SIMS was used to evaluate the in-depth distribution of the elements and to gain information concerning the sample composition. By careful comparison among the different depth profiles, useful information regarding the chemical origin of the elements was obtained.

The SIMS instrument used for this work is a CAMECA IMS-4F ion microscope equipped with a normal incidence electron gun to compensate charging effects (operator: Cinzia Sada, Padova University). Depth profiles have been obtained by 14.5 keV Cs^+ bombardment and negative secondary ion detection (beam current = 10 - 20 nA, stability 0.5 – 0.6 %, raster area = 150 x 150 – 170 x 170 μm^2) from a sub-region of 7 x 7 μm^2 to 10 x 10 μm^2. After reaching the substrate, the thickness of the films was measured by an Alpha-Step 200 Tencor profilometer. The deposit thickness is determined by analyzing the element signal dynamics. The uncertainty on thickness contains therefore contributions from element interdiffusion, film roughness and finally of the technique artefacts.

❖ 8.5.7 X-ray Diffraction (XRD)

X-ray diffraction provides a convenient and practical method for the identification of crystalline compounds. It is based on the scattering of X-rays by the ordered environment in a crystal and on the interference among the scattered rays. The interference can be destructive or constructive. Constructive interference only occurs when the Braggs law is fulfilled (equation 8.4). [*Eberhart-1991*, *Mittemeijer-2004*]

XRD spectra show the intensity of the diffraction signals versus the angle 2θ. The obtained diffraction peaks are confronted with the tables of JCPDS (Joint Committee on Powder Diffraction Standards), where all analyzed specimens are reported. From XRD line broadening it is possible to calculate the average crystallite size, if the size is between 3 and 30 nm. The required relation is given by the Scherrer equation: [*Mittemeijer-2004*]

$$\text{FWHM} = K_\lambda \lambda / (d \sin\theta) \qquad \text{(equation 8.8)}$$

where FWHM is the line broadening, K_λ a constant, λ the wavelength, d the crystallite size, and θ the Bragg angle.

The diffraction geometries used in this thesis are described in **figure 8.10**. [*Brundle-1992*] The Bragg-Brentano geometry is widely used for preferentially and randomly oriented polycrystalline systems. In this geometry (**figure 8.10 (a)**), slits collimate the incident X-rays, which impinge on the specimen at an angle θ_1. After passing through receiving slits, the diffracted X-rays are detected. Since the incident and diffracted X-rays form the same angle to the specimen surface, structural information is obtained only about (*hkl*) planes

parallel to this surface. This limitation can be overcome by Glancing Incidence-XRD (GIXRD, **figure 8.10 (b)**), that also enables X-ray probing depth to be highly reduced and therefore increases surface sensitivity, a main advantage in the analysis of thin films and nanodeposits. It is also possible to get a sort of structural depth profiling (from 50 Å to microns) by varying the incidence angle.

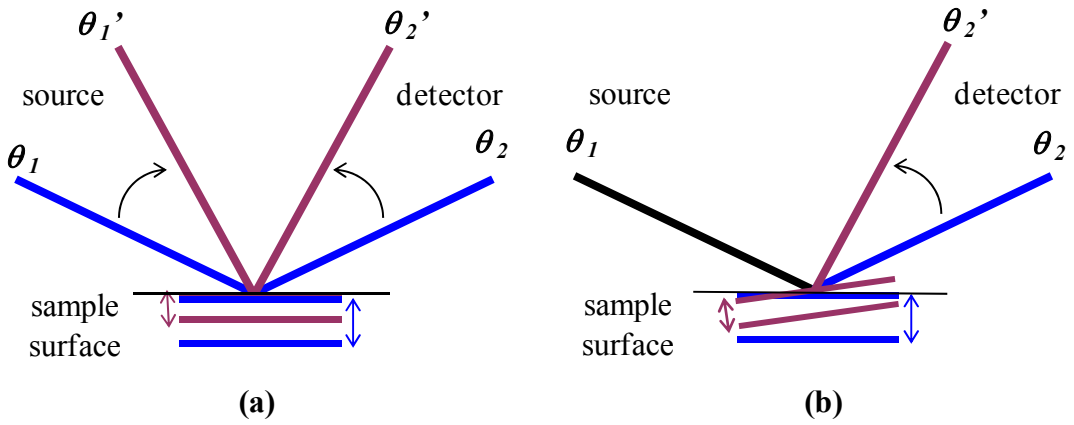

Figure 8.10: (a) Source and detector move, θ_1 and θ_2 are always equal (Bragg-Brentano). (b) θ_1 is fixed, and only the detector is rotated.

In this work, XRD measurements in Bragg-Brentano geometry were performed by using a Bruker AXS D8 Advance diffractometer with Cu $K\alpha$ radiation (1.5418 Å) (operator: Harish Parala, Ruhr-University Bochum). GIXRD patterns were recorded using a Bruker D8 Advance instrument (operators: Alberto Gasparotto and Davide Barreca, Padova University) equipped with a Göbel mirror and a Cu $K\alpha$ source (40 kV, 40 mA), at a constant incidence angle of 1.0° for ZnO, Ag/ZnO and Co_3O_4/ZnO and 3.0° for (F)-Co_3O_4.

❖ 8.5.8 Transmission Electron Microscopy (TEM)

TEM belongs to the group of electron microscopic techniques and is an effective and versatile tool for studying structure and morphology of nanostructures. [*Eberhart-1991*, *Zhang-2009-C*] Detailed information about the form, dimension and distribution of nanoparticles can be derived from TEM, and it allows the identification of the various phases present in the analyzed samples by electron diffraction or Electron Energy Loss Spectroscopy (EELS). In the case of high resolution-TEM (HR-TEM), single crystal

domains can be observed, which is of outmost importance for the study of their internal structuring and connectivity, giving valuable information on the nucleation and growth processes of the target nanomaterials.

In TEM investigations, a highly energetic electron beam is focused on a sample, and the transmitted electrons are analyzed. Basically, two types of information can be obtained: a magnification image of the sample and the corresponding diffraction pattern. [*Feldmann-1986*] The diffraction pattern consists of a series of spots if the sample is a single crystal, and shows concentric pattern in the case of polycrystalline samples due to superimposition of the electron waves. An interpretation is possible taking into consideration analogous diffraction behavior as in the case of X-ray analyses, thus applying Braggs law (equation 8.4).

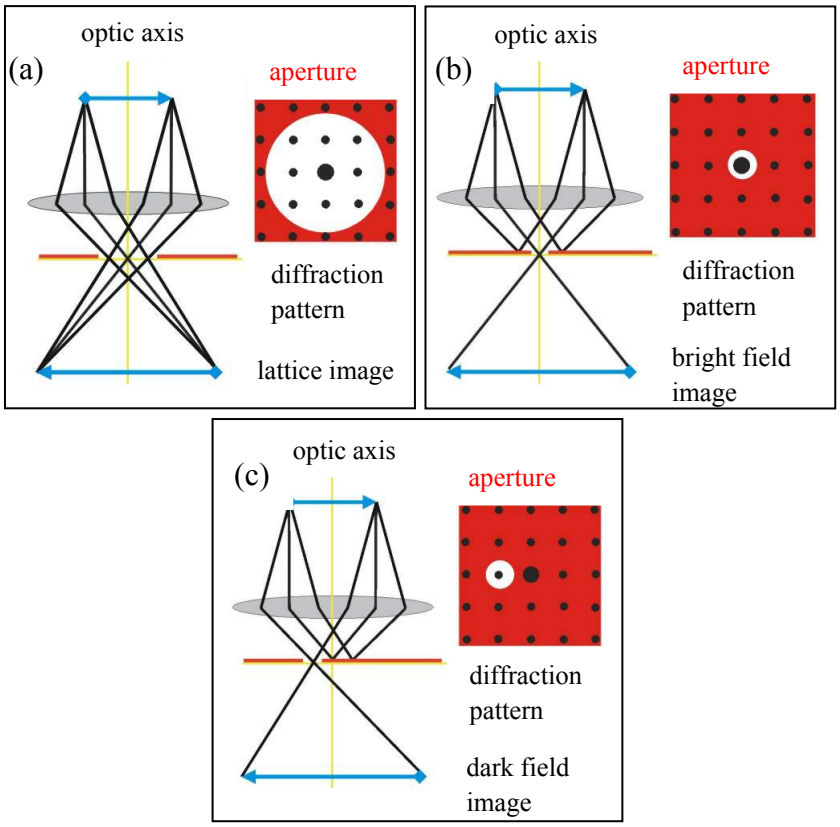

Figure 8.11: TEM imaging: (a) HR-TEM; (b) bright field; (c) dark field.

For the obtainment of a good TEM image, it is necessary to have a good imaged contrast, given by the relation between the number of directly transmitted electrons and the number of elastically diffracted ones. For HR-TEM lattice images, the objective aperture is large (**figure 8.11**) and both the transmitted electrons and the diffracted ones cross the aperture itself, producing thus the sample image. While *bright field* images with a good contrast are derived from the directly transmitted electrons, that have crossed the sample, *dark*

field images are generated by diffracted electrons of a particular angle (**figure 8.11**). [*Bals-2004, Zhang-2009-C*]

Information on the local elemental composition can be derived from EDXS spectra on specific sample regions, which display the characteristic X-ray radiation as a function of energy (see also **paragraph 8.5.3**). Whereas EDXS is suitable for the detection of heavier atoms (beginning from O), EELS enables the analysis of light atoms and can provide further important information on the mutual distribution of various components within the same sample.

In this work, TEM and HR-TEM analyses of Si(100) supported ZnO nanorod arrays were carried out using a JEOL 40000EX microscope operated at 400 kV and having a 0.17 nm point resolution. Samples for observations were prepared by focused ion beam techniques, using a FEI Nova 200 Nanolab DualBeam SEM/FIB system. A dual-cap C-Pt protection layer was used to protect the systems from ion milling damage. TEM and HR-TEM analyses of Ag-doped ZnO nanorods and (F)-Co_3O_4 samples were performed on cross-section samples using a Tecnai G2 30 UT microscope with a 0.17 nm point resolution, operated at 300 kV. Cross-section specimens for TEM were prepared by mechanically grinding down to the thickness of approximately 20 μm, followed by Ar^+ ion beam milling using a Balzers RES 101 GVN apparatus. High angle annular dark field-Scanning Transmission Electron Microscopy (HAADF-STEM) and spatially resolved Electron Energy Loss Spectroscopy (STEM-EELS) were performed on a FEI Titan 80-300 “cubed” microscope fitted with an aberration corrector for the probe forming lens and a GIF QUANTUM spectrometer, operated at 300 kV. The used HAADF detector inner semi-angle, the convergence semi-angle for the EELS experiments and the collection semi-angle were 90, 21, and 90 mrad, respectively. After acquisition, the EELS data were treated using principle component analysis to minimise the effect of random noise. Maps were generated by integrating the EELS signals over an appropriate energy window after power-law background removal. The measurements were carried out by Oleg I. Lebedev (Laboratoire CRISMAT, ENSICAEN, Caen Cedex, France, and Electron Microscopy for Materials Science (EMAT), University of Antwerp, Belgium).

❖ 8.5.9 Fourier Transform Infrared Spectroscopy (FT-IR)

IR spectroscopy uses the region of the electromagnetic spectrum from 400 - 4000 cm^{-1} (corresponding to 25 - 2.5 μm) and enables the identification of unknown components and to study chemical bonds. [*Hesse-2005*, *Zhang-2009-C*] Upon IR irradiation of a sample, electromagnetic energy is absorbed and transformed into the excitement of discrete vibration and rotation modes of molecular dipoles. [*Brundle-1992, Solé-2005*] In IR spectroscopy usually both excitation bands due to vibration and rotation, are observed. [*Atkins-2006*]

The instrumental setup used in this work, was a Fourier transform (FT-)IR spectroscope. In Fourier transform instruments, all wavelengths are detected simultaneously during the whole recording time, enabling a faster sampling compared to conventional IR spectrometers. [*Zhang-2009-C*] Along with the measurement of the sample, an interferogram of a HeNe laser with a known and constant wavelength is recorded as reference, allowing an incertitude of measurement of 0.01 cm^{-1}.

FT-IR spectra were collected with a Nexus 870 FT-IR apparatus (operators: Daniela Bekermann and Alberto Gasparotto, Padova University) in the range 350 – 4000 cm^{-1}. The background was measured by using a bare silicon substrate and subtracted for every collected spectrum.

❖ 8.5.10 Ultraviolet/Visible Light Spectroscopy (UV-Vis)

UV-Vis spectroscopy is one of the most widely used spectroscopic methods in chemistry [*Atkins-2006, Brundle-1992, Hesse-2005, Solé-2005*, *Zhang-2009-C*] to gain information about the electronic structure of molecules, materials transparency and semicondoctur band gap. In this work, the absorption coefficient as well as the band gap of the investigated thin film materials were obtained from UV-Vis spectroscopy, as described below.

In general, absorption spectra are measured, which are mainly based on the absorption of light by the test compound and the consequent electrons excitation The used spectral region ranges from 200 – 800 nm (200 – 380 nm: UV, 380 – 700: nm Vis), corresponding to 50.000 – 12.500 cm^{-1}. [*Atkins-2006, Hesse-2005*] The reduction of the light intensity by interaction with the sample is defined by the Lambert-Beer law:

$I(\lambda) = I_0 \exp(-\alpha(\lambda)\, t)$ (equation 8.9)

where α is the material absorption coefficient dependent on the wavelength. The ratio I / I_0 defines the transmittance T which can be transformed into absorbance A, since it is proportional to the film thickness t.

$A(\lambda) = \ln(1 / T(\lambda)) = -\ln(I_0 / I(\lambda)) = \alpha t$ (equation 8.10)

Neglecting reflection phenomena, the absorption coefficient α can be calculated using the following equation:

$\alpha t = \ln(T^{-1})$. (equation 8.11)

In the region of maximum absorbance, α follows the law: [*Tauc-1972*]

$\alpha(h\nu) \propto (h\nu - E_g)^n$ (equation 8.12)

where E_g is the band gap energy of the SC and n an exponent whose value depends on the nature of the electronic transitions involved. In the case of ZnO, n = 1/2 was used. For the graphical estimation of E_g, the Tauc plot is the most commonly used procedure, giving a value with less than 5% error. It is performed by plotting $(\alpha h\nu)^2$ $(cm^{-1} eV)^2$ versus $h\nu$ (eV) and subsequent linear fitting of the region of interest. The intersection of the linear fit with $(\alpha h\nu)^2$ $(cm^{-1} eV)^2 = 0$ reveals the value of E_g in (eV).
In this work, optical absorption spectra were recorded for samples supported on SiO_2 in transmission mode at normal incidence light by means of a Cary 5E (Varian) UV-Vis-NIR dual-beam spectrophotometer with a spectral bandwidth of 1 nm (operator: Daniela Bekermann, Padova University). For each spectrum, the silica substrate contribution was subtracted.

❖ 8.5.11 Photoluminescence Spectroscopy (PL)

PL is the excited emission of electromagnetic radiation upon light absorption, allowing the investigation of the target materials optical and crystalline quality, electronic bands and defects. [*Brundle-1992*, *Solé-2005*] In PL spectroscopy, the SC sample is exposed to radiation with energy higher than the band gap energy E_g, resulting in the generation of

electron/hole pairs (excitons). These can recombine and emit photons – otherwise, free excitons can diffuse in the SC crystal and be trapped by defects, such as donors, that can trap holes, and acceptors, that can trap electrons.

A bound exciton can recombine under emission of electromagnetic radiation, which can be spectrally recorded. For the same excitation power per area, the intensity of the emitted light depends on the ratio of the electron/hole recombination time to the relaxation time into the investigated nanostructure, as well as on the number of confined levels and capturing defects, and therefore refers to the optical quality of the sample. Further important information can be obtained from the line broadening of the PL signals, occurring due to a slight inhomogeneity of the SC crystallites size, shape, composition and strain. In order to obtain higher spectral resolutions, with a more detailed analysis of the recombination processes involved, low temperature measurements, as in this thesis, can be performed.

PL measurements were performed in reflection mode by using a HeCd (λ = 325 nm) laser source, whose light intensity was modulated by a Chopper, choosing an excitation power of 20 W cm^{-2}. The beam was focused by a system of lenses on the sample, which could be cooled down to 77 K. The PL light emission was spectrally resolved by a 0.5 m Spex500M monochromator (blaze wavelength of 750 or 1000 nm) and measured by a liquid-Nitrogen-cooled InGaAs-detector by using lock-in technique to filter the signal (operators: Daniela Bekermann and Arne Ludwig, Ruhr-University Bochum).

❖ 8.6. Functional Characterization Techniques

❖ 8.6.1 Photo-induced Superhydrophilicity (PSH)

The possibility of monitoring hydrophilicity is of great importance regarding applications such as air and water pollution control, antifogging and self-cleaning glasses, anti-beading windows or mirrors. PSH is correlated with the ability of the material to generate electron/hole pairs upon illumination with UV or Vis light and their interactions with chemical species before their recombination. The considered mechanism involves the reduction of the metal to a lower oxidation state by the electrons, while the strongly oxidizing holes oxidize the O^{2-} anions. [*Fujishima*-2000] As a consequence, oxygen vacancies (V_O) are formed, that are readily available for the dissociative adsorption of H_2O. The thus produced hydroxyl groups at the materials surface result in a photo-

enhanced hydrophilicity of the investigated SC material. PSH properties can be analyzed by monitoring the evolution of water contact angle (WCA) as a function of the UV irradiation time, as done in this work. [*Bekermann-2010-A*, *Gasparotto-2011-A*] The term "superhydrophilicity" is used, if the WCA is << 90°.

In this thesis, for the analysis of the PSH behavior, [*Barreca-2009-C*, *Bekermann-2010-A*] as-grown ZnO and Co_3O_4/ZnO samples were irradiated in a photo-chamber by UV lamps (CLEO 20 W, 438 × 26 mm^2, Philips; broad maximum at 355 nm; photon irradiance: 5.7 10^{-9} einstein cm^{-2} s^{-1}), and WCA values (uncertainty = ± 3°) were measured at regular time intervals. Three repetitions of WCA measurements were made on each sample. PSH measurements were performed in collaboration with the group of Prof. Urška Lavrenčič-Štangar (Laboratory for Environmental Research, Nova Gorica University - Slovenia). [*Bekermann-2010-A*]

❖ 8.6.2 Photocatalytic Oxidation (PCO)

PCO processes are studied in literature due to their potential application for materials that enable purification of air, water or walls by the sole activation of solar light. [*Fujishima-2000, Fujishima-2008*, *Mills-2002*] Some examples are the cleaning of waste waters from industry, prevention of soilage accumulation on walls or the decomposition of bad odors.

As in the case of PSH and photocatalytic H_2 generation (**8.6.3**), generation and separation of electrons and holes is required upon light absorption by the SC material, to activate the latter for catalytic oxidation reactions. The mechanism considered for PCO involves the reduction of O_2 to superoxide radical anions by the electrons, and oxidation of H_2O by holes to produce hydroxyl radicals. These photo-generated, highly reactive radicals can subsequently decompose the organic compound. [*Bekermann-2010-A*, *Fujishima*-2000]

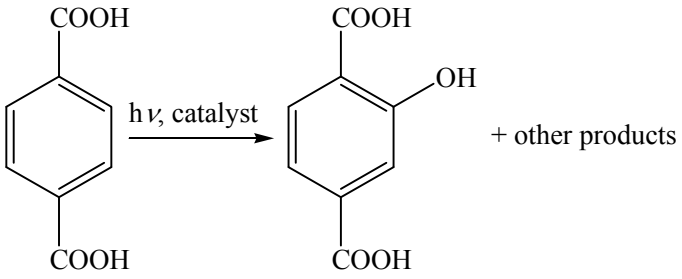

Figure 8.12: Formation of a fluorescent HOTPA in the PCO process.

Several test systems for the investigation of PCO performances of SCs, involving various kinds of organic compounds, have been reported in literature. The two most widely used methods are based on photo-bleaching of methylene blue aqueous solution in contact with thin solid catalyst layer, and on photo-degradation of a solid fatty deposit (e.g. stearic acid) over catalyst layer. While the drawback of the first procedure is the aqueous-solid system itself, being not suitable for investigations of solid-solid and solid-air interfaces, the latter has the disadvantage, that both, oxidation and reduction processes can bleach methyleneblue. [*Černigoj-2010*, *Zita-2009*] In this work, the self-cleaning activity of the synthesized materials was investigated *via* a quantitative and highly sensitive PCO method, based on the monitoring of a TPA oxidation product, namely hydroxyterephthalic acid (HOTPA) (**figure 8.12**). [*Černigoj-2010*]

For PCO measurements, [*Černigoj-2010*] samples (ZnO and Co_3O_4/ZnO) were pre-irradiated for 24 h and subsequently dipped in a sodium terephthalate (NaTPA)/hydroxyethyl-cellulose (HEC) solution, consisting of 10 ml of NaTPA solution and 20 ml of HEC solution. NaTPA was prepared by mixing together TPA (500 mg, 0.0031 mol), an aqueous solution of NaOH (31 ml, 0.201 M) and CH_3CH_2OH (96%, up to 50 ml of final volume). HEC solution consisted of aqueous hydroxyethyl-cellulose (2 wt.%, 10 ml) and CH_3CH_2OH (96%, 30 ml). After solvent evaporation, an organic coating (thickness = 1.04 ± 0.01 mm, determined by a Taylor-Hobson Talysurf profilometer) on the sample surface was obtained. The resulting samples were irradiated under the same conditions adopted for PSH tests. After regular time intervals, the organic coating was washed with a 1/1 CH_3CH_2OH/H_2O mixture and the reaction kinetics was studied by High Performance Liquid Chromatography with Fluorescence Detection (HPLC-FLD) analysis monitoring the HOTPA concentration (uncertainty = ± 2 mg l^{-1}). PCO tests were made on each specimen after different irradiation times, cleaning the sample surface in an ultrasonic bath (CH_3CH_2OH/H_2O) for 15 min, followed by a 3 h pre-irradiation between two consecutive measurements. PCO measurements were performed in collaboration with the group of Prof. Urška Lavrenčič-Štangar (Laboratory for Environmental Research, Nova Gorica University - Slovenia). [*Bekermann-2010-A*, *Černigoj-2010*]

❖ 8.6.3 Photocatalytic H_2 Production

H_2 is considered a highly promising energy vector as an alternative to fossil fuels, since its combustion/oxidation (i.e. in combustion cells) frees considerable amounts of energy in a virtually pollution-free process. [*Gasparotto-2009*] In the present work, the Co_3O_4 films and Ag/ZnO composites on Si(100) have been tested in the photocatalytic production of H_2 starting from aqueous solutions H_2O/CH_3CH_2OH = 1/1 in the presence of O_2, upon UV and Vis irradiation, in collaboration with the group of Prof. P. Fornasiero (Department of Chemical and Pharmaceutical Sciences, University Trieste, Italy). [*Barreca-2010-B*]

The reactions taking place during the photo-assisted processes are highly complex, so that until now they are not understood in detail. Nevertheless, below some general mechanisms, reported in literature, are briefly described, explaining the formation of the main species generated during the photocatalytic H_2 production from CH_3CH_2OH/H_2O solutions.

At the beginning of the photocatalytic process, electromagnetic radiation is partially absorbed by a suitable material, a SC, whose bandgap energy is in the energy range of the incident light. The hereby generated electrons and holes migrate to the catalyst surface and, in the case of pure H_2O, can produce O_2 and H_2 from H_2O. [*Chen-2010-B*] This process, called water photo-splitting, is generally realized by a mechanism involving hydroxyl radical species and H^+ ions, generated from H_2O. While the hydroxyl radicals lead to the formation of O_2, H^+ ions react with the electrons in the conduction band to give H_2. [*Minggu-2010*]

It is often reported that the presence of O_2 in water leads to a competition between the oxygen itself and photo-generated H^+ ions with conduction band electrons. While the latter process is highly desired for the production of gaseous H_2, the reactions between O_2 and electron generated $O_2^{\bullet-}$, that act as H^+ scavengers. As a consequence, the H^+ species are involved in the formation of $HO_2^{\bullet}$ instead of H_2. [*Hameed-2005*] Nonetheless, an oxide SC can, in the presence of photo-produced H_2, be reduced at the surface, which inevitably leads to a reduction of the photocatalytic activity. [*Barreca-2010-B*] To avoid this effect, the experiments were carried out under O_2 flow. Besides the protection against reduction, oxygen can protect the catalytic surface from intoxication by carbon containing residuals, which are formed in the presence of organic species. [*Barreca-2010-B*]

In this work, the photocatalytic H_2 production was performed from water/alcohol (CH_3OH or CH_3CH_2OH) solutions. Alcohols are frequently used for mainly two reasons. First, the alcohol molecules work as sacrificial agents, interacting with the photo-generated holes, thus minimizing electron/hole recombination. [*Chen-2010-B*, *Barreca-2010-B*] Second, it is possible that the alcohol contributes to H_2 generation by photo-reforming. The process typically starts with alcohol adsorption at the semiconductor surface. In the case of CH_3CH_2OH, consequent oxidation to acetaldehyde (CH_3CHO) by the holes occurs. Simultaneously, the produced H^+ species are reduced to H_2 by the photogenerated electrons. [*Hameed-2005*] The process can continue and lead to the formation of CO and CH_4 as well as CO_2 (reaction 8.2): [*Chen-2010-B*]

$$CH_3CH_2OH + H_2O \xrightarrow{h\nu,\ SC} CH_4 + CO_2 + 2\ H_2 \qquad \text{(reaction 8.2)}$$

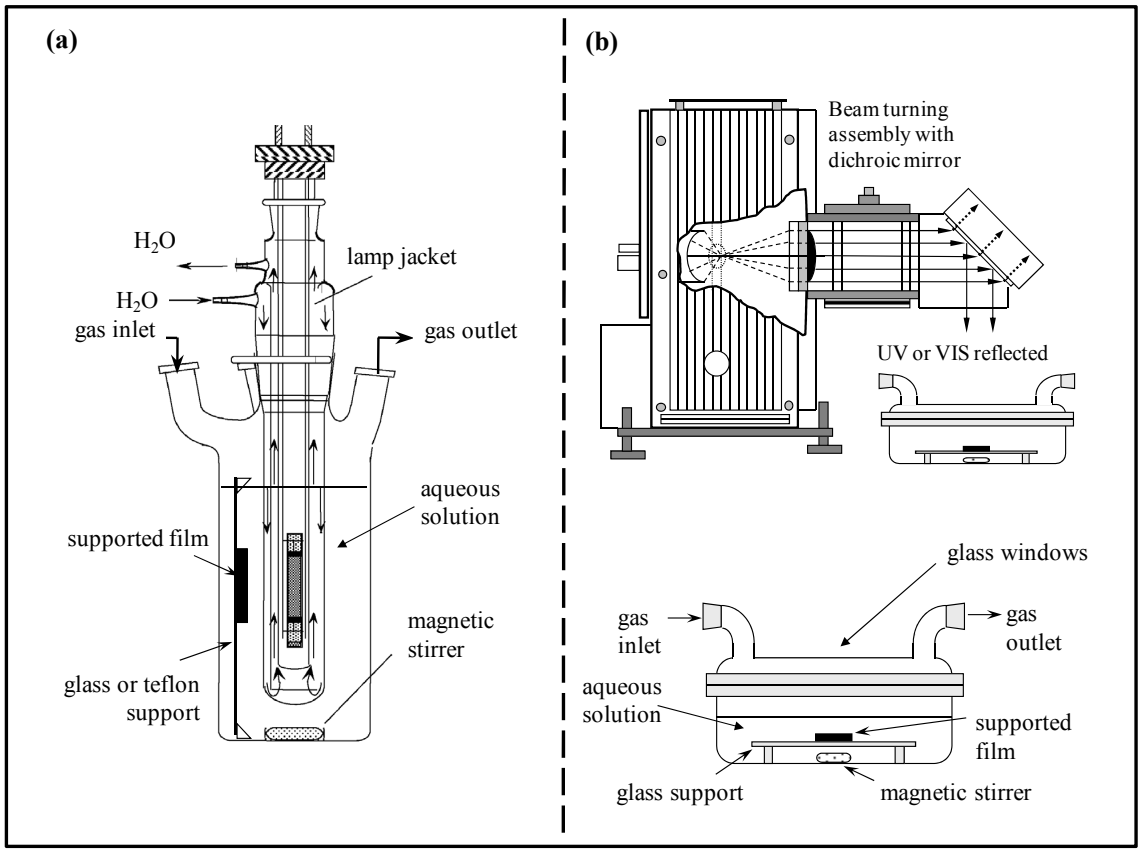

Figure 8.13: Scheme of the experimental setup for: (a) UV-Vis photocatalytic experiments, using a 250 mL pyrex discontinuous batch reactor equipped with a 125 W medium pressure mercury lamp (Helios Italquartz); (b) experiments under simulated solar radiation, using a Solar Simulator (LOT-Oriel) equipped with a 150 W Xe lamp, filtered to reduce the fraction of UV photons.

UV-Vis photocatalytic experiments were carried out in a 250 mL pyrex discontinuous batch reactor maintained at 20°C, filled with a 1:1 H_2O/CH_3OH mixture. Ar gas (15 ml min^{-1}) was used to collect and transfer gaseous products to the analysis system (**figure 8.13 (a)**). A 125 W medium pressure mercury lamp (Helios Italquartz) with pyrex walls was used for UV-Vis excitation (photon flux ϕ_i = 29 mW cm^{-2} (λ = 360 nm) and 100 mW×cm^{-2} (λ = 400÷1050 nm), determined by a DeltaOHM radiometer HD2302.0). Experiments under simulated solar radiation were carried out in a stainless steel photoreactor, using the same temperature and reaction mixture as before (**figure 8.13 (b)**). Illumination was performed using a Solar Simulator (LOT-Oriel) equipped with a 150 W Xe lamp, suitably filtered to reduce the fraction of UV photons. The light intensity for simulated solar light experiment, estimated by radiometry, was 180 mW cm^{-2}. Experiments were repeated three times on different samples to check reproducibility. On-line detection of evolved gases was performed by a gas chromatograph (Agilent HP 6890), that consists of two columns and two detectors. The first column (molsieve 5 Å), with Ar as carrier gas, is connected to a thermal conductivity detector for the analysis of H_2, O_2, N_2, CH_4 and CO. The second column (PoraPLOT Q) uses He as carrier gas and is connected to a methanator followed by a flame ionization detector for the analysis of carbon-containing species.

It is important to note that the measurement of the Ag/ZnO exposed surface is a critical issue in (photo)catalysis. In general, conventional N_2 or Kr physisorption methods fail for supported nanosystems, as the estimation of the mass of the active component with respect to the supporting substrate cannot be performed with accuracy. On the other hand, scratching of the deposited material from the substrate induces further uncertainties. As a consequence, we related the activity to the geometrical surface, which has indeed a practical meaning in terms of technological applications.

The analyses were carried out in collaboration with the group of Prof. P. Fornasiero (Department of Chemical and Pharmaceutical Sciences, Trieste University – Italy).

❖ 8.6.4 Gas Sensing

In order to investigate the gas sensing properties of the target metal oxide nanomaterials (ZnO, (F-)Co_3O_4, Ag/ZnO and Co_3O_4/ZnO), the latter were deposited on polycrystalline

Al_2O_3 substrates (3 mm × 3 mm), a suitable isolating material for this kind of application that does not contribute to the conductivity of the deposit. [*Penza-2009*]

A schematic representation of the devices used for the gas sensor measurements is shown in **figure 8.14**. After the deposition of the target nanomaterial on Al_2O_3, Pt electrodes are sputtered on the deposit surface using a mask. The working temperature (WT) of the sensor is controlled and monitored by a Pt heating element, deposited on the backside of the substrate. Uniform heating of the whole region of interest is ensured by its structure (**figure 8.14**) and the low thickness of the alumina substrates. The sensors, obtained in this way, were mounted on a device (TO8 *package*, **figure 8.15**) and contacted by thin gold wires.

Gas sensing measurements were carried out at atmospheric pressure in a sealed chamber maintained at 20°C, using the flow-through technique. The sensor responses were investigated at temperatures between 100 - 400°C, after pre-heating at each operating temperature for 8 h inside the test chamber for thermal stabilization. A volt amperometric technique was applied to measure the gas sensing characteristics of the sample. The voltage was kept constant at 1 V, and the current was recorded as a function of the atmosphere. As reference served the detection of a mixture of synthetic gas (0.3 l/min) and a known fraction of the analyte. All tests were carried out under a constant and controlled humidity level of 40 %.

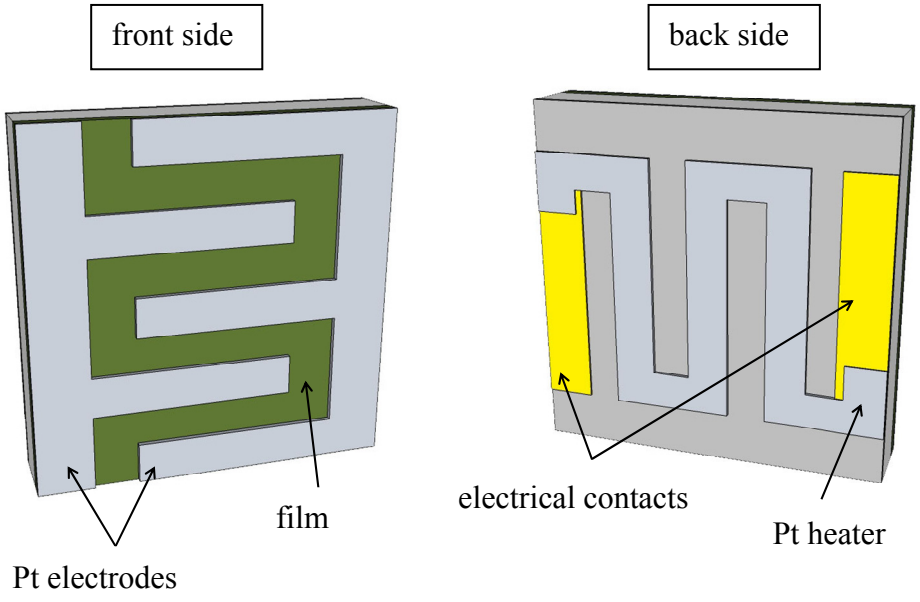

Figure 8.14: Scheme of the devices used for the gas sensor measurements. [*Barreca-2007-D*]

From the ratio of the measured current and the applied potential, it is possible to obtain the conductance (or resistance) value of the tested material. For *n*-type SCs, like ZnO, the conductance increases upon exposure to a reducing gas and decreases upon detection of oxidizing gases. For *p*-type SCs, like Co_3O_4, the opposite behaviour is expected. The sensor response *S* is determined by the relative variation of these values: [*Barreca-2007-D*, *Barreca-2010-A*]

$$S = R_f - R_0 / R_0 = \Delta R / R_0 \qquad \text{(equation 8.13)}$$

(*n*-type sensor and oxidizing gases or *p*-type sensor and reducing gas)

$$S = G_f - G_0 / G_0 = \Delta G / G_0 \qquad \text{(equation 8.14)}$$

(*n*-type sensor and reducing gases or *p*-type sensor and oxidizing gas)

where R_0 and G_0 are the initial resistance and conductance in the presence of artificial air, and R_f and G_f are the corresponding values upon contact with the analyte gas.

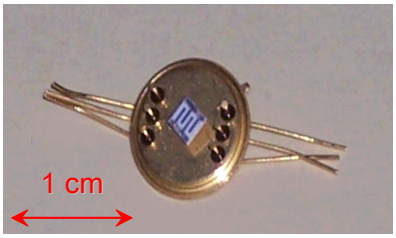

Figure 8.15: Image of a TO8 *package* used for the sensor measurements. Pt electrodes are visible on the sample surface.

The response time is calculated as the time required for reaching 90% of the equilibrium value upon contact with the analyte. The recovery time is the time for the sensor to return to 30% of the original conductance at the end of the target gas pulse. [*Barreca-2007-D*, *Barreca-2010-C*]

The selectivity (*Q*) is defined as:

$$Q = S_T / S_I \qquad \text{(equation 8.15)}$$

i.e., the ratio between the response to the target gas (S_T) and interfering gases (S_I) at the same temperature and analyte concentration.

In this work, measurements were performed in collaboration with Brescia University – Italy (group of Prof. G. Sberveglieri). The data were recorded by a picoamperometer (Keithley 486) and a signal amplifier (Keithley 7001 SWITCH SYSTEM).

9. Bibliography

[*Abe-2010*] R.J. Abe, Photochem. Photobiol., C 11 (2010) 179.

[*Alenzi-2010*] N. Alenzi, W.-S. Liao, P.S. Cremer, V. Sanchez-Torres, T.K. Wood, C. Ehlig-Economides, Z. Cheng, Int. J. Hydrogen Energy 35 (2010) 11768.

[*Alford-2005*] F. Bassini, G.L. Liedl, P. Wyder, Encyclopedia of Condensed Matter Physics, Elsevier Science, 2005.

[*Al-Hardan-2010*] N.H. Al-Hardan, M.J. Abdullah, A. Abdul Aziz, H. Ahmad, L.Y. Low, Vacuum 85 (2010) 101.

[*Ali-2009*] M. Ali, N. Friedenberger, M. Spasova, M. Winterer, Chem. Vap. Deposition 15 (2009) 192.

[*Arabatzis-2003*] I.M. Arabatzis, T. Stergiopoulos, M.C. Bernard, D. Labou, S.G. Neophytides, P. Falaras, Appl. Catal., B 42 (2003) 187.

[*Arii-2006*] T. Arii, A. Kishi, J. Thermal Anal. Calometry 83 (2006) 253.

[*Armaroli-2011*] N. Armaroli, V. Balzani, ChemSusChem 4 (2011) 21.

[*Armelao-1998*] L. Armelao, R. Bertoncello, S. Coronaro, A. Glisenti, Sci. Technol. Cultural Heritage 7 (1998) 41.

[*Armelao-2006*] L. Armelao, D. Barreca, G. Bottaro, A. Gasparotto, D. Leonarduzzi, C. Maragno, E. Tondello, C. Sada, J. Vac. Sci. Technol., A 24 (2006) 1941.

[*Armelao-2007*] L. Armelao, D. Barreca, G. Bottaro, A. Gasparotto, C. Maccato, C. Maragno, E. Tondello, U. Lavrenčič Štangar,, M. Bergant, D. Mahne, Nanotechnol. 18 (2007) 375709.

[*Armelao-2008*] L. Armelao, G. Bottaro, M. Pascolini, M. Sessolo, E. Tondello, M. Bettinelli, A. Speghini, J. Phys. Chem. C 112 (2008) 4049.

[*Armelao-2009*] L. Armelao, D. Barreca, G. Bottaro, A. Gasparotto, C. Maccato, E. Tondello, O.I. Lebedev, S.Turner, G. Van Tendeloo, C. Sada, U.L. Štangar, ChemPhysChem 10 (2009) 3249.

[*Arora-1998*] M.K. Arora, A.S.K. Sinha, S.N. Upadhyay, Ind. Eng. Chem. Res. 37 (1998) 3950.

[*Aroutiounian-2007*] V. Aroutiounian, Int. J. Hydrogen Energy 32 (2007) 1145.

[*Ashraf-2011*] S. Ashraf, A.C. Jones, J. Basca, A. Steiner, P.R. Chalker, P. Beahan, S. Hindley, R. Odedra, P.A. Williams, P.N. Heys, Chem. Vap. Deposition 17 (2011) 45.

[*Atkins-2006*] P.W. Atkins, J. De Paula, M. Baer, Physikalische Chemie, WILEY-VCH, Weinheim, Germany, 2006.

[*Auld-1994*] J. Auld, D.J. Houlton, A.C. Jones, S.A. Rushworth, M.A. Malik, P. O'Brien, G.W. Critchlow, J. Mater. Chem. 4 (1994) 1249.

[*Backman-2009*] L.B. Backman, A. Rautiainen, M. Lindblad, A.O.I. Krause, Appl.Catal. A: General 360 (2009) 183.

[*Badre-2009*] C. Badre, T. Pauporté, Adv. Mater. 21 (2009) 697.

[*Bals-2004*] S. Bals, B. Kabius, M. Haider, V. Radmilovic, C. Kisielowski, Annular dark field imaging in a TEM, Solid State Commun. 130 (2004) 675.

[*Bandoli-2009*] G. Bandoli, D. Barreca, A. Gasparotto, C. Maccato, R. Seraglia, E. Tondello, A. Devi, R.A. Fischer, M. Winter, Inorg. Chem. 48 (2009) 82.

[*Barreca-2001*] D. Barreca, C. Massignan, S. Daolio, M. Fabrizio, C. Piccirillo, L. Armelao, E. Tondello, Chem. Mater. 13 (2001) 588.

[*Barreca-2003-A*] D. Barreca, A. Gasparotto, E. Tondello, C. Sada, S. Polizzi, A. Benedetti, Chem. Vapor Deposition 9 (2003) 199.

[*Barreca-2003-B*] D. Barreca, G.A. Battiston, D. Berto, A. Convertino, A. Gasparotto, R. Gerbasi, E. Tondello, S. Viticoli, Proc. - Electrochem. Soc. 8 (2003) 1153.

[*Barreca-2005*] D. Barreca, A. Gasparotto, C. Maragno, E. Tondello, S. Gialanella, J. Appl. Phys. 97 (2005) 054311.

[*Barreca-2007-A*] D. Barreca, E. Comini, A.P. Ferrucci, A. Gasparotto, C. Maccato, C. Maragno, G. Sberveglieri, E. Tondello, Chem. Mater. 19 (2007) 5642.

[*Barreca-2007-B*] D. Barreca, A.P. Ferrucci, A. Gasparotto, C. Maccato, C. Maragno, E. Tondello, Chem. Vap. Deposition 13 (2007) 618.

[*Barreca-2007-C*] D. Barreca, A. Gasparotto, C. Maccato, C. Maragno, E. Tondello, Surf. Sci. Spectra 14 (2007) 19.

[*Barreca-2007-D*] D. Barreca, A. Gasparotto, C. Maccato, C. Maragno, E. Tondello, E. Comini, G. Sberveglieri, Nanotechnol. 18 (2007) 125502.

[*Barreca-2007-D*] D. Barreca, A. Gasparotto, C. Maccato, C. Maragno, E. Tondello, G. Rossetto, Chem. Vap. Deposition 13 (2007) 205.

[*Barreca-2008-A*] D. Barreca, A. Gasparotto, C. Maccato, E. Tondello, Nanotechnol. 19 (2008) 255602.

[*Barreca-2008-B*] D. Barreca, A. Gasparotto, C. Maccato, E. Tondello, G. Rossetto, Thin Solid Films 516 (2008) 7393.

[*Barreca-2009-A*] D. Barreca, A. Gasparotto, C. Maccato, E. Tondello, U. Lavrenčič Štangar, S.R. Patil, Surf. Coat. Technol. 203 (2009) 2041.

[*Barreca-2009-B*] D. Barreca, E. Comini, A. Gasparotto, C. Maccato, C. Sada, G. Sberveglieri, E. Tondello, Sens. Actuators B: Chem. 141 (2009) 270.

[*Barreca-2009-C*] D. Barreca, P. Fornasiero, A. Gasparotto, V. Gombac, C. Maccato, T. Montini, E. Tondello, ChemSusChem 2 (2009) 230.

[*Barreca-2010-A*] D. Barreca, D. Bekermann, E. Comini, A. Devi, R.A. Fischer, A. Gasparotto, C. Maccato, C. Sada, G. Sberveglieri, E. Tondello, CrystEngComm 12 (2010) 3419.

[*Barreca-2010-B*] D. Barreca, E. Comini, A. Gasparotto, C. Maccato, A. Pozza, C. Sada, G. Sberveglieri, E. Tondello, J. Nanosci. Nanotechnol. 10 (2010) 8054.

[*Barreca-2010-C*] D. Barreca, D. Bekermann, E. Comini, A. Devi, R.A. Fischer, A. Gasparotto, C. Maccato, G. Sberveglieri, E. Tondello, Sens. Actuators, B 149 (2010) 1.

[*Barreca-2010-D*] D. Barreca, A. Gasparotto, O.I. Lebedev, C. Maccato, A. Pozza, E. Tondello, S. Turner, G. Van Tendeloo, CrystEngComm 12 (2010) 2185.

[*Barreca-2010-E*] D. Barreca, M. Cruz-Yusta, A. Gasparotto, C. Maccato, J. Morales, A. Pozza, C. Sada, L. Sánchez, E. Tondello, J. Phys. Chem. C 114 (2010) 10054.

[*Barreca-2010-F*] D. Barreca, P. Fornasiero, A. Gasparotto, V. Gombac, C. Maccato, A. Pozza, E. Tondello, Chem. Vap. Deposition 16 (2010) 296.

[*Barreca-2010-G*] D. Barreca, D. Bekermann, A. Devi, R.A. Fischer, A. Gasparotto, C. Maccato, E. Tondello, M. Rossi, S. Orlanducci, M.L. Terranova, Chem. Phys. Lett. 500 (2010) 287.

[*Barreca-2011-A*] D. Barreca, G. Carraro, E. Comini, A. Gasparotto, C. Maccato, C. Sada, G. Sberveglieri, E. Tondello, J. Phys. Chem. C 115 (2011) 10510.

[*Barreca-2011-B*] D. Barreca, G. Carraro , V. Gombac, A. Gasparotto, C. Maccato, P. Fornasiero, E. Tondello, Adv. Funct. Mater. 21 (2011) 2611.

[*Barreca-2011-C*] D. Barreca, D. Bekermann, E. Comini, A. Devi, R.A. Fischer, A. Gasparotto, M. Gavagnin, C. Maccato, C. Sada, G. Sberveglieri, E. Tondello, Sens. Actuators, B 160 (2011) 79.

[*Barreca-2011-D*] D. Barreca, A. Devi, R.A. Fischer, D. Bekermann, A. Gasparotto, M. Gavagnin, C. Maccato, E. Tondello, E. Bontempi, L.E. Depero, C. Sada, CrystEngComm 13 (2011) 3670.

[*Barreca-2011-E*] D. Barreca, A. Gasparotto, E. Tondello, J. Mater. Chem. 21 (2011) 1648.

[*Barreca-2011-F*] D. Barreca, G. Carraro, A. Gasparotto, C. Maccato, O.I. Lebedev, A. Parfenova, S. Turner, E. Tondello, G. Van Tendeloo, Langmuir 27 (2011) 6409.

[*Basu-2009*] S. Basu, P.K. Basu, J. Sens. 2009 (2009) 861968.

[*Baxter-2009*] J.B. Baxter, E.S. Aydil, J. Electrochem. Soc. 156 (2009) H52.

[*Bayram-2009*] C. Bayram, M. Razeghi, D.J. Rogers, F. Hosseini Teherani, J. Vac. Sci. Technol. B 27 (2009) 1784.

[*Becker-2010*] M. Becker, R. Naumann d'Alnoncourt, K. Kähler, J. Sekulic, R.A. Fischer, M. Muhler, Chem. Vap. Deposition 16 (2010) 85.

[*Bekermann-2009*] D. Bekermann, D. Pilard, R. A. Fischer, A. Devi, Proc. - Electrochem. Soc. 25 (2009) 601.

[*Bekermann-2010-A*] D. Bekermann, A. Gasparotto, D. Barreca, A. Devi, R.A. Fischer, M. Kete, U. Lavrenčič Štangar, O.I. Lebedev, C. Maccato, E. Tondello, G. Van Tendeloo, ChemPhysChem 11 (2010) 2337.

[*Bekermann-2010-B*] D. Bekermann, A. Gasparotto, D. Barreca, L. Bovo, A. Devi, R.A. Fischer, O.I. Lebedev, C. Maccato, E. Tondello, G. Van Tendeloo, Cryst. Growth Des. 10 (2010) 2011.

[*Bekermann-2010-C*] D. Bekermann, D. Rogalla, H.-W. Becker, M. Winter, R.A. Fischer, A. Devi, Eur. J. Inorg. Chem. (2010) 1366.

[*Bekermann-2011*] D. Bekermann, A. Ludwig, T. Toader, C. Maccato, D. Barreca, A. Gasparotto, C. Bock, A.D. Wieck, U. Kunze, E. Tondello, R.A. Fischer, A. Devi, Chem. Vap. Deposition 17 (2011) 155.

[*Bekermann-2012*] D. Bekermann, A. Gasparotto, D. Barreca, C. Maccato, E. Comini, C. Sada, G. Sberveglieri, A. Devi, R.A. Fischer, ACS Appl. Mater. Interfaces 4 (2012) 928.

[*Bhargava-2010*] R. Bhargava, P.K. Sharma, R.K. Dutta, S. Kumar, A.V. Pandey, N. Kumar, Mater. Chem. Phys. 120 (2010) 393.

[*Bhattacharyy-2006*] P. Bhattacharyya, P.K. Basu, H. Saha, S. Basu, Sens. Lett. 4 (2006) 371.

[*Bhattacharyy-2007*] P. Bhattacharyya, P.K. Basu, H. Saha, S. Basu, Sens. Actuators, B 124 (2007) 62.

[*Bhattacharyy-2008-A*] P. Bhattacharyya, P.K. Basu, B. Mondal, H. Saha, Microelectron. Reliab. 48 (2008) 1772.

[*Bhattacharyy-2008-B*] P. Bhattacharyya, P.K. Basu, C. Lang, H. Saha, S. Basu, Sens. Actuators, B 129 (2008) 551.

[*Bie-2007*] L.-J. Bie, X.-N. Yan, J. Yin, Y.-Q. Duan, Z.-H. Yuan, Sens. Actuators, B 126 (2007) 604.

[*Binnig-1986*] G. Binnig, C.F. Quate, C. Gerber, Phys. Rev. Lett., 56 (1986) 930.

[*Black-2008*] K. Black, A.C. Jones, P.R. Chalker, J.M. Gaskell, R.T. Murray, T.B. Joyce, S.A. Rushworth, J. Cryst. Growth 310 (2008) 1010.

[*Black-2010*] K. Black, P.R. Chalker, A.C. Jones, P.J. King, J.L. Roberts, and P.N. Heys,

[*Borras-2009*] A. Borras, J.R. Sanchez-Valencia, R. Widmer, V.J. Rico, A. Justo, A.R. Gonzalez-Elipe, Cryst. Growth Des. 9 (2009) 2868.

[*Boumaza-2009*] S. Boumaza, R. Bouarab, M. Trari, A. Bouguelia, Energy Convers. Manage. 50 (2009) 62.

[*Briggs-1983*] D. Briggs, M.P. Seah, Practical Surface Analysis by Auger and X-ray Photoelectron Spectroscopy, John Wiley and Sons, Chichester, UK, 1983.

[*Briggs-2003*] D. Briggs, J.T. Grant, Surface Analysis by Auger and X-Ray Photoelectron Spectroscopy, IM Publications, Chichester, UK, 2003.

[*Briggs-1990*] D. Briggs, M.P. Seah, Practical Surface Analysis, vol. 1, Wiley, New York, 1990.

[*Brundle-1992*] C.R. Brundle, C.A. Evans, Jr. S. Wilson, Encyclopedia of Materials Characterization, Surfaces, Interfaces, Thin Films, Butterworth-Heinemann, Greenwich, USA, 1992.

[*Cao-2006*] A.M. Cao, J.S. Hu, H.P. Liang, W.G. Song, L.J. Wan, X.L. He, X.G. Gao, S.H. Xia, J. Phys. Chem. B 110 (2006) 15858.

[*Cademartiri-2009*] L. Cademartiri, G.A. Ozin, Concepts of Nanochemistry, WILEY-VCH, Weinheim, Germany, 2009.

[*Calestani-2010*] D. Calestani, M. Zha, R. Mosca, A. Zappettini, M.C. Carotta, V. Di Natale, L. Zanotti, Sens. Actuators, B 144 (2010) 472.

[*Cargill-1976*] R.W. Cargill, J. Chem. Soc., Faraday Trans. 72 (1976) 2296.

[*Cargnello-2011*] M. Cargnello, A. Gasparotto, V. Gombac, T. Montini, D. Barreca, P. Fornasiero, Eur. J. Inorg. Chem. (2011) 4309.

[*Carson-1996*] G.A. Carson, M.H. Nassir, M.A. Langell, J. Vac. Sci. Technol., A 14 (1996) 1637.

[*Casas-Cabanas-2009*] M. Casas-Cabanas, G. Binotto, D. Larcher, A. Lecup, V. Giordani, J.-M. Tarascon, Chem. Mater. 21 (2009) 1939.

[*Çetinörgü-2007*] E. Çetinörgü, S. Goldsmith, R.L. Boxman, J. Cryst. Growth 299 (2007) 259.

[*Černigoj-2010*] U. Černigoj, M. Kete, U. Lavrenčič Štangar, Catal. Today 151 (2010) 46.

[*Chang-2008*] S.-J. Chang, T.-J. Hsueh, I.-C. Chen, B.-R. Huang, Nanotechnol. 19 (2008) 175502.

[*Chatterjee-1999*] A.P. Chatterjee, P. Mitra, A.K. Mukhopadhyay, J. Mater. Sci. 34 (1999) 4225.

[*Chen-1999*] J. Chen, D.F. Ollis, W.H. Rulkens, H. Bruning, Water Res. 33 (1999) 669.

[*Chen-2006*] Y. Chen, C. L. Zhu, G. Xiao, Nanotechnol. 17 (2006) 4537.

[*Chen-2008*] Y.-J. Chen, C.-L. Zhu, G. Xiao, Sens. Actuators, B 129 (2008) 639.

[*Chen-2009*] D. Chen, Z. Jiang, J. Geng, J. Zhu, D. Yang, J. Nanopart. Res. 11 (2009) 303.

[*Chen-2010-A*] S.H. Chen, S. Sun, H. Sun, W. Fan, X. Zhao, X. Sun, J. Phys. Chem. C 114 (2010) 7680.

[*Chen-2010-B*] X. Chen, S. Shen, L. Guo, S.S. Mao, Chem. Rev. 110 (2010) 6503.

[*Chen-2011-A*] M. Chen, Z. Wang, D. Han, F. Gu, G. Guo, Sens. Actuators, B 157 (2011) 565.

[*Chen-2011-B*] M. Chen, Z. Wang, D. Han, F. Gu, G. Guo, J. Phys. Chem. C 115 (2011) 12763.

[*Chithrani-2009*] B.D. Chithrani, W.C.W. Chan, Nano Lett. 7 (2007) 1542.

[*Cho-2009*] S. Cho, S. Kim, J.-W. Jang, S.-H. Jung, E. Oh, B.R. Lee, K.-H. Lee, J. Phys. Chem. C 113 (2009) 10452.

[*Choi-2001*] S.D. Choi, B.K. Min, Sens. Actuators B: Chem. 77 (2001) 330.

[*Choi-2003*] H. Choi, S. Park, Chem. Mater. 15 (2003) 3121.

[*Choi-2010*] K.I. Choi, H.R. Kim, K.M. Kim, D. Liu, G. Cao, J.H. Lee, Sens. Actuators B: Chem. 146 (2010) 183.

[*Chowdhuri-2002*] A. Chowdhuri, P. Sharma, V. Gupta, K. Sreenivas, K.V. Rao, J. Appl. Phys. 92 (2002) 2172.

[*Choy-2003*] K.L. Choy, Prog. Mater. Sci. 48 (2003) 57.

[*Christoulakis-2006*] S. Christoulakis, M. Suchea, E. Koudoumas, M. Katharakis, N. Katsarakis, G. Kiriakidis, Appl. Surf. Sci. 252 (2006) 5351.

[*Chuang-2011*] H.-Y. Chuang, D.-H. Chen, Int. J. Hydrogen Energy 36 (2011) 9487.

[*Coates-1965*] G.E. Coates, D. Ridley, J. Chem. Soc. (1965) 1870.

[*Colombo-1998*] D.G. Colombo, D.C. Gilmer, V.G. Young, S.A. Campbell, W.L. Gladfelter, Chem. Vap. Deposition 4 (1998) 220.

[*Comini-2000*] E. Comini, G. Sberveglieri, V. Guidi, Sens. Actuators B: Chem. 70 (2000) 108.

[*Comini-2005*] E. Comini, G. Faglia, M. Ferroni, G. Sberveglieri, M. Sacerdoti, IEEE Sensors Proc. (2005) 1323.

[*Comini-2009-A*] E. Comini, C. Baratto, G. Faglia, M. Ferroni, A. Vomiero, G. Sberveglieri, Prog. Mater. Sci. 54 (2009) 1.

[*Comini-2009-B*] E. Comini, G. Faglia, G. Sberveglieri, Solid State Gas Sensing, Springer, New York, USA, 2009.

[*Comini-2010*] E. Comini, G. Sberveglieri, Mater. Today 13 (2010) 28.

[*Cong-2009*] H.P. Cong, S.H. Yu, Cryst. Growth Des. 9 (2009) 210.

[*Cotton-1964*] F.A. Cotton, R.H. Soderberg, Inorg. Chem. 3 (1964) 1.

[*Cowley-1993*] J.M. Cowley, Electron diffraction techniques, Oxford University Press, Oxford, UK, 1993.

[*Curri-2010*] M.L. Curri, R. Comparelli, M. Striccolia, A. Agostiano, Phys. Chem. Chem. Phys. 12 (2010) 11197.

[*Czoska-2008*] A.M. Czoska, S. Livraghi, M. Chiesa, E. Giamello, S. Agnoli, G. Granozzi, E. Finazzi, C. Di Valentin, G. Pacchioni, J. Phys. Chem. C 112 (2008) 8951.

[*Das-2010*] S.N. Das, J.P. Kar, J.-H. Choi, T. Il Lee, K.-J. Moon, J.-M Myoung, J. Phys. Chem. C 114 (2010) 1689.

[*Dayan-1997*] N.J. Dayan, S.R. Sainkar, A.A. Belkehar, R.N. Karekar, R.C. Aiyer, J. Mater. Sci. Lett. 16 (1997) 1952.

[*Decremps-2002*] F. Decremps, J.P. Porres, A.M. Saitta, J.C. Chervin, A. Polian, Phys. Rev. B 65 (2002) 092101.

[*Demyanets-2011*] L.N. Demyanets, R.M. Zakalyukin, B.N. Mavrin, Inorg. Mater. 47 (2011) 649.

[*Deng-2009*] S. Deng, H.M. Fan, X. Zhang, K.P. Loh, C.-L. Cheng, C.H. Sow, Y.L. Foo, Nanotechnol. 20 (2009) 175705.

[*Diskus-2011*] M. Diskus, O. Nilsen, H. Fjellvåg, Chem. Vap. Deposition 17 (2011) 135.

[*Dittmar-2004*] A. Dittmar, H. Kosslick, J.P. Müller, M.M. Pohl, Surf. Coat. Technol. 182 (2004) 35.

[*Dong-2008*] X. Dong, B. Zhang, X. Li, W. Zhao, R. Shen, Y. Zhang, X. Xia, G. Du, Semicond. Sci. Technol. 23 (2008) 045020.

[*Du-2008*] H. Du, C. Cao, Mater. Lett. 62 (2008) 1605.

[*Eberhart-1991*] J.P. Eberhart, Structural and Chemical Analysis of Materials, John Wiley & Sons, Chichester, UK, 1991.

[*Elias-2010*] J. Elias, C. Lévy-Clément, M. Bechelany, J. Michler, G.-Y. Wang, Z. Wang, L. Philippe, Adv. Mater. 22 (2010) 1607.

[*Falyouni-2009*] F. Falyouni, L. Benmamas, L. C. Thiandoume, J. Barjon, A. Lusson, P. Galtier, V. Sallet, J. Vac. Sci. Technol., B 27 (2009) 1662.

[*Feldmann-1986*] L.C. Feldman, JW. Mayer, Fundamentals of surface and thin film analysis, North-Holland, New York, USA, 1986.

[*Feng-2004*] X. Feng, L. Feng, M. Jin, J. Zhai, L. Jiang, D. Zhu, J. Am. Chem. Soc. 126 (2004) 62.

[*Fu-2007-A*] Q. Fu, T. Wagner, Surf. Sci. Rep. 62 (2007) 431.

[*Fu-2007-B*] Y.-S. Fu, X.W. Du, S.A. Kulinich, J.-S. Qiu, W.-J. Qin, R. Li, J. Sun, J. Liu, J. Am. Chem. Soc. 129 (2007) 16029.

[*Fu-2008*] X.L. Fu, J.L. Long, X.X. Wang, D.Y.C. Leung, Z.X. Ding, L. Wu, Z. Zhang, Z.H. Li, X.Z. Fu, Int. J. Hydrogen Energy 33 (2008) 6484.

[*Fujii-1995*] E. Fujii, H. Torii, A. Tomozawa, R. Takayama, T. Hirao, J. Mater. Sci. 30 (1995) 6013.

[*Fujishima-2000*] A. Fujishima, T.N. Rao, D.A. Tryk, J. Photochem. Photobiol., C 1 (2000) 1.

[*Fujishima-2008*] A. Fujishima, X. Zhang, D. A. Tryk, Surf. Sci. Rep. 63 (2008) 515.

[*Gangil-2007*] S. Gangil, A. Nakamura, Y. Ichikawa, K. Yamamoto, J. Ishihara, T. Aoki, J. Temmyo, J. Cryst. Growth 298 (2007) 486.

[*Gao-2005*] T. Gao, Q. Li, T. Wang, Chem. Mater. 17 (2005) 887.

[*Gao-2010*] X.-Y. Gao, H.-L. Feng, J.-M. Ma, Z.-Y. Zhang, J.-X. Lu, Y.-S. Chen, S.-E. Yang, J.-H. Gu, Physica B 405 (2010) 1922.

[*Gärtner-2009*] F. Gärtner, B. Sundararaju, A.-E. Surkus, A. Boddien, B. Loges, H. Junge, P.H. Dixneuf, M. Beller, Angew. Chem. Int. Ed. 48 (2009) 9962.

[*Gasparotto-2009*] A. Gasparotto, D. Barreca, P. Fornasiero, V. Gombac, O.I. Lebedev, C. Maccato, T. Montini, E. Tondello, G. Van Tendeloo, E. Comini, G. Sberveglieri, Proc. - Electrochem. Soc. 25 (2009) 1169.

[*Gasparotto-2011*] A. Gasparotto, D. Barreca, D. Bekermann, A. Devi, R.A. Fischer, C. Maccato, E. Tondello, J. Nanosci. Nanotechnol. 11 (2011) 8206.

[*Gasparotto-2011-A*] A. Gasparotto, D. Barreca, D. Bekermann, A. Devi, R.A. Fischer, P. Fornasiero, V. Gombac, O.I. Lebedev, C. Maccato, T. Montini, G. Van Tendeloo, E. Tondello, J. Am. Chem. Soc. 133 (2011) 19362.

[*Gaul-2000*] D.A. Gaul, O.Just, W.S. Rees, Inorg. Chem. 39 (2000) 5648.

[*Gelfi-2004*] M. Gelfi, E. Bontempi, R. Roberti, L.E. Depero, Acta Mater. 52 (2004) 583.

[*Ghosh-2005*] P.K. Ghosh, S. Das, S. Kundoo, K.K. Chattopadhyay, J. Sol-Gel Sci. Technol. 34 (2005) 173.

[*Gong-2000*] H. Gong, Y. Wang, Y. Luo, Appl. Phys. Lett. 76 (2000) 3959.

[*Gong-2006*] H. Gong, J.Q. Hu, J.H. Wang, C.H. Ong, F.R. Zhu, Sens. Actuators, B 115 (2006) 247.

[*Gulino-2000*] A. Gulino, F. Castelli, P. Dapporto, P. Rossi, I. Fragalà, Chem. Mater. 12 (2000) 548.

[*Gulino-2003*] A. Gulino, G. Fiorito, I. Fragalà, J. Mater. Chem. 13 (2003) 861.

[*Gulino-2003-A*] A. Gulino, P. Dapporto, P. Rossi, I. Fragalà, Chem. Mater. 15 (2003) 3748.

[*Grasserbauer-1986*] M. Grasserbauer, H.J. Dudek, M.F. Ebel, Applied Surface Analysis by Secondary Ion Mass Spectrometry, Auger Electron Spectroscopy, and X-Ray Photoelectron Spectrometry, Springer-Verlag, Berlin, Germany, 1986.

[*Grill-1993*] A. Grill, Cold Plasma in Materials Fabrication, IEEE Press, New York, USA, 1993.

[*Hagelin-Weaver-2004*] H.A. Hagelin-Weaver, G.B. Hoflund, D.M. Minahan, G.N. Salaita, Appl. Surf. Sci. 235 (2004) 420.

[*Hameed-2005*] A. Hameed, M.A. Gondal, J. Mol. Catal. A: Chem. 233 (2005) 35.

[*Han-2010*] N. Han, P. Hu, A. Zuo, D. Zhang, Y. Tian, Y. Chen, Sens. Actuators, B 145 (2010) 114.

[*Hazra -2006*] S.K. Hazra, S. Basu, Sens. Actuators, B 117 (2006) 177.

[*Height-2006*] M.J. Height, S.E. Pratsinis, O. Mekasuwandumrong, P. Praserthdam, Appl. Catal., B 63 (2006) 305.

[*Hernandez-Ramirez-2009*] F. Hernandez-Ramirez, J.D. Prades, R. Jimenez-Diaz, T. Fischer, A. Romano-Rodriguez, S. Mathur, J.R. Morante, Phys. Chem. Chem. Phys. 11 (2009) 7105.

[*Herron-1998*] N. Herron, D.L. Thorn, Adv. Mater. 10 (1998) 1173.

[*Hesse-2005*] M. Hesse, H. Meier, B. Zeeh, Spektroskopische Methoden in der organischen Chemie, 7. Auflage, Thieme Verlag, Stuttgart, Germany, 2005.

[*Higashiwaki-2009*] M. Higashiwaki, Z. Chen, R. Chu, Y. Pei, S. Keller, U.K. Mishra, N. Hirose, T. Matsui, T. Mimura, Appl. Phys. Lett. 94 (2009) 053513.

[*Hitchman-1993*] M.L. Hitchman, K.F. Jensen, Chemical Vapor Deposition: Principles and Applications, Academic Press, London, UK, 1993.

[*Hitchman-1995*] M.L. Hitchman, S.H. Shamlian, D.C. Gilliland, D. Cole-Hamilton, J.A.P. Nash, S.C. Thompson, S.L. Cook, J. Mater. Chem. 5 (1995) 47.

[*Hoa-2009*] N.D. Hoa, N.V. Quy, M.A. Tuan, N.V. Hieu, Physica E 42 (2009) 146.

[*Hong-2008*] R.Y. Hong, S.Z. Zhang, G.Q. Di, H.Z. Li, Y. Zheng, J. Ding, D.G. Wei, Mater. Res. Bull. 43 (2008) 2457.

[*Hongsith-2008*] N. Hongsith, C. Viriyaworasakul, P. Mangkorntong, N. Mangkorntong, S. Choopun, Ceram. Inter. 34 (2008) 823.

[*Hsieh-2008*] J.H. Hsieh, P.W. Kuo, K.C. Peng, S.J. Liu, J.D. Hsueh, S.C. Chang, Thin Solid Films 516 (2008) 5449.

[*Hsieh-2011*] J.H. Hsieh, C. Li, Y.Y. Wu, S.C. Jang, Thin Solid Films 519 (2011) 7124.

[*Hsueh-2007-A*] T.-J. Hsueh, Y.-W. Chen, S.-J. Chang, S.-F. Wang, C.-L. Hsu, Y.-R. Lin, T.-S. Lin, I.-C. Chen, J. Electrochem. Soc. 154 (2007) J393.

[*Hsueh-2007-B*] T.-J. Hsueh, C.-L. Hsu, S.-J. Chang, I.-C. Chen, Sens. Actuators, B 126 (2007) 473.

[*Hsueh-2007-C*] T.-J. Hsueh, S.-J. Chang, C.-L. Hsu, Y.-R. Lin, I.C. Chen, Appl. Phys. Lett. 91 (2007) 053111.

[*Hu-1991*] J. Hu, R.G. Gordon, Mater. Res. Soc. Symp. Proc. 202 (1991) 457.

[*Hu-1992*] J. Hu, R.G. Gordon, J. Appl. Phys. 71 (1992) 880.

[*Hu-2008*] L. Hu, Q. Peng, Y. Li, J. Am. Chem. Soc. 130 (2008) 16136.

[*Hu-2009*] Y.-S. Hu, A. Kleiman-Shwarsctein, G.D. Stucky, E.W. McFarland, Chem. Commun. (2009) 2652.

[*Huang-2001*] M.H. Huang, S. Mao, H. Feick, H.Q. Yan, Y.Y. Wu, H. Kind, E. Weber, R. Russo, P.D. Yang, Science 292 (2001) 1897.

[*Hübner-2010*] M. Hübner, C.E. Simion, A. Tomescu-Stănoiu, S. Pokhrel, N. Bârsan, U. Weimar, Sens. Actuators B: Chem. 153 (2010) 347.

[*Hung-2009*] N. Le Hung, E. Ahn, S. Park, H. Jung, H. Kim, S.K. Hong, D. Kim, C. Hwang, J. Vac. Sci. Technol., A 27 (2009) 1347.

[*Hwang-2009*] I.S. Hwang, J.K. Choi, S.J. Kim, K.Y. Dong, J.H. Kwon, B.K. Ju, J.H. Lee, Sens. Actuators, B 142 (2009) 105.

[*Ikeda-1998*] S. Ikeda, T. Takata, T. Kondo, G. Hitoki, M. Hara, J.N. Kondo, K. Domen, H. Hosono, H. Kawazoe, A. Tanaka, Chem. Commun. (1998) 2185.

[*Ikeda-1999*] S. Ikeda, T. Takata, M. Komoda, M. Hara, J.N. Kondo, K. Domen, A. Tanaka, H. Hosono, H. Kawazoe, Phys. Chem. Chem. Phys. 1 (1999) 4485.

[*Irimpan-2008*] L. Irimpan, V.P.N. Nampoori, P. Radhakrishnan, Chem. Phys. Lett. 455 (2008) 265.

[*Jain-1998*] S. Jain, T.T. Kodas, M. Hampden-Smith, Chem. Vap. Dep. 4 (1998) 51.

[*JCPDS-A*] Pattern no. 36-1451, JCPDS 2000.

[*JCPDS-B*] Pattern no. 45-0946, JCPDS, 2000.

[*JCPDS-C*] Pattern no. 42-1467, JCPDS, 2000.

[*JCPDS-D*] Pattern no. 04-0783, JCPDS 2000.

[*JCPDS-E*] Pattern no. 72-2108, JCPDS 2000.

[*Jeong-2004*] M.C. Jeong, G.Y. Oh, W. Lee, J.M. Myoung, J. Cryst. Growth 268 (2004) 149.

[*Jeong-2007*] S.H. Jeong, K.H. Park, H.J. Song, J. Korean Phys. Soc. 50 (2007) 1692.

[*Jeong-2008*] S.H. Jeong, C.B. Lee, W.J. Moon, H.J. Song, J. Nanosci. Nanotechnol. 8 (2008) 5098.

[*Jeong-2009*] S.H. Jeong, E.S. Aydil, J. Cryst. Growth 311 (2009) 4188.

[*Jing-2008*] Z. Jing and J. Zhan, Adv. Mater. 20 (2008) 4547.

[*Jiu-2002*] J. Jiu, Y. Ge, X. Li, L. Nie, Mater. Lett. 54 (2002) 260.

[*Jones-1995*] A.C. Jones, S.A. Rushworth, J. Auld, J. Cryst. Growth 146 (1995) 503.

[*Kakati-2010*] N. Kakati, S.H. Jee, S.H. Kim, J.Y. Oh, Y.S. Yoon, Thin Solid Films 519 (2010) 494.

[*Kamata-1994*] K. Kamata, J. Nishino, S. Ohshio, K. Maruyama, M. Ohtuku, J. Am. Ceram. Soc. 77 (1994) 505.

[*Kang-2005*] B.S. Kang, Y.W. Heo, C. Tien, D.P. Norton, F. Ren, B.P. Gila, S.J. Pearton, Appl. Phys. A 80 (2005) 1029.

[*Kang-2006*] B.S. Kang, H.-T. Wang, L.-C. Tien, F. Ren, B.P. Gila, D.P. Norton, C.R. Abernathy, J. Lin, S.J. Pearton, Sensors 6 (2006) 643.

[*Kang-2009*] D.-S. Kang, S.K. Han, J.-H. Kim, S.M. Yang, J.G. Kim, S.-K. Hong, D. Kim, H. Kim, J. Vac. Sci. Technol., B 27 (2009) 1667.

[*Kanjwal-2011*] M.A. Kanjwal, F.A. Sheikh, N.A.M. Barakat, I.S. Chronakis, H.Y. Kim, Appl. Surf. Sci. 257 (2011) 7975.

[*Kansal-2007*] S.K. Kansal, M. Singh, D. Sud, J. Hazard. Mater. 141 (2007) 581.

[*Kärkkänen-2009*] I. Kärkkänen, A. Floren, H. Mandär, T. Avarmaa, R. Jaaniso, Procedia Chemistry 1 (2009) 654.

[*Katti-2003*] V.R. Katti, A.K. Debnath, K.P. Muthe, M. Kaur, A.K. Dua, S.C. Gadkari, S.K. Gupta, V.C. Sahni, Sens. Actuators, B 96 (2003) 245.

[*Kaufmann-1989*] T. Kaufmann, G. Fuchs, M. Webert, S. Frieske, M. Gäckle, Cryst. Res. Technol. 24 (1989) 269.

[*Kenanakis-2007*] G. Kenanakis, D. Vernardou, E. Koudoumas, G. Kiridiakis, N. Katsarakis, Sens. Actuators, B 124 (2007) 187.

[*Kennedy-1995*] J. Kennedy, IEEE Trans. Magn. 31 (1995) 3829.

[*Kibis-2010*] L.S. Kibis, A.I. Stadnichenko, E.M. Pajetnov, S.V. Koscheev, V.I. Zaykovskii, A.I. Boronin, Appl. Surf. Sci. 257 (2010) 404.

[*Kim-2004*] H.G. Kim, D.W. Hwang, J.S. Lee, J. Am. Chem. Soc. 126 (2004) 8912.

[*Kim-2005-A*] H.G. Kim, P.H. Borse, W.Y. Choi, J.S. Lee, Angew. Chem., Int. Ed. 44 (2005) 4585.

[*Kim-2005-B*] S.-W. Kim, S. Fujita, S. Fujita, Appl. Phys. Lett. 86 (2005) 153119.

[*Kim-2009*] D.C. Kim, B.H. Kong, H.K. Cho, J. Phys. D: Appl. Phys. 42 (2009) 065406.

[*Kim-2009-A*] D.C. Kim, J.H. Lee, H.K. Cho, J.H. Kim, J.Y. Lee, Cryst. Growth Des.10 (2009) 321.

[*Kim-2010*] H.R. Kim, K.I. Choi, K.M. Kim, I.D. Kim, G.Z. Cao, J.H. Lee, Chem. Commun. 46 (2010) 5061.

[*Kitamura-2008*] K. Kitamura, T. Yatsui, M. Ohtsu, G.-C. Yi, Nanotechnol. 19 (2008) 175305.

[*Klabunde-2009*] K.J. Klabunde, R.M. Richards, Nanoscale Materials in Chemistry, Second Edition, John Wiley & Sons, Inc., New Jersey, USA, 2009.

[*Klepper-2007*] K.B. Klepper, O. Nilsen, H. Fjellvåg, J. Cryst. Growth 307 (2007) 457.

[*Klepper-2007-A*] K.B. Klepper, O. Nilsen, H. Fjellvåg, Thin Solid Films 515 (2007) 7772.

[*Kondarides-2010*] D.I. Kondarides, A. Patsoura, X.E. Verykios, J. Adv. Ox. Technol. 13 (2010) 116.

[*Kortidis-2009*] I. Kortidis, K. Moschovis, F. A. Mahmoud, G. Kiridiakis, Thin Solid Films 518 (2009) 1208.

[*Koyano-1996*] G. Koyano, H. Watanabe, T. Okuhara, M. Misono, J. Chem. Soc., Faraday Trans. 92 (1996) 3425.

[*Krishnakumar-2009*] T. Krishnakumar, R. Jayaprakash, N. Pinna, N. Donato, A. Bonavita, G. Micali, G. Neri, Sens. Actuators, B 143 (2009) 198.

[*Kronawitter-2011*] C.X. Kronawitter, J.R. Bakke, D.A. Wheeler, W.-C. Wang, C. Chang, B.R. Antoun, J.Z. Zhang, J. Guo, S.F. Bent, S.S. Mao, L. Vayssieres, Nano Lett. 11 (2011) 3855.

[*Kuang-2005*] Q. Kuang, Z.-Y. Jiang, Z.-X. Xie, S.-C. Lin, Z.-W. Lin, S.-Y. Xie, R.-B. Huang, L.-S. Zheng, J. Am. Chem. Soc. 127 (2005) 11777.

[*Kudo-2009*] A. Kudo, Y. Miseki, Chem. Soc. Rev. 38 (2009) 253.

[*Kumar-2004*] D.S. Kumar, D.S. Sankar, C.B. Manoranjan, B. Upasana, C.M. Kanti, M. Kantam, Patent WO2004056737(A1) and Patent US2004127690(A1)

[*Kumar-2011*] U. Kumar, J. Thomas, R. Nagarajan, N. Thirupathi, Inorg. Chim. Acta 372 (2011) 191.

[*Kuo-2007*] T.J. Kuo, C.N. Lin, C.L. Kuo, M.H. Huang, Chem. Mater. 19 (2007) 5143.

[*Kwak-2008*] G. Kwak, K. Yong, J. Phys. Chem. C 112 (2008), 3036.

[*Lai-2008*] T.-L. Lai, Y.-L. Lai, C.-C. Lee, Y.-Y. Shu, C.-B. Wang, Catal. Today 131 (2008) 105.

[*Lalitha-2010*] K. Lalitha, J.K. Reddy, M.V.P. Sharma, V.D. Kumari, M. Subrahmanyam, Int. J. Hydrogen Energy 35 (2010) 3991.

[*Langell-1999*] M.A. Langell, M.D. Anderson, G.A. Carson, L. Peng, S. Smith, Phys. Rev. B 59 (1999) 4791.

[*Lee-2005*] D.J. Lee, J.Y. Park, Y.S. Yun, Y.S. Hong, J.H. Moon, B.-T. Lee, S.S. Kim, J. Cryst. Growth 276 (2005) 458.

[*Lee-2006-A*] H.-B.-R. Lee, H. Kim, Electrochem. Solid-State Lett. 9 (2006) 323.

[*Lee-2006-B*] J. Lee, H.J. Yang, J.H. Lee, J.Y. Kim, W.J. Nam, H.J. Shin, Y.K. Ko, J.G. Lee, E.G. Lee, C.S. Kim, J. Electrochem. Soc. 153 (2006) G539.

[*Lee-2009-A*] J.-C. Lee, T. G. Kim, W. Lee, S.-H. Han, Y.-M. Sung, Cryst. Growth Des. 9 (2009) 4519.

[*Lee-2009-B*] J.-H. Lee, Sens. Actuators, B 140 (2009) 319.

[*Lee-2010*] H. Lee, C.H. Lee, I.S.Oh, I.M. Lee, Bull. Korean Chem. Soc. 31 (2010) 891.

[*Li-1999*] W.-J. Li, E.-W. Shi, W.-Z. Zhong, Z.-W. Yin, J. Cryst. Growth 203 (1999) 186.

[*Li-2003*] B.S. Li, Y.C. Liu, D.Z. Shen, J.Y. Zhang, Y.M. Lu, X.W. Fan, J. Cryst. Growth 249 (2003) 179.

[*Li-2005*] W.Y. Li, L.N. Xu, J. Chen, Adv. Funct. Mater. 15 (2005) 851.

[*Li-2007-A*] C. Li, G. Fang, N. Liu, J. Li, L. Liao, F. Su, G. Li, X. Wu, X. Zhao, J. Phys. Chem. C 111 (2007) 12566.

[*Li-2007-B*] C.C. Li, Z.F. Du, L.M. Li, H.C. Yu, Q. Wan, T.H. Wang, Appl. Phys. Lett. 91 (2007) 032101.

[*Li-2008-A*] G. Li, T. Chen, B. Yan, Y. Ma, Z. Zhang, T. Yu, Z. Shen, H. Chen, T. Wu, Appl. Phys. Lett. 92 (2008) 173104.

[*Li-2008-B*] C. Li, L. Li, Z. Du, H. Yu, Y. Xiang, Y. Li, Y. Cai, T. Wang, Nanotechnol. 19 (2008) 035501.

[*Li-2008-C*] W.-H. Li, Mater. Lett. 62 (2008) 4149.

[*Li-2008-D*] Z. Li, D.K. Lee, M. Coulter, L.N.J. Rodriguez, R.G. Gordon, Dalton Trans. (2008) 2592.

[*Li-2009-A*] L. Li, T. Sasaki, Y. Shimizu, N. Koshizaki, J. Phys. Chem. C 113 (2009) 15948.

[*Li-2009-B*] C. Li, Z. Du, H. Yu and T. Wang, Thin Solid Films, 517 (2009) 5931.

[*Li-2009-C*] C.C. Li, X.M. Yin, T.H. Wang, H.C. Zeng, Chem. Mater. 21 (2009) 4984.

[*Li-2010*] W. Li, H. Jung, D.H. Hoa, D. Kim, S.K. Hong, H. Kim, Sens. Actuators, B 150 (2010) 160.

[*Liang-2011*] C. Liang, W. Xia, M. van den Berg, Y. Wang, H. Soltani-Ahmadi, O. Schlüter, R.A. Fischer, M. Muhler, Chem. Mater. 21 (2009) 2360.

[*Liangyuan-2010*] C. Liangyuan, L. Zhiyong, B. Shouli, Z. Kewei, L. Dianqing, C. Aifan, C.C. Liu, Sens. Actuators, B 143 (2010) 620.

[*Lim-2003-A*] B.S. Lim, A. Rahtu, R.G. Gordon, Nature Mater. 2 (2003) 749.

[*Lim-2003-B*] B.S. Lim, A.Rahtu, J.-S. Park, R.G. Gordon, Inorg. Chem. 2003, 42, 7951.

[*Lin-2009*] D. Lin, H. Wu, R. Zhang, W. Pan, Chem. Mater. 21 (2009) 3479.

[*Liu-2004-A*] X. Liu, X. Wu, H. Cao, R.P.H. Chang, J. Appl. Phys. 95 (2004) 3141.

[*Liu-2004-B*] H. Liu, L. Feng, J. Zhai, L. Jiang, D. Zhu, Langmuir 20 (2004) 5659.

[*Liu-2009-A*] Y. Liu, Z.H. Kang, Z.H. Chen, I. Shafiq, J.A. Zapien, I. Bello, W.J. Zhang, S.T. Lee, Cryst. Growth Des. 9 (2009) 3222.

[*Liu-2009-B*] Z. Liu, X.D. Wen, X.L. Wu, Y.J. Gao, H.T. Chen, J. Zhu, P.K. Chu, J. Am. Chem. Soc. 131 (2009) 9405.

[*Liu-2009-C*] G. Liu, H.G. Yang, X. Wang, L. Cheng, J. (Max) Pan, G.Q. Lu, H.-M. Cheng, J. Am. Chem. Soc. 131 (2009) 12868.

[*Liu-2010-A*] B. Liu, M. Gu, X. Liu, S. Huang, C. Ni, Appl. Phys. Lett. 97 (2010) 122101.

[*Liu-2010-B*] X. Liu, D. Zhang, Y. Zhang, X. Dai, J. Appl. Phys. 107 (2010) 064309.

[*Liu-2011*] J. Liu, Y. Sun, Z. Li, S. Li, J. Zhao, Int. J. Hydrogen Energy 36 (2011) 5811.

[*Llorca-2008*] J. Llorca, A. Casanovas, T. Trifonov, A. Rodríguez, R. Alcubilla, J. Catal. 255 (2008) 228.

[*Lu-2008*] W. Lu, G. Liu, S. Gao, S. Xing, J. Wang, Nanotechnol. 19 (2008) 445711.

[*Lu-2009*] X.H. Lu, Q.H. Xia, S.Y. Fang, B. Xie, B. Qi, Z.R. Tang, Catal. Lett. 131 (2009) 517.

[*Lupan-2009*] O. Lupan, L. Chow, G. Chai, Sens. Actuators, B 141 (2009) 511.

[*Lupan-2010*] O. Lupan, V.V. Ursaki, G. Chai, L. Chow, G.A. Emelchenko, I.M. Tiginyanu, A.N. Gruzintsev, A.N. Redkin, Sens. Actuators, B 144 (2010) 56.

[*Ma-2010*] C.Y. Ma, Z. Mu, J.J. Li, Y.G. Jin, J. Cheng, G.Q. Lu, Z.P. Hao, S.Z. Qiao, J. Am. Chem. Soc. 132 (2010) 2608.

[*Mahan-2000*] J.E. Mahan, Physical Vapor Deposition of Thin Films, J. Wiley & Sons, Chichester, UK, 2000.

[*Maile-2005*] E. Maile, R.A. Fischer, Chem. Vap. Deposition 11 (2005) 409.

[*Mane-2002*] A.U. Mane, K. Shalini, A. Wohlfart, A. Devi, S.A. Shivashankar, J. Cryst. Growth 240 (2002) 157.

[*Malandrino-2005*] G. Malandrino, M. Blandino, L.M.S. Perdicaro, I.L. Fragala, P. Rossi, P. Dapporto, Inorg. Chem. 44 (2005) 9684.

[*Malandrino-2008*] G. Malandrino, M. Blandino, M.E. Fragalà, M. Losurdo, G. Bruno, J. Phys. Chem. C 112 (2008) 9595.

[*Martín-González-2008*] M.S. Martín-González, J.F. Fernández, F. Rubio-Marcos, I. Lorite, J.L. Costa-Kramer, A. Quesada, M.A. Bañares, J.L.G. Fierro, J. Appl. Phys. 103 (2008) 083905.

[*Martins-2004*] R. Martins, E. Fortunato, P. Nunes, I. Ferreira, A. Marques, M. Bender, N. Katsarakis, V. Cimalla, G. Kiridiakis, J. Appl. Phys. 96 (2004) 1398.

[*Maruyama-1991*] T. Maruyama, T. Nakai, Sol. Energy Mater. 23 (1991) 25.

[*Maruyama-1996*] T. Maruyama, S. Arai, J. Electrochem. Soc. 143 (1996) 1383.

[*Matthews-2006*] J.S. Matthews, O.O. Onakoya, T.S. Ouattara, R.J. Butcher, Dalton Trans. (2006) 3608.

[*Mattsson-2010*] A. Mattsson, L. Osterlund, J. Phys. Chem. C 114 (2010) 14121.

[*McElwee-White-2006*] L. McElwee-White, Dalton Trans. (2006) 5327.

[*Meng-2005*] X.Q. Meng, D.X. Zhao, J.Y. Zhang, D.Z. Shen, Y.M. Lu, L. Dong, Z.Y. Xiao, Y.C. Liu, X.W. Fan, Chem. Phys. Lett. 413 (2005) 450.

[*Meyer-2008*] W. Meyer, K. Beidermann, M. Gubo, L. Hammer, K. Heinz, J. Phys. Condens. Matter 20 (2008) 265011.

[*Meyyappan-2009*] M. Meyyappan, Prog. Cryst. Growth Charact. Mater. 55 (2009) 1.

[*Michaelides-2005*] A. Michaelides, K. Reuter, M. Scheffler, J. Vac. Sci. Technol., A 23 (2005) 1487.

[*Mikrajuddin-2001*] Mikrajuddin, F. Iskandar, K. Okuyama, F.G. Shi, J. Appl. Phys. 89 (2001) 6431.

[*Millard-2002*] L. Millard, M. Bowker, J. Photochem. Photobiol., A 148 (2002) 91.

[*Mills-2002*] A. Mills, S.-K. Lee, J. Photochem. Photobiol. A 152 (2002) 233.

[*Mills-2003*] A. Mills, A. Lepre, N. Elliott, S. Bhopal, I.P. Parkin, S.A. O'Neill, J. Photochem. Photobiol., A 160 (2003) 213.

[*Minami-1994*] T. Minami, H. Sato, H. Sonohara, S. Takata, T. Miyata, I. Fukuda, Thin Solid Films 253 (1994) 14.

[*Minero-2000*] C. Minero, G. Mariella, V. Maurino, D. Vione, E. Pelizzetti, Langmuir 16 (2000) 8964.

[*Minggu-2010*] L.J. Minggu, W.R.W. Daud, M.B. Kassim, Int. J. Hydrogen Energy 35 (2010) 5233.

[*Mitra-2007*] P. Mitra, A.K. Mukhopadhyay, Bull. Pol. Acad. Sci. 55 (2007) 281.

[*Mittemeijer-2004*] E.J. Mittemeijer, P. Scardi, Diffraction Analysis of the Microstructure of Materials, Springer-Verlag, Berlin Heidelberg, Germany, 2004.

[*Miwa-2010*] T. Miwa, S. Kaneco, H. Katsumata, T. Suzuki, K. Ohta, S. Chand Verma, K. Sugihara, Int. J. Hydrogen Energy 35 (2010) 6554.

[*Mizsei-1995*] J. Mizsei, Sens. Actuators, B 23 (1995) 173.

[*Mo-2004*] L. Mo, X. Zheng, C.-T. Yeh, Chem. Comm. (2004) 1426.

[*Montini-2011*] T. Montini, V. Gombac, L. Sordelli, J.J. Delgado, X. Chen, G. Adami, P. Fornasiero, ChemCatChem 3 (2011) 574.

[*Montoya-2010*] J.F. Montoya, P. Salvador, Appl. Catal., B 94 (2010) 97.

[*Morkoc-2009*] H. Morkoc, Ü. Özgür, Zinc Oxide: Fundamentals, Materials and Device Technology, WILEY-VCH, Weinheim, Germany 2009.

[*Moulder-1992*] J.F. Moulder, W.F. Stickle, P.W. Sobol, K.D. Bomben, Handbook of X-ray Photoelectron Spectroscopy, Perkin-Elmer, Eden Prairie, MN, 1992.

[*Mukherjee-2009*] N. Mukherjee, S.F. Ahmed, K.K. Chattopadhyay, A. Mondal, Electrochim. Acta 54 (2009) 4015.

[*Muradov-2008*] N.Z. Muradov, T.N. Veziroğlu, Int. J. Hydrogen Energy 33 (2008) 6804.

[*Murphy-2007*] A.B. Murphy, Sol. Energy Mater. Sol. Cells, 91 (2007) 1326.

[*Na-2011*] C.W. Na, H.-S. Woo, I.-D. Kim, J.-H. Lee, Chem. Commun. 47 (2011) 5148.

[*Nam-2010*] K.H. Nam, P.J. Lee, J.J. Lee, Thin Solid Films 518 (2010) 7029.

[*Navarro-2009*] R.M. Navarro, M.C. Sánchez Sánchez, M.C. Alvarez-Galvan, F. del Valle, J.L.G. Fierro, Energy Environ. Sci. 2 (2009) 35.

[*Ni-2005*] J. Ni, H. Yan, A. Wang, Y. Yang, C.L. Stern, A.W. Metz, S. Jin, L. Wang, T. J. Marks, J. R. Ireland, C. R. Kannewurf, J. Am. Chem. Soc. 127 (2005) 5613.

[*Ni-2007-A*] M. Ni, D.Y.C. Leung, M.K.H. Leung, Int. J. Hydrogen Energy 32 (2007) 3238.

[*Ni-2007-B*] C. Ni, Z. Zhang, M. Wells, T.P. Beebe Jr., L. Pirroli, L.P. Méndez De Leo, A.V. Teplyakov, Thin Solid Films 515 (2007) 3030.

[*Nist*] http://srdata.nist.gov/xps/.

[*Ogawa-1982*] H. Ogawa, M. Nishikawa, A. Abe, J. Appl. Phys. 53 (1982) 4448.

[*Oh-2004*] Y.-C. Oh W.S.J., Jenks, Photochem. Photobiol., A 162 (2004) 323.

[*Oh-2009*] E. Oh, H.-Y. Choi, S.-H. Jung, S. Cho, J.C. Kim, K.-H. Lee, S.-W. Kang, J. Kim, J.-Y. Yun, S.-H. Jeong, Sens. Actuators, B 141 (2009) 239.

[*Ostrikov-2006*] K. Ostrikov, J. D. Long, P.P. Rutkevych, S. Xu, Vacuum 80 (2006) 1126.

[*Ostrikov-2010*] K. Ostrikov, I. Levchenko, U. Cvelbar, M. Sunkara, M. Mozetic, Nanoscale 2 (2010) 2012.

[*Özgür-2005*] Ü. Özgür, Y.I. Alivov, C. Liu, A. Teke, M.A. Reshchikov, S. Doğan, V. Avrutin, S.-J. Cho, H. Morkoç, J. Appl. Phys. 98 (2005) 041301.

[*Özgür-2010*] Ü. Özgür, D. Hofstetter, H. Morkoç, Proc. IEEE 98 (2010) 1255.

[*Öztürk-2011*] S. Öztürk, N. Kılınç, N. Taşaltin, Z.Z. Öztürk, Thin Solid Films 520 (2011) 932.

[*Papadopoulou-2009*] E.L. Papadopoulou, M. Barberoglou, V. Zorba, A. Manousaki, A. Pagkozidis, E. Stratakis, C. Fotakis, J. Phys. Chem. C 113 (2009) 2891.

[*Park-2002*] W.I. Park, D.H. Kim, S.-W. Jung, G.-C. Yi, Appl. Phys. Lett. 80 (2002) 4232.

[*Park-2005*] J.Y. Park, D.J. Lee, Y.S. Yun, Y.S. Hong, B.T. Lee, J.H. Moon, S.S. Kim, Met. Mater. Int. 11 (2005) 165.

[*Park-2006*] J.-H. Park, S.-J. Jang, S.-S. Kim, B.-T. Lee, Appl. Phys. Lett. 89 (2006) 121108.

[*Park-2008*] W.I. Park, Met. Mater. Int. 14 (2008) 659.

[*Park-2009*] J. Park, X. Shen, G. Wang, Sens. Actuators B: Chem. 136 (2009) 494.

[*Pasko-2004*] S. Pasko, A. Abrutis, L.G. Hubert-Pfalzgraf, V. Kubilius, J. Cryst. Growth, 262 (2004) 653.

[*Pasko-2004-A*] S. Pasko, L.G. Hubert-Pfalzgraf, A. Abrutis, J. Vaissermann, Polyhedron 23 (2004) 735.

[*Patil-1998*] P.S. Patil, L.D. Kadam, C.D. Lokhande, Sol. Energy Mater. Sol. Cells 53 (1998) 229.

[*Patil-2010*] D. Patil, P. Patil, V. Subramanian, P.A. Joy, H.S. Potdar, Talanta 81 (2010) 37.

[*Pawar-2008*] B.N. Pawar, D.H. Ham, R.S. Mane, T. Ganesh, B.W. Cho, S.H. Han, Appl. Surf. Sci. 254 (2008) 6294.

[*Pedersen-2011*] J.D. Pedersen, H.J. Esposito, K.S. The, Nanoscale Res. Lett. 6 (2011) 568.

[*Penza-2009*] M. Penza, G. Sberveglieri, W. Wlodarski, Y. Li, Nanomaterials for Chemical Sensing Technologies, Hindawi Publishing Corporation, Journal of Sensors, Volume 2009.

[*Pérez-Hernández-2010*] R. Pérez-Hernández, A. Gutiérrez-Martínez, A. Mayoral, F.L. Deepak, M.E. Fernández-García, G. Mondragón-Galicia, M. Miki, M. José-Yacamán, Adv. Mater. Res. 132 (2010) 205.

[*Periasamy-2009*] C. Periasamy, P. Chakrabarti, J. Vac. Sci. Technol, B 27 (2009) 2124.

[*Petitto-2008*] S.C. Petitto, E.M. Marsh, G.A. Carson, M.A. Langell, J. Mol. Catal. A: Chem. 281 (2008) 49.

[*Pierson-1999*] H.O. Pierson, Handbook of Chemical Vapor Deposition (CVD), Principles, Technology, and Applications, 2nd edition, Noyes Publications/William Andrew Publishing, New York, USA, 1999.

[*Prades-2008*] J.D. Prades, R. Jimenez-Diaz, F. Hernandez-Ramirez, L. Fernandez-Romero, T. Andreu, A. Cirera, A. Romano-Rodriguez, A. Cornet, J.R. Morante, S. Barth, S. Mathur, J. Phys. Chem. C 112 (2008) 14639.

[*Prades-2009*] J.D. Prades, R. Jimenez-Diaz, M. Manzanares, F. Hernandez-Ramirez, A. Cirera, A. Romano-Rodriguez, S. Mathur, J.R. Morante, Phys. Chem. Chem. Phys. 11 (2009) 10881.

[*Premkumar-2007*] P.A. Premkumar, A. Turchanin, N. Bahlawane, Chem. Mater. 19 (2007) 6206.

[*Primo-2011*] A. Primo, A. Corma, H. Garcia, Phys. Chem. Chem. Phys. 13 (2011) 886.

[*Prokes-2007*] S.M. Prokes, O.J. Glembocki, R.W. Rendell, M.G. Ancona, Appl. Phys. Lett. 90 (2007) 093105.

[*Qi-2008*] Q. Qi, T. Zhang, L. Liu, X. Zheng, Q. Yu, Y. Zeng and H. Yang, Sens. Actuators, B 134 (2008) 166.

[*Qi-2010*] H. Qi, D. Alexson, O. Glembocki, S.M. Prokes, Nanotechnol. 21 (2010) 215706.

[*Qurashi-2009*] A. Qurashi, N. Tabet, M. Faiz, T. Yamzaki, Nanoscale Res. Lett. 4 (2009) 948.

[*Ra-2008*] H.W. Ra, K.-S. Choi, J.-H. Kim, Y.-B. Hahn, Y.-H. Im, Small 4 (2008) 1105.

[*Ra-2010*] H.-W. Ra, R. Khan, J.T. Kim, B.R. Kang, Y.H. Im, Nanotechnol. 21 (2010) 085502.

[*Ramesh-2007*] M.N.V. Ramesh, Y. Sundarayya, C.S. Sunandana, Mod. Phys. Lett. B 21 (2007) 1933.

[*Rao-2004*] C.N.R. Rao, A. Müller, A.K. Cheetham, The Chemistry of Nanomaterials – Synthesis, Properties and Application, WILEY-VCH, Weinheim, Germany, 2004.

[*Rees-1992*] W.S. Rees, D.M. Green, W. Hesse, Polyhedron 11 (1992) 1697.

[*Reisner-2011*] E. Reisner, Eur. J. Inorg. Chem. (2011) 1005.

[*Rita-2003*] E. Rita, U. Wahl, A.M.L. Lopes, J.P. Araújo, J.G. Correia, E. Alves, J.C. Soares, Physica B 340-342 (2003) 240.

[*Romero-Gómez-2010*] P. Romero-Gómez, J. Toudert, J.R. Sánchez-Valencia, A. Borrás, A. Barranco, A.R. Gonzalez-Elipe, J. Phys. Chem. C 114 (2010) 20932.

[*Rooth-2006*] M. Rooth, E. Lindahl, A. Hårsta, Chem. Vap. Deposition 12 (2006) 209.

[*Rout-2006*] C.S. Rout, S. Hari Krishna, S.R.C. Vivekchand, A. Govindaraj, C.N.R. Rao, Chem. Phys. Lett. 418 (2006) 586.

[*Rowlette-2009*] P.C. Rowlette, C.G. Allen, O.B. Bromley, A.E. Dubetz, C.A. Wolden, Chem. Vap. Deposition 15 (2009) 15.

[*Roy-2004*] R.K. Roy, S. Bandyopadhyaya, A.K. Pal, Eur. Phys. J. B 39 (2004) 491.

[*Rubio-Marcos-2010*] F. Rubio-Marcos, V. Calvino-Casilda, M.A. Bañares, J.F. Fernandez, J. Catal. 275 (2010) 288.

[*Ryu-2003*] H.-W. Ryu, B.-S. Park, S.A. Akbar, W.-S. Lee, K.-J. Hong, Y.-J. Seo, D.-C. Shin, J.-S. Park, G.-P. Choi, Sens. Actuators, B 96 (2003) 717.

[*Sacuto-1995*] A. Sacuto, C. Julien, V.A. Shchukin, C. Perrin, M. Mokhtari, Phys. Rev. B: Condens. Matter 52 (1995) 7619.

[*Sadek-2007*] A.Z. Sadek, S. Choopun, W. Wlodarski, S.J. Ippolito, K. Kalantar-Zadeh, IEEE Sens. J. 7 (2007) 919.

[*Sakaguchi-2010*] I. Sakaguchi, K. Watanabe, T. Ohgaki, T. Nakagawa, S. Hishita, Y. Adachi, N. Ohashi, H. Haneda, J. Ceram. Soc. Jpn. 118 (2010) 217.

[*Scalisi-2008*] A.A. Scalisi, R.G. Toro, G. Malandrino, M.E. Fragalà, G. Pezzotti, Chem. Vap. Deposition 14 (2008) 115.

[*Sen-2005*] S. Sen, S. Mahanty, S. Roy, O. Heintz, S. Bourgeois, D. Chaumont, Thin Solid Films 474 (2005) 245.

[*Seshan-2002*] K. Seshan, Handbook of Thin-Film Deposition Processes and Techniques, Principles, Methods, Equipment and Applications, 2nd edition, Noyes Publications, New York, USA, 2002.

[*Seyed-Razavi-2010*] A. Seyed-Razavi, I.K. Snook, A.S. Barnard, J. Mater. Chem. 20 (2010) 416.

[*Shalini-2001*] K. Shalini, A.U. Mane, S.A. Shivashankar, M. Rajeswari, S. Choopun, J. Cryst. Growth 231 (2001) 242.

[*Sheldrick-1997*] G. M. Sheldrick, SHELXL-97, Program for refinement of crystal structures, University of Göttingen, Germany, 1997.

[*Shet-2011*] S. Shet, K.-S. Ahn, R. Nuggehalli, Y. Yan, J. Turner, M. Al-Jassim, Thin Solid Films 519 (2011) 5983.

[*Shifu-2009*] C. Shifu, Z. Wei, L. Wei, Z. Huaye, Y. Xiaoling, Chem. Eng. J. 155 (2009) 466.

[*Shim-2008*] H.-S. Shim, V.R. Shinde, H.J. Kim, Y.-E. Sung, W.B. Kim, Thin Solid Films 516 (2008) 8573.

[*Si-2006*] S. Si, C. Li, X. Wang, Q. Peng, Y. Li, Sens. Actuators, B 119 (2006) 52.

[*Simon-2011*] Q. Simon, D. Barreca, D. Bekermann, A. Gasparotto, C. Maccato, E. Comini, V. Gombac, P. Fornasiero, O.I. Lebedev, S. Turner, A. Devi, R.A. Fischer, G. Van Tendeloo, Int. J. Hydrog. Energ. 36 (2011) 15527.

[*Singh-2010*] S.J. Singh, J. Prakash, S. Patnaik, A.K. Ganguli, Physica C 470 (2010) 1928.

[*Smith-1995*] D.L. Smith, Thin-Film Deposition: Principles and Practice, Mc Graw-Hill, USA, 1995.

[*Smith-1995*] F.T.J. Smith, Appl. Phys. Lett. 43 (1983) 1108.

[*Solé-2005*] J. García Solé, L.E. Bausá, D. Jaque, An Introduction to the Optical Spectroscopy of Inorganic Solids, John Wiley & Sons, Chichester, UK, 2005.

[*Stamataki-2009*] M. Stamataki, I. Fasaki, G. Tsonos, D. Tsamakis, M. Kompitsas, Thin Solid Films 518 (2009) 1326.

[*Stampfl-1998*] C. Stampfl, C.G. Van de Walle, Phys. Rev. B 57 (1998) R15052.

[*Steinsland-2000*] E. Steinsland, T. Finstad, A. Hanneborg, Sens. Actuators, A 86 (2000) 73.

[*Sudakar-2008*] C. Sudakar, P. Kharel, G. Lawes, R. Suryanarayanan, R. Naik, Appl. Phys. Lett. 92 (2008) 062501.

[*Su-2011*] P.-G. Su, T.-T. Pan, Mater. Chem. Phys. 125 (2011) 351.

[*Suh-1999*] S. Suh, D.M. Hoffman, L.M. Atagi, D.C. Smith, J. Mater. Sci. Lett. 18 (1999) 789.

[*Suh-2001*] S. Suh, L.A. Mînea, D.M. Hoffman, Z. Zhang, W.-K. Chu, J. Mater. Sci. Lett. 20 (2001) 115.

[*Suh-2001-A*] S. Suh, D.M. Hoffman, L.M. Atagi, D.C. Smith, Chem. Vap. Deposition 7 (2001) 81.

[*Sun-2001*] R. De Sun, A. Nakajima, T. Watanabe, K. Hashimoto, J. Phys. Chem. B 105 (2001) 1984.

[*Sun-2005*] Y. Sun, G.M. Fuge, N.A. Fox, D.J. Riley, M.N.R. Ashfold, Adv. Mater. 17 (2005) 2477.

[*Sun-2010*] H. Sun, S. Wang, H. Ming Ang, O.M. Tadé, Q. Li, Chem. Eng. J. 162 (2010) 437.

[*Syu-2001*] M.J. Syu, Appl. Microbiol. Biotechnol. 55 (2001) 10.

[*Tak-2008*] Y. Tak, K. Yong, J. Phys. Chem. C 112 (2008) 74.

[*Tan-2008*] T. Tan, Y. Li, Y. Liu, B. Wang, X. Song, E. Li, H. Wang, H. Yan, Mater. Chem. Phys. 111 (2008) 305.

[*Teke-2004*] A. Teke, Ü. Özgür, S. Doğan, X. Gu, H. Morkoç, B. Nemeth, J. Nause, H.O. Everitt, Phys. Rev. B 70 (2004) 195207.

[*Tien-2005*] L.C. Tien, P.W. Sadik, D.P. Norton, L.F. Voss, S.J. Pearton, H.T. Wang, B.S. Kang, F. Ren, J. Jun, J. Lin, Appl. Phys. Lett. 87 (2005) 222106.

[*Tompkins-1999*] G.H. Tompkins, A.W. McGahan, Spectroscopic Ellipsometry and Reflectometry, J. Wiley & Sons, New York, USA, 1999.

[*Tricoli-2009*] A. Tricoli, M. Righettoni, S.E. Pratsinis, Langmuir 25 (2009) 12578.

[*Tricoli-2010*] A. Tricoli, A. Teleki, M. Righettoni, Angew. Chem. Int. Ed. 49 (2010) 7632.

[*Trindade-2001*] T. Trindade, P. O'Brien, N.L. Pickett, Chem. Mater. 13 (2001) 3843.

[*Trinh-2011*] T.T. Trinh, N.H. Tu, H.H. Le, K.Y. Ryu, K.B. Le, K. Pillai, J. Yi, Sens. Actuators, B 152 (2011) 73.

[*Tsukazaki-2008*] A. Tsukazaki, A. Ohtomo, D. Chiba, Y. Ohno, H. Ohno, M. Kawasaki, Appl. Phys. Lett. 93 (2008) 241905.

[*Tyczkowski-2007*] J. Tyczkowski, R. Kapica, J. Łojewska, Thin Solid Films 515 (2007) 6590.

[*Umar-2006*] A. Umar, B. Karunagaran, E.K. Suh, Y.B. Hahn, Nanotechnol. 17 (2006) 4072.

[*Uriz-2011*] I. Uriz, G. Arzamendi, E. López, J. Llorca, L.M. Gandía, Chem. Eng. J. 167 (2011) 603.

[*Vanaja-2008*] K. Vanaja, U. Bhatta, R. Ajimsha, S. Jayalekshmi, M. Jayaraj, Bull. Mater. Sci. 31 (2008) 753.

[*Varshni-1967*] Y.P. Varshni, Physica 34 (1967) 149.

[*Vaz-2009-A*] C.A.F. Vaz, H.-Q. Wang, C.H. Ahn, V.E. Henrich, M.Z. Baykara, T.C. Schwendemann, N. Pilet, B.J. Albers, U.D. Schwarz, L.H. Zhang, Y. Zhu, J. Wang, E.I. Altman, Surf. Sci. 603 (2009) 291.

[*Vaz-2009-B*] C.A.F. Vaz, D. Prabhakaran, E.I. Altman, V.E. Henrich, Phys. Rev. B: Condens. Matter 80 (2009) 155457.

[*Wan-2005*] Q. Wan, T.H. Wang, J.C. Zhao, Appl. Phys. Lett. 87 (2005) 083105.

[*Wang-2004-A*] J. Wang, S. Yin, Q. Zhang, F. Saito, T. Sato, Solid State Ionics 172 (2004) 191.

[*Wang-2004-B*] Z.L. Wang, Mater. Today 7 (2004) 26.

[*Wang-2005-A*] X. Wang, J. Song, P. Li, J.H. Ryou, R.D. Dupuis, C.J. Summers, Z.L. Wang, J. Am. Chem. Soc. 127 (2005) 7920.

[*Wang-2005-B*] H.T. Wang, B.S. Kang, F. Ren, L.C. Tien, P.W. Sadik, D.P. Norton, S.J. Pearton, J. Lin, Appl. Phys. A 81 (2005) 1117.

[*Wang-2006*] J.X. Wang, X.W. Sun, Y. Yang, H. Huang, Y.C. Lee, O.K. Tan, L. Vayssiries, Nanotechnol. 17 (2006) 4995.

[*Wang-2008-A*] Z. L. Wang, ACS Nano 2 (2008) 1987.

[*Wang-2008-B*] N. Wang, Y. Cai, R.Q. Zhang, Mater. Sci. Eng. R60 (2008) 1.

[*Wang-2008-C*] K. Wang, J. Chen, W. Zhou, Y. Zhang, Y. Yan, J. Pern, A. Mascarenhas, Adv. Mater. 20 (2008) 3248.

[*Wang-2008-D*] Y.Z. Wang, Y.X. Zhao, C.G. Gao, D.S. Liu, Catal. Lett. 125 (2008) 134.

[*Wang-2008-E*] Y. Wang, X. Li, G. Lu, X. Quan, G. Chen, J. Phys. Chem. C 112 (2008) 7332.

[*Wang-2009-A*] D. Wang, J. Zhang, Y. Hu, G. Li, Z. Bi, X. Zhang, X. Bian, X. Hou, Mater. Lett. 63 (2009) 2157.

[*Wang-2009-B*] J. Wang, D.N. Tafen, J.P. Lewis, Z. Hong, A. Manivannan, M. Zhi, M. Li, N. Wu, J. Am. Chem. Soc. 131 (2009) 12290.

[*Wang-2010*] Z.Q. Wang, J.F. Gong, Y. Su, Y.W. Jiang, S.G. Yang, Cryst. Growth Des. 10 (2010) 2455.

[*Wang-2011-A*] Z.L. Wang, Nanogenerators for self-powered devices and systems, Georgia Institute of Technology, SMARTech digital repository, Atlanta, USA, 2011 (http://hdl.handle.net/1853/39262).

[*Wang-2011-B*] G. Wang, S. Chu, N. Zhan, Y. Lin, L. Chernyak, J. Liu, Appl. Phys. Lett. 98 (2011) 041107.

[*Wang-2011-C*] L. Wang, Y. Zheng, X. Li, W. Dong, W. Tan, B. Chen, C. Li, X. Li, T. Zhang, W. Xu, Thin Solid Films 519 (2011) 5673.

[*Warren-1990*] B.E. Warren, X-ray Diffraction, Dover Publications, New York, USA, 1990.

[*Waterhouse-2001*] G.I.N. Waterhouse, G.A. Bowmaker, J.B. Metson, Appl. Surf. Sci. 183 (2001) 191.

[*Wei-2009*] L. Wei, Z.H. Li, W.F. Zhang, Appl. Surf. Sci. 255 (2009) 4992.

[*Wei-2011*] A. Wei, L. Pan, W. Huang, Mater. Sci. Eng. B 176 (2011) 1409.

[*Williams-1975*] D. Williams, I. Fleming, Spektroskopische Methoden zur Strukturaufklaerung, Thieme Verlag, Stuttgart, Germany, 1975.

[*Wilson-1989*] R.G. Wilson, F.A. Stevie, C.W. Magee, Secondary Ion Mass Spectrometry: a practical handbook for depth profiling and bulk impurity analysis, John Wiley & Sons, New York, USA, 1989.

[*Wisitsoraaat-2009*] A. Wisitsoraaat, A. Tuantranont, E. Comini, G. Sberveglieri, W. Wlodarski, Thin Solid Films 517 (2009) 2775.

[*Wöllenstein-2003*] J. Wöllenstein, M. Burgmair, G. Plescher, T. Sulima, J. Hildenbrand, H. Böttner, I. Eisele, Sens. Actuators, B 93 (2003) 442.

[*Wright-1984*] P.J. Wright, R.J.M. Griffiths, B. Cockayne, J. Cryst. Growth 66 (1984) 26.

[*Wright-1989*] P.J. Wright, P.J. Parbrook, B. Cockayne, A.C. Jones, E.D. Orrell, K.P. O'Donnell, B. Henderson, J. Cryst. Growth 94 (1989) 441.

[*Wright-2010*] J.S. Wright, W. Lim, D.P. Norton, S.J. Pearton, F. Ren, J.L. Johnson, A. Ural, Semicond. Sci. Technol. 25 (2010) 024002.

[*Wu-2002*] J.-J. Wu, S.-C. Liu, J. Phys. Chem. B 106 (2002) 9546.

[*Wu-2008-A*] R.-J. Wu, H.-L. Lin, M.-H. Chen, T.-M. Wu, F. Shih-Sen Chien, Sens. Lett. 6 (2008) 800.

[*Wu-2008-B*] G. Wu, T. Chen, W. Su, G. Zhou, X. Zong, Z. Lei, C. Li, Int. J. Hydrogen Energy 33 (2008) 1243.

[*Wu-2009*] C.C. Wu, D.S. Wuu, P.R. Lin, T.N. Chen, R.H. Horng, Cryst. Growth Des. 9 (2009) 4555.

[*Xia-2003*] Y. Xia, P. Yang, Y. Sun, Y. Wu, B. Mayers, B. Gates, Y. Yin, F. Kim, H. Yan, Adv. Mater. 15 (2003) 353.

[*Xiang-2010*] Q. Xiang, G. Meng, Y. Zhang, J. Xu, P. Xu, Q. Pan, W. Yu, Sens. Actuators, B 143 (2010) 635.

[*Xie-2009*] X.W. Xie, Y. Li, Z.Q. Liu, M. Haruta, W.J. Shen, Nature 458 (2009) 746.

[*Xiu-2008*] Z.-L. Xiu, A.-P. Zeng, Appl. Microbiol. Biotechnol. 78 (2008) 917.

[*Xu-2006-A*] S. Xu, K. Ostrikov, J.D. Long, S. Y. Huang, Vacuum 80 (2006) 621.

[*Xu-2006-B*] H.Y. Xu, Y.C. Liu, R. Mu, C.L. Shao, Y.M. Lu, D.Z. Shen, X.W. Fan, Appl. Phys. Lett. 86 (2005) 123107.

[*Xu-2007*] L. Xu, Y. Su, S. Li, Y. Chen, Q. Zhou, S. Yin, Y. Feng, J. Phys. Chem. B 111 (2007) 760.

[*Xu-2008*] J. Xu, Y. Ao, D. Fu, C. Yuan, Appl. Surf. Sci. 254 (2008) 3033.

[*Xu-2009*] S. Xu, Y. Ding, Y. Wei, H. Fang, Y. Shen, A. K. Sood, L. D. Polla, Z. L. Wang, J. Am. Chem. Soc. 131 (2009) 6670.

[*Yamaoka-2008*] K. Yamaoka, Y. Terai, T. Yamaguchi, Y. Fujiwara, Phys. Status Solidi (c) 5 (2008) 3125.

[*Yang-1997*] J. Yang, J. Liang, D. Jin, S. Ying, W. Tang, G. Rao, J. Phys. Condens. Matter 9 (1997) 1249.

[*Yang-2002*] S.G. Yang, A.B. Pakhomov, S.T. Hung, C.Y. Wong, IEEE Trans. Magn. 38 (2002) 2877.

[*Yang-2009*] S. Yang, B.H. Lin, W.-R. Liu, J.-H. Lin, C.-S. Chang, C.-H. Hsu, W.F. Hsieh, Cryst. Growth Des. 9 (2009) 5185.

[*Yao-2011*] W. Yao, C. Huang, N. Muradov, A. T-Raissi, Int. J. Hydrogen Energy 36 (2011) 4710.

[*Yu-2002*] J.C. Yu, J. Yu, W. Ho, Z. Jiang, L. Zhang, Chem. Mater. 14 (2002) 3808.

[*Yu-2009*] Y.B. Yu, T. Takei, H. Ohashi, H. He, X.L. Zhang, M. Haruta, J. Catal. 267 (2009) 121.

[*Zeng-2008*] H. Zeng, W. Cai, P. Liu, X. Xu, H. Zhou, C. Klingshirn, H. Kalt, ACS Nano 2 (2008) 1661.

[*Zeng-2009-A*] Y. Zeng, T. Zhang, M. Yuan, M. Kang, G. Lu, R. Wang, H. Fan, Y. He, H. Yang, Sens. Actuators, B 143 (2009) 93.

[*Zeng-2009-B*] Y. Zeng, T. Zhang, L. Wang, R. Wang, W. Fu, H. Yang, J. Phys. Chem. C 113 (2009) 3442.

[*Zhang-2005*] S. Zhang, D. Sun, Y.Q. Fu, H. Du, Q. Zhang, J. Metastable Nanocryst. Mater. 23 (2005) 175.

[*Zhang-2006-A*] T. Zhang, W. Dong, M. Keeter-Brewer, S. Konar, R.N. Njabon, Z.R. Tian, J. Am. Chem. Soc. 128 (2006) 10960.

[*Zhang-2006-B*] Y. Zhang, Z. Wang, F. Lu, Y. Zhang, Y. Xiao, L. Zhang, Appl. Phys. Lett. 89 (2006) 113110.

[*Zhang-2007*] Y. Zhang, J. Mu, J. Colloid. Interface Sci. 309 (2007) 478.

[*Zhang-2009-A*] Q. Zhang, C.S. Dandeneau, X. Zhou, G. Cao, Adv. Mater. 21 (2009) 4087.

[*Zhang-2009-B*] Y. Zhang, J. Xu, Q. Xiang, H. Li, Q. Pan, P. Xu, J. Phys. Chem. C 113 (2009) 3430.

[*Zhang-2009-C*] S. Zhang, L. Li, A. Kumar, Materials Characterization Techniques, CRC Press, Taylor & Francis Group, Boca Raton, USA, 2009.

[*Zhang-2010*] Z.Y. Zhang, C.L. Shao, X.H. Li, C.H. Wang, M.Y. Zhang, Y.C. Liu, ACS Appl. Mater. Interfaces 2 (2010) 2915.

[*Zhao-2010*] Y. Zhao, X. Du, X. Wang, J. He, Y. Yu, H. He Sens. Actuators., B 151 (2010) 205.

[*Zheng-2009*] L. Zheng, Y. Zheng, C. Chen, Y. Zhan, X. Lin, Q. Zheng, K. Wei, J. Zhu, Inorg. Chem. 48 (2009) 1819.

[*Zheng-2010-A*] J. Zheng, R. Yang, L. Xie, J. Qu, Y. Liu, X. Li, Adv. Mater. 22 (2010) 1451.

[*Zheng-2010-B*] X.-J. Zheng, Y.-J. Wei, L.-F. Wei, B. Xie, M.-B. Wie, Int. J. Hydrogen Energy 35 (2010) 11709.

[*Zhou-2006*] J. Zhou, N. S. Xu, Z. L. Wang, Adv. Mater. 18 (2006) 2432.

[*Zhou-2008*] X. Zhou, X. Guo, W. Ding, Y. Chen, Appl. Surf. Sc i. 255 (2008) 3371.

[*Zielinska-2009*] A. Zielinska, E. Skwarek, A. Zaleska, M. Gazda, J. Hupka, Procedia Chem. 1 (2009) 1560.

[*Zita-2009*] J. Zita, J. Krýsa, A.Mills, J. Photochem. Photobiol., A 203 (2009) 119.

[*Zolfagahri-2007*] A. Zolfagahri, K. Nasiri Avanaki, H.Z. Jooya, H. Sayahi, Semicond. Sci. Technol. 22 (2007) 653.

[*Zong-2010*] Y. Zong, Y. Cao, D. Jia, S. Bao, Y. Lu, Mater. Lett. 64 (2010) 243.

[*Zou-2011*] J.P. Zou, R.P. Le, I. Musa, S.H. Yang, Y. Dan, C.T. That, T.P. Nguyen, Thin Solid Films 519 (2011) 3997.

[*Zuo-2010*] F. Zuo, L. Wang, T. Wu, Z. Zhang, D. Borchardt, P. Feng, J. Am. Chem. Soc. 132 (2010) 11856.

[*Zhuge-2010*] L.J. Zhuge, X.M. Wu, Z.F. Wu, X.M. Yang, X.M. Chen, Q. Chen, Mater. Chem. Phys. 120 (2010) 480.

Curriculum vitae

Personal Data

Name:	Daniela Bekermann
Address:	Via Lazzarini 13, 35127 Padova, Italy
Email:	daniela.bekermann@arcor.de
Date of birth:	8 January 1983
Place of birth:	Löningen, Germany
Marital status:	Single

Work experience

11/2010 - today	Early Stage Researcher at the department of Chemistry, Padova University, Italy
2008 - 2009	Research associate at the department of Inorganic Chemistry II, Ruhr-University Bochum (RUB), Germany
2007 - 2008	Research assistant at the department of Inorganic Chemistry II (RUB)
2005 - 2006	Research assistant at the department of Physical Chemistry II (RUB)
2004 - 2006	Tutor for mathematics, physics, chemistry, Latin, French, English and German for pupils of secondary school at “Schülerhilfe”, Bochum, Germany

Education and Training

07/2008 - today	Ph.D studies at the department of Inorganic Chemistry II (Materials Science group, RUB) and the department of Chemistry at Padova University (Padova, Italy)
04/2007 - 04/2008	Master of Science (Chemistry) at the Ruhr-University Bochum ➔ *Degree "Master of Science" (Chemistry), major subject: Materials Science*
10/2006 - 03/2007	Studies at ECPM ➔ École Européenne de Chimie, Polymères et Matériaux: International Engineering school of Chemistry, Polymers and Materials Science in Strasbourg, France
10/2005 - 08/2006	Master of Science (Chemistry) at the Ruhr-University Bochum
10/2002 - 08 2005	Bachelor of Science (Chemistry) at the Ruhr-University Bochum ➔ *Degree "Bachelor of Science" (Chemistry)*
08/1995 - 06/2002	High school: Copernicus-Gymnasium Löningen ➔ *Diploma from German secondary school qualifying for university admission or matriculation*

Honors and Activities

Referee for Journals	*CrystEngComm, Desalination and Water Treatment, ECS Transactions, Functional Materials Letters, Gold Bulletin, Journal of Nanoscience and Nanotechnology, Journal of Physical Chemistry, Nanoscience and Nanotechnology Letters, Optical Materials, Sensors and Actuators B-Chemical, Thin Solid Films*
09/2011	Student Oral Presentation Award at the *EUROCVD2011*
05/2011	Graduate Student Award at the *E-MRS 2011 Spring Meeting*
11/2010 - today	Marie Curie fellowship in the *European Community's Seventh Framework Programme* (FP7/2007-2013) under grant agreement number *ENHANCE-238409*
08/2009 - 10/2010	Dissertation grant from the *collaborative research centre/excellence cluster "Metal-substrate interactions in heterogeneous catalysis", SFB558* (Research Department Interfacial Systems Chemistry (IFSC)) (RUB)

10/2006 - 03/2007	*ERASMUS* studies at ECPM (École Européenne de Chimie, Polymères et Matériaux: International Engineering school of Chemistry, Polymers and Materials Science) in Strasbourg, France

Language skills

German:	Mother tongue
English:	Proficient in speaking, proficient in writing
French:	Advanced in speaking, advanced in writing
Italian:	Advanced in speaking, basic in writing

Further training

Patent law and trademark law

Attendance of "Gewerblicher Rechtsschutz: Patentwesen in den Ingenieurwissenschaften I und II", by Prof. Dr.-Ing. Helge B. Cohausz, Bochum, exam 2010

Basic Scientific Presentation for Natural Sciences, Engineering and Life Sciences

by Dr. Sylvia Löhken (textAtrium), Bochum, December 8th – 10th, 2009

Basic Professional Communication in Science

by Dr. Sylvia Löhken (textAtrium), Bochum, December 14th – 16th, 2010

Getting Research Published

by Jana Kaiser (Language Resource Centre, TU Darmstadt), Bochum, March 10th – 12th, 2010

Publications

---

[1] D. Bekermann, A. Gasparotto, D. Barreca, C. Maccato, E. Comini, C. Sada, G. Sberveglieri, "Co_3O_4/ZnO Nanocomposites: From Plasma Synthesis to Gas Sensing Applications", A. Devi, R.A. Fischer, *ACS Appl. Mater. Interfaces*, 4 (**2012**) 928-934.

[2] A. Gasparotto, D. Barreca, D. Bekermann, A. Devi, R.A. Fischer, P. Fornasiero, V. Gombac, O.I. Lebedev, C. Maccato, T. Montini, G. Van Tendeloo, E. Tondello, "F-Doped Co_3O_4 Photocatalysts for Sustainable H_2 Generation from Water/Ethanol", *Journal of the American Chemical Society*, 133 (**2011**) 19362-19365.

[3] Q. Simon, D. Barreca, D. Bekermann, A. Gasparotto, C. Maccato, E. Comini, V. Gombac, P. Fornasiero, O.I. Lebedev, S. Turner, A. Devi, R.A. Fischer, G. Van Tendeloo, "Plasma-assisted synthesis of Ag/ZnO nanocomposites: first example of photo-induced H_2 production and sensing", *International Journal of Hydrogen Energy*, 36 (**2011**), 15527-15537.

[4] A. Gasparotto, D. Barreca, D. Bekermann, A. Devi, R.A. Fischer, C. Maccato, E. Tondello, "Plasma processing of nanomaterials: emerging technologies for sensing and energy applications", *Journal of Nanoscience and Nanotechnology*, 11 (**2011**) 8206-8213.

[5] D. Barreca, D. Bekermann, E. Comini, A. Devi, R.A. Fischer, A. Gasparotto, M. Gavagnin, C. Maccato, C. Sada, G. Sberveglieri, E. Tondello, "Plasma enhanced-CVD of undoped and fluorine-doped Co_3O_4 nanosystems for novel gas sensors", *Sensors and Actuators B-Chemical*, 160 (**2011**) 79-86.

[6] D. Barreca, A. Devi, R.A. Fischer, D. Bekermann, A. Gasparotto, M. Gavagnin, C. Maccato, E. Tondello, E. Bontempi, L.E. Depero, C. Sada, "Strongly oriented Co_3O_4 thin films on MgO(100) and $MgAl_2O_4$(100) substrates by PE-CVD", *Crystengcomm*, 13 (**2011**), 3670-3673.

[7] D. Bekermann, A. Ludwig, T. Toader, C. Maccato, D. Barreca, A. Gasparotto, C. Bock, A.D. Wieck, U. Kunze, E. Tondello, R.A. Fischer, A. Devi, "MOCVD of ZnO films from bis(ketominato)Zn(II) precursors: structure, morphology and optical properties", *Chemical Vapor Deposition*, 17 (**2011**), 155-161.

[8] D. Bekermann, D. Rogalla, H.W. Becker, M. Winter, R.A. Fischer, A. Devi, "Volatile, Monomeric, and Fluorine-Free Precursors for the Metal Organic Chemical Vapor Deposition of Zinc Oxide", *European Journal of Inorganic Chemistry*, 9 (**2010**) 1366-1372.

[9] D. Bekermann, A. Gasparotto, D. Barreca, A. Devi, R.A. Fischer, M. Kete, U. Lavrenčič-Štangar, O.I. Lebedev, C. Maccato, E. Tondello,G. Van Tendeloo, "ZnO Nanorod Arrays by Plasma-Enhanced CVD for Light-Activated Functional Applications", *Chemphyschem*, 11 (**2010**) 2337-2340.

[10] D. Bekermann, A. Gasparotto, D. Barreca, L. Bovo, A. Devi, R.A. Fischer, O.I. Lebedev, C. Maccato, E. Tondello,G. Van Tendeloo, "Highly Oriented ZnO Nanorod Arrays by a Novel Plasma Chemical Vapor Deposition Process", *Crystal Growth & Design*, 10 (**2010**) 2011-2018.

[11] D. Barreca, D. Bekermann, A. Devi, R.A. Fischer, A. Gasparotto, C. Maccato, E. Tondello, M. Rossi, S. Orlanducci,M.L. Terranova, "Novel insight into the alignment and structural ordering of supported ZnO nanorods", *Chemical Physics Letters*, 500 (**2010**) 287-290.

[12] D. Barreca, D. Bekermann, E. Comini, A. Devi, R.A. Fischer, A. Gasparotto, C. Maccato, G. Sberveglieri,E. Tondello, "1D ZnO nano-assemblies by Plasma-CVD as chemical sensors for flammable and toxic gases", *Sensors and Actuators B-Chemical*, 149 (**2010**) 1-7.

[13] ***HOT ARTICLE:*** D. Barreca, D. Bekermann, E. Comini, A. Devi, R.A. Fischer, A. Gasparotto, C. Maccato, C. Sada, G. Sberveglieri,E. Tondello, "Urchin-like ZnO nanorod arrays for gas sensing applications", *Crystengcomm*, 12 (**2010**) 3419-3421.

[14] D. Bekermann, D. Barreca, A. Gasparotto, H.W. Becker, R.A. Fischer,A. Devi, "Investigation of niobium nitride and oxy-nitride films grown by MOCVD", *Surface & Coatings Technology*, 204 (**2009**) 404-409.

[15] D. Bekermann, D. Pilard, R.A. Fischer, A. Devi, "Zinc Malonate Based Precursors for MOCVD of ZnO", *ECS Transactions*, 25 (**2009**), 601-608.

[16] A. Baunemann, D. Bekermann, T.B. Thiede, H. Parala, M. Winter, C. Gemel,R.A. Fischer, "Mixed amido/imido/guanidinato complexes of niobium: potential precursors for MOCVD of niobium nitride thin films", *Dalton Transactions* (**2008**), 3715-3722.

[17] D. Bekermann, D. Barreca, A. Devi, A. Gasparotto, R.A. Fischer, "MOCVD of Niobium Nitrides and Oxy-Nitrides Using an All-Nitrogen-Coordinated Precursor: Thin-Film Deposition and Mechanistic Studies", *ECS Transactions*, 16 (**2008**), 235-242.

Conferences

2011 Perspectives of Organometallics and Materials Chemistry

Talk: D. Bekermann, D. BarrecaE. Comini, A. Devi, R. A. Fischer, A. Gasparotto, M. Kete, U. Lavrenčič-Štangar, O. I. Lebedev, C. Maccato, C. Sada, G. Sberveglieri, E. Tondello, G. Van Tendeloo, "*Multi-functional aligned zinc oxide nanorod assemblies by a novel plasma-assisted chemical vapor deposition process*", 10 September 2011, Bochum, Germany.

2011 EUROCVD 18

Talk: D. Bekermann, D. Barreca, E. Comini, A. Devi, R.A. Fischer, A. Gasparotto, M. Gavagnin, C. Maccato, C. Sada, G. Sberveglieri, E. Tondello, *"Development of Co_3O_4-Based Nanomaterials for Gas Sensing Applications"*, Kinsale, Co. Cork, Ireland, 4-9 September 2011.

Invited talk: A. Gasparotto, D. Barreca, D. Bekermann, A. Devi, R. A. Fischer, C. Maccato, E. Tondello, "*Plasma processing of nanomaterials: emerging technologies for sensing and energy applications*", 4-9 September 2011, Kinsale, Co. Cork, Ireland.

2011 European Materials Research Society Spring Meeting E-MRS ICAM IUMRS

Invited talk: D. Bekermann, D. Barreca, E. Comini, A. Devi, R.A. Fischer, A. Gasparotto, M. Kete, U. L. Štangar, O. I. Lebedev, C. Maccato, C. Sada, G. Sberveglieri, E. Tondello, G. Van Tendeloo, *"Multi-functional ZnO nanorod arrays by plasma-assisted chemical vapor deposition"*, 9-13 May 2011, Nice, France.

Poster: D. Bekermann, D. Barreca, E. Comini, A. Devi, R.A. Fischer, P. Fornasiero, A. Gasparotto, M. Gavagnin, V. Gombac, C. Maccato, T. Montini, O.I. Lebedev, C. Sada, G. Sberveglieri, S. Turner, E. Tondello, *"An innovative plasma-assisted process to Co_3O_4 nanomaterials for energy and sensing applications"*, 9-13 May 2011, Nice, France.

Poster: Q. Simon, D. Bekermann, A. Gasparotto, C. Maccato, D. Barreca, A. Devi, R.A. Fischer, "Ag/ZnO nanocomposites by a novel RF-Sputtering/PE-CVD process", 9-13 May 2011, Nice, France.

2011 International Symposium on Advanced Complex Inorganic Nanomaterials - ACIN 2011

Poster: Q. Simon, D. Bekermann, A. Gasparotto, C. Maccato, D. Barreca, A. Devi , R. A. Fischer, *"M(M = Ag, Cu)/ZnO nanocomposites by a combined RF-Sputtering/PE-CVD process: synthesis and functional properties"*, 11-14 September 2011, Namur, Belgium.

2010 ACS Fall 2010 National Meeting & Exposition

Talk: D. Bekermann, D. Barreca, E. Comini, A. Devi, R.A. Fischer, A. Gasparotto, C. Maccato, G. Sberveglieri, E. Tondello, *"ZnO nanostructures with outstanding gas sensing performance"*, 22-26 August 2010, Boston, Massachusetts, USA.

Poster: D. Bekermann, A. Devi, R.A. Fischer, *"Precursor Chemistry for MOCVD of functional metal oxides of Zn and Co"*, 22-26 August 2010, Boston, Massachusetts, USA.

2010 EMRS 2010:

Poster: D. Barreca, D. Bekermann, A. Devi, R.A. Fischer, A. Gasparotto, U. Lavrenčič Štangar, O.I. Lebedev, C. Maccato, E. Tondello, G. Van Tendeloo, *"Highly oriented ZnO nanorod arrays for advanced light-activated applications"*, 8-10 June 2010, Strasbourg, France.

2010 3. NRW Nano-Konferenz 2010

9-10 September 2010, Dortmund, Germany.

2010 XXXVIII Congresso Nazionale della Divisione di Chimica Inorganica della Società Chimica Italiana

Poster: D. Barreca, D. Bekermann, E. Comini, A. Devi, R.A. Fischer, A. Gasparotto, C. Maccato, C. Sada, G. Sberveglieri, E. Tondello, *"1-D ZnO Nano-Assemblies As Gas Sensors With Outstanding Performances"*, 13-16 September 2010, Trieste, Italy.

2009 ECS 216th Meeting: EUROCVD 17

Poster: D. Bekermann, A. Devi, R.A. Fischer *"Zinc malonate based precursors for MOCVD of ZnO"*, 4-9 October 2009, Vienna, Austria.

2008 ECS 215th Prime Meeting

Poster: D. Bekermann, D. Barreca, A. Devi, A. Gasparotto, R.A. Fischer *"MOCVD of Niobium Nitrides and Oxy-Nitrides Using an All-Nitrogen-Coordinated Precursor: Thin-Film Deposition and Mechanistic Studies"*, 12-17 October 2008, Honolulu, Hawaii, USA.

Schools and Workshops

2011 1st Winter school - ENHANCE

Scopes: Thin film deposition technologies such as Metalorganic Chemical Vapor Deposition (MOCVD), Atomic Layer Deposition (ALD), Plasma-Enhanced MOCVD, PE-ALD, Molecular Layer Deposition (MLD), Electron or Ion Beam Induced Deposition (EBID or IBID)

Poster: D. Barreca, D. Bekermann, E. Comini, A. Devi, R.A. Fischer, P. Fornasiero, A. Gasparotto, M. Gavagnin, V. Gombac, C. Maccato, T. Montini, O. I. Lebedev, C. Sada, G. Sberveglieri, S. Turner, E. Tondello, "*A novel PECVD process for Co_3O_4 nanomaterials functionalized for energy and sensing applications*".

25-26 January 2011, Ruhr-University Bochum, Germany

2011 2nd Workshop (WS-2) - ENHANCE

Scopes: Characterization of Thin Films by X-ray Scattering Methods, Ion Beams and Electron Diffraction

4-8 April 2011, University of Helsinki, Finland

2011 3rd Workshop (WS-3) - ENHANCE

Scopes: Leading technologies for gas phase deposition of materials for Compound, Silicon, and Organic semiconductor device applications

24-26 May 2011, AIXTRON SE, Herzogenrath, Aachen, Germany

2012 2nd Winter school - ENHANCE

Scopes: Fabrication, integration and characterization of new materials, ALD, Intellectual property

Talk: D. Bekermann, A. Gasparotto, D. Barreca, C. Maccato, A. Devi, R. A. Fischer, E. Tondello, "*Multifunctional Co_3O_4/ZnO Nanomaterials by Plasma Assisted CVD*".

9-12 January 2012, University of Helsinki, Finland